THE UNIVERSITY OF CHICAGO

DEVELOPMENT OF LARGE-AREA MCP-PMT PHOTO-DETECTORS FOR A PRECISION TIME-OF-FLIGHT SYSTEM AT THE FERMILAB TEST BEAM FACILITY

A DISSERTATION SUBMITTED TO
THE FACULTY OF THE DIVISION OF THE PHYSICAL SCIENCES
IN CANDIDACY FOR THE DEGREE OF
DOCTOR OF PHILOSOPHY

DEPARTMENT OF PHYSICS

BY
EVAN ANGELICO

CHICAGO, ILLINOIS
AUGUST 2020

TABLE OF CONTENTS

LIST OF FIGURES vii

LIST OF TABLES xviii

ACKNOWLEDGMENTS xix

ABSTRACT xxiii

1 INTRODUCTION TO PARTICLE TIME-OF-FLIGHT USING LARGE AREA PICOSECOND PHOTODETECTORS 1
1.1 Introduction to Large Area Picosecond Photodetectors 1
1.1.1 Conventional photo-multiplier tubes 1
1.1.2 Micro-channel plate based photo-multiplier tubes 2
1.1.3 Large Area Picosecond Photodetectors 4
1.1.4 Incom Inc. 5
1.1.5 Summary 6
1.2 Introduction to time-of-flight 7
1.2.1 Kinematics of particle identification 7
1.3 LAPPDs as a time-of-flight detector 10
1.3.1 Properties of Cherenkov light 11
1.3.2 Timing resolution of LAPPDs 14
1.4 Motivation for an LAPPD time-of-flight system at the Fermilab Test Beam Facility 15
1.5 Structure of thesis 17

2 BATCH PRODUCTION OF LARGE AREA PICOSECOND PHOTODETECTORS 19
2.0.1 Motivation for batch production 19
2.1 Air-transfer batch-production method 19
2.1.1 Experience from PMT batch production 20
2.1.2 Four stages of LAPPD fabrication 21
2.1.3 The dual-vacuum air-transfer method 22
2.1.4 The LAPPD^{TM} package 25
2.1.5 Mechanically supporting the LAPPD package 27
2.1.6 The hermetic indium-alloy seal 28
2.1.7 Barois photocathode synthesis 31
2.1.8 Micro-channel plates during photocathode synthesis 34
2.2 Vacuum-transfer fabrication 36
2.3 Diagnostic tools critical to developing a seal procedure 39

3 LAPPD SIGNAL READOUT . . . 41
3.1 Micro-strip transmission-line readout . . . 41
3.1.1 Position reconstruction using the strip-line readout . . . 43
3.1.2 One-sided readout . . . 44
3.2 Capacitively-coupled pickup . . . 46
3.3 Connecting strips to digitizing electronics . . . 48
3.3.1 The ANNIE Analog Pickup Board . . . 49

4 HARDWARE FOR LAPPD OPERATION IN A TIME-OF-FLIGHT SYSTEM . 51
4.1 The LAPPD frame . . . 52
4.1.1 High voltage distribution . . . 52
4.1.2 The mechanics of safely holding an LAPPD . . . 53
4.1.3 Design considerations for LAPPD frames . . . 54
4.2 The LAPPD station design . . . 55
4.3 Peripheral hardware . . . 56
4.3.1 High voltage dividers . . . 56
4.3.2 Synchronization hardware . . . 59
4.3.3 Control system for front-end electronics . . . 61
4.4 Experimental locations and layouts . . . 61
4.4.1 Radiation length . . . 64

5 FRONT-END ELECTRONICS SYSTEM . . . 66
5.1 Properties of the PSEC4 chip . . . 67
5.1.1 Constant sampling rates . . . 67
5.1.2 Triggering and wraparound sample . . . 68
5.1.3 Timing resolution . . . 69
5.1.4 Noise . . . 70
5.1.5 Synchronization . . . 71
5.2 Architecture of the time-of-flight front-end electronics system . . . 73
5.2.1 ACDC board . . . 74
5.2.2 Annie Central Card (ACC) . . . 77
5.2.3 Control computer . . . 79
5.3 Priority improvements to the electronics system . . . 80
5.3.1 Trigger-rate limitations . . . 81
5.3.2 The USB communication system . . . 83
5.3.3 Minimum trigger-threshold . . . 84
5.3.4 Trigger-location identification . . . 85
5.3.5 ACDC rev C . . . 85
5.3.6 PSEC4a . . . 85
5.3.7 References for users and developers . . . 86

6 EVENT TRIGGER . . . 87
6.1 Trigger structure . . . 87
6.1.1 Beam trigger . . . 88
6.1.2 ACDC self-trigger . . . 88
6.1.3 Trigger-state definitions . . . 89
6.1.4 Simultaneous triggering of multiple LAPPD stations . . . 90
6.2 Mapping of strips to electronics channels . . . 91

7 ANALYSIS OF LAPPD SIGNALS FROM CHARGED PARTICLES . . . 94
7.1 Description of datasets . . . 94
7.1.1 Run plan for the MT6.2 enclosure TOF prototype . . . 94
7.1.2 Observations during the trigger-tuning period . . . 95
7.2 Examples of raw data . . . 96
7.2.1 Signals from Tile 31 . . . 97
7.3 Signal-processing techniques . . . 101
7.3.1 Constant-fraction discrimination . . . 102
7.3.2 Template fitting . . . 104
7.3.3 First-pass pulse discrimination . . . 107
7.4 Transverse-position reconstruction . . . 109
7.5 Longitudinal-position reconstruction . . . 114
7.5.1 Spatial distribution of cosmic rays . . . 117
7.6 Charge spectrum . . . 118
7.6.1 Gain . . . 118
7.6.2 Spectra . . . 119
7.7 Coincident particle events . . . 120

8 ESTIMATE OF THE PARTICLE IDENTIFICATION SENSITIVITY . . . 121
8.1 Qualities of the present setup . . . 121
8.2 Improvements to time-of-flight sensitivity in the next 1 - 5 years . . . 124

9 SUMMARY . . . 126

A NEXT STEPS TOWARD A PERMANENT LAPPD-BASED TOF PID SYSTEM AT THE FTBF . . . 128
A.1 Present particle identification systems at the FTBF . . . 128
A.2 The design of a permanent LAPPD TOF system at MTest . . . 129
A.2.1 Position calibration . . . 131
A.2.2 Analysis and DAQ system . . . 131
A.3 Action-items for the next iteration that have the largest positive impact . . . 132
A.3.1 Electronics firmware . . . 132
A.3.2 Trigger improvements . . . 132
A.3.3 Electronics calibration . . . 133
A.3.4 Readout improvements . . . 134
A.3.5 Studying response at high spill intensities . . . 134

B PSEC4 ELECTRONICS CHARACTERIZATION AND CALIBRATION 136
B.1 Linearity 136
B.2 Wraparound offset and time-base calibration 138
B.3 Relative time-of-arrival jitter between two channels 143

C RADIATION LENGTH CALCULATION 145

D ASSEMBLY PROCEDURE FOR GENERATION-II LAPPDS 149
D.0.1 Assumptions of the preparation of materials 149
D.1 Profiling the tile-base 150
D.1.1 Depth measurements 151
D.1.2 Allocation of buttons and stack test 152
D.2 Conditioning the micro-channel plates 154
D.3 Assembly 155
D.3.1 High voltage electrodes 155
D.3.2 Non-evaporable getter strips 155
D.3.3 Swaging the tubes and leak checking 156
D.3.4 Etching of sealing-surface and indium 156
D.3.5 The capillary-action seal 157
D.3.6 Press mechanism 159
D.3.7 Internal insulation 159
D.4 Sealing cycle 159
D.5 Venting 161
D.5.1 Argon leak signal 161
D.5.2 Helium leak checking 161

E AIR-TRANSFER DEPOSITION AT UNIVERSITY OF CHICAGO 162
E.0.1 Typical Sb quality before sealing 162
E.0.2 Cesium source description 163
E.0.3 Thermal configuration of manifold and LAPPD 164
E.0.4 Measurements of quantum efficiency 164
E.0.5 Initial growth of photocurrent 166
E.0.6 Time dependence of spatial growth 168

F TIME-OF-ARRIVAL STATISTICS OF THE FIRST PHOTOELECTRON 169
F.1 Timing from a Cherenkov-light source 169
F.2 Timing variations of photoelectron arrivals induced by the MCP-pore bias angle 172
F.2.1 For a highly focused laser light-source 172
F.3 Combining timing induced by the Cherenkov emission profile and pore geometry 175
F.3.1 Other contributions to timing 178

LIST OF FIGURES

1.1 Photo-detection starts with a photon impinging on the glass window. The photon is converted by the photocathode into a photoelectron with probability equal to the quantum efficiency. Accelerating high voltage is applied to the internal components to accelerate the photoelectron into an MCP pore. The MCPs are coated with a secondary-emitting layer. Electrons strike the pore walls ~10 times, forming an electron avalanche or cloud. The electron cloud, typically comprised of 10^7 electrons, produces a negative polar pulse with 10% to 90% rise-time on the order of 250-1000 ps depending on the geometry of the internal components, and 10 - 40 mV amplitude on 50 Ω impedance transmission lines. 2

1.2 Photograph of an 8"×8"glass capillary array (GCA) fabricated by Incom Inc, courtesy of Michael J. Minot. Using atomic layer deposition, the GCA will later be coated with resistive and emissive coatings. In this un-coated state, the glass is slightly translucent and has approximately 64% open area from the close packing of 20 μm pores. 3

1.3 Photograph of a Large Area Picosecond Photodetector (LAPPD) fabricated by Incom Inc. next to a Photonis Planacon MCP-PMT for comparison [9, 10]. . . . 5

1.4 Diagram of a general time-of-flight detector system. The detectors can be any sensor that records the time and position of an impinging particle. By measuring the velocity and momentum of the particle, the mass may be inferred. 8

1.5 Contours of detector timing resolution needed to distinguish 68.27% of pions and kaons as a function of momentum and path-length. Contours are calculated using the Equation (1.4) in combination with a Gaussian smeared time-of-arrival with σ equal to the number on the contour. Dotted red lines represent example detector separations. This plot does not include uncertainties in the measurement of momentum and path-length. 9

1.6 The quantum efficiency of LAPPD37 including the transmission of its 5 mm thick Schott Borofloat 33 (B33) window is shown in black with black axis labels. The Cherenkov emission spectrum [27] of a 10 GeV/c pion is plotted in blue in units of number emitted per cm of glass per nanometer wavelength. The product of these two curves, representing the number of photoelectrons per cm of glass, is shown in solid red. An integral of this spectrum from 250 nm to 600 nm gives about 66 photoelectrons per cm of glass. 11

1.7 A comparison of the quantum efficiencies of three LAPPDs fabricated by Incom, Inc. Data are courtesy of Incom, Inc. A significant part of the ultra-violet Cherenkov emission spectrum is available to fused silica windows which transmits down to 200 nm. By integrating over the emission spectrum as in Figure 1.6, the number of detected photoelectrons becomes about 213 per cm, about a factor of 3 larger than B33. No LAPPDs with fused silica windows were used in this thesis. 12

1.8 Cherenkov emission is geometrically constrained such that photons are emitted at an angle of $\cos\theta_c = 1/\beta n$ relative to the particle axis. When there is no dispersion, i.e. n is constant with wavelength, this creates an infinitely thin photon wavefront on the shape of a cone that propagates out from the particle's trajectory. A particle traversing the glass window of an LAPPD (light blue) will produce Cherenkov photons that are converted to photoelectrons by the photocathode (shown as a brown line). The Cherenkov photons have a maximum radius at the photocathode related to the window thickness. 13

2.1 The photomultiplier batch production station purchased from the Photonis Lancaster plant [56]. This system served as a model for the development of the LAPPD batch production system described in this chapter. 20
2.2 The outer low-vacuum vessel that provides thermal insulation to the photodetector during bake-out, a low oxidation environment for the seal metals, and equalization of the pressure across the molten seal interface. 23
2.3 The physical layout and photocathode-metal transport temperatures of the inner vacuum manifold. The manifold connects to the LAPPD inner volume via tubulation that penetrates the outer vacuum vessel. The inner vacuum volume and outer vacuum volume are hermetically isolated after the LAPPD seal is formed. 24
2.4 The three main components of an LAPPD: (a) the UC monolithic ceramic tile base; (b) the micro-channel plates, shown here with a dark-colored secondary emitting coating; (c) the entrance window, shown here with a pre-deposited antimony layer and thin-film metallic layers around the perimeter for sealing. . . . 25
2.5 Copper tubes that connect the tile base to the UHV manifold and copper pins that provide high voltage to internal components. This image also features a close-up of a seal metalization, consisting of 200 nm 80-20 NiCr bonded to the ceramic, followed by 200 nm of Cu without a vacuum break in-between coatings. 26
2.6 On the left, the tile base during assembly showing the button columns, non-evaporable getter stacks, and high voltage electrodes connected to pins in the sidewall. On the right, a finite-element analysis of the stress on a B33 window under vacuum. 27
2.7 An assembled tile clamped in place in the compression fixture prior to sealing. The indicated components are: (1) the lower NiCr heater assembly; (2) the bottom compression fixture plate; (3) the tile assembly consisting of ceramic base, internal components, and glass window; (4) the compression mechanism; (5) floating rigid press bars; (6) the upper compression fixture plate; and (7) the upper NiCr heater assembly. 29
2.8 The thermal cycle temperature (top) and dual-vacuum pressure (bottom) from the Tile 31 seal-and-bake procedure. The feature around 220 °C is due to the formation of the capillary seal, isolating the outer and inner vacuum volumes from each other after the In-Ag allow has melted at around 143 °C. 30

2.9 Diagram of the alkali vapor source. The left-hand section is the ampoule chamber; the right-hand section is the source chamber. The cesium is distilled into the right-hand section to avoid possible oxidizing reaction with the glass and other contaminants on the ampoule. 31
2.10 A 2D stage for mapping photo-response during and after photocathode synthesis. The LAPPD seen here is still mounted on the fixture inside of the outer vacuum vessel. After the seal procedure is complete, photocathode monitoring hardware is easily placed on top of the tile assembly while it is still connected to the pump. 32
2.11 Successive maps of the photo-response for Tile 31 during photocathode synthesis. 33
2.12 The resistance of the stack of two micro-channel plates and spacers during a cesiation cycle, showing that the plate resistance recovers after an initial large drop. 34
2.13 An illustration of both the air-transfer and vacuum-transfer LAPPD fabrication processes, emphasizing their differences. The vacuum transfer process does not rely on the existence of inlet tubes and a dual vacuum topology. However, the vacuum transfer process may benefit from the use tubulation to allow for leak checking the indium seal and keeping the internals on a dedicated pump. 36
2.14 A conceptual drawing of an air-transfer production chamber that fabricates 18-LAPPDs at once [70]. The LAPPDs may be stacked vertically, stack having heating elements, sealing hardware, and photocathode diagnostic hardware. All LAPPDs have tubulations that lead to a common manifold that sources high vacuum and photocathode metals. The outer chamber, with its base in black, is not heated and may be low vacuum. 37
2.15 A conceptual drawing of a modular LAPPD bake-and-seal stack. Three LAPPDs are assembled in a vertical stack with tubes connected to a common UHV manifold. Heaters above and below control the seal-and-bake thermal cycle, with insulation for thermal uniformity not shown. 38
2.16 Demonstrations of the four main diagnostic tools used for diagnosing failed indium seals. The four methods are (top-left) physically removing the bonded window using a variety of destructive tools; (top-right) observing exposed indium surfaces with a scanning electron microscope (SEM) with built-in electron dispersive spectroscopy (EDS) [71]; (bottom-left) dental x-ray while the window is still bonded; (bottom-right) depth-profiling optical microscopy of seal surfaces before and after sealing [73]. 40

3.1 Photograph of a strip-line pickup geometry. This pickup pattern was designed and characterized by the authors of Reference [74]. The perimeter is a top-down view of the sealing surface. Each strip has 50 Ω characteristic impedance when a ground-plane is attached to the air-side of the glass substrate. 42
3.2 The digitized signals of 14 adjacent strip-lines of LAPPD 43 induced by a charged particle. The signal from each strip-line is offset by 25 mV on the y-axis for clarity. The amplitudes as a function of strip number can be used to constrain the position of the electron cloud in the dimension transverse to the strip-lines to around 700-1000 μm [8, 5]. 43

3.3 An LAPPD pulse showing the left (blue) and right (green) sides of a single strip-line. The time-of-arrival difference multiplied by the average propagation velocity is the parallel position of the electron-cloud-induced image. 45
3.4 Photograph of the hand-made capacitively-coupled pickup used in this thesis work. The glass strip-line substrate and PCB adapter cards are glued to a copper-coated G10 substrate using silicone and soft epoxy. The PCB internal ground planes are connected to the strip-line back-plane using an exposed ground on the underside of the PCB and RF spring fingers. The interface between silver strips and PCB adapters is bridged by 3-mil-thick copper shims soldered to the strip-lines and PCB ports. 46
3.5 Photograph of the pogo-board that electrically adapts the ends of strip-lines to a printed circuit board. The base PCB contains holes located such that small screws may compress the pogo pins against the strips. The pogo pins also hold the LAPPD in mechanical compression to the PCB backplane, which may then be mounted to a fixturing structure. 49
3.6 Photograph of the ANNIE Analog Pickup Board designed by Bernhard Adams at Incom Inc. Trace lengths are matched to a tolerance of 0.2 mm. Pogo pin contacts, and 10 kΩ drainage resistors mounted on the surface, can be seen on the left and right sides of the board. Mounting holes that allow for pogo-board compression are seen nearby the pogo pin electrical contacts. 50

4.1 The front face of Incom LAPPD 42 instrumented with high voltage inputs, digitizing electronics, and mechanical fixturing for use in the FTBF LAPPD TOF system. A dark-box comes down from above and mates with the black cardboard rim seen at the bottom of the photograph. In this particular photo, two LAPPDs are stacked one after the other for a close-proximity particle-coincidence measurement. Photograph credit: Giulio Stancari. 51
4.2 The underside of the Incom LAPPD frame reveals sping-loaded pogo pins that apply mechanical force to the HV electrodes of the LAPPD. On the left, a vertically oriented pogo pin makes electrical contact with a strip on the base, electrically connected to a micro-channel plate surface. On the right, a horizontally oriented pogo pin makes electrical contact with the photocathode. These pins are soldered to SHV connectors mounted to the frame. 53
4.3 An orthogonal projection of the LAPPD frame, emphasizing the mechanical elements. The only elements that make contact with the LAPPD packaging are the pogo pins of the pogo-board shown in the top projection, and the high-voltage pogo pins which are not shown. The plastic LAPPD frame does not contact the LAPPD directly. 54
4.4 The second-iteration dark-box design consists of an aluminum base-plate machined by undergraduates, an 80/20 t-slot rim [88], and black foam board box sized to fit in the slot of the 80/20. The rim is bolted to the aluminum frame. The aluminum frame is bolted to an exterior 80/20 bar. All interfaces are covered with black silicone. A hole in the base plate covered by a slotted packing foam allows for cables to be fed through. 56

4.5 An example high-voltage divider diagram for LAPPD 43, which has 16.5 MΩ and 15.7 MΩ MCPs. Zener diodes with a breakdown voltage of 200 V are used to set a constant voltage across the gap between the MCPs and above the anode. Capacitors may be used to ground high-frequency ripple from supplies. Anode strip-lines are grounded to drain charge buildup if strips are un-terminated. . . . 57
4.6 Photograph of a White Rabbit (WR) test-setup in the Fermilab Lab 6 dark-room facility. A WR-Switch and two WR-ZEN modules are installed on the rack. They are synchronized with each other over the yellow optical fibers on the right. . . . 60
4.7 The MT6.2 beam-dump configuration. The concrete beam-dump is on the right-hand side with triggered particles going from right to left. This 5-foot-long crawl-space is behind the cable and materials cabinets at the Meson West FTBF building. 62
4.8 The installation of the LAPPD TOF system in the MT6.2 enclosure. The beam dump is shown on the right-hand side. Three LAPPD stations were installed for redundancy and further constraints on path-length. The multi-wire proportional chamber hardware seen on the far right is part of the FTBF standard-diagnostics instrumentation. Photo credit, Giulio Stancari. 63
4.9 Top-down diagram of all experimental hardware for the MT6.2 enclosure configuration. The three LAPPD stations are represented by their dark-boxes as black rectangles. "RPi" objects are raspberry-pi electronics controllers. Low voltage DC (LV DC) supplies source power to front-end electronics. The two scintillator paddles on left and right of the entire TOF system are one component of the trigger. 64

5.1 The waveforms of five calibration channels overlayed for board 0 and board 2. These signals are sourced by a single White Rabbit ZEN module whose output is split. The "trigger location" is the region where the sine waves have a glitch. The initial time of sampling is just after the trigger location, with circular buffer wrapping around the end of this displayed wave. 68
5.2 Noise data accumulated from 4 uncalibrated boards while they are connected to LAPPD strip-line anodes. The bins contain measured signal on 256 samples of 30 channels on four boards from 1,000 events before a calibration of voltage linearity. The obvious excesses from the main peak are due to the corrupt trigger samples, which affect some channels more than others. The samples not contained in the trigger region have a noise of 1.89 mV standard deviation. The strip-lines that are attached to the electronics in this dataset may increase the noise level due to their RF-antenna-like geometry. 70
5.3 An example of two outputs from the WR-ZEN modules: 250 MHz 1.2 Vpp sine wave digitized by a Tektronix DPO7500 series oscilloscope. 71
5.4 Phase jitter measured from 15k events of two WR-ZEN outputs separated by 300 m is 5.2 psec standard deviation. The non-gaussian tails are suspected to be generated by the active feedback mechanisms of the WR system throughout the course of measurement. 72

5.5 This diagram shows the control and communication structure of a DAQ system for recording LAPPD data using the PSEC4 electronics. Lines of communication, as well as their communication protocol, connect the control computer, Raspberry Pi [95], Annie Central Card (ACC), and up to 8 ACDC boards. Raw data are transferred upstream from the ACDC, to the ACC, and to the control computers which have hard memory. 74
5.6 Photograph of the ACDC rev B board with (1) LVDS communication lines to the ACC, (2) 5V 2A power input, (3) five PSEC4 chips, (4) 5-way synchronization splitter board, (5) SAMTEC cable signal input, and (6) White Rabbit synchronization input. 75
5.7 Photograph of the Annie Central Card (ACC) developed by Mircea Bogdan in the Electronics Design Group at University of Chicago. This board has hardware to control up to 8 ACDC boards. It manages a number of ACDC operations including data transfer and the Level 2 trigger which enters through one of the SMAs shown in the photograph. 78

6.1 A diagrammatic top-down view of the MT6.2 beam-dump configuration, emphasizing the elements of the trigger. Particles travel from left to right. The black rectangles are scintillation counters. The LAPPDs and front-end electronics are between the counters and trigger asynchronously. Data are latched and held until the delayed coincidence trigger arrives. 87
6.2 Diagram of the map between front-end board number, channel number, and strip number for the ANNIE readout board. The chip that channels belong to is indicated by the green brackets on the edges. Using this particular readout design, both ends of the strip are digitized by the same board, but not always by the same chip. 91
6.3 Photo of the PCB for distributing WR-ZEN synchronization signals to one channel on each PSEC4 chip. This board bridges the two SAMTEC connector inputs on the ACDC board. The next iteration of the PCB should not consider trace length matching (the "trombones" and squiggles seen in light green) as each chip already has a constant relative time offset that requires calibration. 93

7.1 An event from data-set # 1 with LAPPDs 43 and 42 in close proximity measuring the same cosmic ray particle. Both sides of four strips are shown, with the left side of each strip at 50% opacity and the right side at 100% opacity. The sharing of charge among neighboring strips allows for transverse position reconstruction. Statistical distributions of charge sharing are used to measure the effective transverse size of the charge-cloud image. 97
7.2 A 2-D display of raw data from two simultaneously triggered LAPPDs in data-set # 1. Each sub-plot represents half of a digitized LAPPD area. The left sides of strips are on the bottom half of each sub-plot, and right sides on the top. The location of a de-coupled strip, as described in the text, is called out. More can be seen from y = [0, -3] on the right-hand subplot. 97

7.3 A photograph of Tile 31 instrumented with a modified Incom frame for distributing high voltage to brazed copper pins. The smaller MCP-PMT on the right is a Photonis Planacon. 98
7.4 Raw data from 6 neighboring strips on Tile 31 detecting a cosmic ray particle. The open-ended readout scheme is demonstrated here, showing prompt and reflected pulses on each channel. The transverse spread of the amplitudes is larger than the directly coupled LAPPD, due to the geometrical layout of the strips and their distance to the internal anode. A few samples at about 36 ns on strip 25 are corrupt. 99
7.5 The heat-map view of a different event from Tile 31, showing prompt and reflected pulses over the full 8"×8"face of the LAPPD. The PSEC4-chip constant-timing offsets appear as vertical discontinuities in the image. Trailing ripples seen here are not always present in the direct coupled case for Generation-I LAPPDs. . . 100
7.6 The median waveform for cosmic rays measured by LAPPD 43 as a function of pulse-amplitude. Left: the median waveforms of 20 bins of increasing pulse-amplitude. Right: the 20 median waveforms normalized by their peak amplitude. The procedure for producing the median waveform is described in the main text. Error-bars on the right-hand plot are enlarged by a factor of 20 to emphasize spread in the tails and leading edge. Error-bars represent the standard deviation of each sample divided by $\sqrt{N}$ where N is the number of pulses processed, ranging from 500 to 7,000 pulses depending on the amplitude bin (see Figure 7.7). . . . 102
7.7 The number of pulses contained in each of the 20 pulse height bins used to reconstruct the median waveforms shown in Figure 7.6. The LAPPD 43 has a 5 mm thick B33 window, predicting about 20 - 30 photoelectrons per charged particle at a gain of about 1-2 $\times$ 10^6. The ordinate is used to calculate the standard error of each sample in Figure 7.6 103
7.8 The NNLS matrix element $\mathbf{A}$ and solution vector x in cartoon form. The blue pulses in the matrix represent noiseless templates encoded in each row of the matrix. Each element of the solution vector represents a "component" of the full waveform appearing at a time indexed by the vector index with scale equal to the value of the vector at that index. The vector elements on the right, if representing a result of the NNLS algorithm, would represent a few photons arriving near the end of the event window. 105
7.9 The output of the NNLS method is a vector that represents components of the full fit shown in solid black. The sum of all components is the solid blue curve. The fit results are sensitive to the template waveform used. 106
7.10 Rise-times of pulses from both LAPPDs in the cosmic ray data-set. This measurement uses the time difference between the 10% and 90% of max calculated by a CFD algorithm on the raw waveform. The raw waveforms are sampled at 156 ps time interval. The coarse, un-interpolated sampling causes the CFD to occasionally over or under approximate the rise-time due to noise on the raw wave. This is the main contribution to the tails of this distribution. 108

7.11 The linear relationship between pulse height and pulse integrals for two integration ranges: (top row) the 5 ns interval shown in Figure 7.6 containing the tails of the pulses and (bottom row) from 2 ns before the peak time to when the pulse starts returning to baseline and falls below 90% of its peak value. Residuals indicate a 7-15 mV·ns RMS deviation from linearity. 110
7.12 An example of the transverse charge distribution for one cosmic ray particle event digitized on half of an LAPPD. The top plot is the right side of the strips and the bottom plot is the left. Each black data point represents the position and charge on each strip-line, integrated over the time of the primary pulse. Strip-widths of 5.13 mm are shown as black horizontal bars. A gaussian is fit to a range that includes 4-5 strips around the peak. Unquantified charge errors are not included in the fit. 111
7.13 Left: the transverse FWHM distribution for 24,000 events from dataset # 1 with LAPPD 43 and 42. The distributions have been normalized for comparison. The width of the distribution quoted in the legend is the standard deviation. Right: the mean of the Gaussian fit to the transverse-charge profile. The peaks of this distribution, due to a threshold effect described in the main text, are located at the center of each strip. 112
7.14 A comparison between the Gaussian fit and charge centroid position reconstruction methods. Strip positions are shown as vertical lines. On the right, the positions for the filtered data-set are shown for both methods. On the left, the event-by-event position difference between the two methods show that they agree to about 1.1 mm. 114
7.15 The pulse-pair time-delays for strip number 10 on LAPPD 42 from a uniform flux of cosmic rays from dataset # 1. The dips halfway through the distribution are inactive area occluded by the x-spacer. The bias from symmetry about zero is due to a constant chip-to-chip timing offset of the digitizing channels used on either end of the strip. 116
7.16 A 2-D histogram of reconstructed positions for LAPPD 42 (left) and LAPPD 43 (right), with the longitudinal position in units of delay time. A 0.8 σ gaussian filter has been applied to the image so that the x-spacer feature is more noticeable. 117
7.17 Charge distributions for LAPPDs 43 and 42 with 0 V (left) and -20 V (right) applied to the photocathode gap. The signal source is 120 GeV/c protons from datasets # 3 and # 4. 119

8.1 The contours of maximum momentum where 68.27% of particles are correctly identified for 14 ps and 19 ps time-of-flight resolution. The LAPPD TOF system at present has a maximum detector separation of 5 m. A proposed permanent system could have separations of 5, 10, 30, and 45 m. These distances are pointed out in red with maximum momentum annotated for each detector separation. The momentum of the pion and kaon is the same, and the momentum and path length is perfectly known. 123

A.1 The top-down layout of MTest with four possible locations for LAPPD stations shown as red rectangles, labeled A, B, C, and D. The stations have a small footprint, mounting to new or existing 80/20 structures in the beam enclosures. The range of LAPPD separations allows for a variety of momentum ranges to be probed. Station placement maximizes coverage for experiments located in the main experimental areas. 130

B.1 The waveforms of five calibration channels overlayed for board 0 and board 2. These signals are sourced by a single White Rabbit ZEN module. The trigger location is visible as the region in time where the sine wave deviates. About 30 samples covering the trigger location are ignored for the analysis of this section. 139
B.2 This ellipse formed by 10,000 events sampled by one adjacent pair of sample indices is a result of the parameterization described in the text. Two visible features of this ellipse are likely due to a lack of linearity calibration described in Section B.1: the peaked cusps at $V_{n+1} + V_n < 100\text{mV}$ and the slight rotation of the ellipse. The cusp-like samples shown in blue were ignored in the fit. A few data points lie significantly interior to the ellipse, possibly indicating trigger synchronization issues [143]. The fit uses the least-squares method of the python module numpy.linalg.lstsq to fit with arbitrary rotation parameter. 140
B.3 The n to $n + 1$ time delay of 256 samples of five calibration channels (columns) for two boards (rows). The median of these distributions is close to that expected from the nominal constant sampling rate of 10.24 GSPS. The standard deviation represents the spread in the constant deviation from nominal sampling rate. . . 141
B.4 An estimate of the aperture jitter of the PSEC4 sample times using a re-casting of the residual to the each ellipse. 142
B.5 Phase-offset timing-jitter of calibration channels 6, 12, 24, 30 (left to right) relative to channel 18 sourced by the same sine-wave input. The top row is board 0 and bottom row is board 2. This includes time-base calibration and wraparound offset calibration. See text for possible explanations of the constant phase-offset (median of the distribution). 143

D.1 Components that are significant during the first stage of assembly: the button columns that hold the MCPs and window under load, the non-evaporable getter (NEG), and the internal high-voltage electrodes. 151
D.2 The setup for measuring the profile of the tile-base. From bottom to top: granite flat, aluminum base-plate, shims and gauge blocks with total height greater than the tile-base height, aluminum hole-block, and depth micrometer. 152
D.3 On the left is the output of the tile-base depth measurement. On the right, a plot of the depths of the button locations relative to the sidewall after including the heights of ceramic spacers and thicknesses of MCPs. The heights of the button columns at each location are chosen such that the window will sit on the buttons 1.5 to 2 mils above the sidewall. 153
D.4 A sealing metalization being pre-conditioned with a short soak in acetic acid. . . 157

D.5 A closeup of the (A) copper sawtooth shim, (B) ceramic sidewall, (C) wettable metalized sealing surface, and (D) the SS indium wire holder. The sawtooth shim holds the window above the sidewall sealing surface by 2 mils while allowing gaps for molten indium to wick between the two wettable surfaces. The SS indium holder allows the indium wire to sit outside of the seal area until it melts and is wicked by the wettable copper surfaces. The copper teeth may be replaced by a built-in positive stop machined into the surface of the sidewall. 158
D.6 A Stanford Research Systems 200 (SRS200) RGA scan taken at the end of the sealing cycle shown in Figure 2.8 after cooling to 150 C. This is a close proxy to the chemical state of the gas inside the LAPPD volume during the growth of the photocathode. Partial pressures are not easily converted to absolute pressures inside the LAPPD due to the uncharacterized conductance to the pump and LAPPD as well as the cross-section dependence on gas species of the RGA. Carbon based compounds in this spectra are known to be sourced primarily by the RGA measurement head. 160

E.1 One method used to measure QE. A diode light source shines light on the LAPPD with a pulsed frequency set by a function generator. That frequency is fed to a lock-in amplifier which measures the current extracted from the cathode. The voltage source that biases the cathode gap consists of a set of four 9 V batteries in series. 165
E.2 This is an alternative QE measurement setup that allows for a simultaneous measurement of the low-voltage DC series resistance of the MCPs. Hardware not shown is similar to that in Figure E.1 166
E.3 The evolution of the Tile 31 photocathode over the history of its growth. Total integrated cesiation time is indicated by titles above each figure. The highest value of the colored quantum efficiency scale changes from 0.6% to 4% at the rightmost figure of the top row. Quantum efficiency color scale is linear. The LAPPD outline is indicated by the red dotted line. The two copper tubes are indicated by red and blue triangles at the bottom of each figure, red being the cesium inlet tube. The rightmost bottom figure shows the quantum efficiency after a long period of waiting after cesiation. 167

F.1 A zoomed-in diagram of a side view of an MCP pore, with distances not to scale and neighboring pores not shown. photoelectrons can strike the inside of the pore at different depths. The maximum depth is shown as a dotted line, and is related to the pore angle and diameter. An accelerating voltage V is applied to the gap between the photocathode and MCP surface. 173
F.2 The arrival times of the earliest arriving photoelectron including Cherenkov timing dynamics generated by geometry and pore depth variations due to the pore bias angle. This monte-carlo includes 10,000 events, each with 33 photoelectrons generated by the charged particle over a 5 mm thick window. 177

F.3 The scaling of the variance of earliest arrival time as a function of number of photoelectrons detected from different window thicknesses, holding the Cherenkov emission density constant at 66.4 photoelectrons per centimeter. Each data-point represents a 10,000 event simulation, with error-bars smaller than the data points. The variation in electron arrival 1st order statistic does not change as the earliest arrival is determined by the timing spread of the first Cherenkov photons. With larger window thicknesses, the later arriving photons do not contribute additional timing information. 178
F.4 The scaling of the variance of earliest arrival time as a function of number of photoelectrons per centimeter in a 5 mm window. Each data-point represents a 10,000 event simulation, with error-bars smaller than the data points. Fluctuations like those near 65 and 90 photoelectrons may be due to inconsistencies in the psuedo-random generator, numpy.random.uniform. The scaling is fitted to an inverse power-law with best-fit being order 0.84. The Kolmogorov-Smirnov fit test statistic is reported in the legend for the best-fit parameters. 179

LIST OF TABLES

7.1 Summary and labeling of datasets used in this chapter. The quoted beam diameters are rough and may have errors on the order of 1-2 cm. 94

8.1 Summary of some improvements to the elements of the time-of-flight system and the effects on maximum momentum to distinguish pions and kaons at 1-sigma. . 124

B.1 Wraparound offsets in picoseconds for two boards and five calibration channels. These offsets were measured using the ellipse procedure described in this chapter for 10,000 sine wave inputs. 141

C.1 Result of calculating compositional radiation lengths using the weight fraction of elements in the composition. Radiation lengths of MCPs are estimated by applying a density reduction equal to the loss from open area ratio of the micropores. 146

C.2 Thicknesses in centimeters of materials used in the calculation for each path length and each LAPPD. Values are not necessarily representative of true values for each LAPPD, but this is a best attempt. References are the LAPPD test-reports distributed by Incom Inc. upon sale, and material specifications for U. of C. tile design found in Reference [60] 146

C.3 Materials used in the calculation for each path length and each LAPPD. References are the LAPPD test-reports distributed by Incom Inc. upon sale, and material specifications for U. of C. tile design found in Reference [60]. "PM*" stands for proprietary metal. 147

ACKNOWLEDGMENTS

This work would not be possible without the vast support I received from my thesis adviser, Henry Frisch. Henry's wisdom, experience, encouragement, and guidance have helped shape me as a scientist. Henry is also an excellent story-teller. I am forever grateful for these stories, having the quality that they contain lessons that may be applied to being a scientist. I am also thankful for our shared interest in music, culture, politics, pedagogy, and the standard model.

I am grateful to my Fermilab advisor, Sergei Nagaitsev, who supported my interest in accelerator physics and its connections with particle physics. This support gave me the opportunity to experience cross-disciplinary research. I'll treasure the experience of learning accelerator physics from stage zero while also applying my skills from particle physics to exciting ideas.

Andrey Elagin always offers encouraging words when the challenges in the lab get rough. From Andrey, I learned how to take a step back, re-assess, and continue moving forward when presented with daunting challenges in physics. Your scientific insight and wisdom, collected from years of being in multiple fields of particle physics, is unique and always appreciated.

Matthew Wetstein has been both a mentor and a friend during my graduate studies. I would like to thank him for being sympathetic to the technical challenges surrounding the electronics system. I would also like to thank him for inviting me to participate in meetings with the ANNIE collaboration.

I am so thankful to have had the opportunity to work with two of the most knowledgeable people in the world: Eric Spieglan and Bernhard Adams. Eric and I have built our research skills together over the past five years as lab partners and friends. Eric is often a teacher and role model. He has filled many gaps in my understanding of physics, and is often involved when "Eureka!" moments occur in the lab. I will cherish our team's thrilling adventures in detector development.

Bernhard Adams is deeply expert in a broad range of topics surrounding physics and engineering. Without his dedicated contribution and expertise, the LAPPD technology would not be where it is today. With Bernhard, I feel uniquely comfortable asking questions about any topic or wild idea. From Bernhard, I've learned to always carry a supply of tools, electronics components, and epoxy in my car. He also has inspired me to stay in touch with politics and current events. Thank you for being a good friend and role model.

I would like to thank Eric Oberla, who dedicated many hours of his free time to aiding the development of the electronics system. Though the trails of his past work, Eric has effectively taught me the basics of high signal-integrity digital-electronics design and integration.

The Electronics Development Group at University of Chicago has also contributed to my education in electronics. From Mircea Bogdan, Fukun Tang, Mark Zaskowski, Mary Heintz, and Gabrielle Dye, I learned how to design and fabricate analog and digital electronics systems. Mircea and Tang have always kept their doors open to questions. I am thankful for their openness to providing expert insight to novices like myself.

Mary Heintz has been our networking technical expert over the entire course of my graduate studies. Without her support, our lab would not have been able to make measurements, record electronic logs, hold presentations at meetings, or receive e-mails. Mary is friendly, warm, and also one of the most expert networking specialists I have ever had the opportunity to work with.

Special thanks goes to Holly Jaffey, Ramona Echols, Cassandra Heinz, and Catherine Burroughs, whose administrative support allowed our group to stay blissfully ignorant. Thank you for always being responsive and friendly!

This thesis work would not have been possible without the flexibility and dedication of Todd Nebel, Jim Wish, Ewa Skup, Evan Niner, Mandy Rominsky, and Eugene J. Schmidt at the Fermilab Test Beam Facility. Their technical knowledge, diligence, and welcoming nature makes working at the test-beam a joyful experience.

I am thankful to the team at Incom Inc. for welcoming my interest in operating the first commercial LAPPD modules. I am also thankful that they have strong communication skills and are willing to stay highly involved in the development process.

I would like to thank Fransisco Girela for his dedication to helping scientists like ourselves use synchronization systems from Seven Solutions. Francisco went out of his way, driving long distances and making calls at strange hours, to provide expert support throughout the development of the time-of-flight system.

Luca Cultrera at Cornell University provided me with the opportunity to experience photocathode synthesis from the perspective of an expert. Our conversations over lunch were always intriguing, leading to creative new ideas and possible paths for detector development. Thank you for being a good friend and mentor of photocathode physics.

Many undergraduate students working with us during the summers and school year have given me experience as a teacher and allowed me to find holes in my own physics knowledge. Contributors to the test-beam effort of this thesis include Finn Clark, Naixin Liang, Vasily Soloview, Cici Hannah, John Podczerwinski, Runyu Jiang, and Livio Verra. But many others contributed in indirect ways, including Madeline Bernstein, Hannah Tomlinson, Benji, Nicole Dombrowski, Hayward Melton, Max Huang, Fangjian Wu, Audrey Whitmer, Charles Whitmer, Erick Orozco, John Judge, Rohan Lopez, Mesut Caliskan, Roy Garcia, Jinseo Park, and others.

I would like to thank my brother, Russell Angelico, who has been my primary role model since birth. You are my best friend. Your wisdom throughout my graduate studies has kept me sane and balanced. Our musical connection represents a level of ease and intuition that I strive to achieve in physics. Thank you for teaching me drums and holding Shabbat.

I would like to acknowledge both of my parents, Phyllis and Dean Angelico, for their unending support of my passion for physics. Their parental guidance has taught me how to pursue an academic career while also balancing life with art, athletics, and social interaction.

I am privileged, able to pursue physics because of the sacrifices they have made for me and Russell. Dad, thank you for giving me page-long arithmetic problems at the dinner table in second grade, fun hardware experiences in the garage, and an interest in strange scientific phenomena. Mom, thank you for teaching me how to accomplish great feats without needing to use standard techniques. This quality generates a fountain of creativity in all aspects of my life, including physics.

The Sugarman foundation and the Winstein foundation has supported my growth as a physicist through multiple awards during my graduate studies. I particularly would like to thank the Winstein foundation for encouraging me to explore my interests in education outreach, as well as my interest in accelerator physics.

This thesis is based upon work supported by the U.S. Department of Energy, Office of Science, Office of Workforce Development for Teachers and Scientists, Office of Science Graduate Student Research (SCGSR) program. The SCGSR program is administered by the Oak Ridge Institute for Science and Education (ORISE) for the DOE. ORISE is managed by ORAU under contract number DE-SC0014664. All opinions expressed in this paper are the authors and do not necessarily reflect the policies and views of DOE, ORAU, or ORISE.

I would like to thank the director of the Enrico Fermi Institute, Scott Wakely, and the Dean of the Physical Sciences Division, Angela Olinto, for their support throughout this project. The University of Chicago is supported by the HEP Division of the Department of Energy under Contract No. DE-SC-0008172, the National Science Foundation under Grant No. PHY-106601 4, and the Physical Sciences Division of the University. The LAPPD time-of-flight effort at the test-beam is supported by Contract No. DE-SC-0020078. The development at Incom is supported by the DOE Nuclear Physics Division through Award No. DE-SC0015267.

ABSTRACT

A system of Large Area Picosecond Photodetectors (LAPPD^{TM}) has been constructed at the Fermilab Test Beam Facility (FTBF) to measure charged particles in a time-of-flight configuration. Cherenkov photons produced by charged particles passing through the glass window induce signals that mark the particle's time-of-arrival and position at each LAPPD. A method for batch fabrication of LAPPDs developed at University of Chicago is described in detail. Four LAPPDs were instrumented into a time-of-flight system, three simultaneously, including one Generation-II capacitively-coupled LAPPD fabricated at University of Chicago. The time-of-flight system is designed with the intention of evolving into a permanent measurement system for the FTBF, providing users with a mass measurement of particles on an event-by-event basis. A draft procedure for analyzing charged particle data using LAPPDs is presented. The pion and kaon 1-sigma separation sensitivity is estimated to be 7-8 GeV/c at 5 m separation and 22-25 GeV/c at 45 m separation. Sensitivities are also projected, taking into account already identified design improvements that may be implemented in the next 1-5 years. A summary of the next-steps and a design of a permanent system is presented.

CHAPTER 1

INTRODUCTION TO PARTICLE TIME-OF-FLIGHT USING LARGE AREA PICOSECOND PHOTODETECTORS

1.1 Introduction to Large Area Picosecond Photodetectors

1.1.1 Conventional photo-multiplier tubes

Conventional photo-multiplier tubes (PMTs) are a vacuum-tube single photon detecting technology employed in countless physics experiments. The PMT was invented in 1935 [1]. The industry of fabricating PMTs has matured over the past many decades, to the point of many companies around the world being able to produce thousands of PMTs per year with a wide range of specifications and capabilities. Photo-multiplier tubes are also robust to long-term use; it is not uncommon for PMTs to last decades, with the same tube being implemented into multiple experiments throughout its lifetime.

The photo-multiplier tube detects a photon by converting it into a single electron inside of the vacuum volume through the photoelectric effect. The electron is accelerated towards a set of metal objects, or dynodes, that are coated in a secondary emitting material. The dynodes emit additional electrons when hit with an electron of kinetic energy on the order of 100 eV or greater [1]. As the electrons are accelerated towards ~ 5-10 dynodes, an avalanche of electrons ensues, eventually being collected by an anode. For additional information on photo-multiplier tubes and their operation, see References [2] and [3].

Photo-multiplier tubes are typically single pixel devices because they have one amplification stage and one charge collection anode [2]. This couples the position resolution to the

1. Secondary emission is a process where impinging electrons with kinetic energy on the order of 100's of electron volts strike a material and induce the emission of one or more additional electrons. The probability of emitting N electrons is a function of the incident electron energy and is often referred to as secondary emission yield (SEY).

2. There are many types of PMTs, even those with multiple amplification stages and anodes. The variety

area of the photo-sensitive surface.

The timing resolution of PMTs is dominated by the variety of paths that electrons take during the amplification process [2]. This couples the timing resolution with size of the PMT in the direction of the electron traversal. The length of PMTs is often on the order of inches.

1.1.2 Micro-channel plate based photo-multiplier tubes

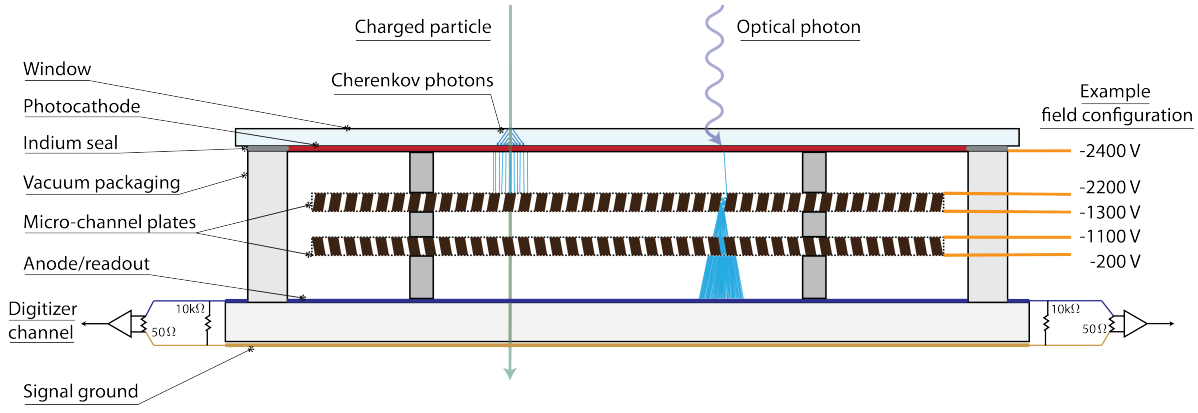

Figure 1.1: Photo-detection starts with a photon impinging on the glass window. The photon is converted by the photocathode into a photoelectron with probability equal to the quantum efficiency. Accelerating high voltage is applied to the internal components to accelerate the photoelectron into an MCP pore. The MCPs are coated with a secondary-emitting layer. Electrons strike the pore walls ~10 times, forming an electron avalanche or cloud. The electron cloud, typically comprised of 10^7 electrons, produces a negative polar pulse with 10% to 90% rise-time on the order of 250-1000 ps depending on the geometry of the internal components, and 10 - 40 mV amplitude on 50 Ω impedance transmission lines.

Micro-channel plate technology decouples both the timing resolution and position resolution with the size of the photo-multiplier tube. Micro-channel plates (MCPs) are a single-electron amplification technology, reviewed in detail in Reference [4]. A glass substrate is fabricated with many closely-packed pores having diameters on the order of 10s of μm and lengths on the order of 1 mm. The insides of the pores are coated with a secondary emitting material. With modern fabrication techniques using atomic layer deposition, amplification

of PMTs available for experimenters is vast. The comments in this section are related to what may be subjectively defined as a *vanilla* PMT, or common PMT

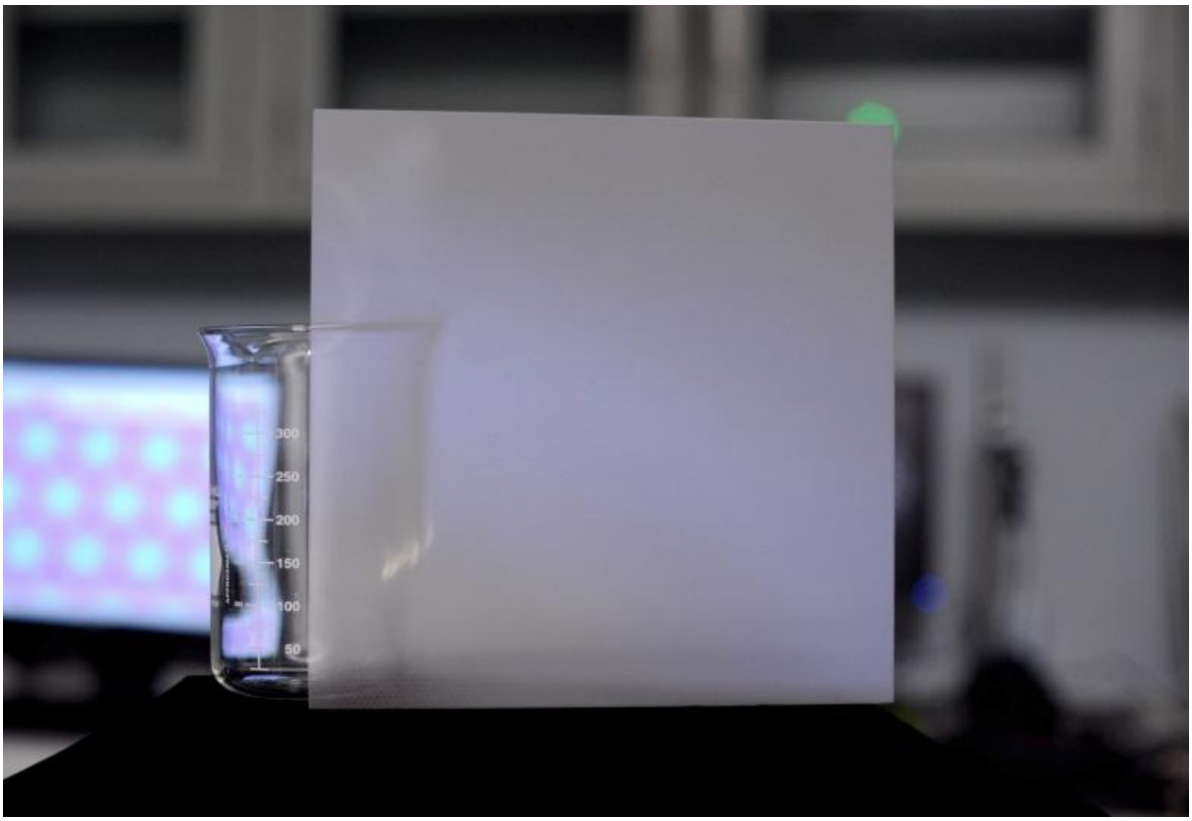

Figure 1.2: Photograph of an 8"×8"glass capillary array (GCA) fabricated by Incom Inc, courtesy of Michael J. Minot. Using atomic layer deposition, the GCA will later be coated with resistive and emissive coatings. In this un-coated state, the glass is slightly translucent and has approximately 64% open area from the close packing of 20 μm pores.

factors, or gains, of 10^7 are typical when placing two MCPs in succession with a gap in between in a "Chevron" configuration [4, 5]. The high gain-bandwidth and thin geometry of micro-channel plates is what allows MCP-PMTs to achieve 10s of picoseconds timing resolutions on single photons.

An example of the operating principle of a micro-channel plate based photo-multiplier tube (MCP-PMT) is shown in Figure 1.1. The detection of photons using MCP-PMTs is similar to conventional PMTs with the following differences: there are millions of amplification stages that allow for excellent spatial resolution and the amplification stages have a total thickness on the order of 1 mm for total detector lengths on the order of 10s of mm.

The MCP pores confine the electron cloud such that the transverse location of a charge

cloud arriving at the anode determines the transverse location of the impinging photon. The ultimate position resolution of an MCP-based detector is set by the pore diameter, the size of the gaps where the electron cloud is allowed to diffuse transversely, and the geometry of the signal readout (see Chapter 3). In this thesis, the position resolution is limited by the geometry of the signal readout which is optimized for timing resolution and low channel count.

In the past ten years, micro-channel plate manufacturing processes have made a number of breakthroughs that enable the production of 8"×8" MCPs using commercially-available low-cost glass as an alternative to the specialty lead-glass materials used in previous decades [6]. Lead-glass MCPs are typically lower gain, lower lifetime, and less structurally stable [7]. In this thesis, all mention of MCP properties refer to MCPs fabricated using atomic layer deposition and a fiber-drawn glass-capillary-array substrate.

1.1.3 Large Area Picosecond Photodetectors

Large Area Picosecond Photodetectors (LAPPD$^{\mathrm{TM}}$) are a 400 cm^2 sensitive-area photo-detecting technology designed to maximize sensitivity to the position and time-of-arrival of single photons. The amplification stages, made of micro-channel plates (MCP), are the key technology that enables LAPPDs to have large sensitive area independent of its position and timing resolution.

One major technological advancement that was overcome in the development of LAPPDs was the ability for a company, Incom Inc. (see next subsection), to fabricate robust 8"×8" MCPs using common glass materials [6]. Once the MCPs were made available in this large format, a prototype detector was operated at Argonne National Laboratory. This prototype demonstrated the nominal characteristics of an LAPPD; namely, on order 1 mm or better spatial resolution with a strip-line anode geometry, gains greater than 10^7, and 50 ps standard deviation transit-time spread on single photoelectrons [8].

1.1.4 Incom Inc.

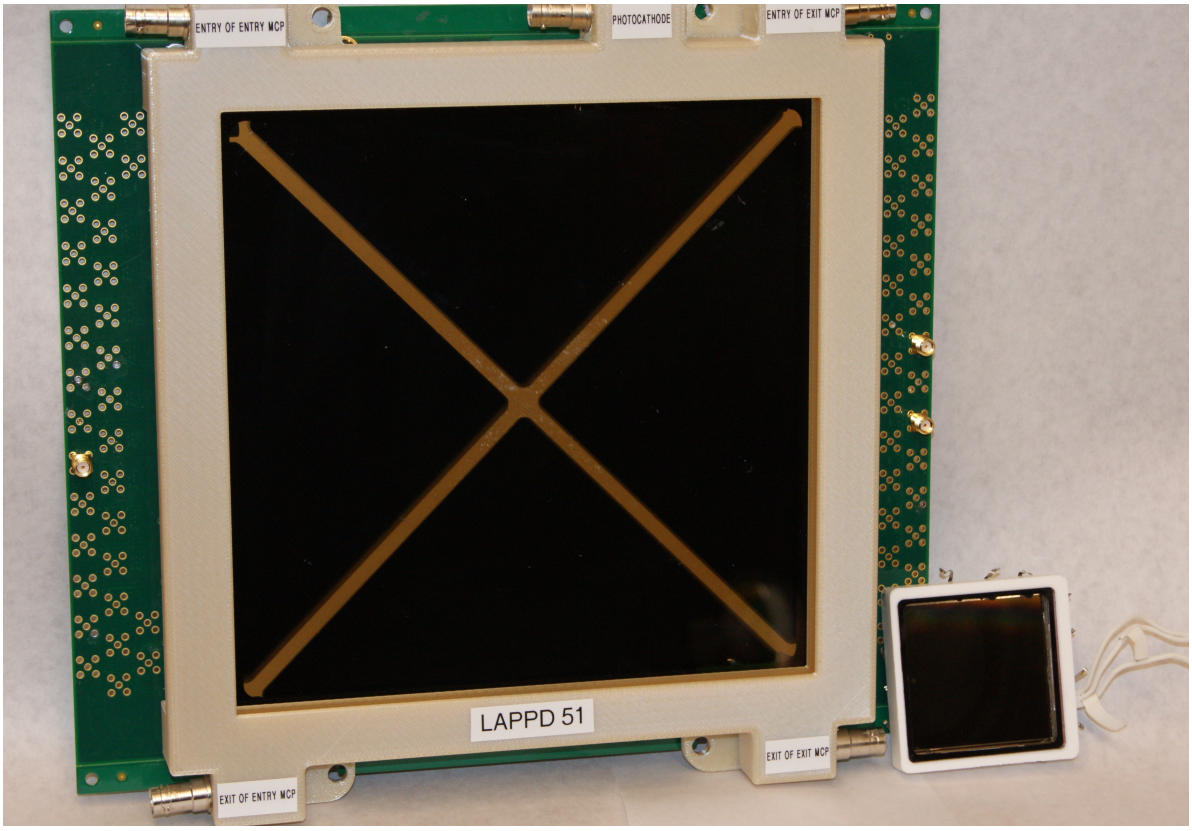

Figure 1.3: Photograph of a Large Area Picosecond Photodetector (LAPPD) fabricated by Incom Inc. next to a Photonis Planacon MCP-PMT for comparison [9, 10].

Incom Inc. [10], a technology-based, innovative small business based out of Charlton, Massachussettes that specializes in fiber optics is commercially fabricating 8"×8" MCPs using a method of drawing hollow glass fibers until they have reached a diameter of 20 μm. Incom Inc. has also developed a fabrication process that initiated the pilot production and sale of LAPPDs starting in 2018. The LAPPD development team, a small subsection of the ~200 person company, has developed a clean room facility, fabrication chambers, component pipe-line, and test-procedure for the sale of LAPPDs at a rate of about 20-40 per year.

An example of an Incom produced LAPPD is shown in Figure 1.3. For years, commercial micro-channel-plate based photo-detectors have been available in smaller area formats ranging from 4 cm^2 to 25 cm^2. The "Planacon" from Photonis, for example, is shown beside

the Incom LAPPD [9]. In parallel, Argonne National Laboratory has been developing a non-commercial MCP-based photo-detector with 36 cm^2 active area [11, 12, 6].

1.1.5 Summary

The large area micro-channel plate photo-multiplier technology has the potential for long-term impacts on physics and society. Possible applications of LAPPDs include large-liquid-volume neutrino detectors [13, 14, 15], correlated precision time and space information in high-energy particle collider and fixed-target events [16], reconstruction of neutral mesons decaying to photons in searches for rare meson decays [15, 17, 18], low-dose whole body time-of-flight positron-emission-tomography [19, 20, 21, 22].

A batch production process needs to be developed to handle the demand of experiments that require large photo-sensitive surface areas. Experiments like JUNO [13], KOTO [17], THEIA [14], and ATLAS [23] have surface areas that would require 1,000 - 10,000s of LAPPDs. The physics impact of this technology, as well as its price, will scale dramatically as the production volume scales. A batch production process developed at University of Chicago is driven by the need for high-volume production to satisfy the demand of large-scale physics experiments. This process is described in Chapter 2.

Before being applied to the large-scale applications above, the first commercial LAPPDs need to be operated on a regular basis in a particle physics environment. A time-of-flight system at the Fermilab Test Beam Facility is an ideal environment to operate LAPPDs, testing their robustness to regular use, providing a world-class time-of-flight measurement as a resource to test-beam users, and allowing LAPPDs to interact with a broad community of physicists. This thesis represents the first use of LAPPDs to detect charged particles, and a construction and operation of a first-iteration LAPPD-based time-of-flight system.

1.2 Introduction to time-of-flight

A *time-of-flight* (TOF) system is a set of detectors that measure the traversal time and path length of a particle to infer its velocity. A measurement of the velocity of a particle adds a constraint to its other kinematic quantities. For example, a relativistic particle with velocity $v = \beta c$ traversing a path-length d between two detectors has a time of flight of

$$\Delta t = d/\beta \tag{1.1}$$

$$\Delta t = d\sqrt{1 + \frac{m^2}{p^2}} \tag{1.2}$$

$$\Delta t = \frac{Ed}{p} \tag{1.3}$$

where m is the particle's mass, p is the magnitude of its momentum, and E is its total energy. If any two kinematic quantities in the set $[E, m, p, \Delta t]$ are measured, then the other two are implied by $E^2 = p^2 + m^2$ [24, 25]. For example, a time-of-flight measurement combined with a knowledge of the particle's mass is an energy and momentum measurement. A time-of-flight measurement combined with an energy or momentum measurement is a particle-identification (PID) system.

1.2.1 Kinematics of particle identification

A time-of-flight particle identification system can be characterized by its ability to distinguish two particles of similar mass. Consider the case where a beam of particles containing a mixture of pions (mass 139.57 MeV/c^2) and kaons (mass 493.68 MeV/c^2) [26] pass through a time-of-flight system. An example diagram is shown in Figure 1.4. For detector separations on the order of meters, the time-of-flight is on the order of 1-10s of nanoseconds. To distinguish a pion from a kaon, the TOF system measures the *difference* between the time-of-flights of the two particles:

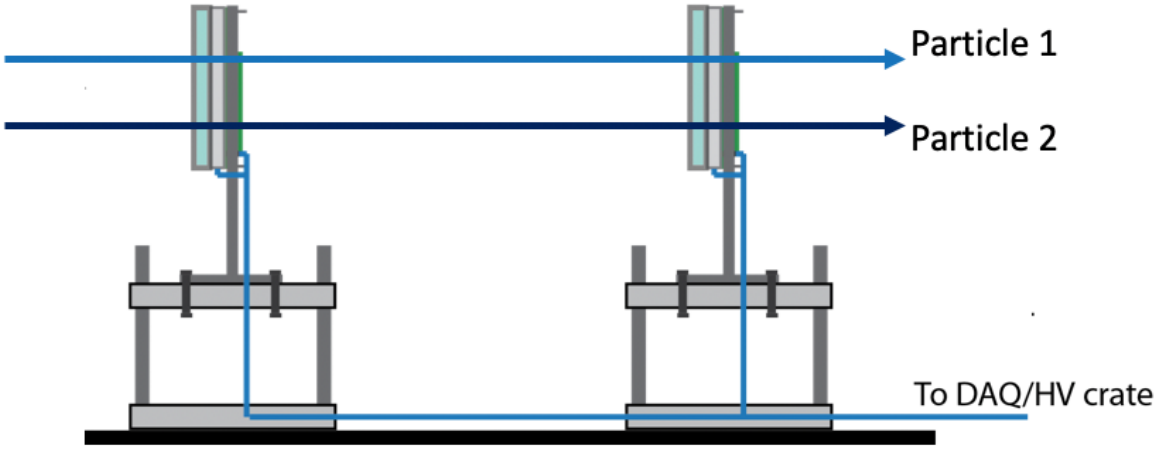

Figure 1.4: Diagram of a general time-of-flight detector system. The detectors can be any sensor that records the time and position of an impinging particle. By measuring the velocity and momentum of the particle, the mass may be inferred.

$$\begin{aligned}\tau_{12} &= \Delta t_1 - \Delta t_2 \\ &= d\left(\sqrt{1 + m_1^2/p_1^2} - \sqrt{1 + m_2^2/p_2^2}\right)\end{aligned} \tag{1.4}$$

where m_i and p_i are the mass and momentum of the two particles in question. If the momenta are the same and the particles are relativistic ($p \gg m$), τ_{12} approximates to

$$\tau_{12} \approx \frac{d}{2p^2}(m_1^2 - m_2^2) \tag{1.5}$$

The sensitivity of a TOF mass measurement system to a particular pair of particle types is determined by its resolution on the time-of-arrival, path length, momentum, and mass-squared difference of the particles. Figure 1.5 shows contours of detector timing resolution needed to distinguish pions and kaons as a function of momentum and path-length assuming that the momentum and path length is known perfectly.

If the momentum has an uncertainty ϵ on the percent level, as is the case in the Fermilab

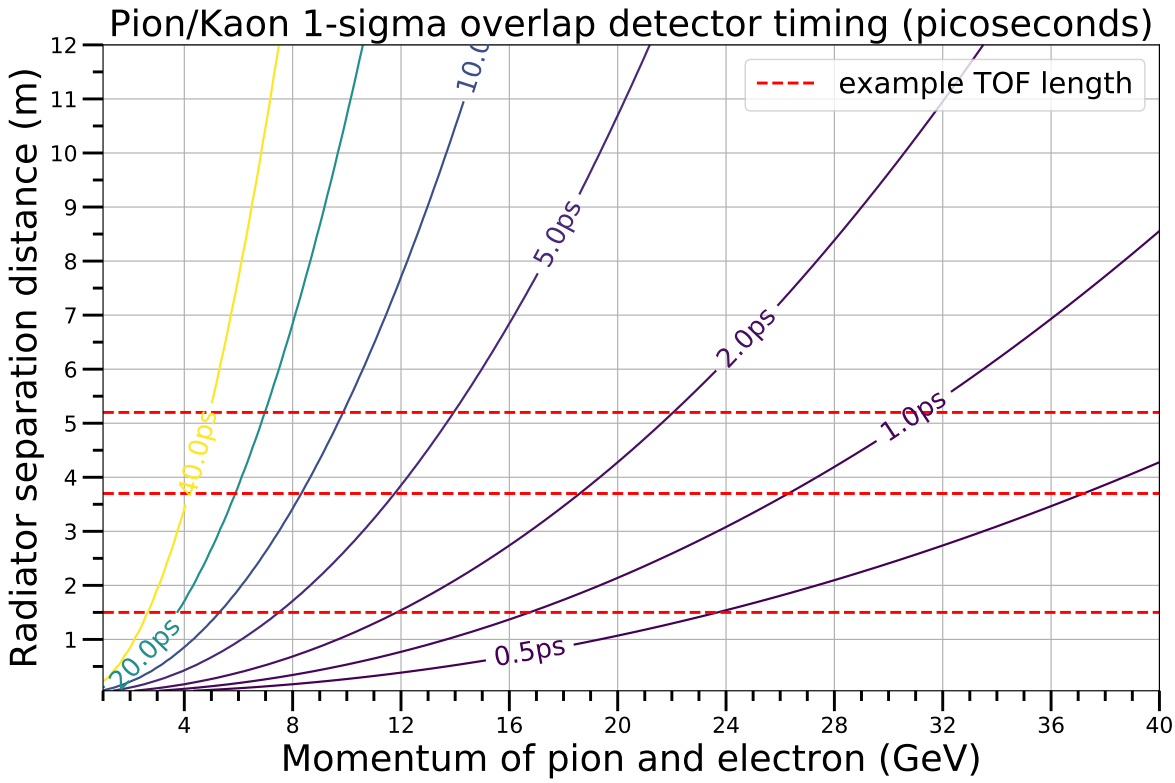

Figure 1.5: Contours of detector timing resolution needed to distinguish 68.27% of pions and kaons as a function of momentum and path-length. Contours are calculated using the Equation (1.4) in combination with a Gaussian smeared time-of-arrival with σ equal to the number on the contour. Dotted red lines represent example detector separations. This plot does not include uncertainties in the measurement of momentum and path-length.

Test Beam Facility, then the time-of-flight equation 1.2 approximates to

$$\Delta t = d\sqrt{1+\frac{m^2}{p^2(1+\epsilon)^2}} \tag{1.6}$$

$$\simeq d\big[1+\frac{1}{2}\frac{m^2}{p^2(1+\epsilon)^2}+\mathrm{O}(m^4/p^4)\big] \tag{1.7}$$

$$\simeq d\big[1+\frac{1}{2}\frac{m^2}{p^2}-\epsilon\frac{m^2}{p^2}\big] \tag{1.8}$$

where ϵ is considered to be a statistical quantity, normally distributed, with zero mean and

percent level standard deviation. For 8 GeV/c momentum pions, epsilon varying by 4% leads to a time-uncertainty equivalent of 0.04 ps per meter of detector separation.

1.3 LAPPDs as a time-of-flight detector

Any detector technology that can measure the time-of-arrival and position of an incident particle without significantly altering its momentum may be used as a time-of-flight detector element. Systems for TOF in particle beams may be constructed using scintillators and PMTs, for example. Detectors with better timing and position resolution will lead to a more sensitive measurement of particle velocity. Detectors that can provide small position uncertainties over large areas are advantageous for experimental environments with a wide variety of particle trajectories. An LAPPD is an ideal TOF detector element due to its large active area and excellent timing and position resolution.

Charged particles may be detected by LAPPDs using the Cherenkov light produced in the front window (see Figure 1.1). The physics of Cherenkov emission preserves timing at the picosecond level [27]. After traveling through the glass window, Cherenkov photons localized on the particle trajectory are converted to photoelectrons by the photocathode.

Many Cherenkov photons are created when a charged particle passes through an LAPPD window. A calculation is performed in the next subsection. The time-of-arrival uncertainty on a source improves when a large number of photoelectrons are created simultaneously from that source. If the electron transit times are normally distributed with standard deviation σ, the mean of their transit-times varies as $\sigma/\sqrt{N}$ due to the central limit theorem, where N is the number of photoelectrons produced simultaneously by the incident particle. If the statistics of the transit times is different, or the timing uncertainty is not dominated by transit-time spread, this scaling law may be stronger in favor of better timing resolution. This is discussed in Appendix F.

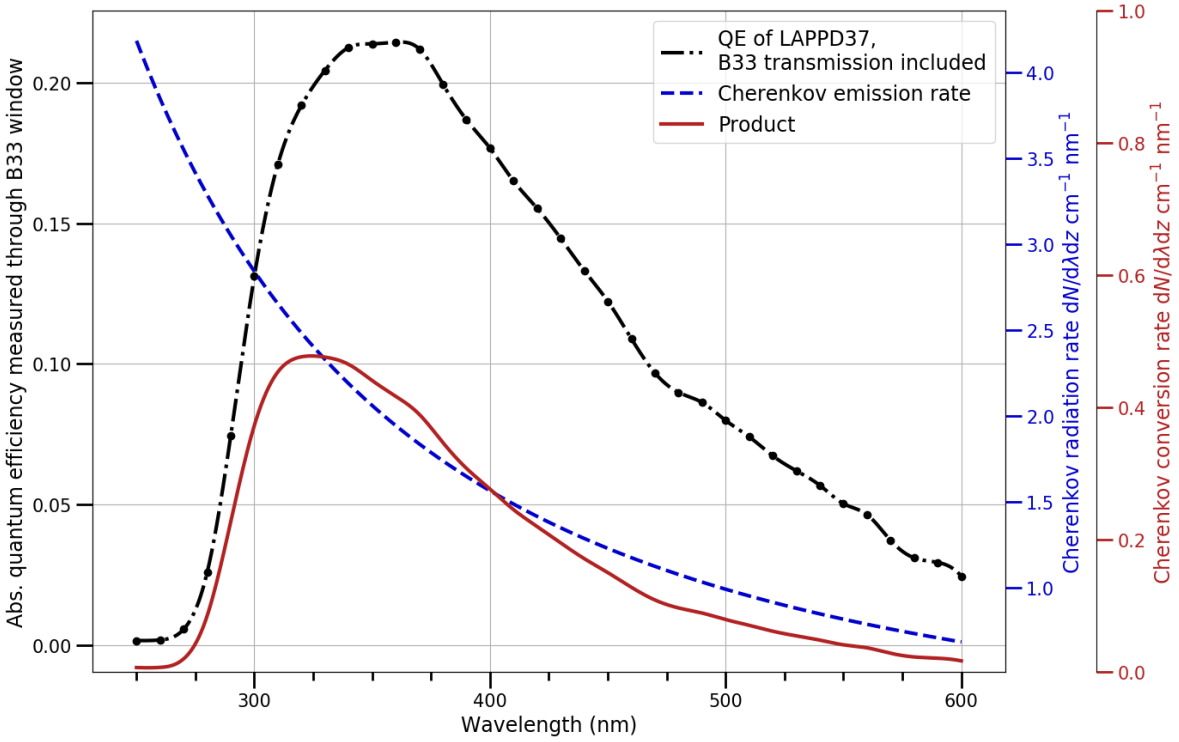

Figure 1.6: The quantum efficiency of LAPPD37 including the transmission of its 5 mm thick Schott Borofloat 33 (B33) window is shown in black with black axis labels. The Cherenkov emission spectrum [27] of a 10 GeV/c pion is plotted in blue in units of number emitted per cm of glass per nanometer wavelength. The product of these two curves, representing the number of photoelectrons per cm of glass, is shown in solid red. An integral of this spectrum from 250 nm to 600 nm gives about 66 photoelectrons per cm of glass.

1.3.1 Properties of Cherenkov light

Cherenkov photons are emitted when a charged particle travels faster than the speed of light in a medium. The photons are emitted along the path of the particle at an angle θ_c such that $\cos\theta_c = \frac{1}{\beta n(\lambda)}$ [27]. Figure 1.8 defines coordinates and presents a picture of Cherenkov light being emitted in an LAPPD glass window from a normally-impinging particle. The photons that hit the photocathode are spatially distributed in the plane of the photocathode as a circle of radius $T\tan\theta_c$, where T is the thickness of the window. For LAPPD windows made of B33 glass or fused silica, $\theta_c = 48.3°$ (300 nm) to $47.1°$ (700 nm) and T =3-5 mm, resulting in a spot of 3-5 mm radius. [27]

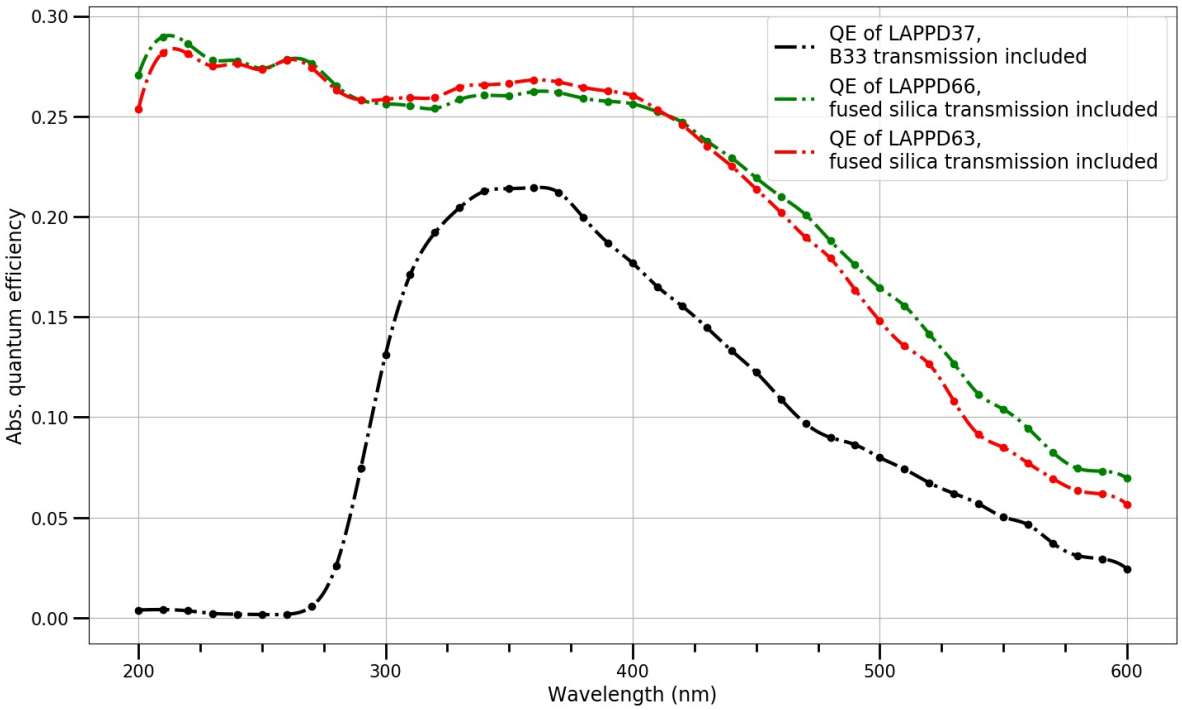

Figure 1.7: A comparison of the quantum efficiencies of three LAPPDs fabricated by Incom, Inc. Data are courtesy of Incom, Inc. A significant part of the ultra-violet Cherenkov emission spectrum is available to fused silica windows which transmits down to 200 nm. By integrating over the emission spectrum as in Figure 1.6, the number of detected photoelectrons becomes about 213 per cm, about a factor of 3 larger than B33. No LAPPDs with fused silica windows were used in this thesis.

Define polar coordinates ρ and ϕ in the plane of constant z at the photocathode layer. For a particle passing perpendicular through the window, the number of Cherenkov photons per unit area n_a is independent of ϕ and proportional to $\frac{1}{\rho}$ due to this geometrical relationship:

$$N = \int_0^{2\pi} \mathrm{d}\phi \int_0^{\rho_{max}} n_a(\rho)\rho \mathrm{d}\rho = n_l T \tag{1.9}$$

where N is the total number of photons emitted, ρ_{max} is the sharp cutoff radius due to finite radiator thickness, n_l is the number of photons emitted per cm path length, and T is the window thickness. This equality implies that

$$n_a(\rho) = \left(\frac{n_l T}{2\pi\rho_{max}}\right)\frac{1}{\rho} = \left(\frac{n_l}{2\pi\tan\theta_c}\right)\frac{1}{\rho} \tag{1.10}$$

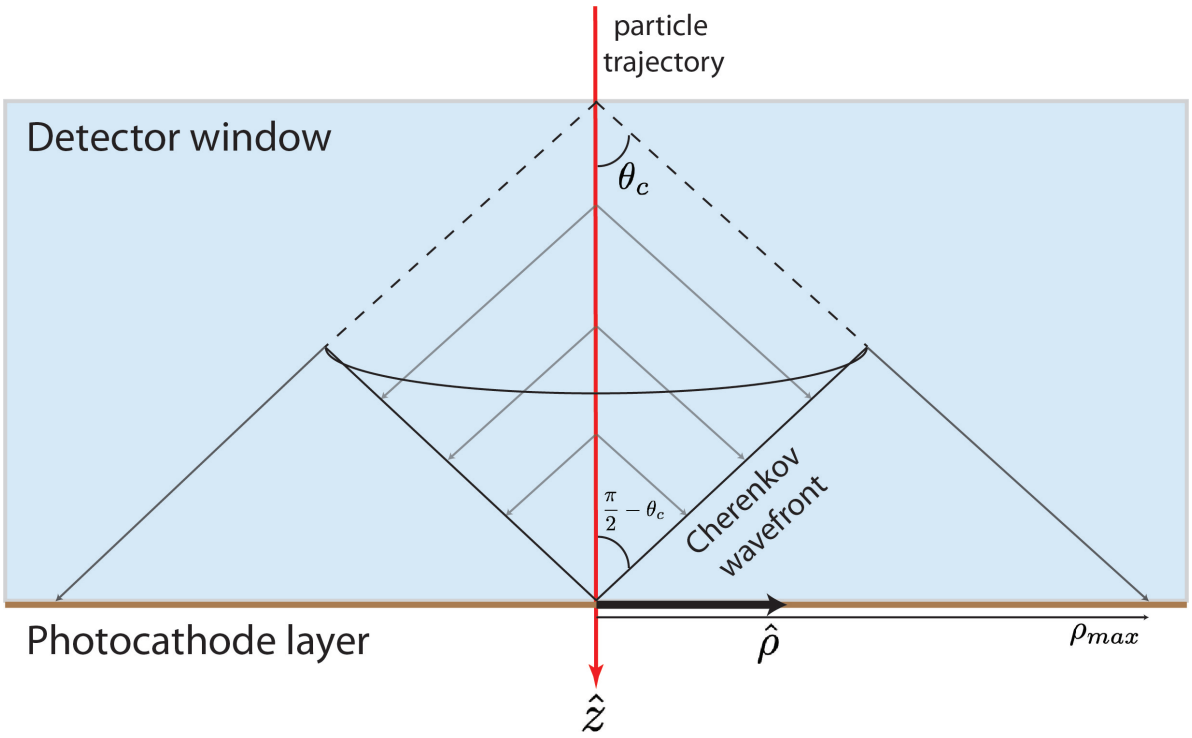

Figure 1.8: Cherenkov emission is geometrically constrained such that photons are emitted at an angle of $\cos\theta_c = 1/\beta n$ relative to the particle axis. When there is no dispersion, i.e. n is constant with wavelength, this creates an infinitely thin photon wavefront on the shape of a cone that propagates out from the particle's trajectory. A particle traversing the glass window of an LAPPD (light blue) will produce Cherenkov photons that are converted to photoelectrons by the photocathode (shown as a brown line). The Cherenkov photons have a maximum radius at the photocathode related to the window thickness.

where in the final step, the geometrical relation between the cutoff radius and the path length $T = \rho_{max}/\tan\theta_c$ was used.

The number of Cherenkov photons emitted in the wavelength range 300 - 700 nm by a charge-1 particle with $\beta \sim 1$ is about 874 $\sin^2\theta_c$ cm^{-1}, or about 562 cm^{-1} for glass [3].

When including the window transmission spectrum, QE spectrum, and Cherenkov spectrum as shown in Figure 1.6, the expected number of photoelectrons created at the photocathode becomes about 66 per cm or 33 for a 10 GeV/c pion passing perpendicular through a

3. Note that a common rule of thumb number of 480 $\sin^2\theta_c$ is often seen in literature using the range 400 - 800 nm. Because of the steep UV tail of the Cherenkov spectrum, the number of photons per cm nearly doubles when including the photons between 300 - 400 nm

5 mm Schott Borofloat 33 (B33) window. The peak of the detected photoelectron spectrum is at 324 nm which corresponds to a Cherenkov angle of 48.08°.

Fused silica windows may be used to detect additional photons in the UV part of the Cherenkov emission spectrum. Figure 1.7 shows the difference in quantum efficiency with transmission included between three LAPPDs with different window materials. The number of detected photoelectrons after integrating with the Cherenkov emission spectrum down to 200 nm is about 213 per cm or 107 for a 5 mm fused silica window. The number of Cherenkov photons and the spot size of the photoelectrons may also be increased by optically coupling glass or fused silica slabs to the LAPPD window.

Not all of the photoelectrons find their way into an MCP pore. The MCP pores are closely packed, but some space exists in-between. Electrons may hit the top surface of the MCP and not induce amplification. The "open area ratio" is the fraction of MCP top-surface area which is "open", or represents a pore. The MCPs used in this thesis have an open area ratio of greater than 64% [28], which reduces the number of amplified photoelectrons by at most 36%.

1.3.2 Timing resolution of LAPPDs

Generation-I Incom Inc. LAPPDs with 20 micron pores are being characterized in laser test stands as having transit time spreads of 55-65 ps on single photoelectrons [5, 29][4]. This implies that the timing resolution for 30 to 200 photoelectrons per charged particle results in charged particle arrival uncertainties of 4-10 ps using the $1/\sqrt{N}$ scaling law.

Multiple design changes and proposed ideas could affect the LAPPD charged-particle timing resolution within the next few years:

- The single photoelectron timing uncertainty is dominated by the transit-time spread

4. In these measurements, a 405 nm laser with 40 ps FWHM is reduced to produce occupancies of less than 1 single photoelectron per pulse.

generated in the evolution of the electron avalanche in the MCP pores [30, 31, 32]. Small-format MCP-PMTs have been commercialized with 10 μm pores as opposed to the present LAPPD modules with 20 μm pores. Production of LAPPDs with 10 μm pores are within the reach of the next few years.

- Timing resolution is dependent on the gain of the amplification stage, which is a highly sensitive function of the high-voltage settings of the LAPPDs [31, 32]. These settings will become more optimized as LAPPDs are used more regularly.

- Some contributions to transit-time spread and gain are due to design elements such as the gap between the photocathode and the top MCP. Higher accelerating fields in this gap improve gain and timing [33, 34, 5]. Field shaping grids and photocathode material deposited directly on the top of the MCP-pore surfaces are two examples of design changes that could improve overall timing.

- A careful characterization of timing resolution as a function of number of photoelectrons may conclude that the scaling law is stronger than $1/\sqrt{N}$.

1.4 Motivation for an LAPPD time-of-flight system at the Fermilab Test Beam Facility

The Fermilab Test Beam Facility (FTBF) at Fermi National Accelerator Laboratory (Fermilab, or FNAL) is a flexible test-beam facility with relatively-low bureaucratic overhead [35]. A controlled particle beam is available for use by tens of domestic and international user groups per year. Scientific fields that make measurements at the FTBF include particle physics, astrophysics, and material science [36].

Measurements made at the FTBF can be highly controlled due to the flexibility of the beam, the ability to use diagnostic tools, and the dedication of beam operators and FTBF staff. Diagnostic tools such as calorimeters and beam profile monitors positively impact a

user's ability to make meaningful measurements. An LAPPD-based TOF system will be an additional resource to users at the FTBF, providing a particle mass measurement on an event-by-event basis over a large beam acceptance for a significant portion of the available momentum spectrum. Present particle identification systems at the FTBF include two gas Cherenkov counters and a PMT-based time-of-flight system. For information about the current particle-identification capabilities at the FTBF, please see Appendix A.

Time-of-flight systems may be used to reject unwanted backgrounds in experiments that attempt to observe interactions from a specific flavor of particle [37, 38, 39]. Some systems require information on the particle's flavor to calibrate the response of a detector element [40, 41]. [5]

The ability of a TOF system to infer particle masses is particularly useful in collider detectors where every kinematic property of every particle in an interaction is sought after. A momentum measurement is usually performed by precision tracking systems close to the interaction point of a particle collision. The ATLAS inner detector, for example, was designed for a transverse momentum resolution of $\sigma_{p_T}/p_T = 0.05\% \, p_T$ GeV $\oplus 1\%$ [42]. The combination of a precise measurement of the interaction time, the inner tracker momentum measurement, and a precision timing measurement a few meters away provides a non-destructive mass and energy measurement. This mass reconstruction technique is particularly useful for identifying long-lived massive particles with displaced vertices [43]. If pions and kaons can be distinguished up to 20 GeV/c momenta, and position resolution is superb, the flavor of individual particles in jets may be reconstructed. The flow of hadron flavor could provide better jet energy reconstruction [44] and strict handles on highly Cabibbo-suppressed signature-based searches [45].

Until this thesis work, LAPPDs had not yet been tested on a charged particle source due

5. Reference [40] points out that the ATLAS calorimeter response does not depend on hadron type for momenta above 20 GeV/c. This is one possible motivation to have a TOF system that can cover the momentum range 1-20 GeV/c for all particle types.

to their low availability. In addition to the benefits an LAPPD TOF system could provide to FTBF users, the regular use of this system tests the robustness of LAPPDs in real physics environments. Over time, the sensitivity of LAPPDs to charged particles, and properties of the signals, will be fully characterized by the data collected from the LAPPD TOF system.

1.5 Structure of thesis

Some of the chapters of this thesis are intended for a broad audience and others are intended for a technical audience. Most chapters are independent of one-another except where explicitly stated. Chapter 2 describes a system for batch production of LAPPDs developed at University of Chicago during this thesis work, pulling directly from the recent publication [46]. Most chapters in the thesis have some dependency on the content in Chapters 3 and 4. Chapter 3 defines terminology used in the later chapters regarding LAPPD signal-readout hardware. Chapter 4 describes the hardware and detector configurations installed at the FTBF. Chapter 5 requires the most technical knowledge, covering the properties of the front-end digitizing electronics system. The firmware for this electronics system is the most limiting factor, or weakest link, for the robust operation of the FTBF LAPPD TOF system. The architecture of the trigger, as well as ways that it may be improved, are found in Chapter 6. In Chapter 7, datasets from the FTBF are described, raw data are examined, a draft analysis structure is presented, and some properties of charged particle signals are extracted. Chapter 8 presents an estimate of the sensitivity to distinguishing pions and kaons for the present setup and a setup that includes identified improvements to be implemented in the next few years.

Following the Summary, the Appendices provide additional information for readers who are interested the following: a summary of the required next-steps for a permanent LAPPD based TOF system at the FTBF (A), a procedure for calibrating the front-end electronics (B), the materials and thicknesses of the LAPPDs, (C) the details of the LAPPD fabrication

method (D), properties relevant to photocathode formation in the air-transfer process (E), and some theoretical timing boundaries of the LAPPD TOF system (F).

CHAPTER 2

BATCH PRODUCTION OF LARGE AREA PICOSECOND PHOTODETECTORS

2.0.1 Motivation for batch production

Applications for large-area coverage of photo-detectors with excellent time and space resolution include: correlated precision time and space information in high-energy particle collider and fixed-target events [16]; simultaneous measurements in near and far detectors of neutrino oscillations using time-selected energy spectra [47]; imaging double-beta decay events in large liquid scintillator detectors using timing to separate Cherenkov and scintillation light [48, 49, 50, 51, 52, 53]; reconstruction of neutral mesons decaying to photons in searches for rare meson decays [15, 17, 18]; low-dose whole body Time-of-Flight Positron-Emission Tomography [19, 20, 21, 22]; and nuclear non-proliferation and reactor monitoring [54].

Most of these applications require thousands to tens of thousands of 8"×8" photo-detectors. The Jiangmen Underground Neutrino Observatory (JUNO), for example, is presently installing 18,000 20" diameter photo-multiplier tubes (PMTs) and 25,000 3" diameter PMTs to achieve ~78% photo-sensitive coverage [13, 55]. A production line with a yield of 70 LAPPDs per week would be able to produce that many modules in 5 years.

2.1 Air-transfer batch-production method

This section follows the structure of Angelico et. al in Reference [46]. The work presented here is a result of years of research with our group at University of Chicago consisting of Evan Angelico, Andrey Elagin, Henry Frisch, Eric Spieglan, Bernhard Adams, with feedback and communication with Incom Inc.

2.1.1 Experience from PMT batch production

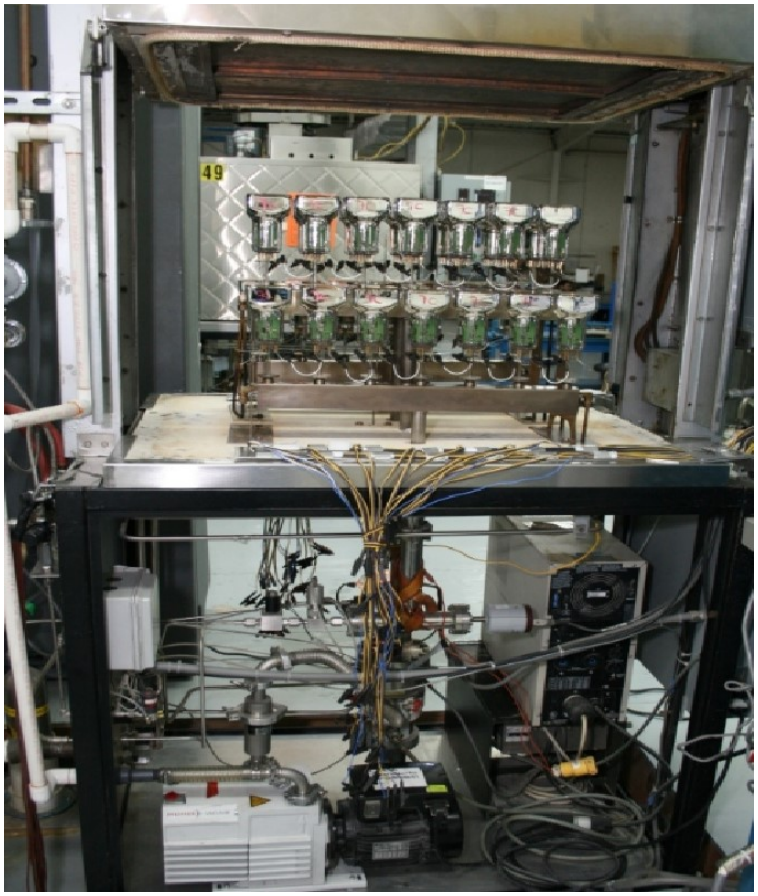

Figure 2.1: The photomultiplier batch production station purchased from the Photonis Lancaster plant [56]. This system served as a model for the development of the LAPPD batch production system described in this chapter.

Commercial photo-multiplier tubes (PMTs) are produced using a batch production station that processes multiple modules per cycle. A commercial PMT batch production facility [56] shown in Figure 2.1 was purchased by the LAPPD Collaboration [6] and served as a model for the batch LAPPD production system described in this chapter.

The key features of PMT batch production that influence LAPPD batch production are as follows. The glass envelope of the PMT is brought to low vacuum (LV) by pumping through long, low-conductance plumbing. The low-conductance plumbing of each PMT in the batch is connected to a common pump through a low-vacuum o-ring gland. An oven is placed

over the assembly for bake-out and subsequent photocathode formation. The antimony pre-cursor layer is evaporated by line-of-sight onto the inside surface of the PMT window, and alkali vapors that create photo-sensitivity are generated by sources inside of the glass envelope. After bake-out, the ultra-high vacuum (UHV) inside the glass package is provided by an internal getter as well as the natural gettering properties of residual alkali metals. The individual PMTs are then isolated from the pump by flame sealing the glass-inlet tubulation.

A batch production method for LAPPDs has been developed following a similar structure as PMT batch production. However, large-area MCP-PMTs present unique challenges, requiring a more robust package that can transmit large numbers of electrical signals for pad or strip readout from inside the vacuum volume, hermetically sealing the large-perimeter window-body interface, synthesizing the photocathode in a large flat geometry, and recovery of the large surface-area MCPs after exposure to alkali metals.

The term "Air-Transfer" refers to a stage of the production process where an antimony (Sb) photocathode pre-cursor layer is deposited on the photocathode window prior to sealing the window to the packaging of the detector. This usually implies that the Sb pre-cursor is at some point exposed to air and stored in a clean nitrogen environment before being sealed to the detector package. This process is currently being used commerically by Hamamatsu [2] and MELZ in Russia to make multi-anode photomultipliers [57].

2.1.2 Four stages of LAPPD fabrication

The fabrication of LAPPDs can be segmented into four stages, not necessarily in this order:

1. **The hermetic seal:** the internal volume of an LAPPD requires ultra-high vacuum to maintain secondary emission properties of micro-channel plates, to ensure high voltage stability, and to protect the photocathode layer from chemically decomposing. The seal is made at the interface between the body and window of the LAPPD.

2. **Photocathode synthesis:** alkali-based photocathodes react with water in the air

and become insensitive. The alkali metals that enable photo-sensitivity are introduced in vacuum after it is clear that the photocathode will never see ambient air.

3. **Micro-channel plate conditioning:** the efficiency of MCPs to emit secondary electrons depends sensitively on surface chemistry. If the photocathode synthesis occurs in proximity to the MCPs, they may exhibit reduced resistance, increased spontaneous emission rates, increased gain, or reduced high voltage stability. One stage of fabrication includes recovering MCPs after photocathode synthesis. Another conditioning of the MCPs, called "scrubbing", usually occurs before photocathode synthesis. This conditioning involves exposing and MCP to large fluxes of ultra-violet light while applying a high voltage bias and letting charge avalanches bombard other MCPs placed in succession. The large fluxes of electrons affect the surface chemistry of the MCPs.

4. **Assessing the lifetime:** one reason that PMTs are so commonly used in physics and industry is that they last for decades without significant changes in performance. Testing of LAPPD performance as a function of time is one stage of fabrication. This is the least explored of the four stages at the present date, but will develop further over the next few years through routine use of the detectors.

2.1.3 The dual-vacuum air-transfer method

The LV/UHV-dual-vacuum fabrication technique uses an outer vacuum vessel which fully contains the LAPPD. The outer vessel provides thermal insulation for a high-temperature bake-out of the photo-detector ("tile"), reduces the formation of oxides in the metals that enable hermetic sealing, and ensures that no mechanical pressure differential exists across the molten solder seal interface. The components of the LAPPD are assembled inside the outer vessel with the entrance window clamped in place. The internal volume of the detector is connected to an independent UHV manifold and pump via tubulations. Initially, before

the hermetic seal is formed, the internal and external volumes can communicate through the unsealed seam between the window and tile base. A bake-out cycle forms the seal between the window and base, and activates the getter inside. After cooling below the melting temperature of the seal, the internal and external vacuum volumes become independent and the outer volume may be vented to atmospheric pressures. Alkali vapors are introduced into the inner volume through the tubulation at the start of photocathode synthesis.

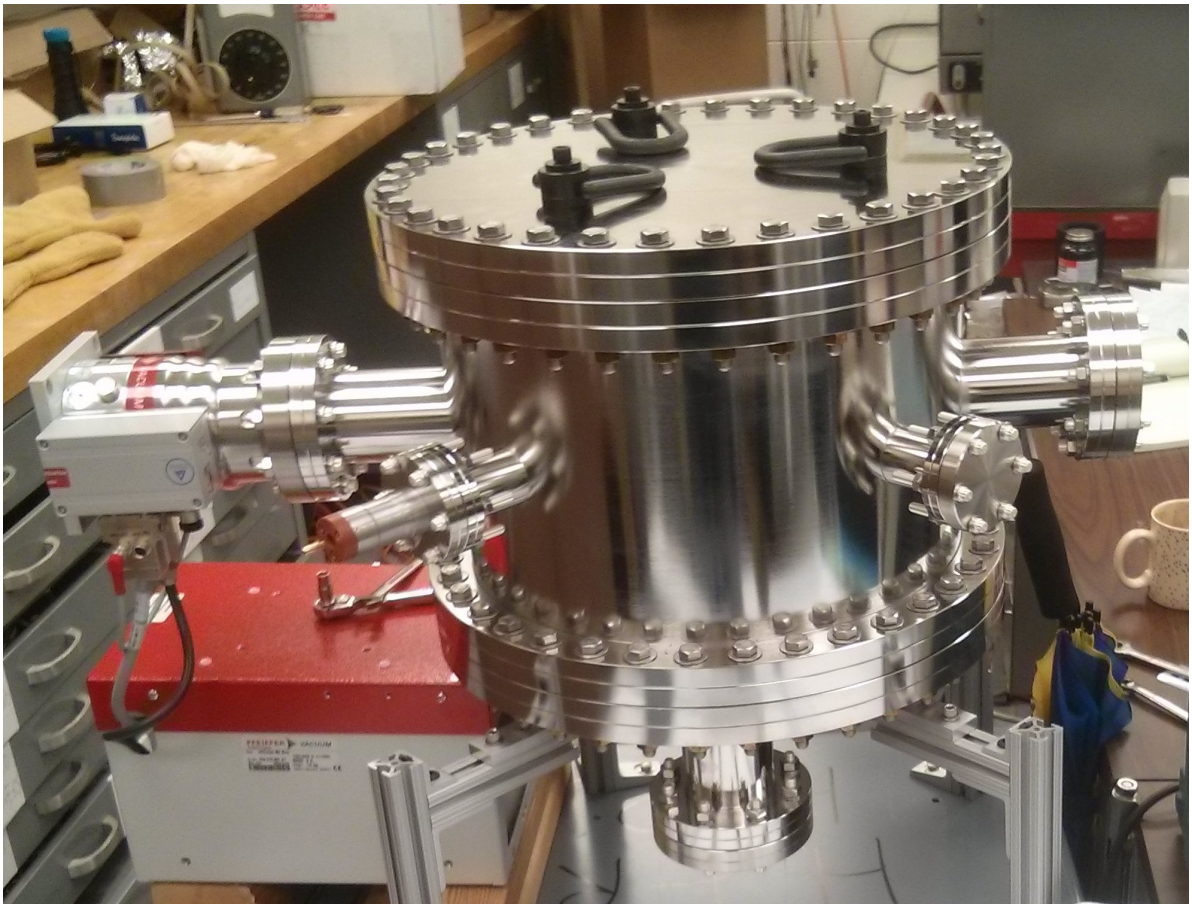

Figure 2.2: The outer low-vacuum vessel that provides thermal insulation to the photodetector during bake-out, a low oxidation environment for the seal metals, and equalization of the pressure across the molten seal interface.

Figure 2.2 shows a photograph of the outer vacuum vessel. The vacuum pump for the outer vessel can be seen on the left; the connections to the inner vacuum tubulation enter through the flange on the bottom. The upper part of the vessel can be lifted off after sealing,

exposing the sealed LAPPD for leak-checking and subsequent photocathode synthesis.

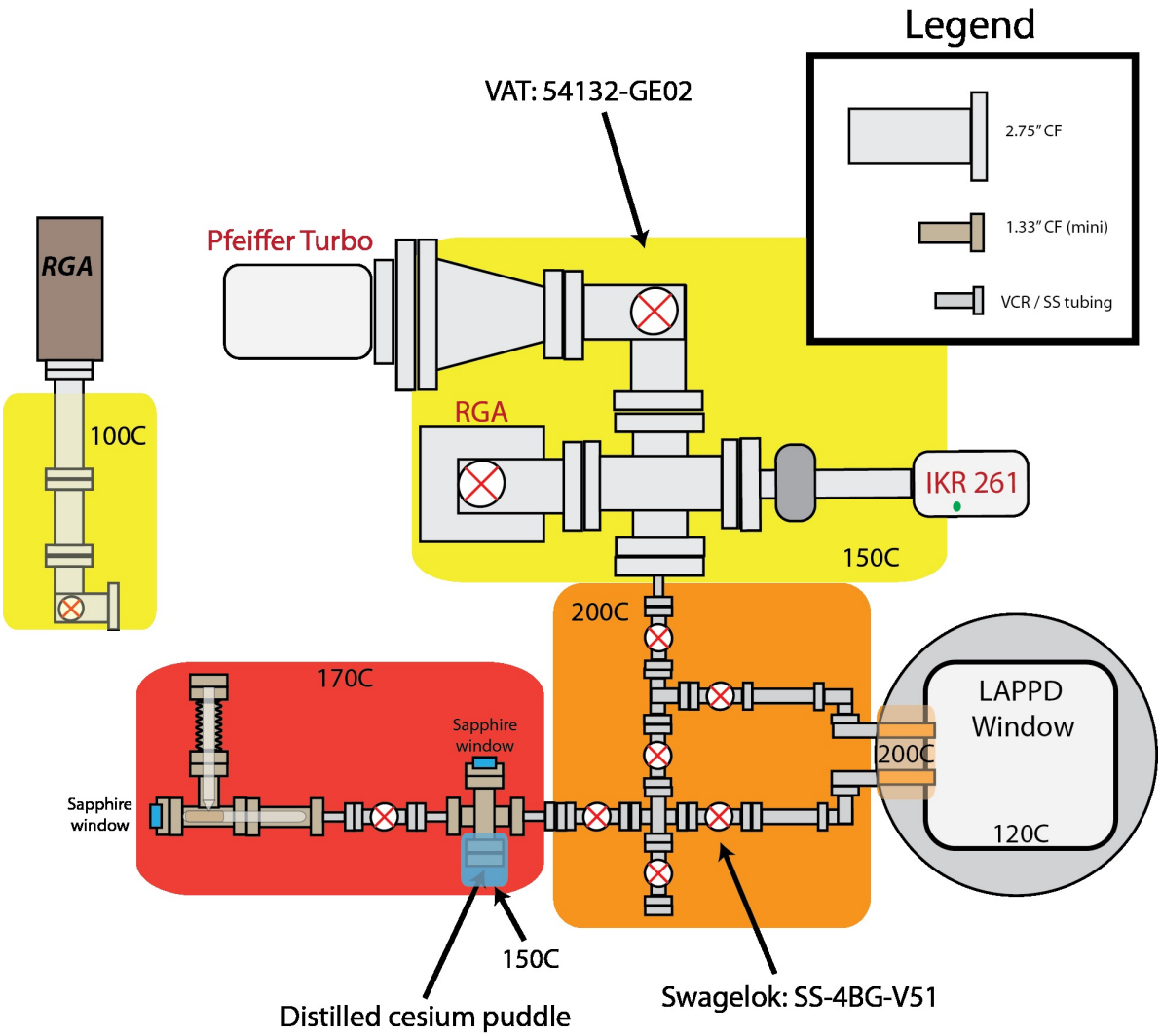

Figure 2.3: The physical layout and photocathode-metal transport temperatures of the inner vacuum manifold. The manifold connects to the LAPPD inner volume via tubulation that penetrates the outer vacuum vessel. The inner vacuum volume and outer vacuum volume are hermetically isolated after the LAPPD seal is formed.

The inner volume is pumped independently through tubulation connected to a vacuum manifold. This manifold is also used to transport photocathode metals to the LAPPD after sealing. A diagram of the inner vacuum manifold is shown in Figure 2.3 along with temperatures during the photocathode synthesis processing stage.

2.1.4 The LAPPD^{TM} package

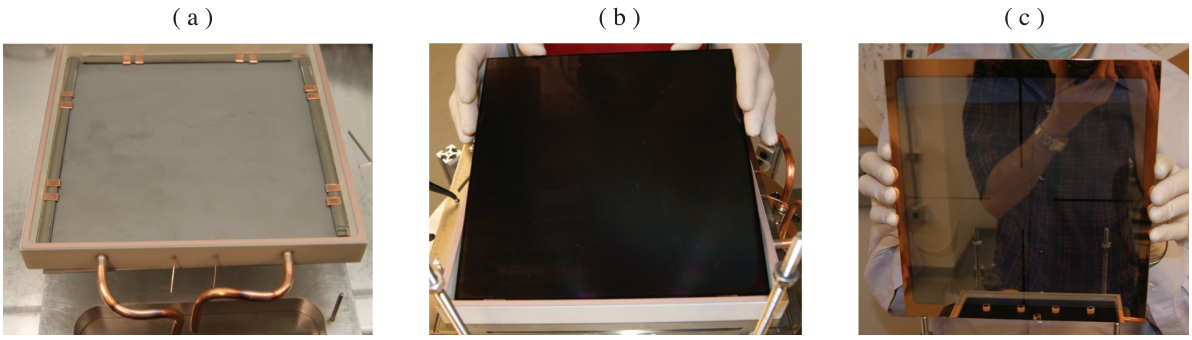

Figure 2.4: The three main components of an LAPPD: (a) the UC monolithic ceramic tile base; (b) the micro-channel plates, shown here with a dark-colored secondary emitting coating; (c) the entrance window, shown here with a pre-deposited antimony layer and thin-film metallic layers around the perimeter for sealing.

The University of Chicago has developed a ceramic bodied LAPPD package with design features that are coupled to the production process described here. This package is flexible enough to used in other fabrication processes. The UC ceramic tile package consists of a monolithic ceramic tile base with capacitively-coupled anode and a transparent entrance window, shown in Figure 2.4. The fast signal pulses from the MCPs are capacitively-coupled through the thin-film metal anode on the bottom plate, avoiding the need for brazing a large number of pins or electrodes through the ceramic base. See Section 3.2 or Reference [58] for more information on capacitively-coupled readout.

The tile base is one-piece, composed of high-purity Al_2O_3 ceramic [59, 60]. Two 1/4" OFHC copper tubes are brazed through the sidewall to provide an inlet for pump-down and alkali vapor transport. The present design uses 6 copper pins, 3 per side, brazed through opposing walls for high voltage distribution to internal components. Figure 2.5 shows a close-up of the tubes, pins, and metal-coated sealing surface.

The top surface of the ceramic packaging mates with the window perimeter to form the hermetic seal. In this batch production procedure, an extruded wire of indium-silver alloy is chosen as a low-temperature solder seal. This type of hermetic seal relies on both surfaces

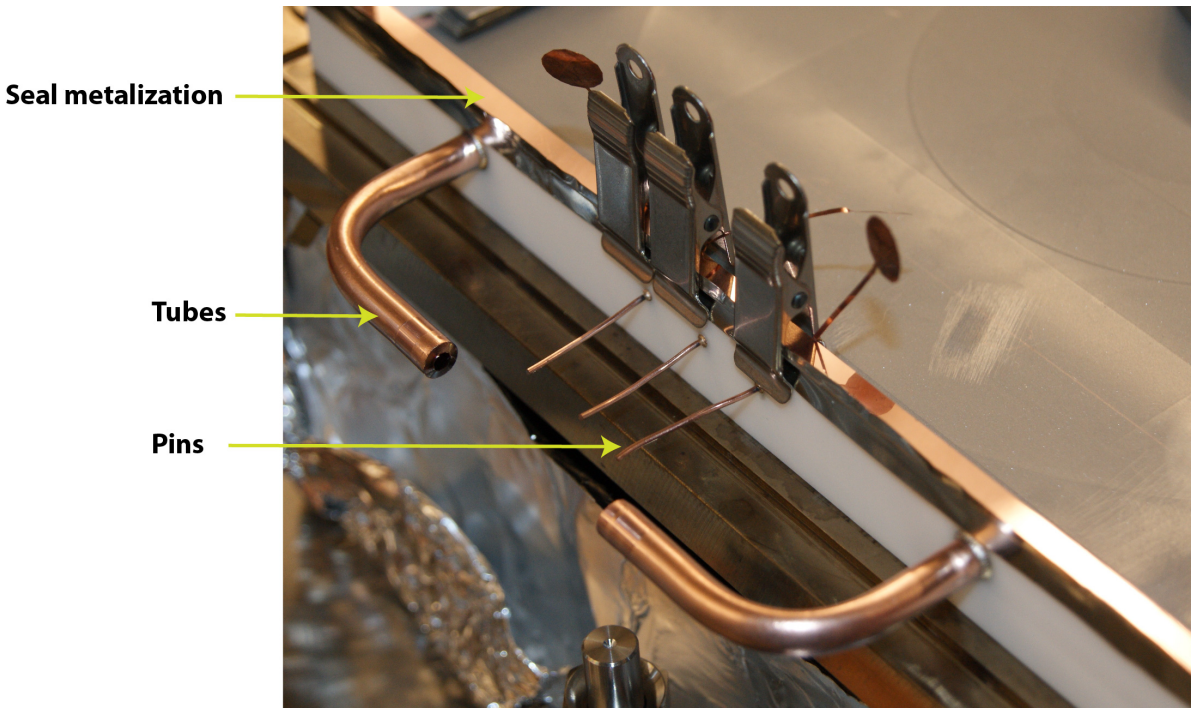

Figure 2.5: Copper tubes that connect the tile base to the UHV manifold and copper pins that provide high voltage to internal components. This image also features a close-up of a seal metalization, consisting of 200 nm 80-20 NiCr bonded to the ceramic, followed by 200 nm of Cu without a vacuum break in-between coatings.

to be coated with a wettable metallic layer. At least one component of this layer or set of layers, called the "tie layer", must chemically bond with the ceramic or glass substrate.

The majority of trials used thin film evaporation to deposit 200 nm of 80-20 NiCr followed by 200 nm of Cu without a vacuum break on the sealing surface, with the other surfaces protected by masks. This sealing surface is visible in Figure 2.5. At the same time, the bottom interior surface of the tile is coated by evaporation. The first step is evaporation of 10 nm of NiCr on the anode for capacitively coupling to exterior signal boards [58]. A second set of evaporation masks are used to deposit a metallic border overlapping the NiCr anode and connected to a copper pin, providing a charge drainage path to ground. This border is also 200 nm of NiCr followed by 200 nm of Cu [61].

After sealing, the UHV inside the LAPPD is maintained by non-evaporative getter strips. Two stacks, each containing 174 mm by 8 mm of SAES ST707, are held and electrically

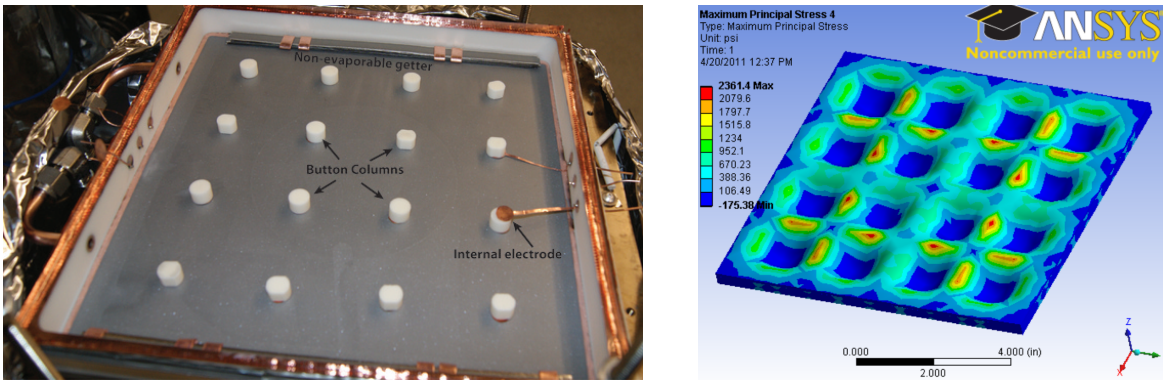

Figure 2.6: On the left, the tile base during assembly showing the button columns, non-evaporable getter stacks, and high voltage electrodes connected to pins in the sidewall. On the right, a finite-element analysis of the stress on a B33 window under vacuum.

grounded to the anode border using copper clips. The getter is activated during the sealing cycle and bake-out procedure.

2.1.5 Mechanically supporting the LAPPD package

The unsupported spans of the window and tile base need to support almost 1000 lbs of compressive force from atmospheric pressure. Sixteen columns of 3/8"-diameter ceramic cylinders ("buttons") are placed internally at 1.8" spacing in the gaps between the window, MCP's, and anode. The buttons serve three purposes:

1. Supporting the package against the compressive force of atmospheric pressure
2. Setting the gaps between the MCP's, tile base, and photocathode
3. Applying mechanical force between the MCP surfaces and the high-voltage internal electrodes. These electrodes connect the copper pins to the surfaces that need to be set at high voltage to accelerate primary and secondary electrons

The left-hand panel of Figure 2.6 shows the placement of button columns, the non-evaporable getter, and the high voltage electrodes connected to pins in the sidewall. The

window flexes under the force of atmospheric pressure, holding the MCPs from moving laterally via the supporting force of the button columns.

The thicknesses of the button columns and MCPs are measured precisely and matched to the depths of the tile base at each button location. A procedure for measuring and determining the thickness of each button column is described in detail in Appendix D. The space between the anode and bottom MCP and photocathode to top MCP is set to 0.25". A pair of MCPs are separated by 0.08" and oriented in the chevron configuration [62, 63, 4].

The thickness of the indium seal is *not* set by the heights of the button columns. Instead, the window sits upon a "hard-stop" on the side-wall that allows indium to fill a fixed gap between the window and sidewall surfaces (see the next section, Section 2.1.6). The measured precision of the button column heights is about 0.5 mils.

2.1.6 The hermetic indium-alloy seal

One of the challenges of scaling the size of MCP-PMTs is the increased difficulty of the hermetic seal. A sealing method that is not robust will have a higher probability of failing for larger perimeters. A sealing solution consists of clamping the window in place on a "hard-stop" on top of the tile base sealing perimeter. The hard-stop, typically 2 mils thick, is such that molten indium is wicked into the gap between the sealing surfaces by the chemical forces of the wettable metal films. This is the same mechanism of capillary-action observed when placing a drop of water at the edge of two microscope slides. The hard-stop may be a machined lip on the inner surface of the side wall; or, in the case of Tile 31 showcased in this chapter, a copper shim with a saw-toothed cut-out and teeth folded over.

A photograph of the tile assembly is shown in Figure 2.7. The tile base, inner components, and window are assembled on top of a 0.5" thick SS fixture plate. The copper inlet tubes are connected to the vacuum manifolding using a combination of Swagelok and VCR joints. The stack of components is compressed between the fixture plate and a compression plate

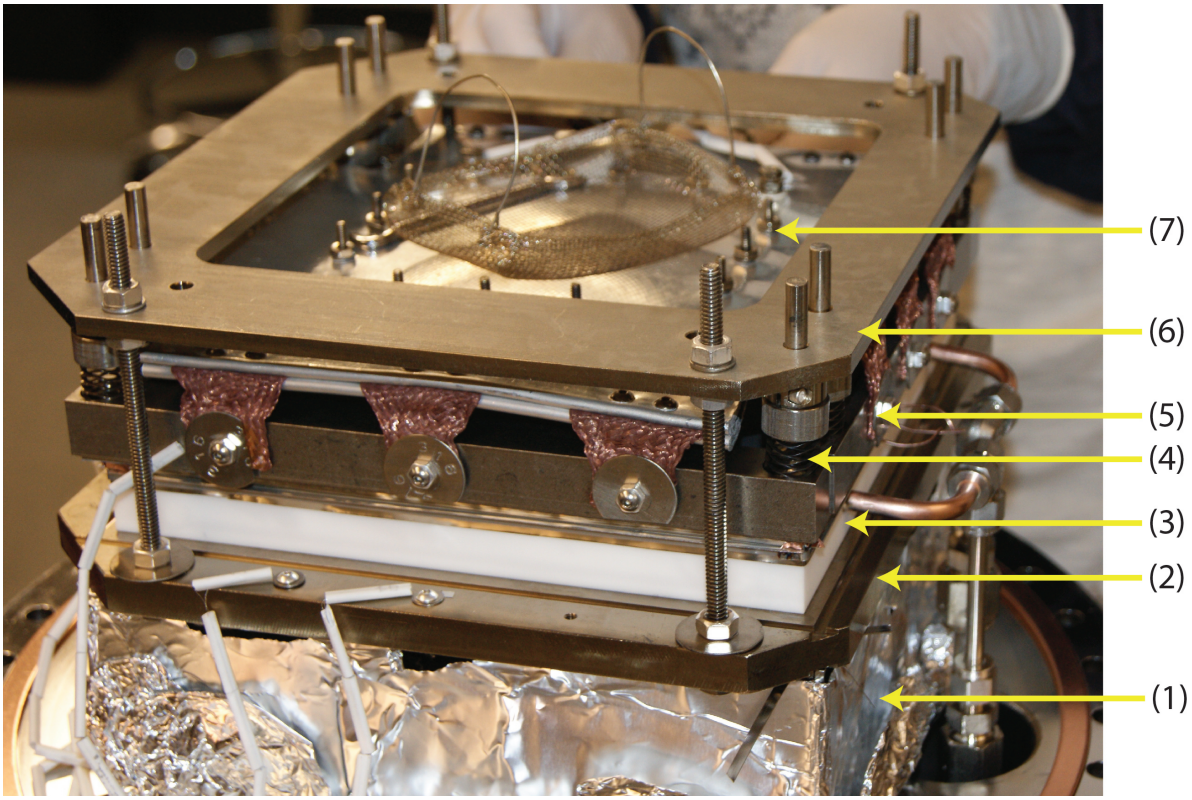

Figure 2.7: An assembled tile clamped in place in the compression fixture prior to sealing. The indicated components are: (1) the lower NiCr heater assembly; (2) the bottom compression fixture plate; (3) the tile assembly consisting of ceramic base, internal components, and glass window; (4) the compression mechanism; (5) floating rigid press bars; (6) the upper compression fixture plate; and (7) the upper NiCr heater assembly.

using 8 springs set to about 8 lbs-force each. Two heaters made of NiCr ribbon wrapped around ceramic plates are pre-placed beneath the SS fixture plate. An identical NiCr heater is placed above the tile assembly, connected via copper braids to 1" thick SS bars that make contact with the seal perimeter.

A key feature of this sealing system is that the outer vacuum chamber vessel is not heated. Instead, the tile assembly is heated directly above and below by nearby heaters. Figure 2.8 shows the thermal cycle for Tile 31. The cycle consists of a ramp-up of approximately 15 hours, a bake-out of 18 hours at 290 °C, followed by cool-down to room temperature. The feature around 220 °C is due to the formation of the indium-alloy capillary seal.

A key advantage to the dual-vacuum assembly is having the option to leak check the

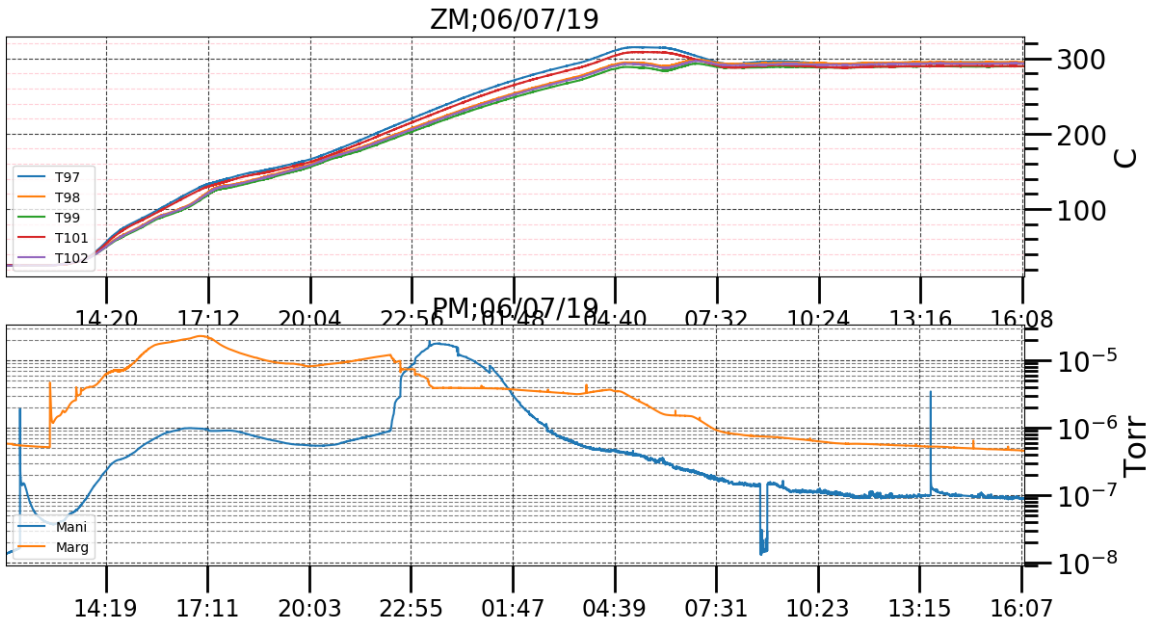

Figure 2.8: The thermal cycle temperature (top) and dual-vacuum pressure (bottom) from the Tile 31 seal-and-bake procedure. The feature around 220 °C is due to the formation of the capillary seal, isolating the outer and inner vacuum volumes from each other after the In-Ag allow has melted at around 143 °C.

indium perimeter. Leak checking after the indium has solidified is performed in two steps. A global check is made by filling the outer vacuum chamber with a calibrated partial pressure of argon gas and closing the valves that connect the LAPPD inner volume to the manifold pump. If a leak exists, argon will slowly fill the LAPPD inner volume. After several hours, the valves are opened while monitoring the gas content with a downstream residual gas analyzer (RGA). The leak-rate is estimated using an estimate of the conductance to the LAPPD inner volume. We estimate the sensitivity of the global leak check to be 1-2 $\times$ 10^{-13} mbar-liters/sec.

If a leak is detected, the outer vessel is lifted and a local leak check is performed using a helium leak detector in combination with a helium needle probe source slowly tracing the seal perimeter. We estimate the sensitivity of the local leak check to be several 10^{-11} mbar-liters/sec.

2.1.7 Barois photocathode synthesis

The synthesis of bialkali photocathodes by exposing an antimony (Sb) layer pre-deposited on a substrate by thermal evaporation was described by Sinclair in 2009 [64]. It was recently discovered that the chemistry of photocathode synthesis based on a pre-deposited Sb layer had been explored in detail by Barois et al. in 1989 [65, 66], and that the air-transfer process is commerically used by Hamamatsu [2] and MELZ in Russia to make multi-anode photomultipliers [57].

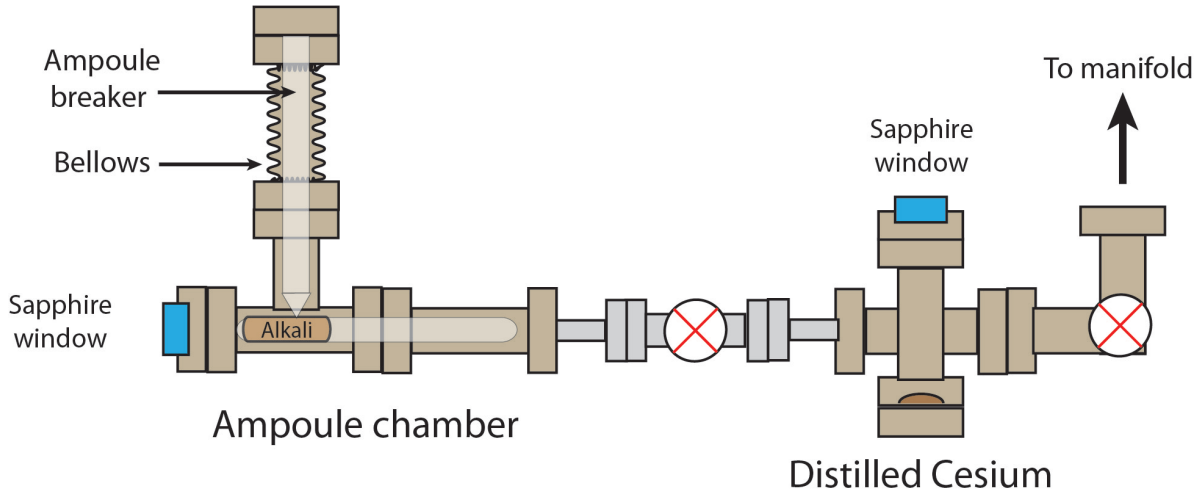

Figure 2.9: Diagram of the alkali vapor source. The left-hand section is the ampoule chamber; the right-hand section is the source chamber. The cesium is distilled into the right-hand section to avoid possible oxidizing reaction with the glass and other contaminants on the ampoule.

The air-transfer assembly process involves depositing a Sb pre-cursor layer on the window prior to sealing the window to the detector body. The photocathode is synthesized after the seal has been made and tested for leaks. In the process described here, only a single alkali, cesium (Cs), was used for development purposes and simplicity.

The photocathode, once synthesized, consists of a Cs-Sb compound with fractional composition, or stoichiometry, that may vary over the large surface area of the LAPPD window. Cs-Sb compounds may be formed by equilibrium reaction of Sb with Cs vapor [65], with stoichiometry set by temperatures and pressures in the system. Some stoichiometries are

optimal for high quantum efficiency. Since the Sb is immobile, a cathode of uniform thickness and composition is set by an Sb layer of uniform thickness and crystal structure [66].

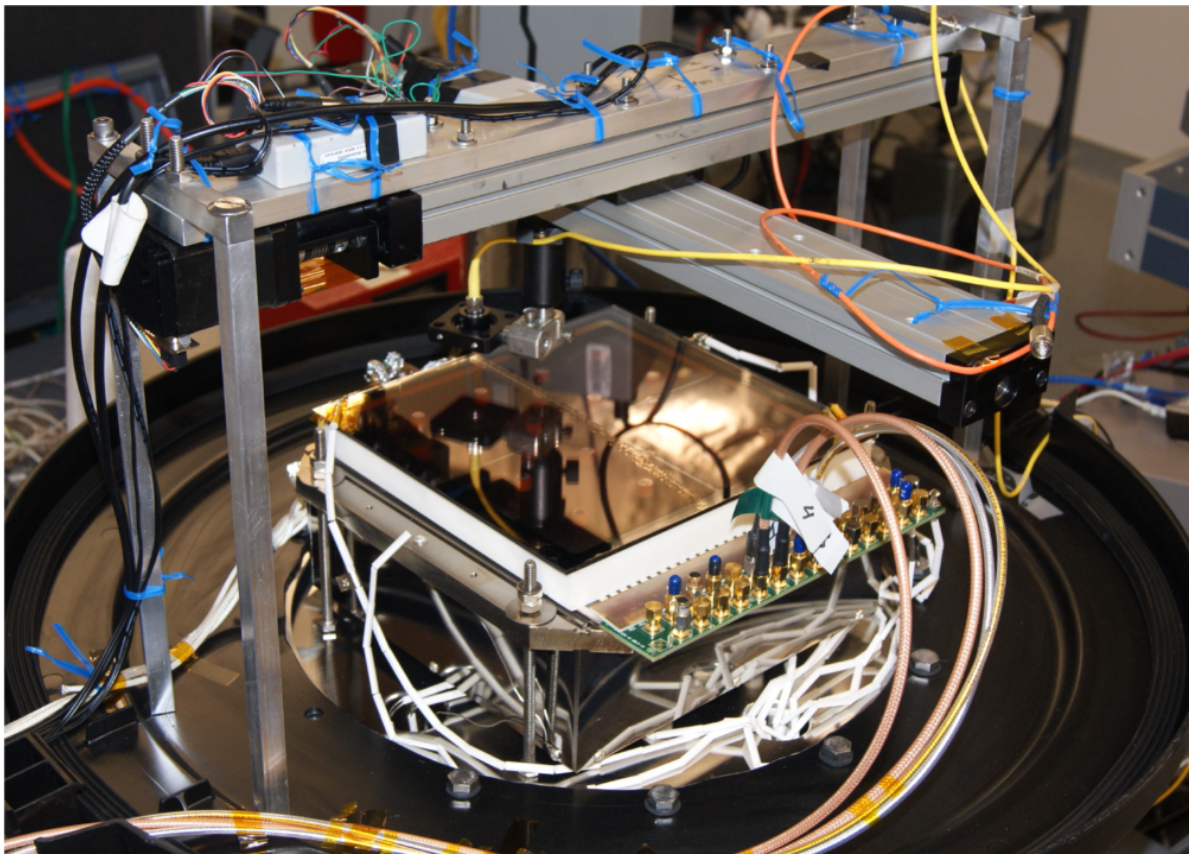

Figure 2.10: A 2D stage for mapping photo-response during and after photocathode synthesis. The LAPPD seen here is still mounted on the fixture inside of the outer vacuum vessel. After the seal procedure is complete, photocathode monitoring hardware is easily placed on top of the tile assembly while it is still connected to the pump.

The cesium vapor source is shown schematically in Figure 2.9. The glass ampoule of Cs [67, 68] is inserted into the horizontal section of the tee seen in the left-hand chamber. The ampoule is broken from above by a ceramic rod attached to a compressible bellows. The Cs liquid and glass ampoule can be observed through a sapphire window. The liquid Cs is then evaporated away from the glass shards of the ampoule into the right-hand chamber by creating a thermal differential, heating the ampoule chamber to 300 °C and above. Non-evaporable getter pellets are placed in both the ampoule chamber and the source volume,

activated during the distillation process. The sapphire window in the source chamber allows visual monitoring of the condensing puddle of Cs. Cesiation of the tile is initiated by opening the valve to the manifold with the source chamber at 150-155 °C. The temperatures of other components are shown in Figure 2.3

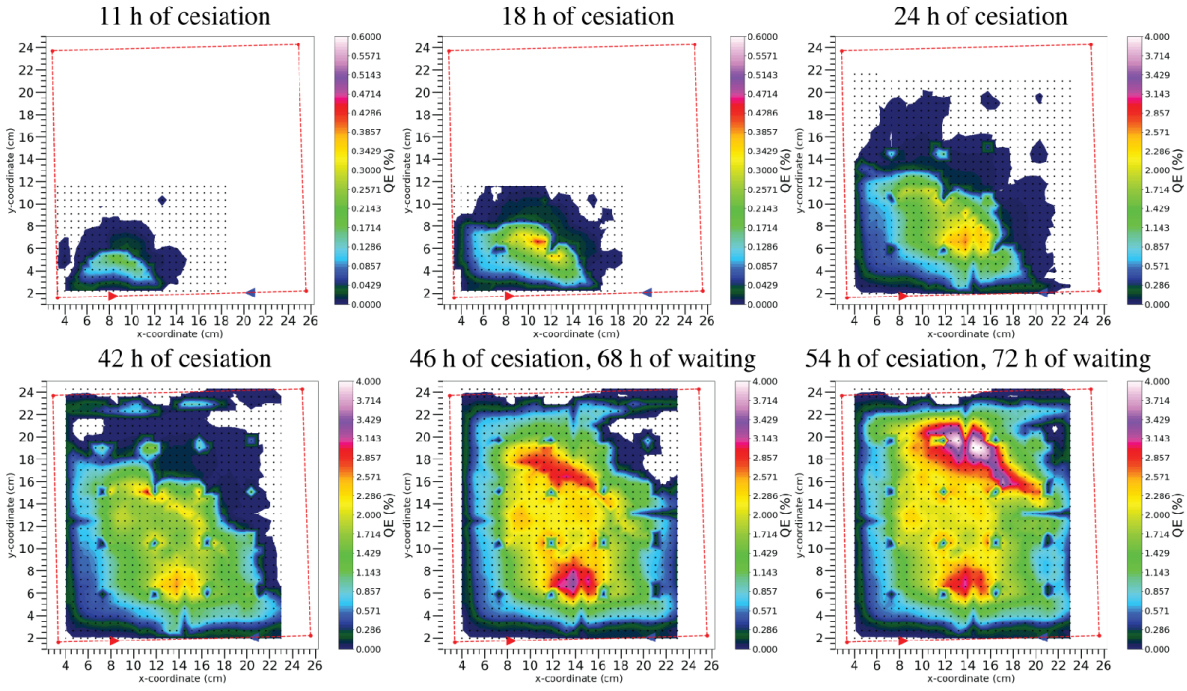

Figure 2.11: Successive maps of the photo-response for Tile 31 during photocathode synthesis.

A 2-dimensional motion stage for mapping the photocathode response during photocathode synthesis is shown in Figure 2.10. The LAPPD internal volume is still connected to the manifold and pump. Figure 2.11 shows successive maps of the photo-response during the activation of the pre-cursor Sb layer by Cs vapor. The response grows to a saturation value near the inlet and then continues to the far side of the 8.26"-square window. The response saturates near 3% quantum efficiency (QE).

Neither the uniformity nor the end-point QE are satisfactory for a useable commercial device. We attribute the lower quantum efficiency near the edges to a non-uniform temperature of the window during synthesis. The tile was heated through its contact with the

fixture lower plate, and was subject to convective cooling from above. We attribute the lower-than-typical QE for Cs_3Sb cathode to an overly-thick Sb pre-cursor layer.

2.1.8 Micro-channel plates during photocathode synthesis

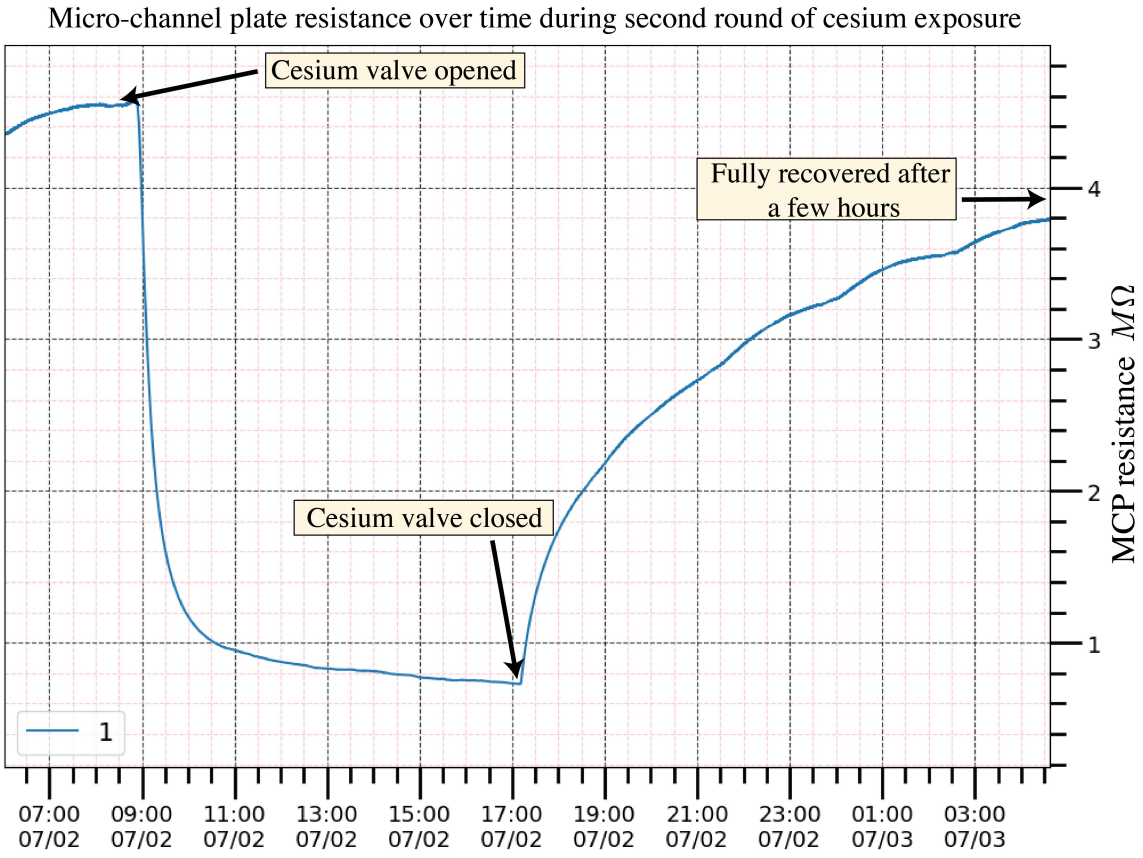

Figure 2.12: The resistance of the stack of two micro-channel plates and spacers during a cesiation cycle, showing that the plate resistance recovers after an initial large drop.

The metals involved in phothocathode synthesis are highly reactive and can change the surface chemistry of the micro-channel plates. Figure 2.12 shows a snapshot of the dynamics of the MCP series resistance over a short period of time during photocathode synthesis. The window and tile body is held at 120 °C during the synthesis, which reduces the resistance by a large factor.

The hot DC resistance of both MCPs in series held at 20 V is measured during the

cesiation process. Over the first 5 hour cesiation period, the total series resistance drops from 6 MΩ to 1 MΩ. Upon closing the cesium source valve, the resistance recovers to 4.6 MΩ over 13 hours. During this period, the LAPPD internal volume is connected to a pump via the manifold tubing. After a second cesiation, the plates recover from 0.8 MΩ to 4.8 MΩ over 30 hours, and then to the original 6 M Ω on the timescale of a few days.

Following this recovery, the MCPs were cooled to operational temperatures. Pulses on the order of 10-20 mV amplitude were observed in coincidence with triggered laser pulses from a PiLas 405 nm pulsed laser.

Pinch-off

After photocathode synthesis and characterization, the copper tubulations are hermetically sealed by pinching with a hydraulic tool [69]. The force from the hydraulic tool cold-welds the copper tubes shut, creating a razor-sharp edge. This edge is potted with silicone for safety, and the tile may be removed from the fixture for use.

Closing comment

We have shown that each of the potential "show-stopper" obstacles to LAPPD batch fabrication is technical rather than fundamental. The system described above is a proof-of-principle solution. However, the development of an optimized industrial batch process for bringing volume up and cost down for wide-spread use in particle physics, medical imaging, and nuclear security remains a task for commercialization [46].

A detailed outline of the procedure described in this chapter for fabricating LAPPDs may be found in Appendix D, intended for those who may be struggling with the challenges of LAPPD fabrication or are developing a next iteration batch production facility.

2.2 Vacuum-transfer fabrication

The vacuum transfer process is a fabrication method whereby the photocathode is synthesized prior to sealing the window to the detector body. Figure 2.13 shows a diagram that emphasizes the difference between air-transfer and vacuum transfer processes.

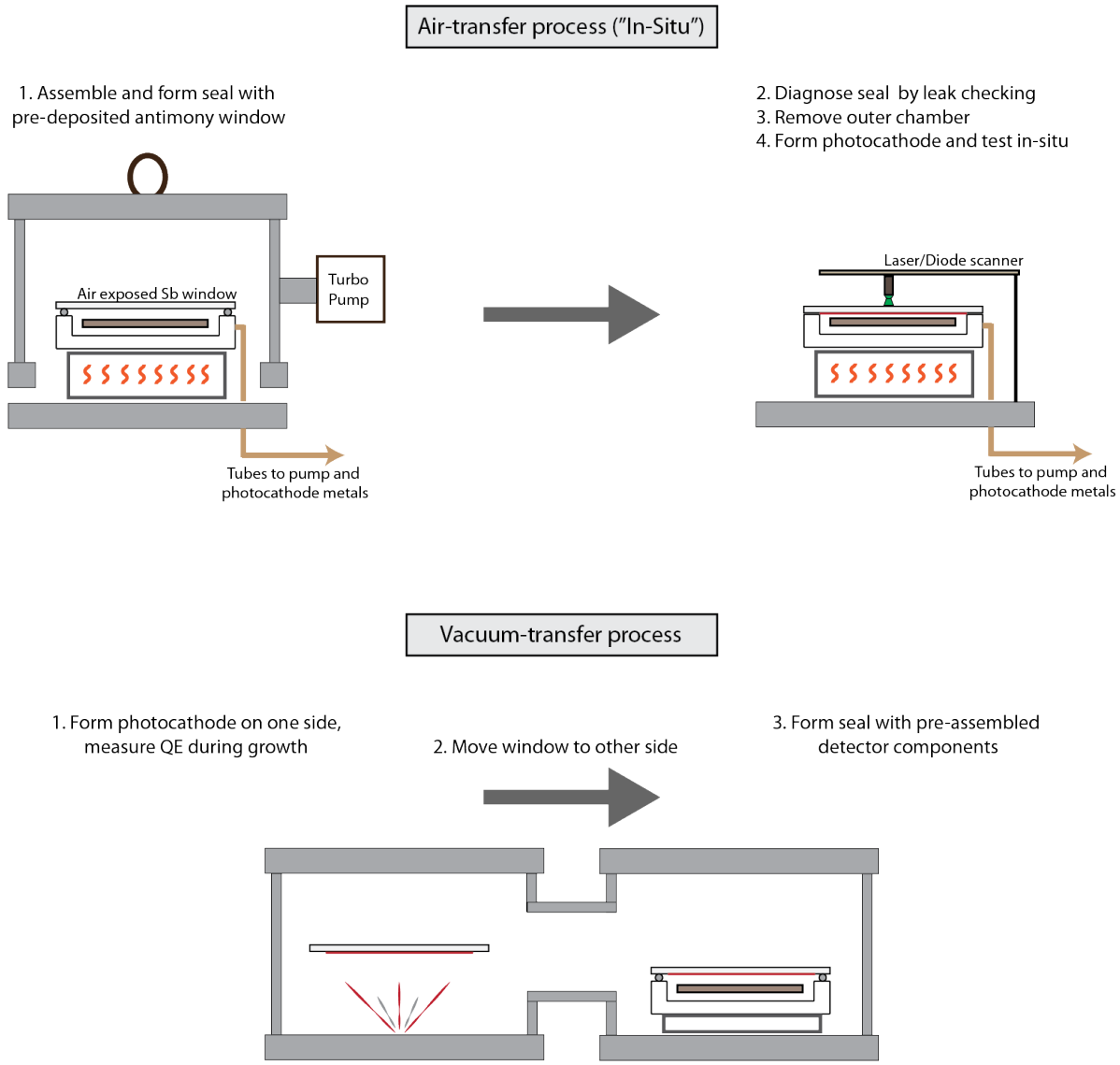

Figure 2.13: An illustration of both the air-transfer and vacuum-transfer LAPPD fabrication processes, emphasizing their differences. The vacuum transfer process does not rely on the existence of inlet tubes and a dual vacuum topology. However, the vacuum transfer process may benefit from the use tubulation to allow for leak checking the indium seal and keeping the internals on a dedicated pump.

A vacuum transfer process could be described as follows. A UHV vacuum chamber is constructed with two connected sections not in line-of-sight with one another, here called the left and right side (see Figure 2.13). The LAPPD base and components are prepared in the right section of the chamber. The sealing surface of the LAPPD is pre-tinned with indium or indium alloy. On the left side of the chamber, a window is suspended over antimony and alkali sources. The chamber is brought above the temperature of the indium melting point. Heating elements are removed and the system cools radiatively. The photocathode is synthesized in the left chamber, using the method of line-of-sight evaporation. The MCPs and other LAPPD components are not significantly exposed to photocathode metals because that section of the chamber is not in line-of-sight with the metal sources.

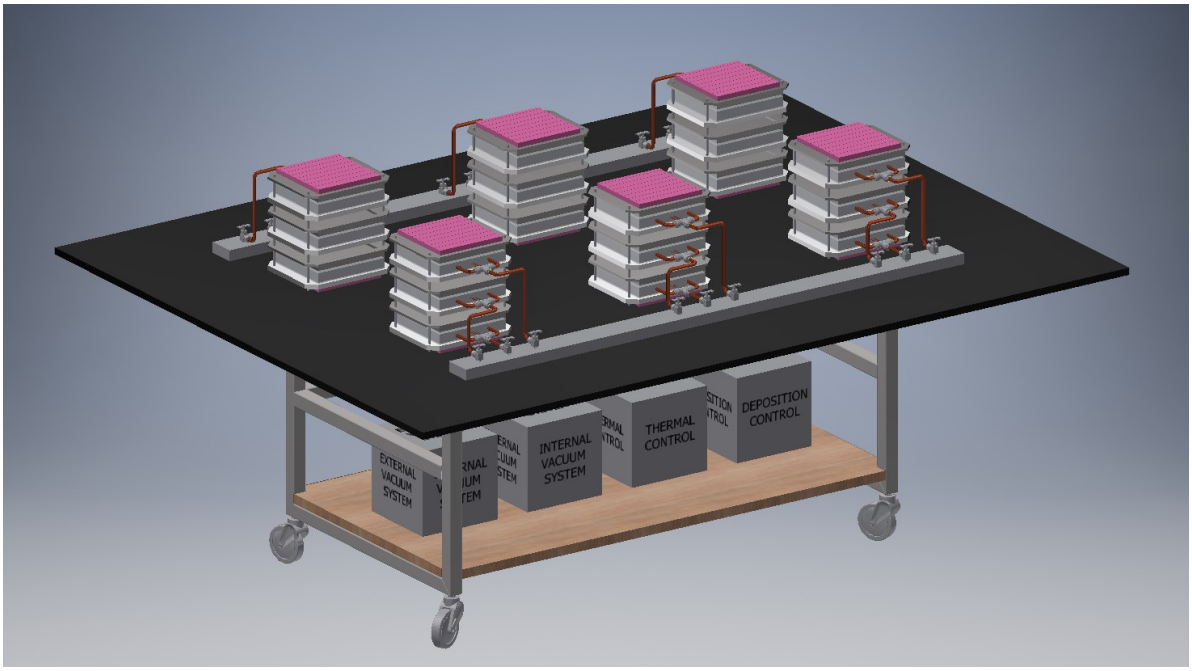

Figure 2.14: A conceptual drawing of an air-transfer production chamber that fabricates 18-LAPPDs at once [70]. The LAPPDs may be stacked vertically, stack having heating elements, sealing hardware, and photocathode diagnostic hardware. All LAPPDs have tubulations that lead to a common manifold that sources high vacuum and photocathode metals. The outer chamber, with its base in black, is not heated and may be low vacuum.

Once the desired photocathode has been synthesized, the window is carefully transferred to the other section of the chamber using motion stages or carrying feedthroughs. The

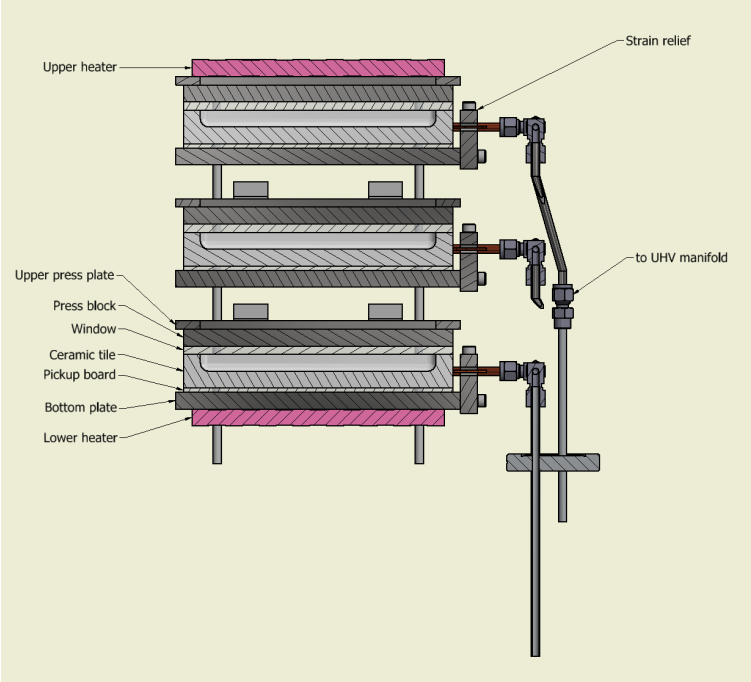

Figure 2.15: A conceptual drawing of a modular LAPPD bake-and-seal stack. Three LAPPDs are assembled in a vertical stack with tubes connected to a common UHV manifold. Heaters above and below control the seal-and-bake thermal cycle, with insulation for thermal uniformity not shown.

window is set down on the side wall while the indium is still above melting point.

The air-transfer process has an advantage in that multiple LAPPD-fabrication modules may be stacked vertically in the same vacuum chamber, with all modules on a common internal-vacuum manifold and pump. The space above the LAPPD assembly is constrained in the vacuum-transfer process, as it must be reserved for lateral motion of the window. Figure 2.14 shows a conceptual drawing of a large outer low-vacuum chamber containing 18 stacked LAPPD modules tied to common manifolds, taken from Patent [70]. Figure 2.15 shows three LAPPDs modules stacked on one another on a common internal vacuum manifold, with hardware such as heaters that are necessary for the sealing process.

2.3 Diagnostic tools critical to developing a seal procedure

The development of the sealing method described in the process of Section 2.1 involved many failed trials, multiple fabrication chambers, sealing metalizations, and detector package designs. Some questions were answerable using a small-sample format, with either 4" square perimeter or 1" diameter circular perimeter. However, the difficulty of the seal and the mechanical forces involved scale directly with the perimeter. Successful trials on the small-format samples did not always correlate with successful trials on the large-format.

The diagnostic tools for inspecting failed indium seals were critical to determining the incremental changes for each successive sealing trial. Figure 2.16 shows examples of four methods used to diagnose failed or successful seals. The four methods are (top-left) physically removing the bonded window using a variety of destructive tools; (top-right) observing exposed indium surfaces with a scanning electron microscope (SEM) with built-in electron dispersive spectroscopy (EDS) [71]; (bottom-left) dental x-ray while the window is still bonded [72]; (bottom-right) depth-profiling optical microscopy of seal surfaces before and after sealing [73].

The use of dental x-rays to observe structure in the indium directed the research towards the capillary-action seal strategy [72]. The advantage of the x-ray is that macroscopic structures may be observed while the indium seal is still in-tact. We found that many indium seals that contained the wire within the seal region exhibited "voids" similar to the ones seen in the bottom-left sub-figure of Figure 2.16. These voids imply that some parts of the molten indium have enough surface tension to sustain an interface over relatively large distances. We suspect that these voids are caused by indium oxide that is either not removed from the indium wire during pre-processing or is formed during the bake-out and seal thermal cycle.

The solution that the capillary-action strategy provides is to keep the easily-oxidizable indium wire out of the seal region. Instead, only unoxidized indium, which has a wetting potential with the seal-surface metalization, is pulled into the seal gap.

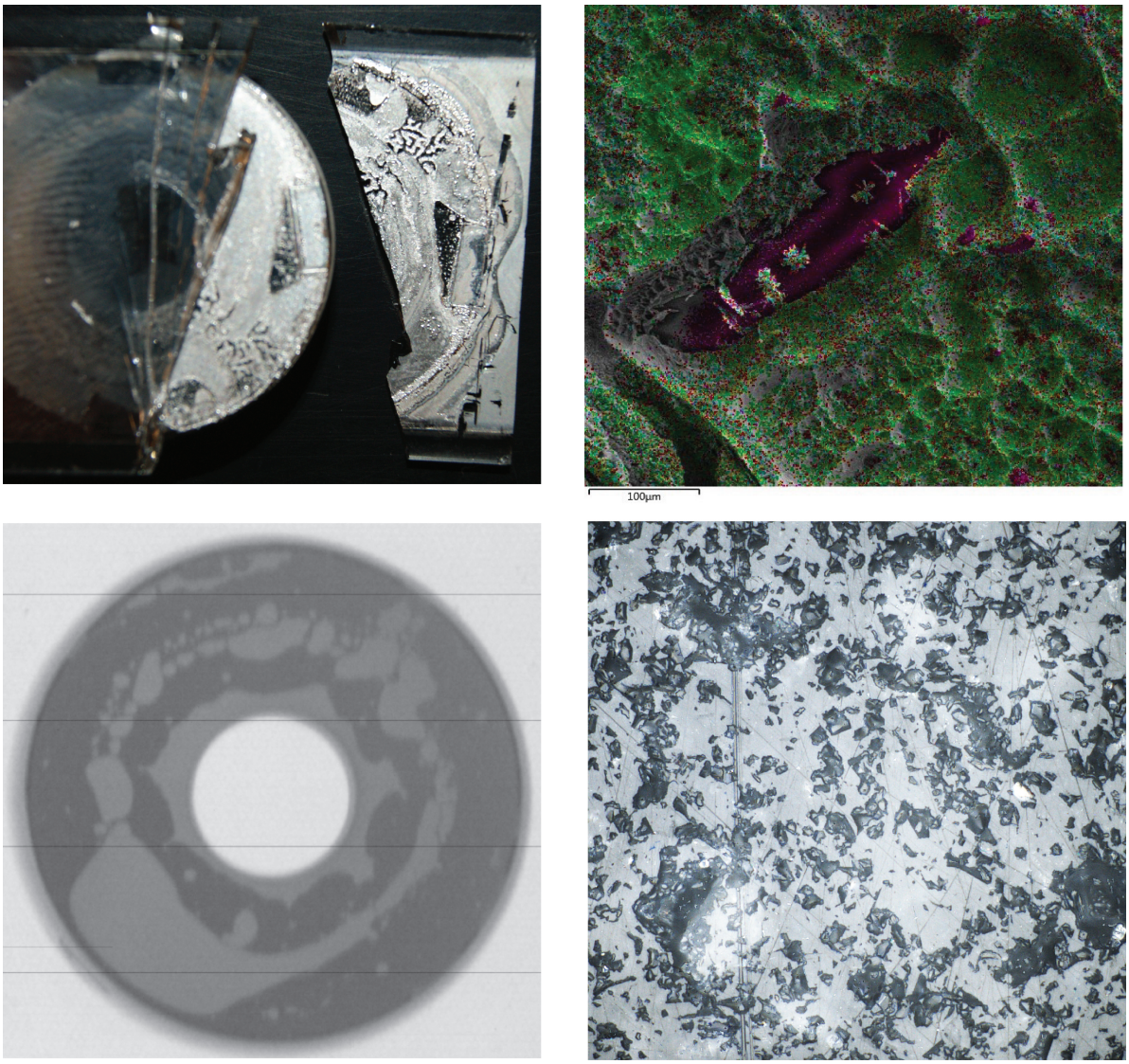

Figure 2.16: Demonstrations of the four main diagnostic tools used for diagnosing failed indium seals. The four methods are (top-left) physically removing the bonded window using a variety of destructive tools; (top-right) observing exposed indium surfaces with a scanning electron microscope (SEM) with built-in electron dispersive spectroscopy (EDS) [71]; (bottom-left) dental x-ray while the window is still bonded; (bottom-right) depth-profiling optical microscopy of seal surfaces before and after sealing [73].

CHAPTER 3

LAPPD SIGNAL READOUT

Defining terms

The "readout" of an LAPPD refers to the system that extract signals from the micro-channel plates (MCPs) and transfers them to digitizing electronics. The spatial resolution, time resolution, rate capabilities, and signal-to-noise ratio are all dependent on the readout configuration.

The "anode" is the component of the LAPPD that physically interacts with the charge clouds produced by the MCPs. The anode is one element of the readout and is contained inside the LAPPD vacuum-volume. The "signal-pickup" or "pickup" is the component that distributes electrical signals on a set of conductors, directing them to digitizing-electronics channels. Common pickup geometries include arrays of copper pads, parallel transmission lines, and crossed delay-lines. The geometry of the pickup determines the number of channels per unit area. In some cases, the anode is the signal pickup, and in other cases the two are separate objects.

3.1 Micro-strip transmission-line readout

Prior to this thesis work, a radio-frequency (RF) strip-line anode was designed for optimizing the timing resolution of LAPPDs while minimizing the number of channels per unit area [75, 74]. An example of a strip-line anode that has not been sealed inside an LAPPD is shown in Figure 3.1. This anode is also a signal-pickup, as the conductors are segmented to distribute signals directly to the digitizing electronics.

The analog bandwidth of this rf-stripline anode is roughly 1.6 GHz when coupled to a signal ground-plane on the other side of the glass substrate. A high-analog-bandwidth pickup will preserve the timing information contained in the ~750 ps leading edge of LAPPD pulses

Figure 3.1: Photograph of a strip-line pickup geometry. This pickup pattern was designed and characterized by the authors of Reference [74]. The perimeter is a top-down view of the sealing surface. Each strip has 50 Ω characteristic impedance when a ground-plane is attached to the air-side of the glass substrate.

[1]. Some of the factors that determined the ultimate timing resolution of an MCP-PMT

1. Pulses from LAPPDs and PMTs are negative polar, having a "falling edge" whereas many other timing sensors have pulses with "rising edges" determining the time of arrival. In this thesis, "leading edge" will be used when possible to avoid confusion.

detector include the bandwidth of the pickup and digitizing electronics, the signal-to-noise ratio, and the rise-time of the pulse [76, 77].

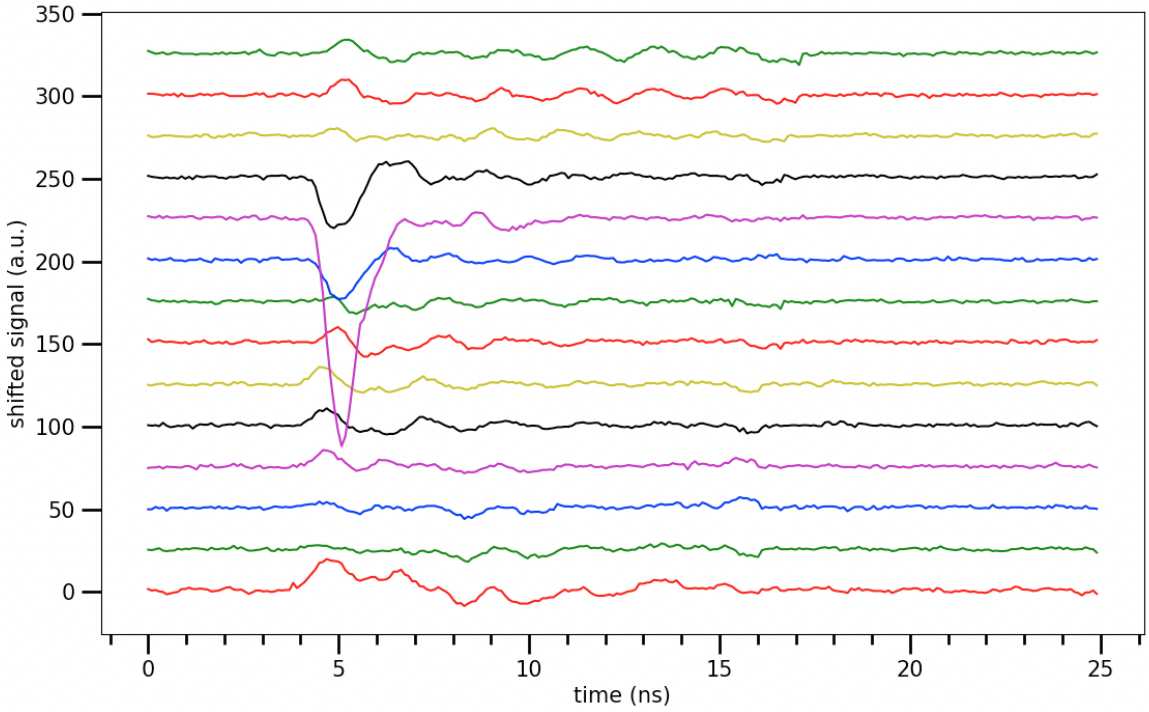

Figure 3.2: The digitized signals of 14 adjacent strip-lines of LAPPD 43 induced by a charged particle. The signal from each strip-line is offset by 25 mV on the y-axis for clarity. The amplitudes as a function of strip number can be used to constrain the position of the electron cloud in the dimension transverse to the strip-lines to around 700-1000 μm [8, 5].

3.1.1 Position reconstruction using the strip-line readout

The transverse position of charge clouds can be reconstructed by comparing the amount of image charge induced on each strip. The relative distribution of signal as a function of strip number is analyzed to produce a transverse position of the center of the image. One method used in Chapter 7 is the "charge centroid" method. This analysis chooses the transverse position by calculating the "center-of-charge", identical to the equation for center-of-mass. If strip-line i at transverse position y_i captures charge q_i, then the charge centroid

reconstructs the transverse position as

$$y_{\text{reco}} = \frac{1}{\sum_i q_i} \sum_i q_i y_i \tag{3.1}$$

One may also fit the transverse charge distribution using a Gaussian or a well-calibrated template. These methods are compared in Chapter 7.

An example of an LAPPD pulse that has signals shared among neighboring pads is shown in Figure 3.2. The amplitude of the primary-pulse in this event indicates that it represents many photoelectrons. Charge in the cloud diverges in the gap between the final MCP and the anode, which is about 1/8 " - 1/4 " for various pilot LAPPD designs. Signal-sharing also occurs for single electrons. In this case, due to the 10-40 mV amplitudes of single photoelectrons, the signal amplitudes on neighboring strips are often close to the digitization voltage-noise floor.

The parallel position of the charge cloud, also referred to as its longitudinal position, is measured as a time-of-arrival difference between the two ends of the strip multiplied by the propagation velocity. An example of the digitized pulses on two ends of the same strip is shown in Figure 3.3. The position resolution in the parallel dimension is determined by the resolution of reconstructing the time of the leading edge of a pulse.

In 2015, a femptosecond laser at Argonne National Laboratory was used to test a prototype LAPPD [8]. These measurements resulted in a 5.1 ps differential timing resolution between signals on both ends of a strip for large signals, resulting in a parallel position resolution of about 500 μm. This resolution becomes better for higher signal-to-noise ratios.

3.1.2 One-sided readout

One of the design goals of the strip-line geometry is to minimize the number of digitizing channels per unit area. The number of digitizing channels required for a measurement is

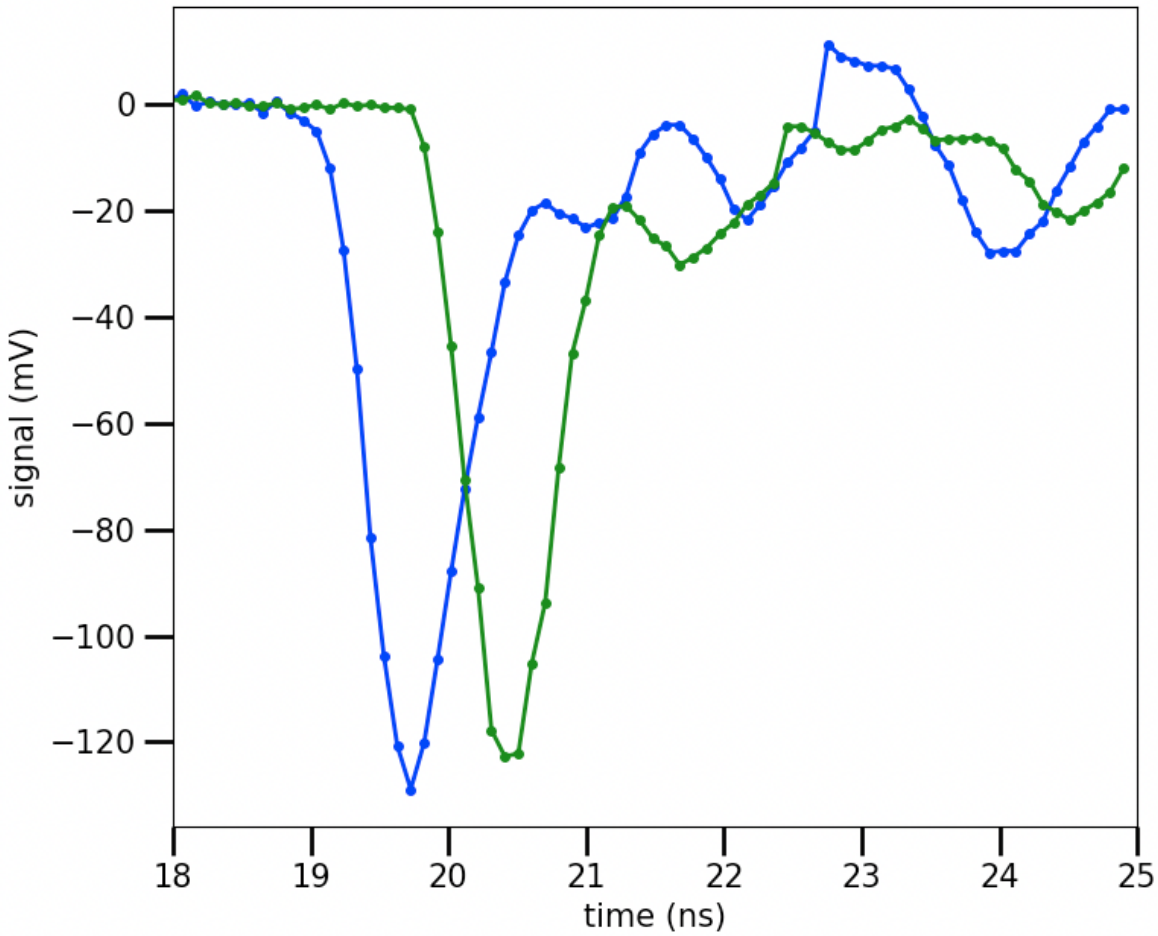

Figure 3.3: An LAPPD pulse showing the left (blue) and right (green) sides of a single strip-line. The time-of-arrival difference multiplied by the average propagation velocity is the parallel position of the electron-cloud-induced image.

often a significant cost driver.

The number of digitizing channels for a strip-line readout geometry may be further reduced by leaving one end of each strip open-circuit relative to the digitizer ground. Pulses propagating towards the unterminated end will reflect with the same polarity. The time difference between prompt and reflected pulses determines the parallel position.

All pulses will have a distinguishable reflected pulse that does not overlap in time with the prompt pulse if the lengths of the strips are extended using cables or PCB traces. However, the geometry of this pickup pattern and its method of longitudinal reconstruction limit the

maximum rate capabilities.

Another advantage of the one-sided readout is that the prompt and delayed components of the pulse are digitized by the same electronics channel. Compared with the two-sided readout, this removes an additional timing uncertainty associated with synchronizing two separate digitizing channels.

3.2 Capacitively-coupled pickup

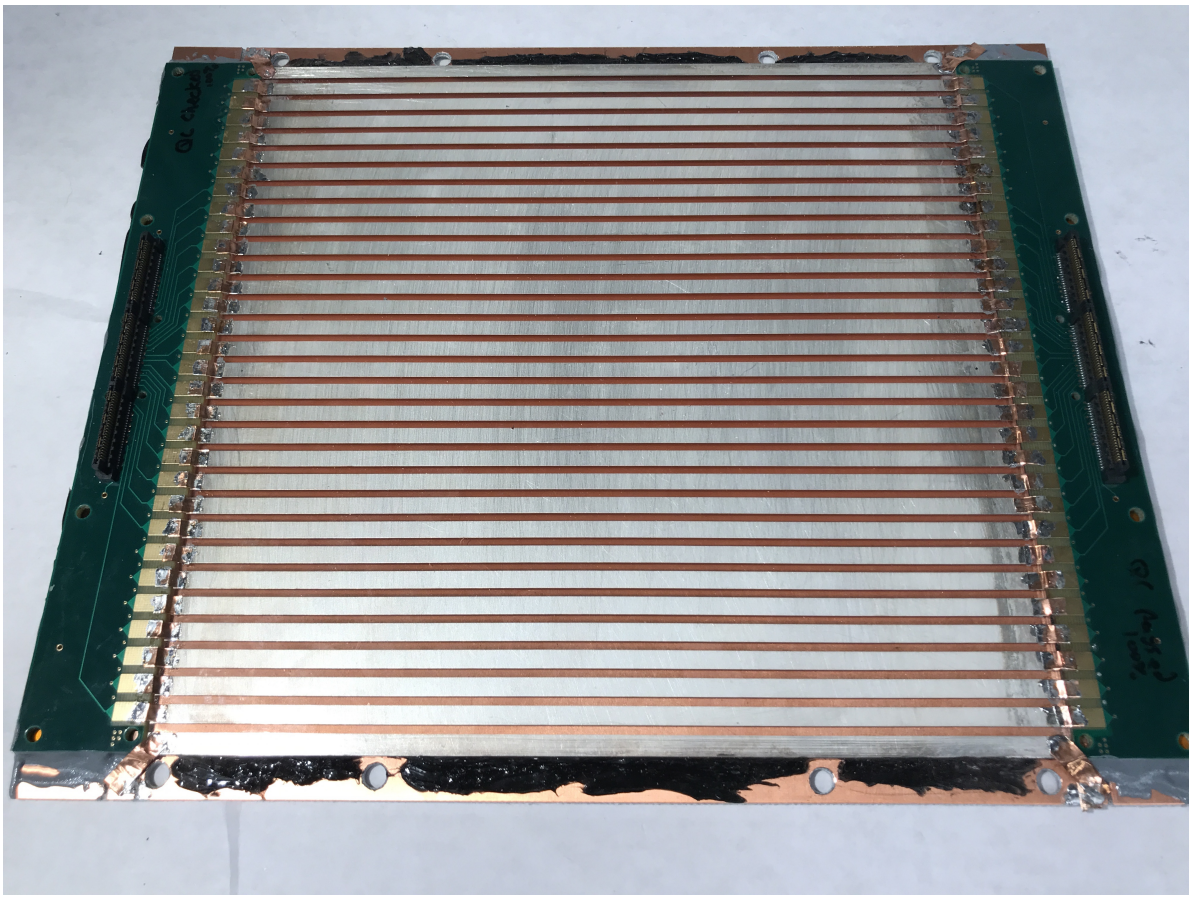

Figure 3.4: Photograph of the hand-made capacitively-coupled pickup used in this thesis work. The glass strip-line substrate and PCB adapter cards are glued to a copper-coated G10 substrate using silicone and soft epoxy. The PCB internal ground planes are connected to the strip-line back-plane using an exposed ground on the underside of the PCB and RF spring fingers. The interface between silver strips and PCB adapters is bridged by 3-mil-thick copper shims soldered to the strip-lines and PCB ports.

The spatial and timing properties of the readout cannot be modified after detector fabrication if the anode is segmented to take on the role of both anode and signal-pickup. This is the case in the Generation-I LAPPD design, where a strip-line anode is hermetically sealed to the internal vacuum volume of the LAPPD at the time of detector fabrication.

If instead the hermetically sealed anode is a uniform, continuous layer with some non-negligable resistance, high frequency signals may be capacitively-coupled through the vacuum packaging to a set of conductors placed nearby. A "capacitively-coupled pickup" is a pattern of segmented conductors, possibly on a printed circuit board (PCB), mounted outside of the LAPPD vacuum packaging.

Capacitively-coupled MCP-PMT anodes have been implemented using resistive thick films or semi-conductors [78, 79, 80, 81, 82, 83, 84], and MCP-PMTs with resistive capacitively-coupled anodes are commercially available [80, 85]. During this thesis work, it was demonstrated that a thin-metal layer made of NiCr can also transmit the high-frequency components of MCP-PMT pulses to an external array of electrodes, provided that the resistance is greater than about 1 kΩ per square [58].

The advantage of a capacitively-coupled pickup is that the geometry, which determines the position and time resolution, may be changed without destroying the detector. The detector and pickup geometry are decoupled and interchangeable. This allows for a broader variety of experimental applications of LAPPDs, as the detector fabrication process is not coupled to the spatial-temporal requirements of the experiment.

The University of Chicago (U. of C.) and Incom Inc. have been fabricating ceramic bodied LAPPDs with internal metallic and semiconductor anodes. These LAPPDs will be referred to as Generation-II (Gen-II) LAPPDs or capacitively-coupled LAPPDs. One U. of C.-fabricated Gen-II LAPPD, "Tile 31", measured cosmic rays in the Fermilab Test Beam Facility as a part of this thesis work.

A photograph of a capacitively-coupled pickup is shown in Figure 3.4. Ideally, a capacitive

pickup would have the controlled-impedance properties and bandwidth provided by printed circuit board fabrication processes. Due to time constraints, the capacitive pickups used in this thesis were hand-made using existing glass-substrate strip-line pickup planes.

The glass strip-line pickup is glued to a copper-coated G10 slab using silicone rubber. Two PCB boards are positioned and glued to either end of the strip-line substrate. These adapter PCBs convert the 5.13 mm wide strips to a 0.18 mm PCB-trace using ground planes at various depths and trace-width tapers for maintaining 50 Ω impedance [74]. The impedance is only expected to be roughly matched.

3.3 Connecting strips to digitizing electronics

Capacitively-coupled pickups may be designed in a PCB format with the digitizing-electronics systems on-board. In the case of the hand-made capacitive pickup, the adapter PCBs are soldered to the strip-lines using a low-temperature solder[2] and 3 mil copper shim-stock. The PCB traces are routed to high-channel-density SAMTEC connectors that mate to the front-end PSEC4 electronics system (See Chapter 5).

When the strip-lines are sealed to the vacuum packaging of the LAPPD, as in the Generation-I LAPPDs, electrical connections are made using electro-mechanical means. It is not recommended to use solder to connect to the strip-lines due to (1) the proximity to the low-temperature melting-point hermetic seal and (2) the possibility of permanently damaging or de-bonding the silver-strip coating on the glass substrate. Mechanical methods of making electrical contact must also consider the possibility of breaking or cracking the glass anode. The lip of the LAPPD anode extending from the packaging and allowing for connections to be made to the strips is only about 1/4". If this lip breaks, it is likely that a leak is introduced and the detector becomes inoperable.

2. ChipQuik, `https://www.digikey.com/en/product-highlight/c/chip-quik/solder-paste-and-flux`

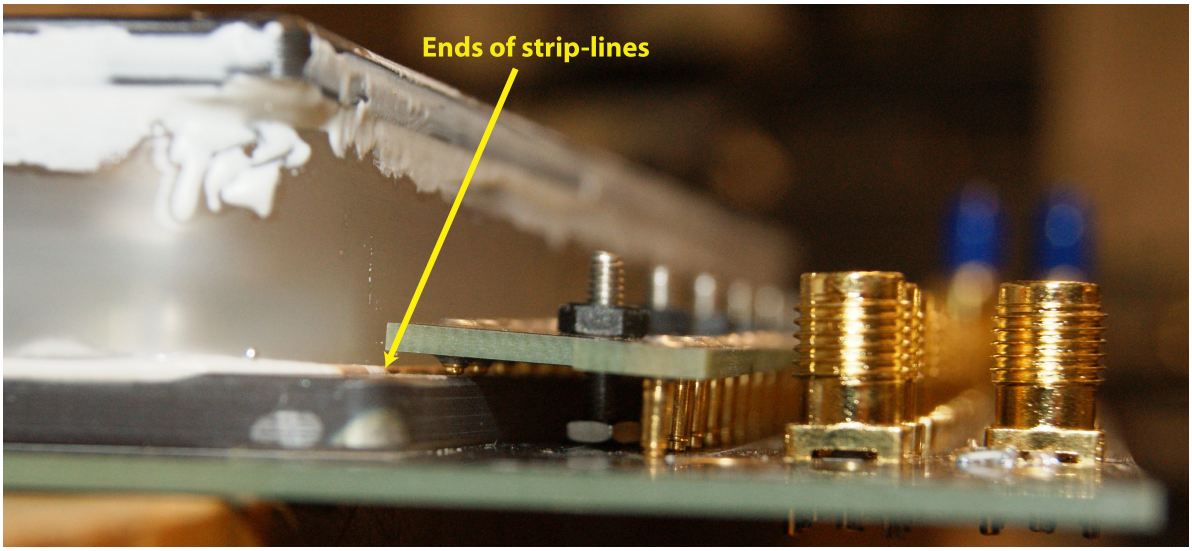

Figure 3.5: Photograph of the pogo-board that electrically adapts the ends of strip-lines to a printed circuit board. The base PCB contains holes located such that small screws may compress the pogo pins against the strips. The pogo pins also hold the LAPPD in mechanical compression to the PCB backplane, which may then be mounted to a fixturing structure.

Bernhard Adams has designed a PCB board that uses spring-loaded "pogo pins" to apply safe mechanical forces to the edge of the anode. A close-up of these pogo pins is shown in Figure 3.5. Signals are transferred from the strip-lines, through a bridge-PCB, landing on route inputs of the base PCB.

3.3.1 The ANNIE Analog Pickup Board

The Accelerator Neutrino Neutron Interaction Experiment (ANNIE) at Fermilab is a 26-ton water-based neutrino detector that plans to install 5 - 10 LAPPDs for precision tracking of neutrino interactions using the technique of optical time projection [86, 87, 48]. Many of the hardware and software components of this thesis are shared or transferable to the ANNIE experiment.

Bernhard Adams designed a PCB board specifically for the readout of ANNIE LAPPDs using pogo pins and strip-lines, called the ANNIE Analog Pickup Board (APB)[3]. The pogo

3. The use of "pickup" in this name does not follow the definition of pickup used in this thesis. The name

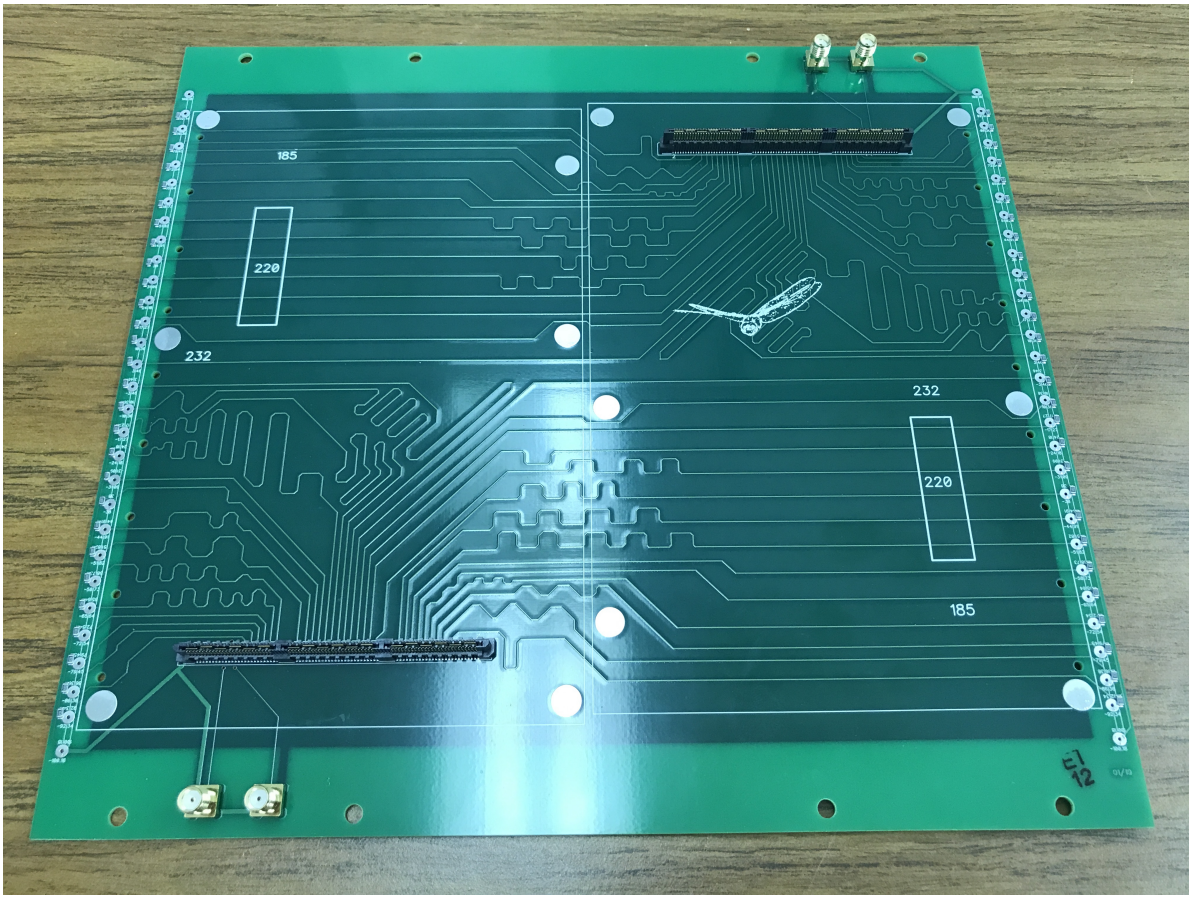

Figure 3.6: Photograph of the ANNIE Analog Pickup Board designed by Bernhard Adams at Incom Inc. Trace lengths are matched to a tolerance of 0.2 mm. Pogo pin contacts, and 10 kΩ drainage resistors mounted on the surface, can be seen on the left and right sides of the board. Mounting holes that allow for pogo-board compression are seen nearby the pogo pin electrical contacts.

pin board transfers the strip-line signals to the terminals on the ANNIE APB. These terminals are routed to two SAMTEC connectors. The ANNIE APB is designed for two-sided strip-line readout, implying the need for two front-end PSEC4 electronics boards mounted directly to the readout board. The mapping of strip-number to channel number may be found in Section 6.2.

is used here to stay consistent with the ANNIE experiment's preferred terminology.

CHAPTER 4

HARDWARE FOR LAPPD OPERATION IN A TIME-OF-FLIGHT SYSTEM

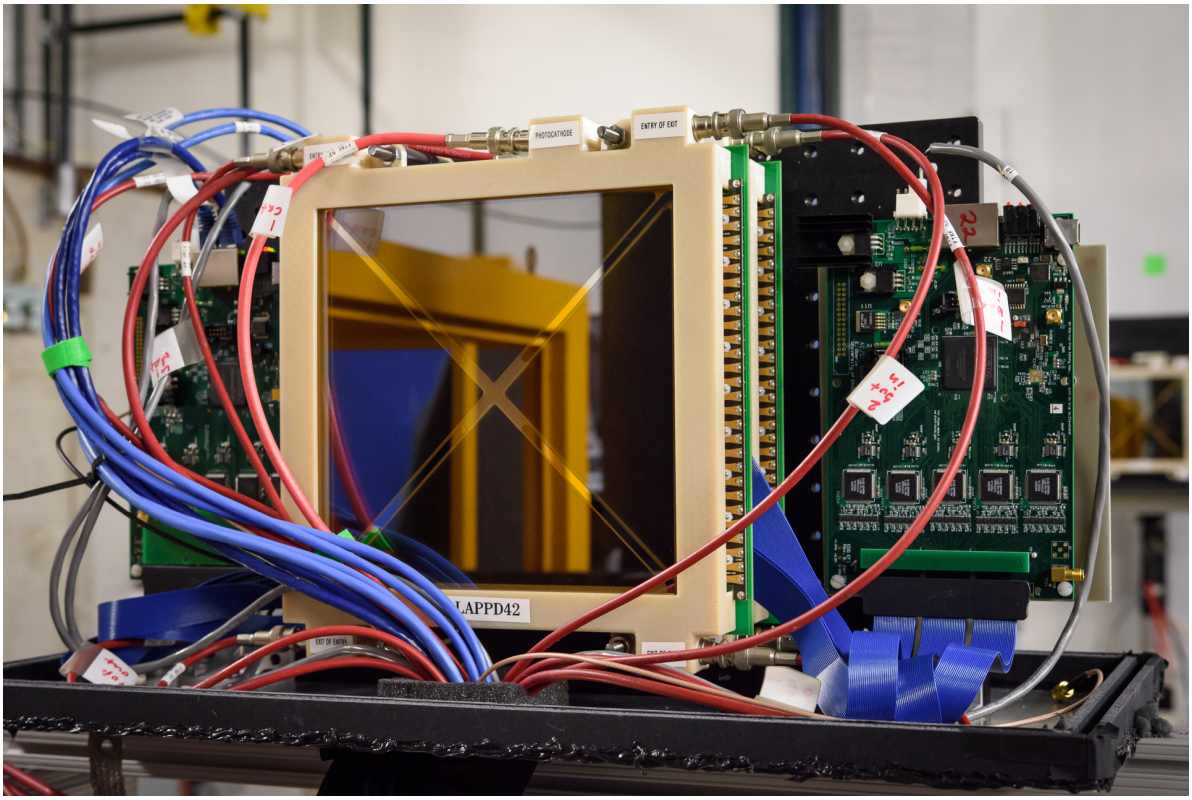

Figure 4.1: The front face of Incom LAPPD 42 instrumented with high voltage inputs, digitizing electronics, and mechanical fixturing for use in the FTBF LAPPD TOF system. A dark-box comes down from above and mates with the black cardboard rim seen at the bottom of the photograph. In this particular photo, two LAPPDs are stacked one after the other for a close-proximity particle-coincidence measurement. Photograph credit: Giulio Stancari.

A large component of this thesis work includes the design, installation, and testing of LAPPD time-of-flight (TOF) stations in the Fermilab Test Beam Facility (FTBF). An LAPPD station consists of a detector instrumented with high voltage distribution, digitizing electronics, and peripheral hardware enclosed in a dark-box. The detector and station is firmly mounted to a structure that may be adjusted to capture beam particles. The LAPPD

stations are designed to be flexible and modular, allowing for the swapping of detectors and peripherals. An example of two LAPPDs mounted one after the other in an LAPPD station is shown in Figure 4.1.

This Chapter describes hardware related to the construction of an LAPPD time-of-flight system as described in Section 1.2. At each stage of development, multiple LAPPD stations were placed in succession to either detect diffuse beam particles behind the MTest beam-dump, cosmic rays, or beam particles in the MTest 6 Section 2 enclosure.

4.1 The LAPPD frame

Similar to conventional photo-multiplier tube (PMT) technology, the integration of LAPPDs into experimental environments requires an enclosing frame to (1) protect the breakable vacuum packaging from mechanical forces, (2) distribute high voltage (HV) to electrodes that penetrate the vacuum packaging, and (3) provide mounting points that can be used to hold the LAPPD to a structure without applying dangerous forces to the packaging. In contrast to conventional PMTs, the frame does not take on the role of magnetic shielding, as LAPPD spatial-temporal resolutions are not as strongly affected compared to PMTs.

An early design from Incom Inc. has been implemented for baseline LAPPD models, shown in Figure 4.1 [10]. Design revisions of this frame are expected in the near future.

4.1.1 High voltage distribution

High voltage is distributed via safe high voltage (SHV) connectors mounted to the LAPPD frame. These SHV connectors are electrically connected to spring-loaded pogo pins like the ones described in Chapter 3. A photograph of the underside of the LAPPD frame is shown in Figure 4.2. The pogo pins make contact with high-voltages strips on the anode plane. These strips penetrate the vacuum packaging and are internally connected to the micro-channel plates.

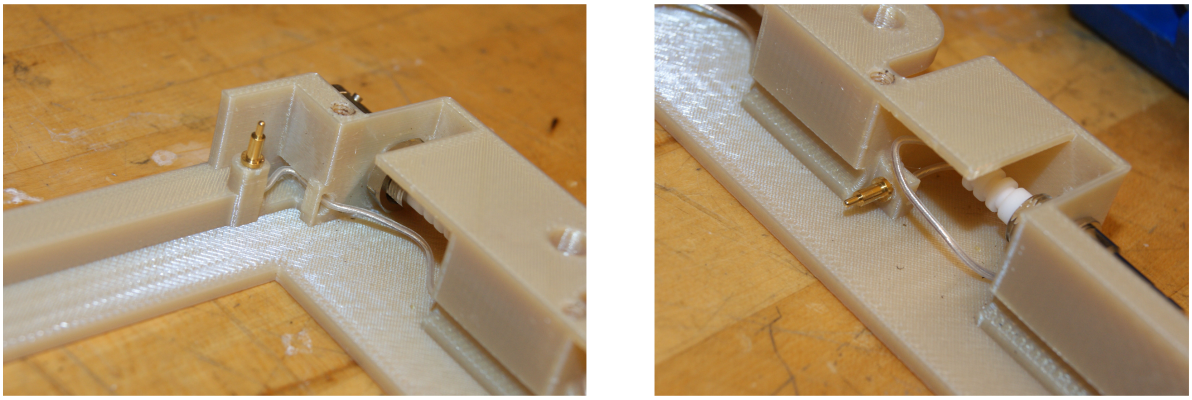

Figure 4.2: The underside of the Incom LAPPD frame reveals sping-loaded pogo pins that apply mechanical force to the HV electrodes of the LAPPD. On the left, a vertically oriented pogo pin makes electrical contact with a strip on the base, electrically connected to a micro-channel plate surface. On the right, a horizontally oriented pogo pin makes electrical contact with the photocathode. These pins are soldered to SHV connectors mounted to the frame.

For the photocathode high-voltage contact, a horizontally oriented pogo pin makes contact with a conductive metallic paste on the side of the LAPPD. The paste is in contact with the indium seal, which is in electrical contact with the photocathode due to the overlap of the seal metals and the cathode thin film. This sideways pogo pin is shown in the right hand side of the Figure 4.2.

4.1.2 The mechanics of safely holding an LAPPD

The Incom LAPPD frame allows the LAPPD to be mounted firmly to a holding structure and attempts to reduce the chance of damaging mechanical forces being distributed to the detector vacuum packaging. A diagram illustrating the mechanical elements of the frame is shown in Figure 4.3.

The mechanical functions of the frame are coupled and dependent on the existence of a readout board described in Chapter 3. The readout board includes a pogo pin bridge that makes contact with the strip-lines that penetrate the glass packaging. The 56 spring-loaded pogo pins hold the LAPPD to the readout, which is then mounted to the frame's tapped holes. These pogo pins, and the five high voltage distribution pins of the frame, are the only

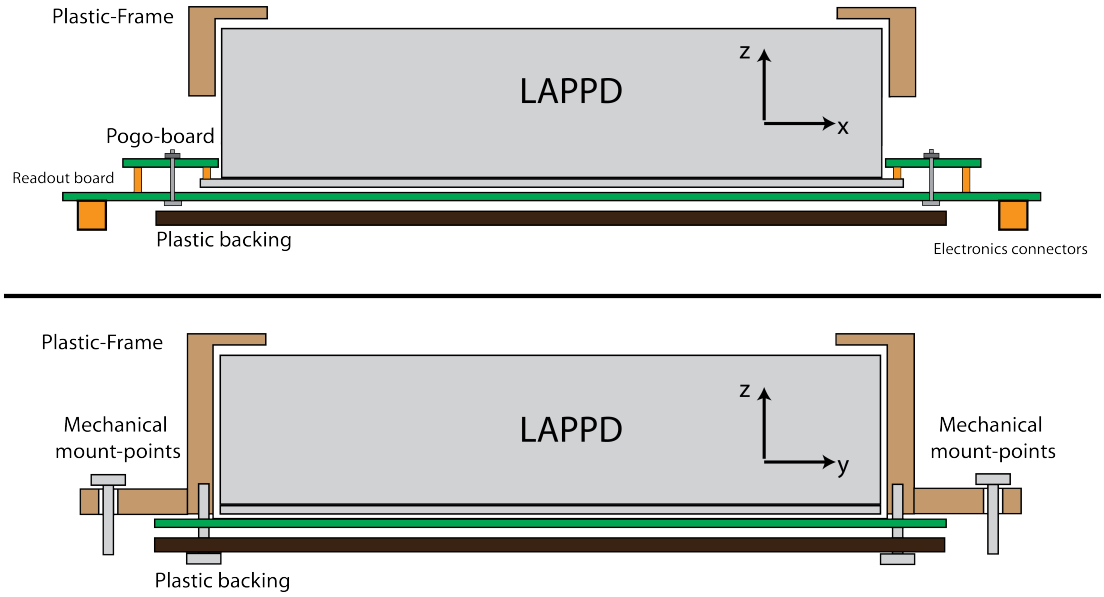

Figure 4.3: An orthogonal projection of the LAPPD frame, emphasizing the mechanical elements. The only elements that make contact with the LAPPD packaging are the pogo pins of the pogo-board shown in the top projection, and the high-voltage pogo pins which are not shown. The plastic LAPPD frame does not contact the LAPPD directly.

locations where contact is made with the vacuum packaging. The readout pogo pins apply enough force to hold the LAPPD in any orientation relative to Earth's gravity. Mounting holes for 1/4-20 bolts extend from the edge of the LAPPD, used to fix the entire assembly to a holding structure that references the experimental apparatus.

4.1.3 Design considerations for LAPPD frames

Throughout the testing of this FTBF LAPPD TOF system, the following challenges informed improvements for the next design iteration:

1. When the frame is centered, the high voltage pogo pins are less than 1 pogo pin radius away from the edge of the strip-line anode. This makes them susceptible to falling off and losing high voltage contact to the micro-channel plates.

2. The ability to hold LAPPDs to a fixture relies on tapped holes in 3D printed material (not advised in 3D print design). These tapped holes failed in one or two instances.

3. The lip and side-walls of the frame are close enough to the vacuum packaging such that a small amount of force can bend the frame into contact with the LAPPD. This is a liability to the vacuum packaging, and can be avoided by increasing the size of the frame, thus increasing the gap between the frame and the LAPPD.

4. The frame does not need to function as an enclosure for high-voltage safety. An LAPPD will never be operated in an unenclosed environment due to its sensitivity to light. This may relax some of the design constraints so that more focus can be placed on the mechanical features.

Incom Inc has been welcoming of this feedback and is working on an improved LAPPD frame.

4.2 The LAPPD station design

An LAPPD station consists of a detector instrumented with high-voltage distribution, digitizing electronics, and other peripherals enclosed in a dark-box. The LAPPD and station are firmly mounted to a structure that may be adjusted to align with beam particles. In an LAPPD time-of-flight system, multiple stations are placed in succession 1-100 meters from each other. Each station may have a small footprint for flexibility of placement.

Two types of dark-boxes were constructed during this thesis. The latter design consisting of an aluminum base-plate, an 80/20 t-slot rim [88], and a black foam board box is shown in Figure 4.4. A feed-through hole is cut into the base-plate for cables. The hole is covered with packing foam that has a slot. Mounting holes in the aluminum base-plate are used in combination with an 80/20 right-angle bracket to fix the bottom of the base-plate to an 80/20 bar on the outside of the box. The other half of the right-angle bracket is used to mount an aluminum optical breadboard [89].

The optical breadboard acts as a mounting point for the LAPPD, front-end electronics,

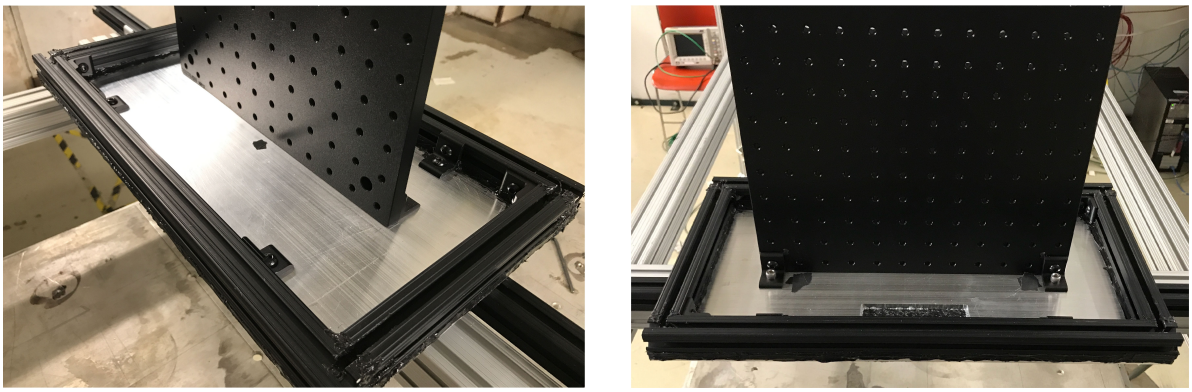

Figure 4.4: The second-iteration dark-box design consists of an aluminum base-plate machined by undergraduates, an 80/20 t-slot rim [88], and black foam board box sized to fit in the slot of the 80/20. The rim is bolted to the aluminum frame. The aluminum frame is bolted to an exterior 80/20 bar. All interfaces are covered with black silicone. A hole in the base plate covered by a slotted packing foam allows for cables to be fed through.

and strain relief structures. Four 1/4-20 threaded rods are placed on the optical breadboard, matching the pitch of the mounting holes of the LAPPD frame. Plastic spacers are placed on the threaded rods to separate the LAPPD back-face from the breadboard. Nuts squeeze the LAPPD frame against the plastic spacers, holding the LAPPD firmly in place.

The 80/20 bar fixed to the dark-box base plate may be fixed to a structure that holds the LAPPD at the desired height. For this thesis, these structures were typically made of 80/20 constructed with the help of Todd Nebel and the FTBF staff. The layout is discussed in Section 4.4 below.

4.3 Peripheral hardware

4.3.1 High voltage dividers

The photocathode and MCP surfaces need to be set at successive potentials in order to amplify single electrons. Unlike PMT high-voltage dividers, which are often attached directly at the base of the PMT, the LAPPD high voltage dividers used in this thesis are located far from the LAPPD stations.

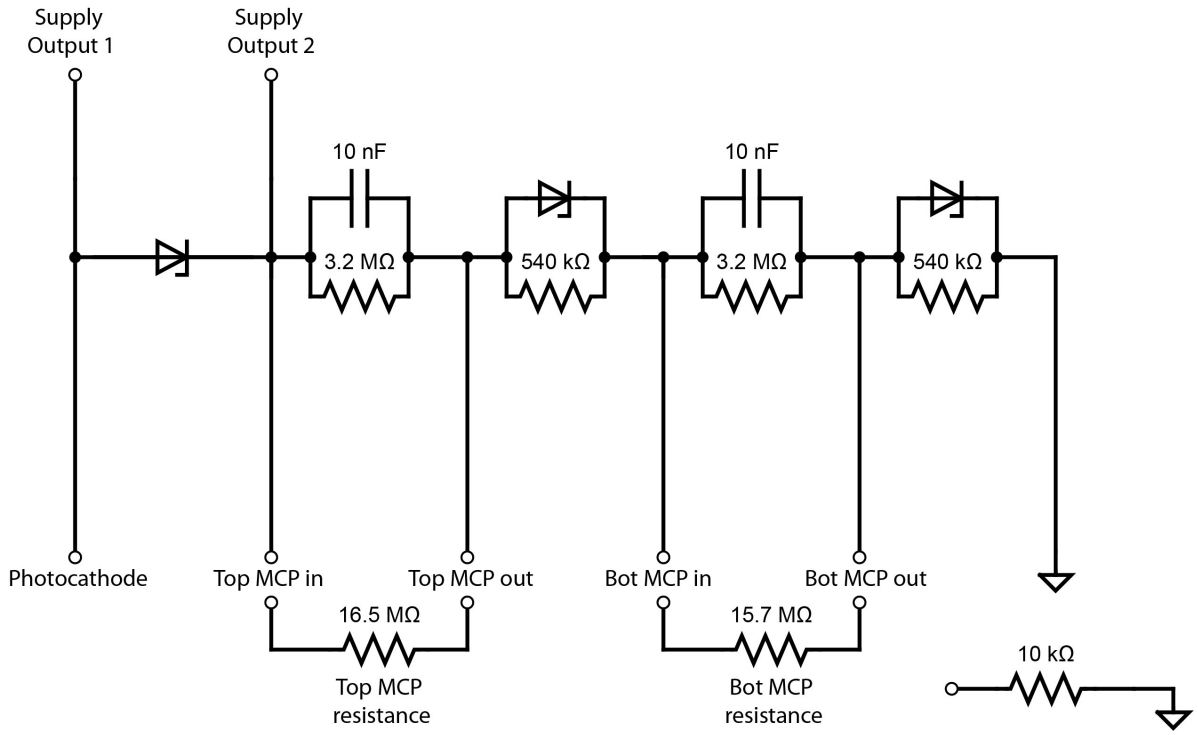

Figure 4.5: An example high-voltage divider diagram for LAPPD 43, which has 16.5 MΩ and 15.7 MΩ MCPs. Zener diodes with a breakdown voltage of 200 V are used to set a constant voltage across the gap between the MCPs and above the anode. Capacitors may be used to ground high-frequency ripple from supplies. Anode strip-lines are grounded to drain charge buildup if strips are un-terminated.

The high-voltage-divider circuits constructed for this thesis are similar to the one shown in Figure 4.5. The photocathode voltage is controlled independently of the amplification stages using a second supply output. For a top-MCP input voltage of -2300 V, this sets the top-MCP differential bias to 960 V, bottom-MCP bias to 953 V, and gaps to 200 V.

The gap between the bottom MCP and anode strip-lines typically has 200 V bias. The strip-lines see charge avalanches from the amplification stages. If the strip-lines are un-terminated and left floating, they will charge to 200 V. This presents a hazard to digitizing electronics if strips are connected while the LAPPD is powered. If a strip is disconnected from its terminating digitizer during normal operation, the charging of this strip will affect the acceleration of the charge clouds. A parallel 10 kΩ resistor does not alter the impedance properties of the transmission line to a significant degree and maintain the condition of

close-to-zero volts on the strips.

A high-voltage divider circuit is constructed for each LAPPD that is matched to the measured MCP resistances. A single Fluke model 415B supply provides negative high voltage for a Fermi: ES-7092 "Berkeley Cow" zener divider. The Berkeley Cow distributes individually-controllable voltages to the photocathode and top-MCP inputs.

High voltage performance

Each LAPPD from Incom Inc. is delivered with a test-report that outlines various specifications of the LAPPD as well as measured characteristics. For example, maximum values of bias voltages applied to the MCPs and the photocathode gap are provided in the test-report.

The high voltage stability of each LAPPD produced by Incom is a sensitive function of the photocathode voltage relative to the MCP voltages. The divider circuit described above is configured to have a total DC current of 350 μA at the max bias. If a high-voltage threshold is breached, sustained current jumps of 100s to 1000s of μA may be observed, suggesting the ignition of sustained current sources inside the LAPPD. This threshold is most easily crossed by increasing the photocathode-gap voltage above suggested values. The high-voltage stability barrier is a surface in the phase space of all voltages, and is most sensitive to the top-MCP and photocathode biases.

The high-voltage instability of the photocathode gap limits the ultimate timing resolution of the detector. It has been shown that the timing resolution of an MCP-PMT is dependent on the number of secondary electrons liberated from the first strike of the primary electron in a pore [33, 34, 5]. A high photocathode-gap voltage leads to increased yield from the higher-energy primary electron and shorter transit time in the first gap, both of which lead to significant improvement to timing resolution [5]. It is critical that future LAPPDs improve the stability of high-voltage operation of the photocathode gap.

Innovative design changes surrounding the first-strike have been proposed to improve

timing. For example, depositing the photocathode material directly on the micro-channel plate top surface and inner-pore surface [90]. Also, field-shaping grids in between the window and top-MCP could allow for much higher field gradients in the first gap [70].

The high intensities of particles in the FTBF beam enclosure cause significant current increase coincident with beam spills. A test was performed with 250,000 incident 120 GeV/c protons over a 4 second beam spill and 1 cm^2 area, producing Cherenkov photoelectron fluxes of 124 kHz/cm^2 [1]. During the test, the LAPPD 43 MCPs were biased at 920 V bias and the photocathode-gap voltage was incrementally set. With 0 V bias across the photocathode-to-MCP gap, no change in the overall divider current was observed during the 4 second beam spill. At a 40 V gap voltage, the current of the divider circuit increases by 0.2-0.3 μA as measured by a Droege-supply current monitor [91, 92]. At 80 V photocathode bias, the additional current becomes 0.7-0.8 μA. At 100 V, the particle spill induces a current increase of greater than 300 μA, tripping the high-voltage supply so that the total increased current could not be measured. This massive current increase represents a unique high-voltage instability, possibly due to the combination of high photocathode-gap voltage and many simultaneous MCP avalanches.

4.3.2 Synchronization hardware

The digitizing electronics of a precision time-of-flight system must be synchronized at a level comparable to the timing resolution of the detectors. For this thesis, a commercial relative-timing synchronization system called White Rabbit (WR) from Seven Solutions is used to synchronize multiple front-end boards over 300 m [93, 94]. A photograph of the rack-mountable White Rabbit Switch (WR-Switch) and White Rabbit ZEN (WR-ZEN) is shown in Figure 4.6.

In the time-of-flight setup, the WR-Switch is mounted on an electronics rack and the WR-

1. Based on the optical spectra of Section 1.3.1, this is a photon flux of 372 kHz/cm^2

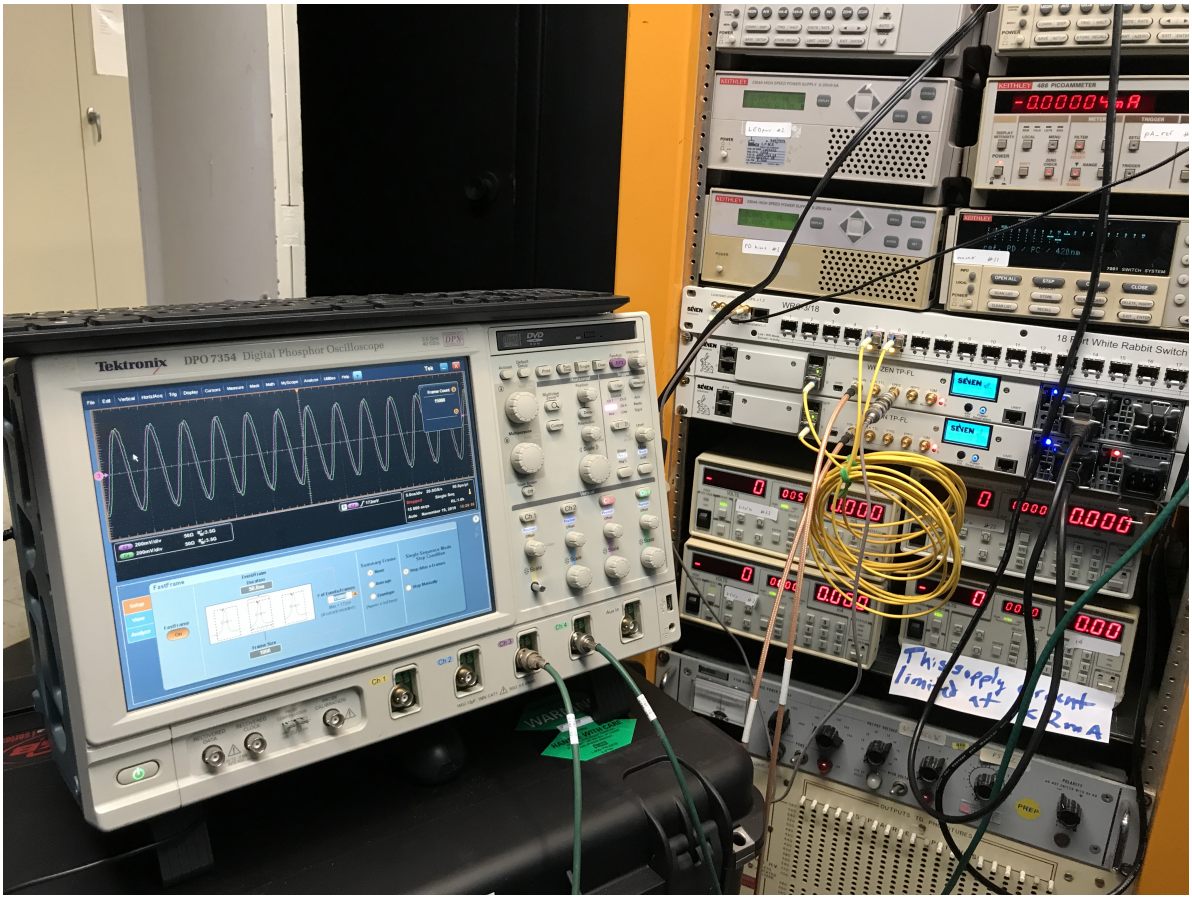

Figure 4.6: Photograph of a White Rabbit (WR) test-setup in the Fermilab Lab 6 dark-room facility. A WR-Switch and two WR-ZEN modules are installed on the rack. They are synchronized with each other over the yellow optical fibers on the right.

ZEN modules are placed as close to the LAPPD stations as possible. The switch and WR-ZENs are synchronized over optical fiber. Outputs from the WR-ZEN modules distribute phase synchronized 250 MHz 1.2 Vpp sine waves to front-end electronics channels. These sine waves are digitized along with the LAPPD-pulse waveforms in each event.

A characterization of the WR system with a high-bandwidth oscilloscope is presented in Section 5.1.5, resulting in < 6 ps phase synchronization over 300 m of optical fiber using a fast-sampling oscilloscope. In this measurement, the timing resolution of the oscilloscope is folded in quadrature and may be comparable or dominant to the White Rabbit phase-synchronization jitter.

The WR-Switch may be located far away in a control room, with fibers connecting the LAPPD stations. A measurement of front-end board-to-board synchronization using the PSEC4 electronics is presented in Appendix B and also results in < 6 ps synchronization[2].

4.3.3 Control system for front-end electronics

The front-end electronics system discussed in Chapter 5 is controlled using USB-serial communication from a Linux computer. In this thesis, the control computer consists of a Raspberry Pi 3B+ or 4 (RPi) [95] mounted on the support frame of the LAPPD stations. This RPi was sometimes configured on the Fermilab public network for ssh-control and data transfer. Later, this RPi was taken off of the network and routed with ethernet cable directly to a laptop in the control room. The RPi was also used to control set-voltages of low-voltage power supplies over USB-serial.

4.4 Experimental locations and layouts

Three experimental layouts were used to test the LAPPD TOF system, referred to as *MT6.2 beam-dump*, *MT6.2 enclosure*, and *cosmic ray* configurations.

The MT6.2 beam-dump setup was located in a small space outside of the beam enclosure, downstream of the 3.2 m thick concrete beam-dump. It consisted of a 3-foot-long 80/20 frame with enough space to hold two LAPPD stations joined by a common rail. The separation of the LAPPD photocathodes was adjustable between 2" to 24".

When the MTest beam is configured with pions as the primary particle, muons from the decay of stopped pions exit the concrete beam-dump. Two 8"$\times$ 12" scintillation counters placed on both ends of the LAPPD stations detect 100s to 1000s of particles over the 4 second beam-spill depending on the intensity settings of the beam. These beam-dump muons

2. The characterization of Appendix B is not a measurement of the WR system synchronization, but rather a measurement of the timing resolution of the digitizing electronics in response to WR signals.

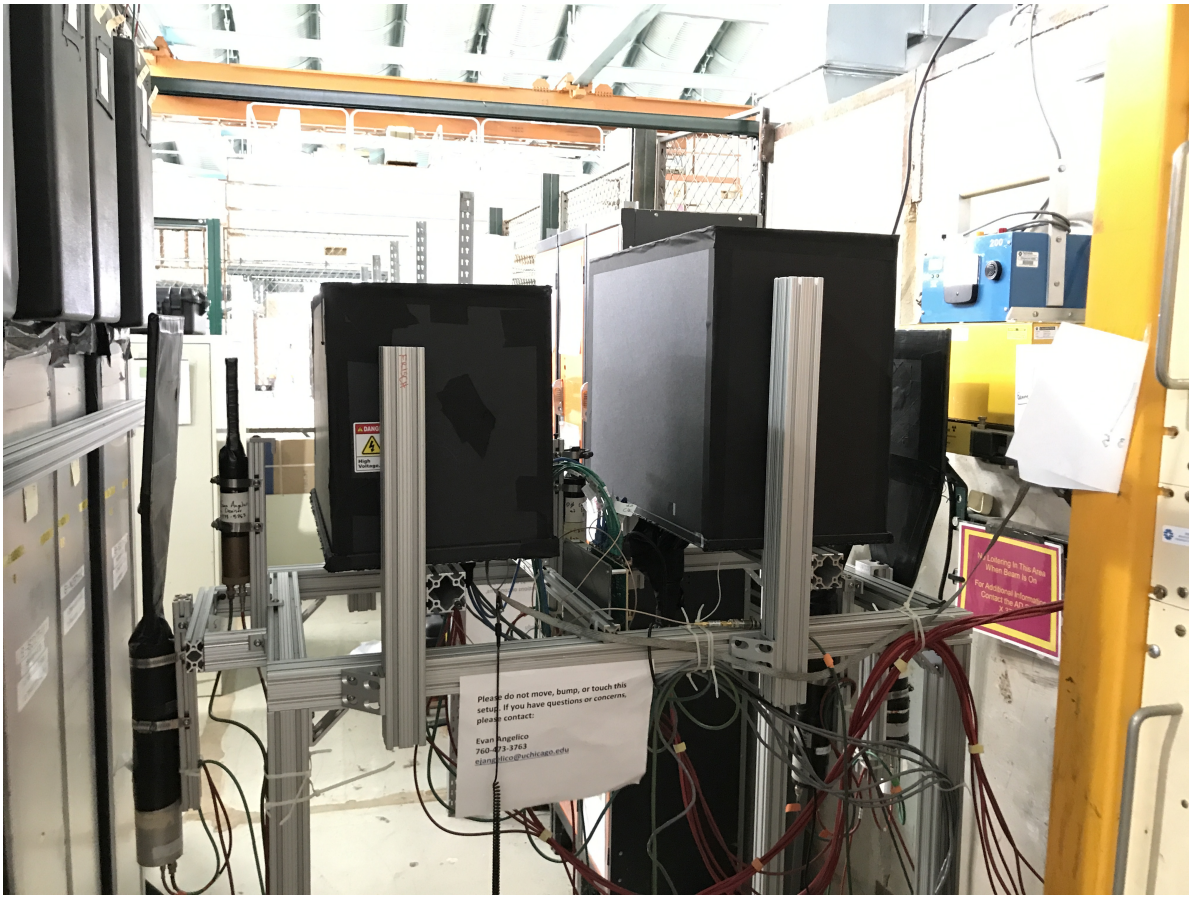

Figure 4.7: The MT6.2 beam-dump configuration. The concrete beam-dump is on the right-hand side with triggered particles going from right to left. This 5-foot-long crawl-space is behind the cable and materials cabinets at the Meson West FTBF building.

were characterized in Reference [96]. The beam is diffuse in energy from two-body decay kinematics and spatially distributed over a roughly 10 cm radius. This area is a treasured resource for debugging detector systems without the overhead of controlled access. A photograph is shown in Figure 4.7. The cosmic ray configuration is nearly identical to the MT6.2 beam-dump configuration but turned on its side.

The region inside of the MT6.2 enclosure just before the beam-dump, called MT6.2D, has enough available space for 3 movable LAPPD stations. A photograph of the LAPPD TOF system in the MT6.2 enclosure is shown in Figure 4.8 with an experimental-layout diagram shown in Figure 4.9. The spaces between the LAPPD stations allow for adjustable

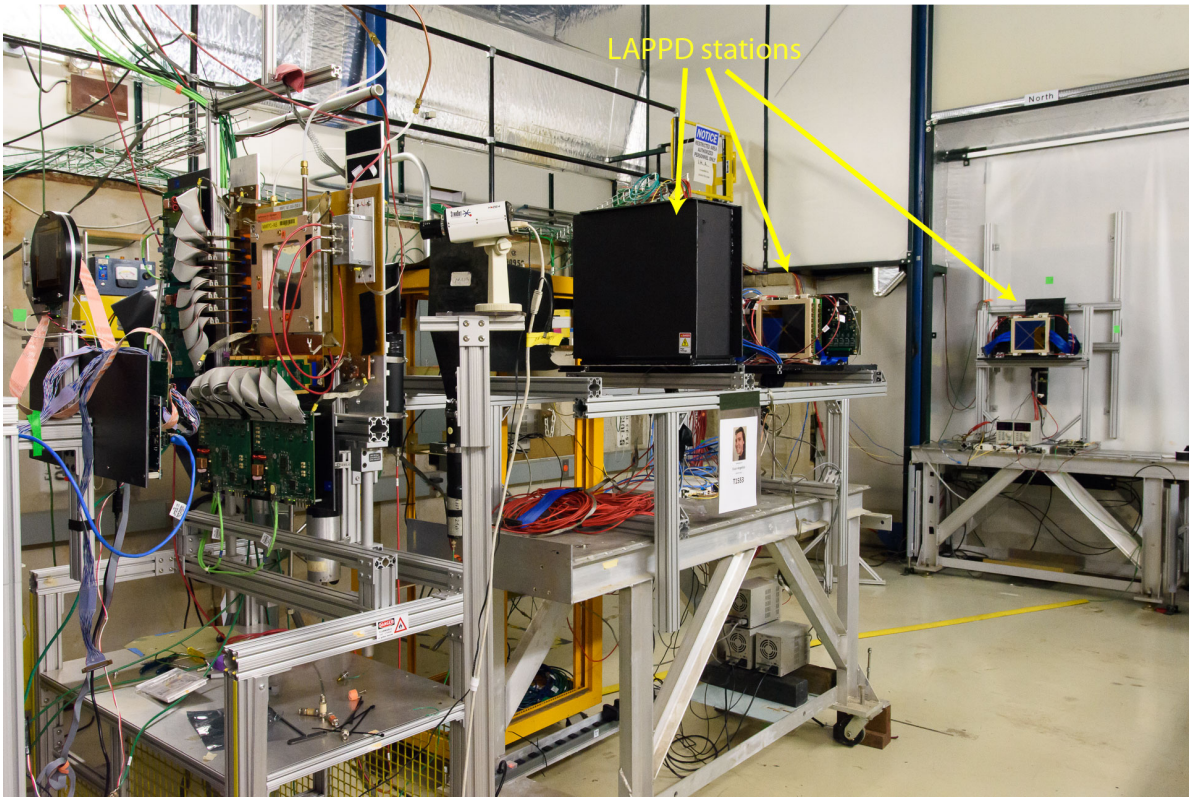

Figure 4.8: The installation of the LAPPD TOF system in the MT6.2 enclosure. The beam dump is shown on the right-hand side. Three LAPPD stations were installed for redundancy and further constraints on path-length. The multi-wire proportional chamber hardware seen on the far right is part of the FTBF standard-diagnostics instrumentation. Photo credit, Giulio Stancari.

TOF detector separations from 0.3 m to 5.2 m. Beam modes available in this location are described on the FTBF website [35]. They include 120 GeV/c protons, low-energy pions with a large fraction of kaon contamination, and higher-energy pions with lower fraction of kaons. One result of the construction and operation of this setup is a list of next-steps toward a permanent LAPPD TOF installation, as discussed in Appendix A.

In all three of these experimental configurations, it was possible to place two LAPPDs back-to-back inside the same dark-box for a minimum photocathode separation of about 5 cm. This allows for the measurement of time-of-arrival jitter between two detectors independent of particle type or particle kinematics. This "close-proximity" configuration is ideal for characterizing and calibrating the detectors before TOF operation.

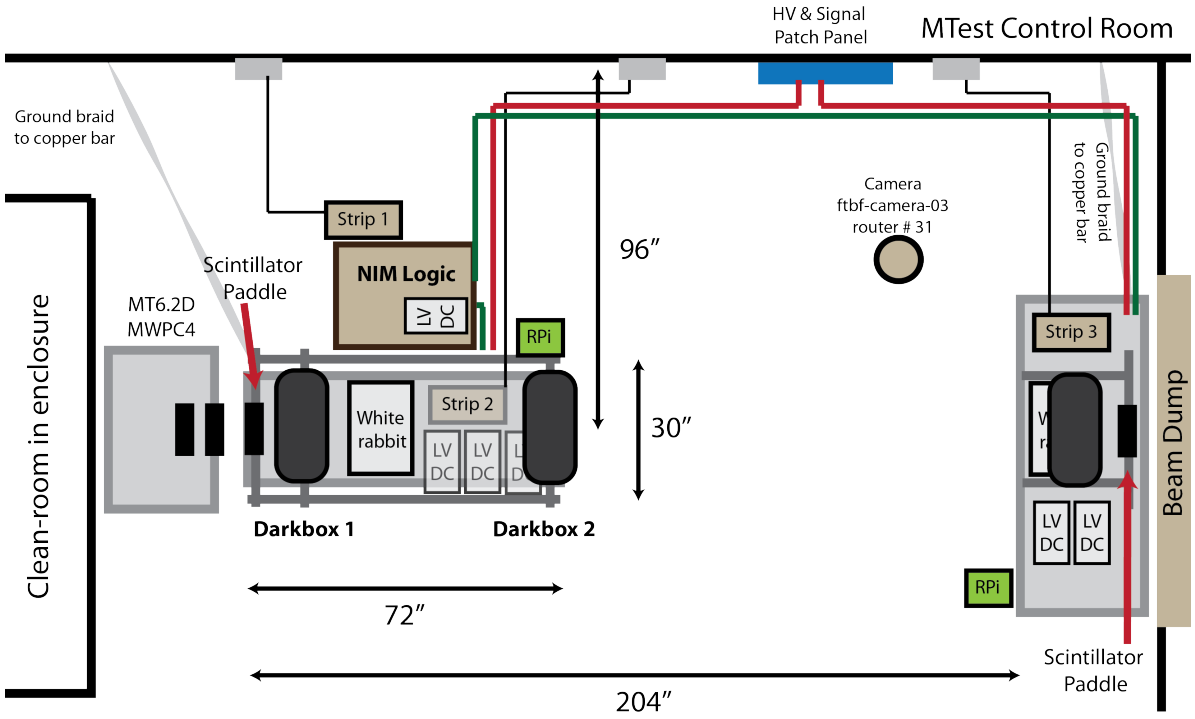

Figure 4.9: Top-down diagram of all experimental hardware for the MT6.2 enclosure configuration. The three LAPPD stations are represented by their dark-boxes as black rectangles. "RPi" objects are raspberry-pi electronics controllers. Low voltage DC (LV DC) supplies source power to front-end electronics. The two scintillator paddles on left and right of the entire TOF system are one component of the trigger.

4.4.1 Radiation length

At the time of writing this thesis, four LAPPDs had been placed in the beam: LAPPD43, LAPPD42, LAPPD51, and Tile 31 (from University of Chicago). Each of these LAPPDs have slightly different materials and material thicknesses. The result of a calculation of the radiation length as defined by the Particle Data Group [26] is presented below. The details of the calculation may be found in Appendix C. Three scenarios can produce three different radiation lengths depending on where the particle passes through the detector: a nominal photo-detecting region, a region obstructed by an "x-spacer" (see Figure 4.1), and the side wall of the vacuum packaging.

- LAPPD43:

  - If particle passes through active fraction: 7.44%
  - If particle passes through x-spacer: 18.81%
  - If particle passes through sidewall: 17.17%

- LAPPD42:
  - If particle passes through fraction: 10.41%
  - If particle passes through x-spacer: 21.78%
  - If particle passes through sidewall: 27.08%

- LAPPD51:
  - If particle passes through fraction: 13.94%
  - If particle passes through x-spacer: 25.31%
  - If particle passes through sidewall: 30.61%

- Tile 31:
  - If particle passes through fraction: 14.68%
  - If particle passes through button column (see Chapter 2): 29.08%
  - If particle passes through sidewall: 37.12%

CHAPTER 5

FRONT-END ELECTRONICS SYSTEM

The arrival time of photons in micro-channel plate based photo-multiplier tubes (MCP-PMTs) such as Large Area Picosecond Photodetectors (LAPPDs) is best obtained by digitizing entire waveforms at a high sampling rate [76]. The timing resolution of a sampling electronics system measuring MCP-PMT pulses is directly related to the magnitude of the rise-time, the signal-to-noise ratio, the sampling rate, and the bandwidth of the readout and analog-to-digital converters (ADC) [77].

This chapter describes one front-end digitizing electronics system designed for use on LAPPDs and MCP-PMTs. Other chapters do not critically dependent on this chapter; however, those who skip this chapter should be aware that the most significant limitation of the LAPPD TOF system presented in this thesis is the front-end electronics system.

The electronics system is based on an application specific integrated circuit (ASIC) called PSEC4 [97]. This chapter is intended to help those who are considering the use of PSEC4 electronics. It is also intended for readers who are modifying and improving the Fermilab Test Beam Facility (FTBF) LAPPD based time-of-flight (TOF) system. Because this is a somewhat technical topic, an intermediate understanding of fast analog-to-digital conversion systems, as well as systems controlled by field programmable gate arrays (FPGA), is assumed.

The most critical next step for developing the LAPPD TOF system is to improve the electronics system. Understanding which aspects of the electronics system need to be changed in order to perform precise particle identification is one major outcome of this thesis work. These next-steps are primarily discussed in Section 5.3 at the end of the chapter.

Some of the planned precision measurements of the TOF system require a careful calibration of the electronics system. These calibrations were scheduled for a period of time in which the coronavirus of 2020 interrupted progress. This affects the fidelity of results in Chapter 7. However, a calibration of some electronics channels was performed and is presented in

Appendix B. This same procedure can be applied to all electronics channels to allow for higher precision on analyses that require timing information at the 10s of picoseconds level.

5.1 Properties of the PSEC4 chip

The PSEC4 fast-waveform digitizing chip was designed by Eric Oberla, Hervé Grabas, and Mircea Bogdan in the Electronics Development Group at University of Chicago [98]. The chip was designed to retain the intrinsic timing information provided by MCP-PMTs and LAPPDs. A detailed discussion and table of the chip's properties is omitted here for brevity but may be found in Eric Oberla's thesis [99] and Reference [97]. Each channel of the PSEC4 chip contains a switched capacitor array (SCA) timed by a voltage-controlled delay line (VCDL) and a linear-ramp analog-to-digital converter (ADC). The result of the chip architecture is 6 channels of 10.5 bit-effective resolution at 1.6 GHz -3dB bandwidth with a dynamic range of 1.2V [97]. Each ADC input is capacitively-coupled with an adjustable DC pedestal so that signals may be shifted into the ADCs 1.2 V range. Noise levels are about 700 μV RMS after a calibration of capacitance variations due to ASIC manufacturing variations [99].

5.1.1 Constant sampling rates

The PSEC4 sampling process is based on a servo-controlled VCDL that acts as a delay-locked loop (DLL), triggering the latch and hold of the SCA. An input clock to the PSEC4 chips sets the VCDL frequency. The nominal sampling rates used in this thesis are 10.24 giga-samples per second (GSPS) and 6.4 GSPS, corresponding to VCDL clock rates of 40 MHz and 25 MHz with event windows of 25 ns and 40 ns respectively.

Variations in ASIC fabrication lead to deviations from constant sampling rate. The procedure for calibrating the sample-times, or "time-base", of each channel is detailed in Appendix B. This calibration procedure uses the synchronization signals provided by the

White Rabbit ZEN system. At 10.24 GSPS nominal sampling rate, deviations from constant sampling rate are on the order of 10 ps (see Appendix B and Reference [99]). In addition to the non-constant sampling rate, there exists a jitter in the sample-times of each sample, called the aperture jitter. This is found to be on the order of 3-5 ps, comparable to the timing resolution of the PSEC4 chips.

5.1.2 Triggering and wraparound sample

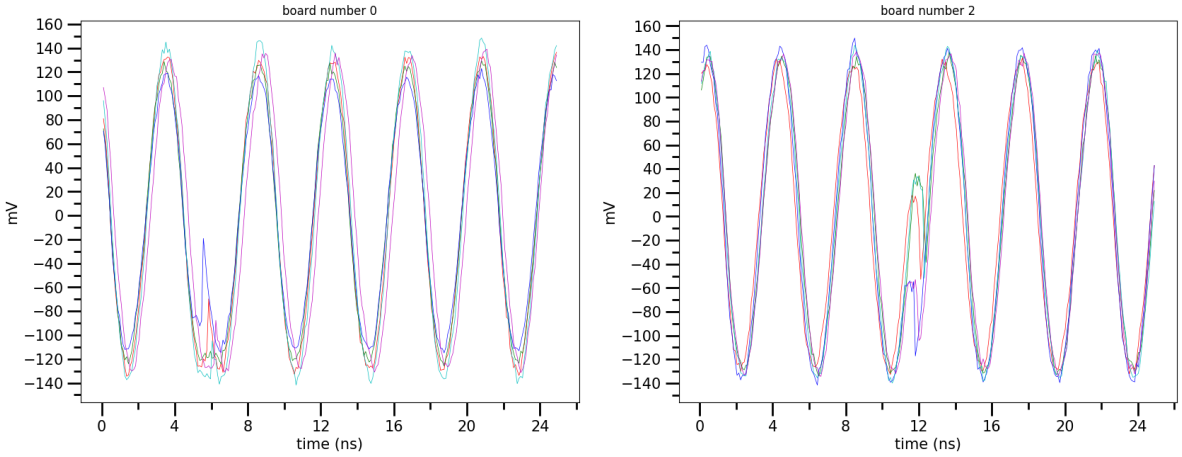

Figure 5.1: The waveforms of five calibration channels overlayed for board 0 and board 2. These signals are sourced by a single White Rabbit ZEN module whose output is split. The "trigger location" is the region where the sine waves have a glitch. The initial time of sampling is just after the trigger location, with circular buffer wrapping around the end of this displayed wave.

When a trigger signal is sent to a PSEC4 chip, typically from an FGPA, the capacitors of the SCA are sequentially switched open, starting with the capacitor currently indexed by the VCDL. At the beginning of this sequence, i.e. the time at which the trigger signal reaches the chip, about 7 of the sample cells are corrupted by a large current injection [99]. These samples are visible on Figure 5.1, where the sine wave looks to be interrupted in the center. The start-time of this digitized sine wave is the sample just after the trigger location. In the rest of this text, these samples are referred to as the *trigger samples* or *trigger location*. The trigger samples are not useful and could add noise to an LAPPD pulse analysis if not

properly masked off. In LAPPD pulse data, the trigger samples occasionally truncate the leading edge of a primary pulse. This occurs when the trigger signal is not sent by the FPGA or received by the PSEC4 before the circular buffer starts overwriting relevant parts of the event. In a majority of events, the trigger signal makes it to the chips in time to retain relevant pulse information.

The 256 samples of the PSEC4 SCA are read-out in a circular ring-buffer configuration. When the capacitors are being latched by the VCDL, there is a fixed latency when wrapping around from the 255th to the 0th sample. This latency is longer than the average constant sampling time. This is referred to as the wraparound offset. The wraparound offset is fixed; a calibration procedure is detailed in Appendix B. The characterization of the boards used in this thesis finds the wraparound offset to be about 530 - 605 ps.

5.1.3 Timing resolution

The electronics timing resolution will contribute in quadrature to the overall timing resolution of an LAPPD time-of-flight system. As an attempt to characterize the timing resolution of the individual systems, the PSEC4 chip-to-chip timing resolutions are measured independently. A measurement of the timing resolution in response to 250 MHz sine waves using the synchronization hardware described in 4.3.2 and 5.1.5 is reported in Appendix B, resulting in a chip-to-chip (channel-to-channel) timing jitter of 4-6 ps. Eric Oberla measured timing resolution in response to MCP-PMT like pulses on the order of 4-9 ps for calibrated chips and about a factor of two larger for uncalibrated chips [99]. Calibration of each channel of the TOF system is necessary for measurements with a desired precision of less than 15 ps 1σ. A procedure is outlined in Appendix B.

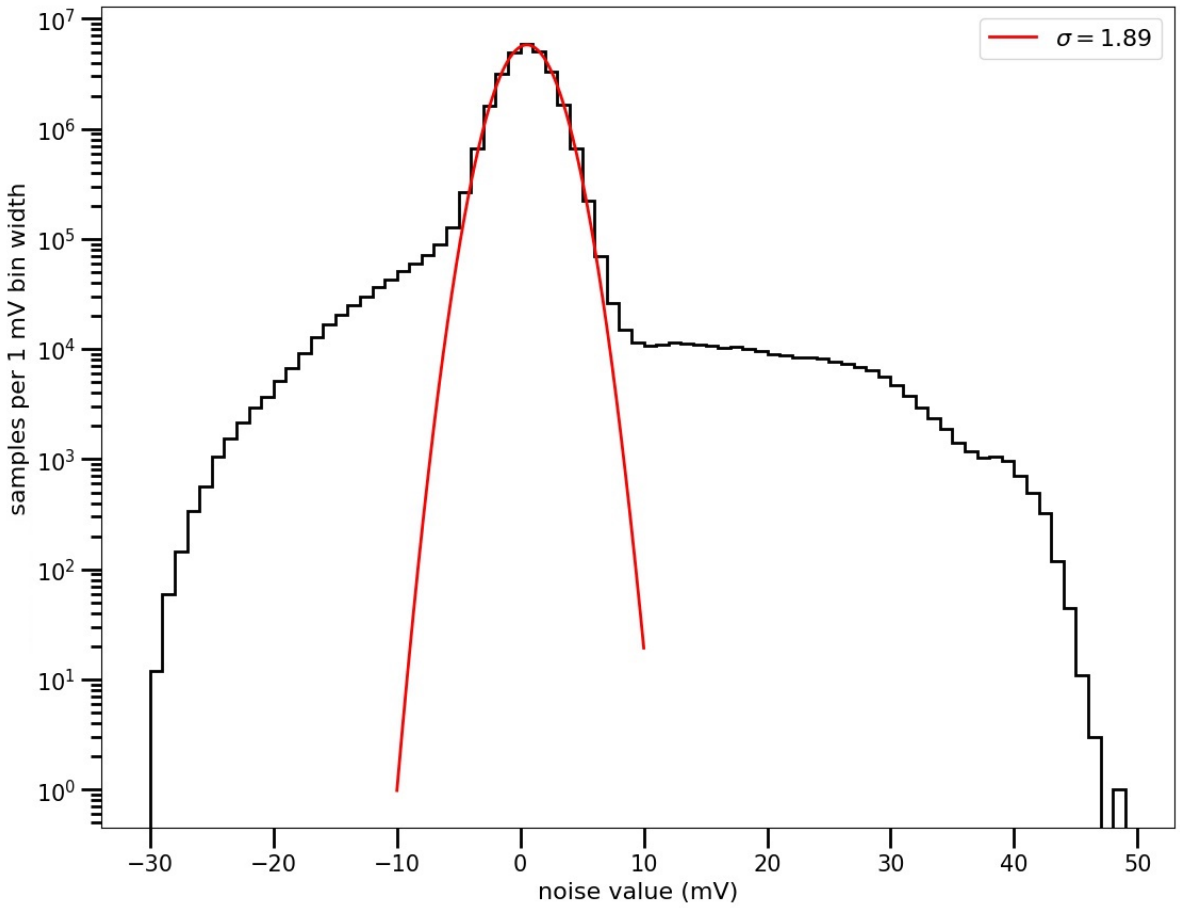

Figure 5.2: Noise data accumulated from 4 uncalibrated boards while they are connected to LAPPD strip-line anodes. The bins contain measured signal on 256 samples of 30 channels on four boards from 1,000 events before a calibration of voltage linearity. The obvious excesses from the main peak are due to the corrupt trigger samples, which affect some channels more than others. The samples not contained in the trigger region have a noise of 1.89 mV standard deviation. The strip-lines that are attached to the electronics in this dataset may increase the noise level due to their RF-antenna-like geometry.

5.1.4 Noise

The noise of the PSEC4 chips in isolation has been characterized in References [99, 100] as being about 700 μV RMS for linearity-calibrated data. Figure 5.2 shows a noise histogram for data acquired before a linearity calibration and while the PSEC4 inputs were connected using 18" SAMTEC cables [101] to un-powered LAPPDs with strip-line anodes, resulting in 1.89 mV standard deviation. This histogram contains the sample value of every sample of

every channel from 4 boards and 1,000 events. The tails extending out to about ± 20 mV are due to the corrupted samples at the trigger location as described above.

5.1.5 Synchronization

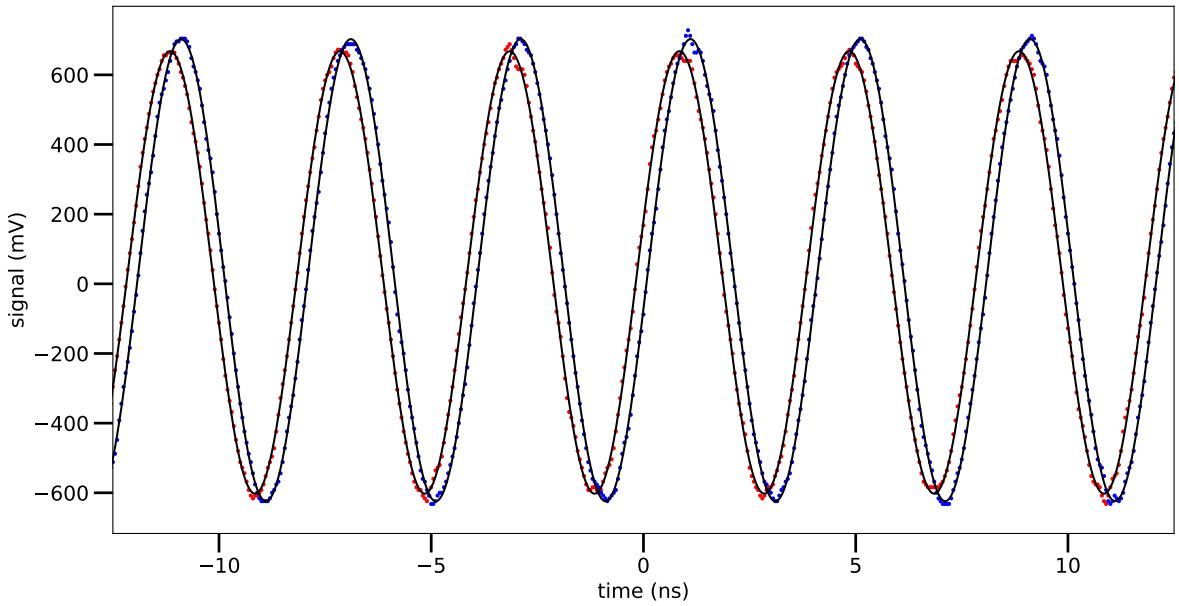

Figure 5.3: An example of two outputs from the WR-ZEN modules: 250 MHz 1.2 Vpp sine wave digitized by a Tektronix DPO7500 series oscilloscope.

To retain picosecond-level timing information from detectors, the front-end electronics system must be synchronized at the picosecond level. One method of synchronization chosen for this thesis is to send a sine-wave signal into digitization channels on the front-end electronics. The sine waves are recorded in each particle-detection event.

Commercial relative and absolute timing synchronization systems are readily available from the company Seven Solutions [93]. The White Rabbit (WR) system can be configured to provide relative synchronization over kilometers at the 1-10 ps level. The system purchased for the FTBF LAPPD TOF setup consists of two WR-ZEN modules synchronized by a master module called the WR-Switch [1]. Each WR-ZEN, located close to the front-end

1. The White Rabbit Switch used in this thesis is not a standard version, but is modified as a low-jitter

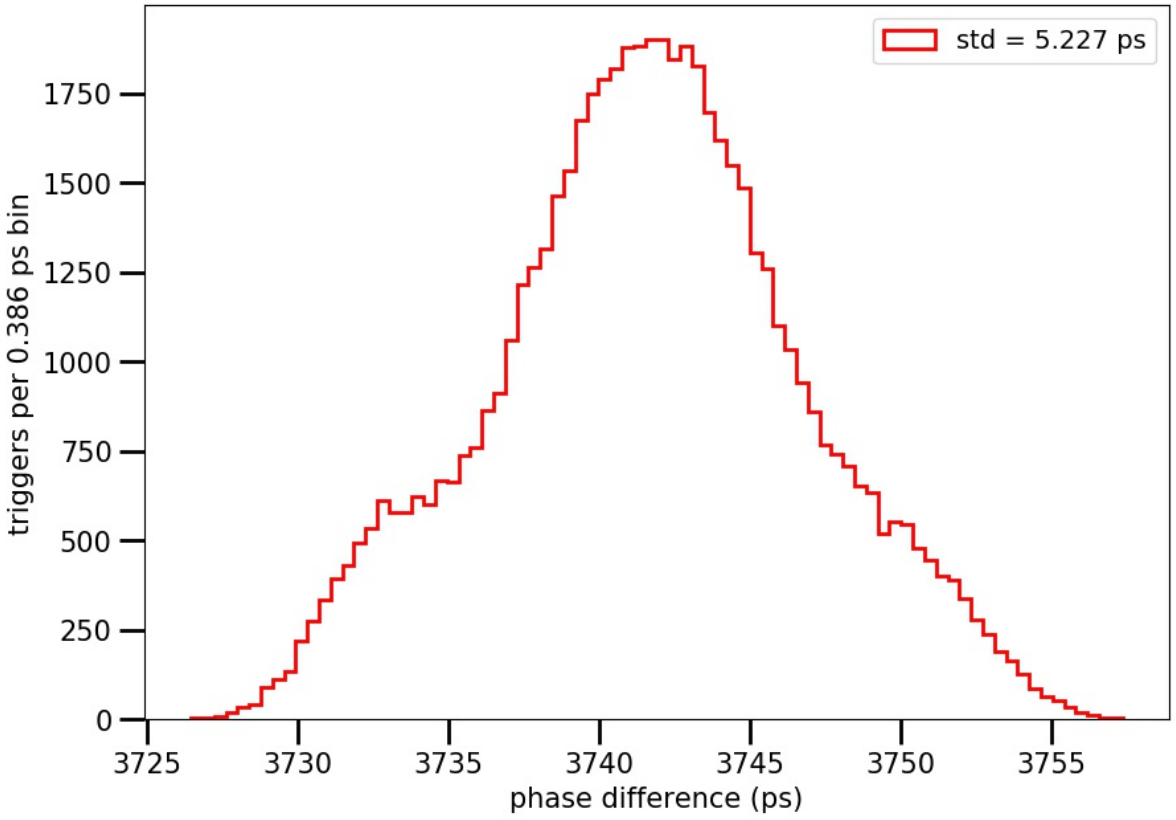

Figure 5.4: Phase jitter measured from 15k events of two WR-ZEN outputs separated by 300 m is 5.2 psec standard deviation. The non-gaussian tails are suspected to be generated by the active feedback mechanisms of the WR system throughout the course of measurement.

electronics, has been configured to output a 250 MHz 1.2 Vpp sine wave. The output signal from two WR-ZEN modules downstream 10 ft of old BNC cable is shown in Figure 5.3.

A characterization of the WR relative synchronization is performed using a Tektronix DPO7354 oscilloscope at 3.5 GHz bandwidth, 20 GSPS sampling rate, containing 40 ns (10 periods). Sine waves are fit using a least-squares fitting algorithm with floating frequency, amplitude, phase, and offset from the python package scipy.optimize.curve_fit. By fitting only one of the two outputs over 15k events, the frequency stability is measured as 250 MHz $\pm$ 8.8 kHz at one standard deviation. The analysis of the phase jitter is performed with the frequency fit parameter fixed at 250 MHz.

---

model.

Data are collected from two WR-ZEN modules separated by 300 m of opical fiber, outputting signals on 10 ft of BNC cable. Over 60k events the fitted phase differences between the two channels vary by 5.2 ps standard deviation, as shown in Figure 5.4. This jitter represents a quadrature sum of the White Rabbit synchronization properties and the timing resolution properties of the oscilloscope at 250 MHz input frequency. These timing uncertainties are taken into account when estimating the properties of the time-of-flight system in Chapter 8.

The timing resolution of the PSEC4 electronics in response to the WR signal is measured in Appendix B as 3 - 7 ps.

5.2 Architecture of the time-of-flight front-end electronics system

Five PSEC4 digitizing ASICs are mounted to a board controlled by an Altera Cyclone IV GX FPGA [102] called the "ACDC". A master board, called the ANNIE Central Card (ACC) [103] [2], is Altera Arria V FPGA [104] controlled and has the potential to control up to 8 ACDC boards. The ACDC board was designed by Eric Oberla and Mircea Bogdan and the ACC was designed by Mircea Bogdan in the University of Chicago Electronics Design Group [98, 99].

The control and communications architecture for the PSEC4 electronics is shown in Figure 5.5. Each entity in the architecture requires its own control code: the ACDC firmware, the ACC firmware, and the control software. Functions of each entity are described below.

One result of this thesis work is determining what aspects of the electronics system need modification for a robust, permanent LAPPD time-of-flight system for the FTBF. These are described at the end of the chapter. A list of references intended for users who would like to begin using or designing setups around this electronics system may be found at the end

2. This board is named as such due to its intended use in the ANNIE experiment [87]

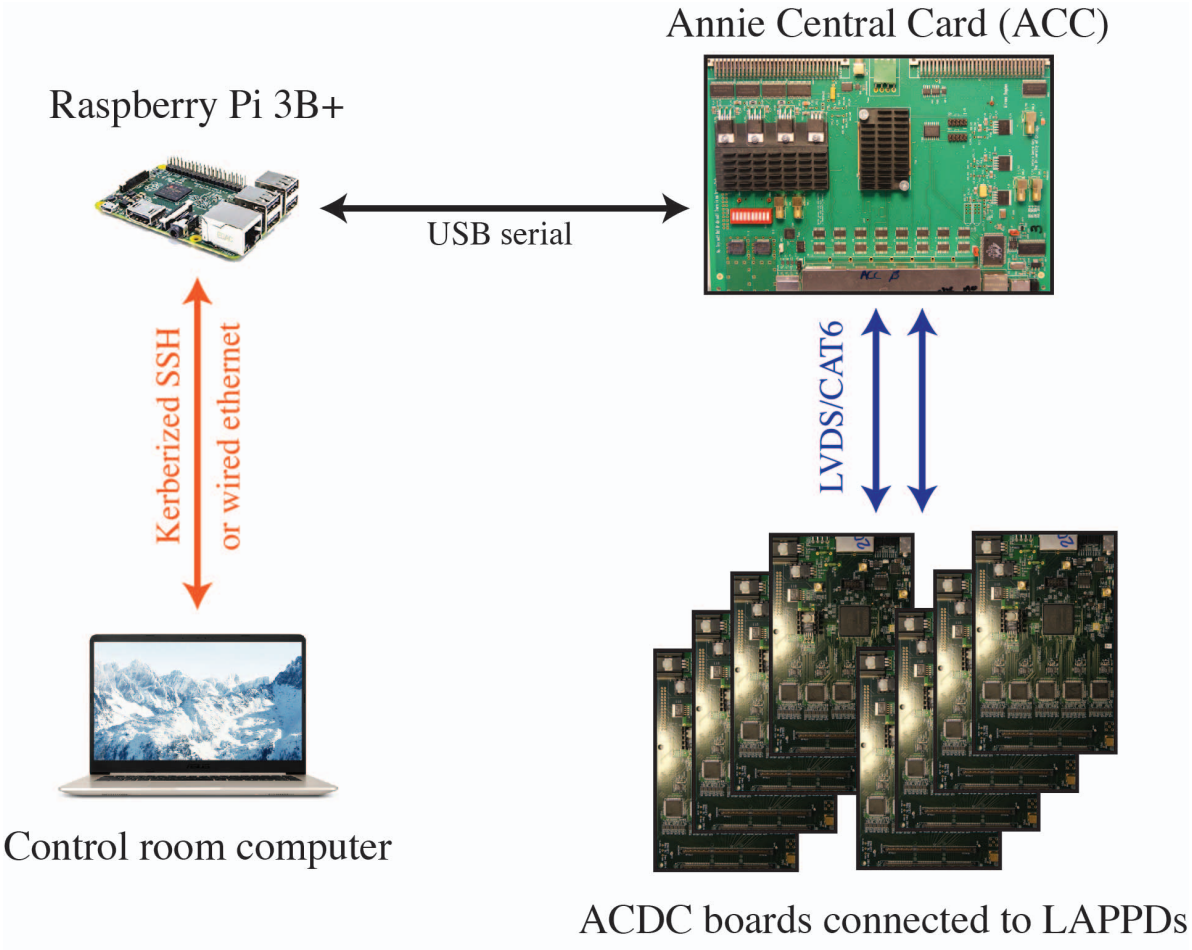

Figure 5.5: This diagram shows the control and communication structure of a DAQ system for recording LAPPD data using the PSEC4 electronics. Lines of communication, as well as their communication protocol, connect the control computer, Raspberry Pi [95], Annie Central Card (ACC), and up to 8 ACDC boards. Raw data are transferred upstream from the ACDC, to the ACC, and to the control computers which have hard memory.

of the chapter.

5.2.1 ACDC board

The ACDC rev B board is shown in Figure 5.6. The board houses five PSEC4 chips for a total of 30 capacitively-coupled, 50 Ω terminated ADC inputs. The interface between LAPPD strips and digitizing channels is a SAMTEC[3] 156-conductor high-density jack [101].

3. QRF8-78-05.0L-D-A or QRM8-78-05.0L-D-A

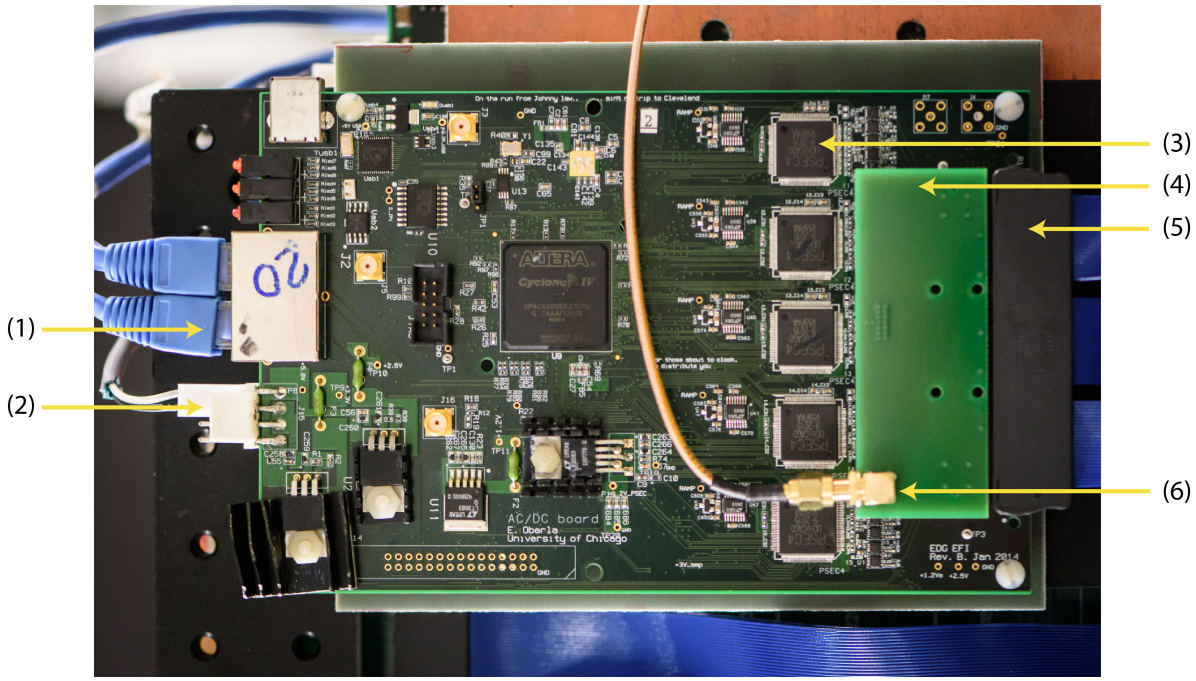

Figure 5.6: Photograph of the ACDC rev B board with (1) LVDS communication lines to the ACC, (2) 5V 2A power input, (3) five PSEC4 chips, (4) 5-way synchronization splitter board, (5) SAMTEC cable signal input, and (6) White Rabbit synchronization input.

A second SAMTEC jack allows for the addition of custom mezzanine boards, such as the small rectangular PCB shown in Figure 5.6 that distributes WR signals to the last channel of each PSEC4 chip. The board is populated with linear regulators powered by 5 V, 2 A DC input. Data are transferred to and from the ACDC via 8 twisted pair LVDS lines connected to RJ45 jacks.

Some functions of the firmware and hardware that are presently fully functional include

- Trigger the PSEC4 chips, halting their SCA sampling and measuring signals on 30 channels
- Hold one event with up to 16 bit data of 1536 samples of PSEC4 (10.5 bit effective from the PSEC4 ADCs)
- Set digital-to-analog converter (DAC) outputs to apply DC offsets to the ADC inputs, shifting polar pulses into the 1.2 V range of the ADC

- Configure "self-trigger" trigger thresholds for each chip. A discriminator outputs HIGH to the FPGA if an SCA capacitor passes threshold during one clock cycle
- Require trigger-logic configurations to pass before reading out PSEC4s, including 30 channel-mask bits, coincidence logic, and more
- Given a trigger signal from the ACDC FPGA, hold PSEC4 capacitors and wait a configurable number of clock cycles to receive a trigger signal from the ACC before reading out
- Manage metadata

With the present firmware and hardware configuration, the event buffer of the ACDC board consists of 256 samples of ADC data for 30 PSEC4 channels. Additionally, each digitized-data packet includes the following metadata [4]:

- For each PSEC4 chip:
  - The actual and target frequencies of the ring oscillator that clocks the ADC ramp-compare
  - Self-trigger threshold value (software set)
  - DC offset, or "pedestal", value (software set)
- The number of channels triggered, the channels that had discriminators above trigger threshold, and the channels that were set to be masked off in the self-trigger
- The trigger mode, be it sent from the ACC, from a SubMiniature version A (SMA) input on the ACDC, or from the self-trigger discriminators.

4. Some metadata and settings are omitted from this list as they are either not functional in the present firmware version or are not understood by the author

- Settings for coincidence of the self-trigger, including channel-to-channel coincidence or chip-to-chip coincidence, and a time window for coincidence to occur.
- The number of clock cycles, relative to the time of board start-up, at which a trigger signal was sent from the FPGA to the PSEC4 chips.
- The duration from when the FPGA sent a trigger signal to the PSEC4 chips to when the FPGA stores the fully digitized event to RAM
- *An attempt to locate the portion of the 256-sample event window where the trigger threshold was passed. This trigger-time identification is not fully functional, and is one of the key improvements in Section 5.3 due to its potential to locate the corrupted trigger-sample region
- The number of digitized events since board start-up
- The number of events, digitized or not since board start-up
- A firmware version number

5.2.2 Annie Central Card (ACC)

The Annie Central Card (ACC) is a board controlled by an Altera Arria V FPGA [104], designed to facilitate the flow of data and commands to and from up to 8 ACDC boards. A photograph of the ACC is shown in Figure 5.7. This board was designed by Mircea Bodgan in the Electronics Design Group [98, 105].

The communications system between the ACC and ACDC boards is based on the Low Voltage Differential Signaling (LVDS) logic standard. The two boards are connected by a shielded CAT6 cable that includes transmit and receive data lines, a trigger signal line, and a clock signal for clock-domain alignment.

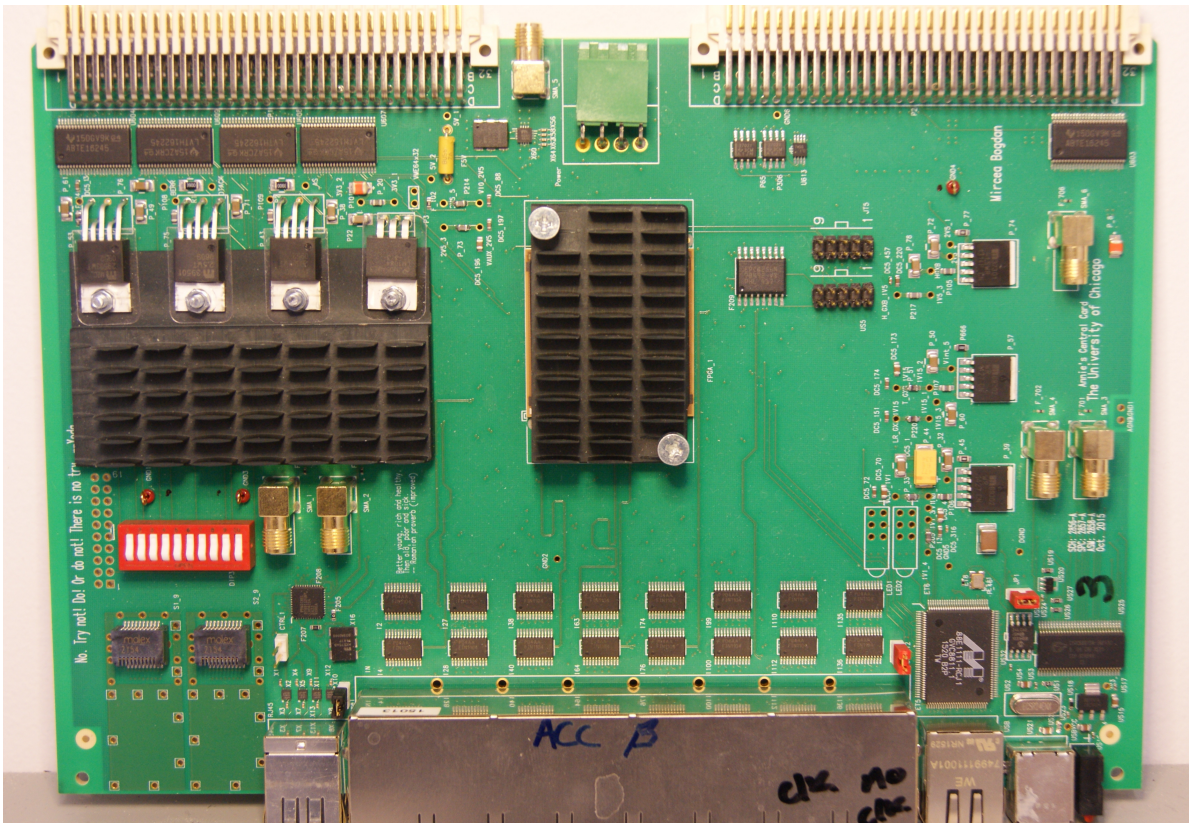

Figure 5.7: Photograph of the Annie Central Card (ACC) developed by Mircea Bogdan in the Electronics Design Group at University of Chicago. This board has hardware to control up to 8 ACDC boards. It manages a number of ACDC operations including data transfer and the Level 2 trigger which enters through one of the SMAs shown in the photograph.

The ACC has a USB-serial buffer chip that receives and transmits data from the control computer at 48 Mbps. The 32-bit commands from the control computer are parsed and distributed to the ACDC boards downstream. Features of the ACC that are fully functional include:

- Distribute instructions and data to and from the control computer (USB)
- Distribute instructions and data to and from 4 downstream ACDCs (LVDS) [5]
- Send any ACDCs a trigger signal

5. The ACC has hardware for 8 ACDC boards. Firmware is presently only configured for 4

- Store one event worth of data from each ACDC to RAM, available on request from the control computer
- Flag (1) whether an ACDC FPGA has triggered its PSEC4 chips and is reading out, and (2) whether ACDC RAM has been filled with event data
- Manage metadata

Metadata contained in each event of the ACC includes a total clock count and event count relative to the time of powering up.

5.2.3 Control computer

The control computer is the entity that sends 32-bit USB-serial commands to the ACC. This computer also stores PSEC4 data en-mass to hard memory. The hardware and software requirements are that it have the USB communication drivers required by the control software suite, as well as compilers for the software.

For the present front-end electronics system at Fermilab, the software is written in C++17 using a C++ USB-driver library called "usb.h", a legacy version of the cross-platform libusb library [106]. This code is hosted on a Raspberry Pi 3B+ (RPi) computer with Raspbian OS, a derivative of the Linux Debian operating system. The RPi is equipped with 16 GB of hard memory for data storage. The RPi is configured to be controlled over kerberized SSH on the Fermilab network. It has also been controlled in an offline state by a hard-wired ethernet line and static IP address.

The control software is designed around the constraints and communication systems of the ACC and ACDC firmware. The most recent version of the control software is structured using class data-structures representing an ACC that contains ACDCs that contain Metadata structures. The software is structured such that class objects contain all information about digitized events, including waveform data, metadata, and board settings. At present, the

metadata and waveform data for events are stored as ASCII text files for a total of about 16 kB per event per board. A next step for software developers using the PSEC4 electronics system is to implement run-time storage of ACDC objects without the need for ASCII parsing. This could also enable the use of identical data structures for both the DAQ system and analysis code of an experiment using the PSEC4 electronics.

5.3 Priority improvements to the electronics system

The most significant improvement that can be made to the FTBF LAPPD TOF system tested in this thesis is to re-design the firmware for the ACC/ACDC system. The firmware of the ACDC and ACC boards are at a first-draft stage. The structure of the firmware propagates to all upstream entities, affecting control software and analysis procedures. Drawbacks in the firmware can affect many aspects of data interpretation and processing.

This section will describe a few of the limitations of the ACC/ACDC front-end electronics system as well as suggested adjustments for improving the robustness of the LAPPD TOF system. The PSEC4 chips and design of the ACDC/ACC boards are solid and sophisticated, in contrast to the firmware. For context, it is helpful to present a few of the hardware features that are presently unused and can be implemented in the next firmware version:

- ACC control of 8 ACDC boards as opposed to the 4 presently implemented
- Ethernet and/or VME data input-output (I/O) interface on the ACC to replace the USB interface
- Small form-factor pluggable transceiver (SFP) interfaces on the ACC, possibly for daisy chaining of lower-level ACCs to a control ACC
- Unused ACC RAM and ACDC RAM that may be implemented to store ~100 digitized events during a test-beam spill.

- PSEC4 trigger-threshold control on a channel-to-channel basis, as opposed to the chip-to-chip threshold control at present

5.3.1 Trigger-rate limitations

The rate limitation of the front-end electronics, coupled with the asynchronous triggering of detectors separated by long lever arms, presents the most significant challenge for acquiring useful particle information at the test-beam. The maximum photon flux limited by the micro-channel plates of the LAPPD is about 100-1000 kHz per square centimeter [107]. Analog signals from PSEC4 chips can be digitized and read-out at a maximum rate of about 50 kHz per chip [99]. In comparison, the present firmware and hardware of the ACDC/ACC system results in maximum event rates of 3-5 Hz. An explanation is below.

This author's understanding of the rate limiting processes comes largely from lessons from Jonathan Eisch and Eric Oberla.

Calculated rate-limit

Most of the event-rate limitation is generated by the time delay for transferring data from the ACDC boards to the ACC. The data transfer scheme from ACDC to ACC uses a single LVDS twisted pair as a universal-asynchronous receiver-transmitter (UART) line [108]. The 8-bit words from PSEC4 data are framed using a start and stop bit encoded in the 8b/10b encoding scheme [109]. The UART bit rate tested in this section is 10 Mbps for 10-bit codes. This implies that 8-bit words are clocked at an effective rate of 8 Mbps. The asynchronous communication scheme may reduce this rate by as much as a factor of two, to 4 Mbps [110]. Each ADC value of the PSEC4 chip is transferred as two 8-bit words. The data from each ACDC is transferred successively in serial to the ACC.

Define N as the number of ACDC boards controlled by the ACC. The approximate rate limit (within a factor of 2) is

$$\text{Transfer time} = N \times 30\,\text{channels} \times 256\,\text{samples} \times 2\frac{\text{bytes}}{\text{sample}} \times 8\frac{\text{bits}}{\text{byte}} \times \frac{1\text{s}}{4\text{Mbits}} \qquad (5.1)$$

producing a transfer time of about 31 ms per board. The same calculation, but for the 48 Mbps clock rate of the USB transfer from the ACC to the control computer, produces an additional delay of 2.56 ms per board. Any control-software wait-statements or on-line computations with significant delay will also contribute.

For comparison, the PSEC4 SCAs are fully digitized in 4 μs and data from all channels are stored to RAM after an additional 9.6 μs [99, 97].

A configuration of $N = 3$ ACDC boards was tested for rate limitations at the test-beam. Hard-coded wait statements were placed into the control software on either end of the USB command for readout of the ACDC data. For example, a readout of an ACDC data buffer would follow the sequence: wait, read USB data, wait. These wait statements were varied from 0 ms to 6 ms per board. If the wait statements were less than 5-6 ms, either the USB driver would report a time-out of 50 ms, indicating lack of response from the ACC, or the USB driver would report a lost connection to the USB line [6]. The measured stable readout rate of 1000 events is about 4.5 Hz, which agrees with the 12 ms software delay combined with rates calculated above.

Improving the rate capabilities in the test-beam

Beam particles are sent to the FTBF every minute, at which point anywhere from 1000 to 1 million particles are delivered over a 4 second period. Following the spill, there is 56 seconds of wait time.

6. The USB chip on the ACC is the Cypress EZ-USB FX2LP USB Micrcontroller [111]

The ACDC and ACC boards use FPGAs that have unused RAM after accounting for the space used by firmware logic. Up to 100-200 events could be stored in unused ACDC RAM while the particles in the FTBF are spilling [7]. Following the spill, during 56 seconds of down-time, these events could be transferred to the upstream control board and control computer. This would increase the maximum event recording rate by about a factor of 100, to 500 Hz for capturing 2000 events per spill compared to the 20 at present.

5.3.2 The USB communication system

As was mentioned in Subsection 5.3.1, hard-coded software delays are required during data readout due various failure modes in the USB communications. Even in the stable operating mode, some of these failure modes are observed randomly during data-logging on useful particle beams.

One failure mode involves the USB driver reporting a time-out due to no data on the USB line. This particular failure can be alleviated with a command to the ACC telling it to reset its USB firmware signals to their initial state. Another failure mode involves the USB driver reporting a loss in connection. This failure mode can only be alleviated by power cycling the USB chip [111] on the ACC. This requires one to physically unplug the USB cable.

The USB chip receives power from the host computer USB socket. However, the USB chip specification makes it clear that driving the input/output pins while the chip has no input supply voltage will shorten the lifetime of the device [111][8]. Some symptoms related to USB failure could be caused by long-term use of the ACC while the USB chip is not plugged into the control computer.

The next firmware revision should include the implementation of an ethernet commu-

7. The implementation of the ACDC firmware for this thesis has 4.1 Mb of unused memory

8. This discovery came out of conversations between David Greenshields of University of Warwick and Mircea Bogdan.

nication system between the control computer and the ACC. This will likely improve the communication fidelity and is generally a more preferable hardware format. The hardware for this communication scheme already exists on the ACC.

5.3.3 Minimum trigger-threshold

The "self-trigger" is a term used in this thesis to describe the use of on-chip threshold discriminators to pass a Level 0 trigger (see Section 6.1). Each PSEC4 channel has a threshold discriminator that asynchronously latches when an input analog signal passes a pre-configured threshold [99]. The polarity and threshold is set by on-board DACs routed to pins on the PSEC4 chips. The ACDC boards used in this thesis only have one DAC per chip, resulting in a common trigger threshold for each of the 6 channels on one chip.

In 2018, John Podczerwinski investigated the properties of the PSEC4 threshold discriminators at thresholds close to 0 mV [112]. This study found that manufacturing variations of the PSEC4 chips result in a channel-to-channel variation in the actual trigger thresholds of the discriminators. The actual thresholds are a constant offset from the input DAC value by 10s of mV. Because only one DAC output is fanned out to all of the 6 PSEC4 channels, the channel with the worst offset determines the minimum trigger threshold for the entire chip [9].

The result is that either high thresholds are set, reducing sensitivity to small photoelectron signals, or small thresholds are set and over-sensitive channels are masked, introducing spatially non-uniform trigger distributions.

The solution to this problem is to include 30 DACs on the ACDC board, one for each channel's threshold discriminator. This hardware change has already been implemented in the next iteration ACDC board, the ACDC rev C [113].

9. "A chain is only as strong as its weakest link", Thomas Reid

5.3.4 Trigger-location identification

As is mentioned in Section 5.1.2, approximately 7-10 samples of each digitized waveform are corrupted due to a current injection when the PSEC4 chips are told by the FPGA to halt their sampling. This is called the "trigger location". The first non-corrupt sample after the trigger location represents the t = 0 reference for the circular PSEC4 buffer.

It is critical to identify the trigger location so that these corrupt samples do not introduce noise in the waveform analysis and so that a t = 0 reference may be identified. The present ACDC firmware includes a "bin counter" that attempts to identify which 1/10th of the event window, or "bin", contains the trigger samples. This consists of a PLL-multiplied clock at 10 times the board's clock rate, counting and latching when the FPGA passes the Level 0 trigger (see Section 6.1).

During this thesis work, the corrupt trigger samples were observed to have no correlation with the event-window bin reported by the bin counter. This feature needs to be fixed during the next firmware revision as it effects the fidelity of the analysis in Chapter 7.

5.3.5 ACDC rev C

The ACDC board used in this thesis is revision B ("ACDC rev B"). During the summer and fall of 2019, Eric Oberla designed and fabricated 6 ACDC rev C boards that include the following hardware modifications: re-designed clocking scheme; completely re-done power distribution, bringing the power consumption from 10 W to < 1 W and allowing for any voltage input between 5-24 V; individual trigger threshold DACs for each PSEC4 channel; and gain-boosted calibration line for simultaneous calibration of all channels.

5.3.6 PSEC4a

A version of the PSEC4 chip called the PSEC4a has been designed. This 1.9 GHz bandwidth 8 channel chip has the ability to sample from 1-10 GSPS using a primary 132-sample SCA

that can be written to a bank of 8 randomly-accessible blocks [114, 115]. The multi-event buffer capability can be programmed to allow for either effectively dead-time-less digitization or a 4x longer event buffer than the PSEC4. At the time of this thesis, a small number of chips have been fabricated and tested using a single chip evaluation board. Unfortunately, the chip was designed using a now deprecated format.

5.3.7 References for users and developers

A number of references and documents exist that are useful for starting work with the PSEC4 electronics system. These references may also help firmware and hardware designers understand the state of the current system.

1. For an introduction to using ACDC and ACC boards in the lab, see Reference [116]
2. For properties and characterization of the PSEC4 chips, see References [97] and [99]
3. Schematic of the ACC [103]; Schematic of the ACDC rev B [117]; Schematic of the ACDC rev C [113]
4. Git group containing repositories for the ACDC firmware, ACC firmware, and control software [118]

CHAPTER 6

EVENT TRIGGER

6.1 Trigger structure

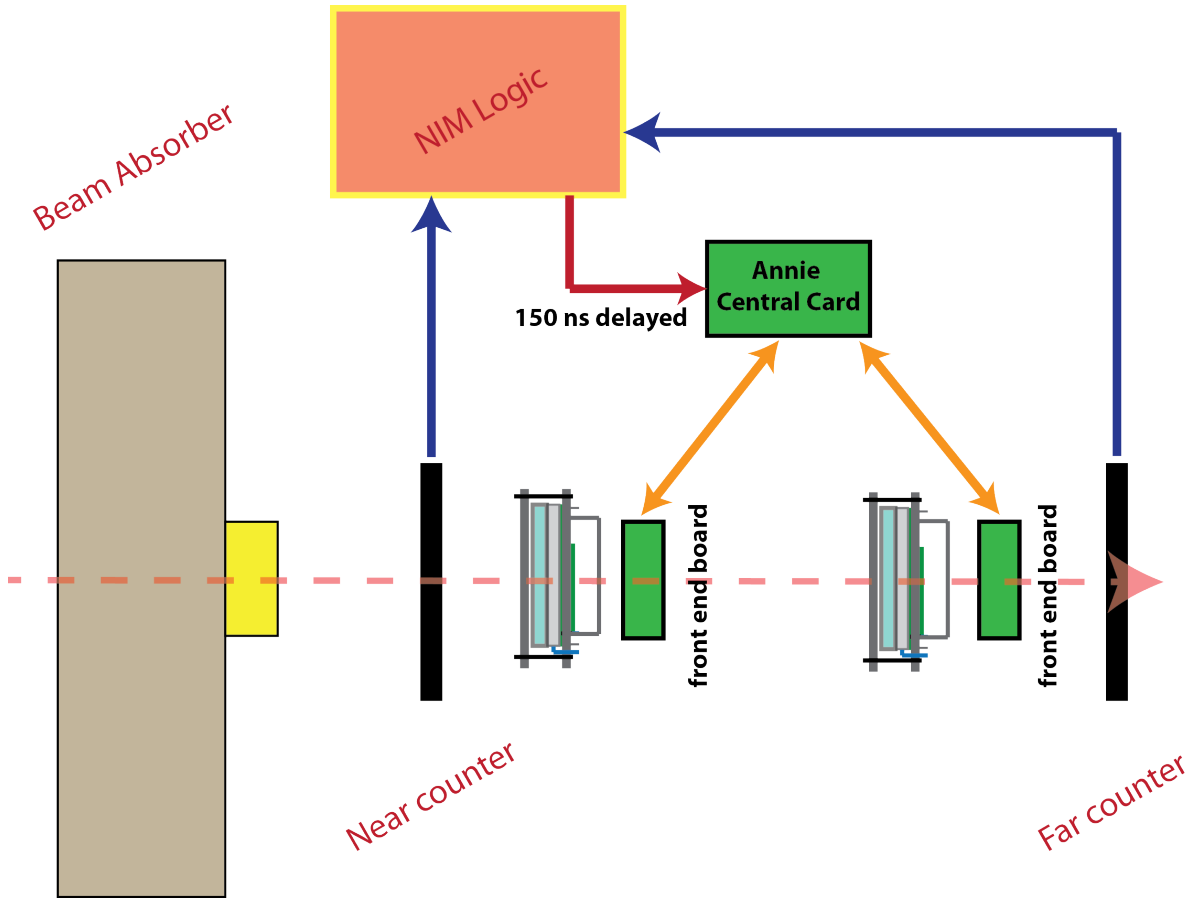

Figure 6.1: A diagrammatic top-down view of the MT6.2 beam-dump configuration, emphasizing the elements of the trigger. Particles travel from left to right. The black rectangles are scintillation counters. The LAPPDs and front-end electronics are between the counters and trigger asynchronously. Data are latched and held until the delayed coincidence trigger arrives.

This chapter relies on some knowledge of the front-end electronics system described in Chapter 5. If you are unfamiliar with some of the terms used, it is suggested that you go back and read the beginning of that chapter.

6.1.1 Beam trigger

Beam particles are detected using the coincidence of two 8" × 12" scintillating paddles with attached PMTs[1]. The PMT-anode outputs are connected to a NIM threshold discriminator set to -50 mV. Discriminator outputs are timed for coincidence using a logic coincidence NIM module. Outputs of the coincidence module are sent to a visual-display scaler and the Annie Central Card (ACC).

The output of the coincidence module has about a 100-150 ns delay relative to the particle arrival time at the LAPPDs. This delayed NIM pulse is converted to TTL and discriminated by an input pin on the ACC FPGA. The ACC then sends a trigger signal to all downstream ACDCs. This scheme is shown schematically in Figure 6.1

6.1.2 ACDC self-trigger

Each channel of the PSEC4 chips has a configurable constant-threshold discriminator. Each discriminator outputs HIGH if any switched capacitor array (SCA) sample passes threshold during a particular board clock cycle. The outputs of these discriminators are routed directly to the ACDC FPGA to be interpreted at each clock cycle. The FPGA can be programmed to apply self-trigger logic conditions such as channel masks, channel coincidence, and chip coincidence.

A major constraint of the trigger is that the decision to latch the PSEC4 samples must be made in less than a board clock cycle (25 ns or 40 ns), as the circular buffer SCA will start to overwrite itself. The delayed signals from the coincidence system of scintillation counters will not arrive at the ACDC boards in time to latch the PSEC4 chips.

The solution is to latch-and-hold the PSEC4 samples if any event passes the self-trigger logic condition. The board waits for a delayed signal from the upstream ACC, holding the voltages on the switched capacitor array. If a delayed signal does not arrive within a

1. Courtesy of Todd Nebel and the FTBF

pre-configured time, the digitizing channels re-start their analog sampling.

6.1.3 Trigger-state definitions

The full trigger configuration consists of four states and three trigger levels that transition between the states. The states and levels were defined with advice and input from Luciano Ristori.

ACDC trigger states

1. **Quiescent:** the analog signals on each PSEC4 channel are continuously passing over the switched capacitor array (SCA). The voltages of each capacitor are not held. Each channel's discriminator output is connected directly to the FPGA, with logic high output if the voltage passes a pre-configured threshold during one board clock cycle.

2. **Hold:** the capacitors of the SCA are held open circuit, latching their voltages. Leakage currents in the SCA are small: a 600 mV signal is affected by $\pm 100\mu$V over 4 μs [99]. This is a negligible effect on the 100s of nanoseconds delays of the beam coincidence trigger.

3. **Digitize:** the voltages on each capacitor are measured using the ramp-compare ADC and stored in ACDC RAM.

4. **Transfer:** the single event is sent to the ACC over the LVDS data line.

Trigger levels

Level 0 moves from state 1-Quiescent to 2-Hold. This occurs when a pre-configured logic condition, such as a channel coincidence or channel mask, is met by the discriminator outputs.

Level 1 moves from state 2-Hold to 3-Digitize. This occurs when a trigger signal arrives at the ACDC from the ACC, usually induced by a delayed beam-trigger coincidence. If a signal from the ACC does not arrive within a pre-configured time, the system returns to state 1-Quiescent.

Level 2 moves from state 3-Digitize to 4-Transfer. This occurs when the ACC is informed that digitization has completed, and the ACDC is ready to transfer data.

In summary, pulses from noise or from charged particles pass the Level 0 trigger. The scintillation paddles generate a delayed coincidence signal discriminated by the ACC. The ACC sends a trigger signal to the ACDC. If the ACDC has passed Level 0 and receives the ACC trigger, it passes Level 1. The ACC waits for the ACDC boards to store their events in RAM before passing Level 2.

6.1.4 Simultaneous triggering of multiple LAPPD stations

The most significant limitation of this trigger scheme is that the 3-4 LAPPD stations trigger asynchronously, and therefore may not pass Level 0 from the same beam particle. This event is therefore not useful for particle time-of-flight. The collection efficiency of events that comprise of the same particle are detailed in Section 7.7 and is heavily dependent on the beam and trigger configuration.

One improvement to data purity involves implementing a time window in the Level 1 trigger. The time at which a particle arrives at each detector station is known roughly by dividing the separation distances by the speed of light. The clock cycle that passes Level 0 at each board can be compared with their separation distances. The delays will be assessed at Level 1 with the arrival of the delayed ACC coincidence signal. An implementation could look like the following:

1. Calibrate the relative clock offsets of all ACDC boards before data logging.

2. Set individual trigger window times with a width equal to one clock cycle and aligned to the expected time delay of a particle passing through each successive LAPPD station at the speed of light

3. Require the delayed beam coincidence signal to arrive at the front-end boards within this small predicted time window for Level 1 trigger to pass.

This would allow for low thresholds to be set on each self-trigger channel. Another solution is to increase the self-trigger thresholds. This could also reduce the event recording rate.

6.2 Mapping of strips to electronics channels

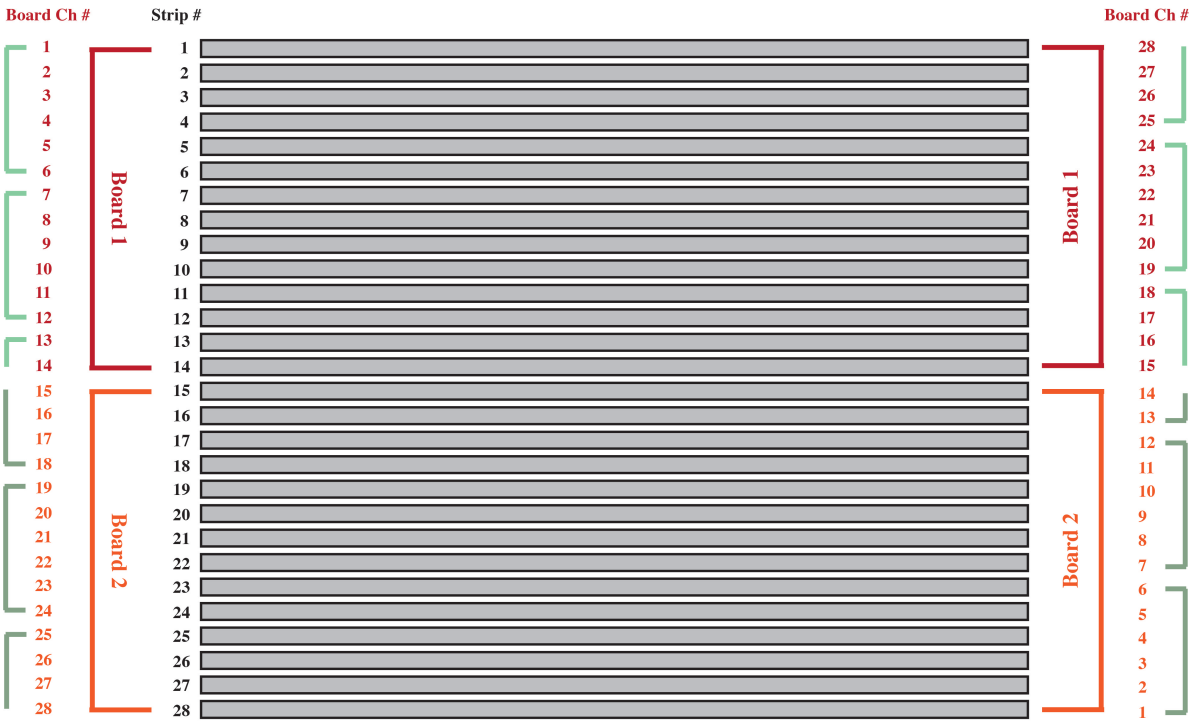

Figure 6.2: Diagram of the map between front-end board number, channel number, and strip number for the ANNIE readout board. The chip that channels belong to is indicated by the green brackets on the edges. Using this particular readout design, both ends of the strip are digitized by the same board, but not always by the same chip.

The ANNIE Analog Pickup Board (APB), designed by Bernhard Adams, is a PCB board specifically designed to transfer strip-line signals from Generation-I Incom LAPPDs to ACDC-board channels. This readout board is introduced and photographed in Chapter 3.

The layout of the pickup board and readout, along with its mapping to the front-end electronics, influences the analysis implementation. For example, the mapping function of the ANNIE APB needs to be encoded in an analysis with the position and left-right polarity of each channel. This mapping is is shown in Figure 6.2.

One advantage that may be drawn from the ANNIE APB mapping is that a single strip does not require board-to-board synchronization for longitudinal position reconstruction. However, a constant chip-to-chip timing offset must be accounted for because the ends of the strips are usually digitized by different PSEC4 chips [2].

Another readout configuration used intermittently is the capacitively-coupled pickup board shown in Figure 3.4. With this readout configuration, the strips are digitized on one side only and mapped 1-to-1 to channels on a single ACDC board. A switch-case in the analysis code determines the method used for particle reconstruction depending on which of these two readout configurations is active.

Synchronization signals are funneled into channels 6, 12, 18, 24, and 30 via an RF-splitter mezzanine board shown in Figure 6.3. The use of one synchronization channel per chip complicates a position analysis due to the existence of interspersed, inactive strip-lines. The result of testing with this synchronization board is a measurement that concludes that the chips do not have significant relative timing jitter (see Appendix B). Only one channel per board need be used for synchronization in the future.

Synchronization was only implemented during the final data-taking run that occurred in the MT6.2 enclosure. This data-taking run was cut short by the coronavirus. Due to its

2. See calibration procedure in Appendix B

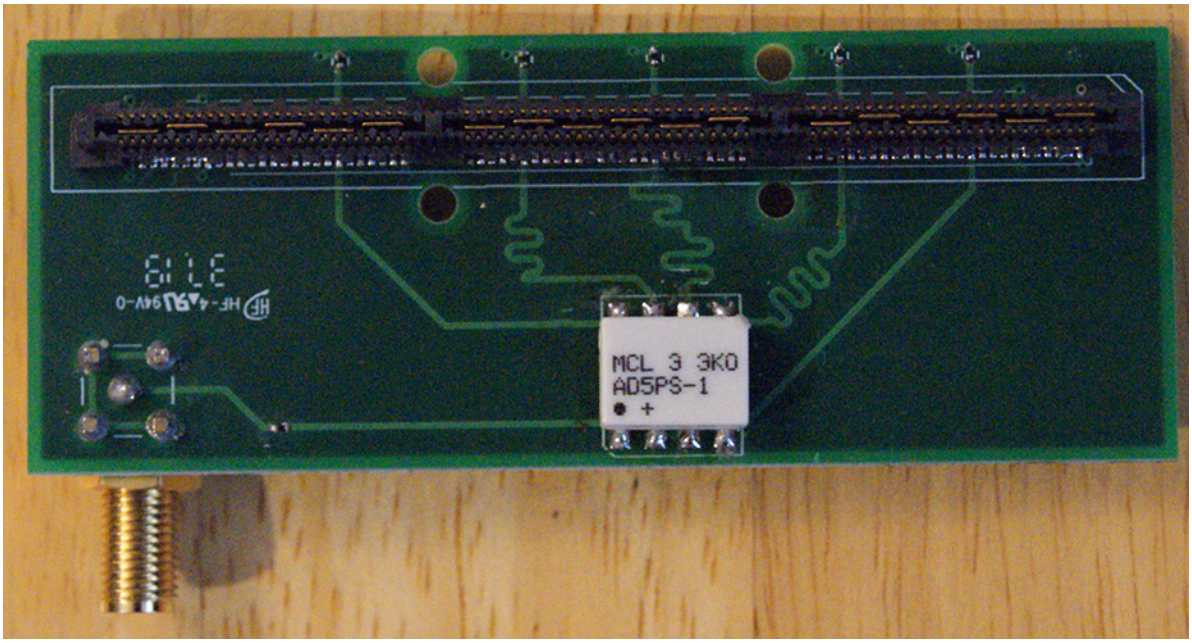

Figure 6.3: Photo of the PCB for distributing WR-ZEN synchronization signals to one channel on each PSEC4 chip. This board bridges the two SAMTEC connector inputs on the ACDC board. The next iteration of the PCB should not consider trace length matching (the "trombones" and squiggles seen in light green) as each chip already has a constant relative time offset that requires calibration.

low statistics, this data-set is used to characterize synchronization and act as a sample for drafting time-of-flight analysis code.

CHAPTER 7

ANALYSIS OF LAPPD SIGNALS FROM CHARGED PARTICLES

7.1 Description of datasets

ID #	1	2	3	4
Location	beam-dump	beam-dump	enclosure	enclosure
Primary particle	cosmic rays	muons from dump	120 GeV/c protons	120 GeV/c protons - no photocathode
Beam diameter	–	20 cm	6 cm	6 cm
LAPPDs	Tile 31, L43, L42	L43, L42	L43, L42	L43, L42
Digitized fraction	1, 0.5, 0.5	1, 1	0.5, 0.5	0.5, 0.5
LAPPD sep.	0.75 m, 5 cm	0.75 m	5 cm	5 cm
Synchronization	no	no	yes	yes
Self-trigger	-12 mV	-44 mV	-30 mV	-30 mV
Sample interval	156 ps	156 ps	98 ps	98 ps
Unfiltered events	50,000	5,600	3000	2000

Table 7.1: Summary and labeling of datasets used in this chapter. The quoted beam diameters are rough and may have errors on the order of 1-2 cm.

7.1.1 Run plan for the MT6.2 enclosure TOF prototype

Table 7.1 summarizes relevant qualities of the datasets used in this chapter. They include runs from the three locations described in Section 4.4. Datasets # 3 and 4 are from the installation into the MT6.2 enclosure. This system, which allows for the installation of up to 5 LAPPDs in 3 LAPPD stations, was installed during the period between 3/2/2020 and 3/11/20.

The run plan for the MT6.2 setup included one week of tuning the trigger, optimizing on efficiency of coincident triggers between multiple LAPPD stations. The following week was allocated for making a measurement of timing resolution of LAPPDs 43, 42, 51, and Tile 31

by placing LAPPDs in close succession, 5 cm apart, and measuring the relative-arrival times of a focused beam of 120 GeV/c protons. The final week was allocated for distinguishing pions and kaons at a variety of beam energies using the natural contamination of kaons in the low-energy pion beam modes of MTest.

The coronavirus outbreak lead to this run plan being cut short. The trigger configuration was tuned over a period of three night shifts before the accelerator shut-down. This trigger tuning was informative, resulting in the datasets # 3 and 4 in Chapter 7, and providing input for the next stage of the run plan. The run may be continued and carried out as soon as beam returns to the FTBF. The timing-resolution measurement may be performed using cosmic rays before the return of beam. The system may continue to be tested in the present location. A next-iteration system is proposed in Appendix A.

7.1.2 Observations during the trigger-tuning period

Until this period in the MTest enclosure, it was suspected that different PSEC4 chips on the same ACDC board have significant relative timing-jitter. To test this, a custom PCB was installed that distributed synchronization signals to one channel on each PSEC4 chip on each ACDC board. This measurement required rendering 30% of the useful LAPPD strip-lines inactive.

The conclusion of testing during the MT6.2 enclosure run was that the chips have a calibrate-able relative-timing offset and a relative-timing jitter consistent with the channel-to-channel timing-jitter of the PSEC4 chips (see Appendix B). In the next run, only one electronics channel is needed for synchronization and all strips may be digitized.

The micro-channel plates can exhibit significant gain reduction at high flux densities. The flux was reduced to as low as the test-beam operators could provide. To further reduce the flux density of particles in the test-beam, the RMS beam size was set to about 5 cm. Setting the beam divergence this wide was later found to be unnecessary. In the next run,

the beam should be focused on a single strip to reduce triggers from dark-noise and increase the efficiency on simultaneous triggers of LAPPD stations.

Charged particle signals are expected to be 10s of photoelectrons (see Section 1.3.1). Constant thresholds for passing Level 0 trigger were set to about -30 mV before accounting for variations in the discriminator values in the PSEC4 chips as described in Section 5.3. Higher trigger thresholds will be used in the next run to reduce dark-noise and increase simultaneous trigger efficiency.

The timing of particles arriving at successive LAPPD stations may be used to define a short trigger window for passing Level 1 (see 6.1.3). This improvement requires a small change to the electronics firmware system and is described in further detail in Section 5.3. The inefficiency on simultaneous triggering of LAPPD stations on the same particle due to a lack of constrained Level 1 timing was noted during the analysis of the datasets from the short MT6.2 enclosure run.

7.2 Examples of raw data

Figure 7.1 shows raw data from an event occurring with LAPPDs 43 and 42 aligned and separated by 5 cm. Digitized waveforms from both ends of four neighboring strip-lines are shown. The two LAPPDs may be transversely offset by a few millimeters, or the particle may be angled by a few degrees, as indicated by the primary pulse on LAPPD 43 being one strip off from the primary pulse on LAPPD 42.

Figure 7.2 shows a 2-D display of a similar event, this time with both ends of all strips displayed separately. This display of raw data reveals features that may be due to cross-talk. This display also reveals that in this data-set, a few strip-line ends failed to couple to their respective electronics channels.

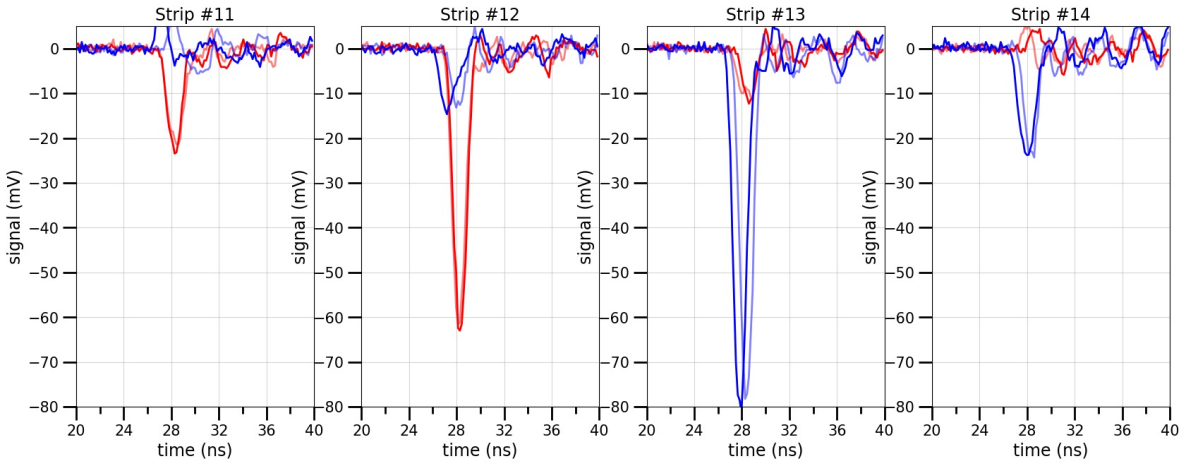

Figure 7.1: An event from data-set # 1 with LAPPDs 43 and 42 in close proximity measuring the same cosmic ray particle. Both sides of four strips are shown, with the left side of each strip at 50% opacity and the right side at 100% opacity. The sharing of charge among neighboring strips allows for transverse position reconstruction. Statistical distributions of charge sharing are used to measure the effective transverse size of the charge-cloud image.

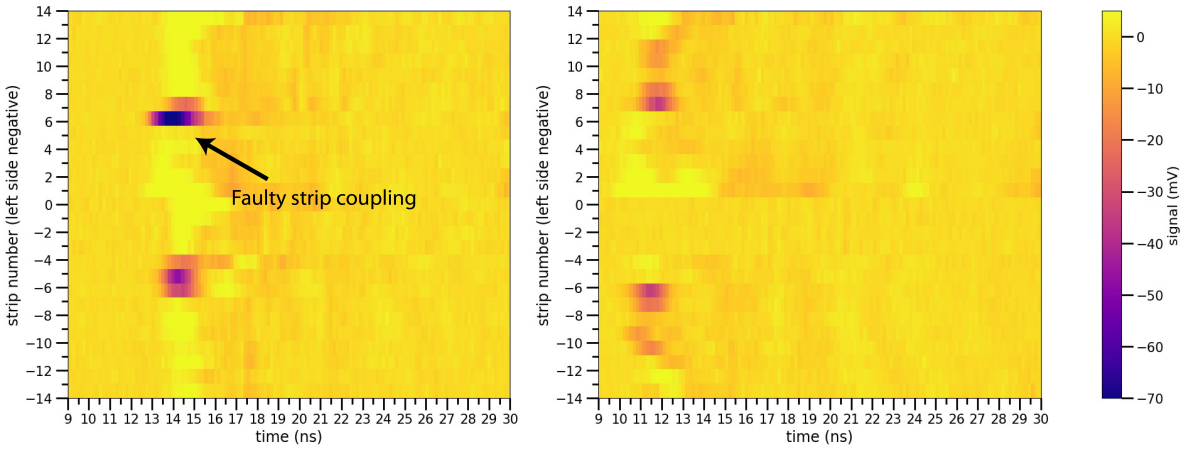

Figure 7.2: A 2-D display of raw data from two simultaneously triggered LAPPDs in data-set # 1. Each sub-plot represents half of a digitized LAPPD area. The left sides of strips are on the bottom half of each sub-plot, and right sides on the top. The location of a de-coupled strip, as described in the text, is called out. More can be seen from y = [0, -3] on the right-hand subplot.

7.2.1 Signals from Tile 31

Tile 31 is a ceramic capacitively-coupled Generation-II LAPPD that was fabricated using the batch production process described in Chapter 2 and Reference [46]. A 3% Cs-Sb pho-

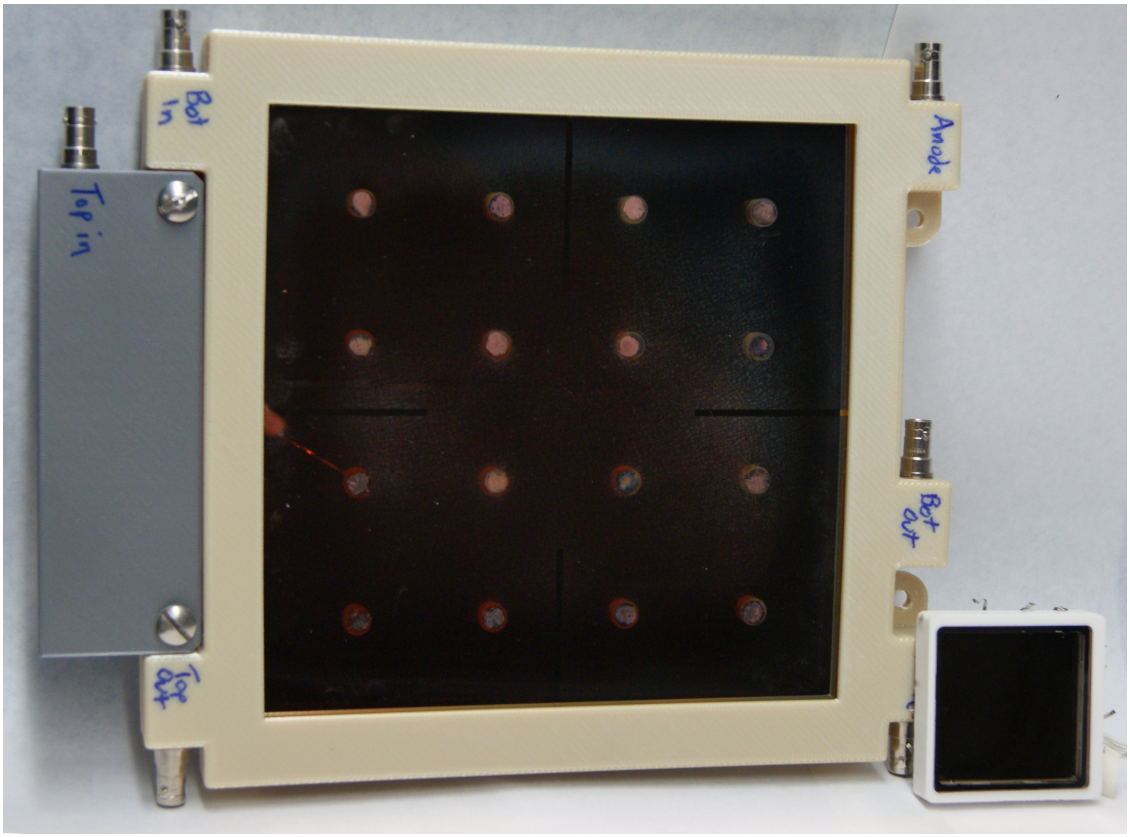

Figure 7.3: A photograph of Tile 31 instrumented with a modified Incom frame for distributing high voltage to brazed copper pins. The smaller MCP-PMT on the right is a Photonis Planacon.

tocathode was formed in the fabrication chamber while the LAPPD internal volume was attached to a pump. After cooling to room temperature, the micro-channel plates were biased and pulses were observed using a pulsed-laser source and an oscilloscope. The high voltage settings were chosen to be around 800-850 V per MCP.

The LAPPD cesium inlet-tubes were hermetically cold welded and the LAPPD was transported to Fermilab. Tile 31 was installed into an LAPPD TOF station to observe cosmic rays. An Incom frame as described in Chapter 4 was modified to allow for high voltage distribution to the copper pins brazed into the side of the LAPPD. The anode layer is connected to one brazed pin, which is then connected to the shield of a high-voltage jack using a solder lug. The modified frame as installed is shown in Figure 7.3.

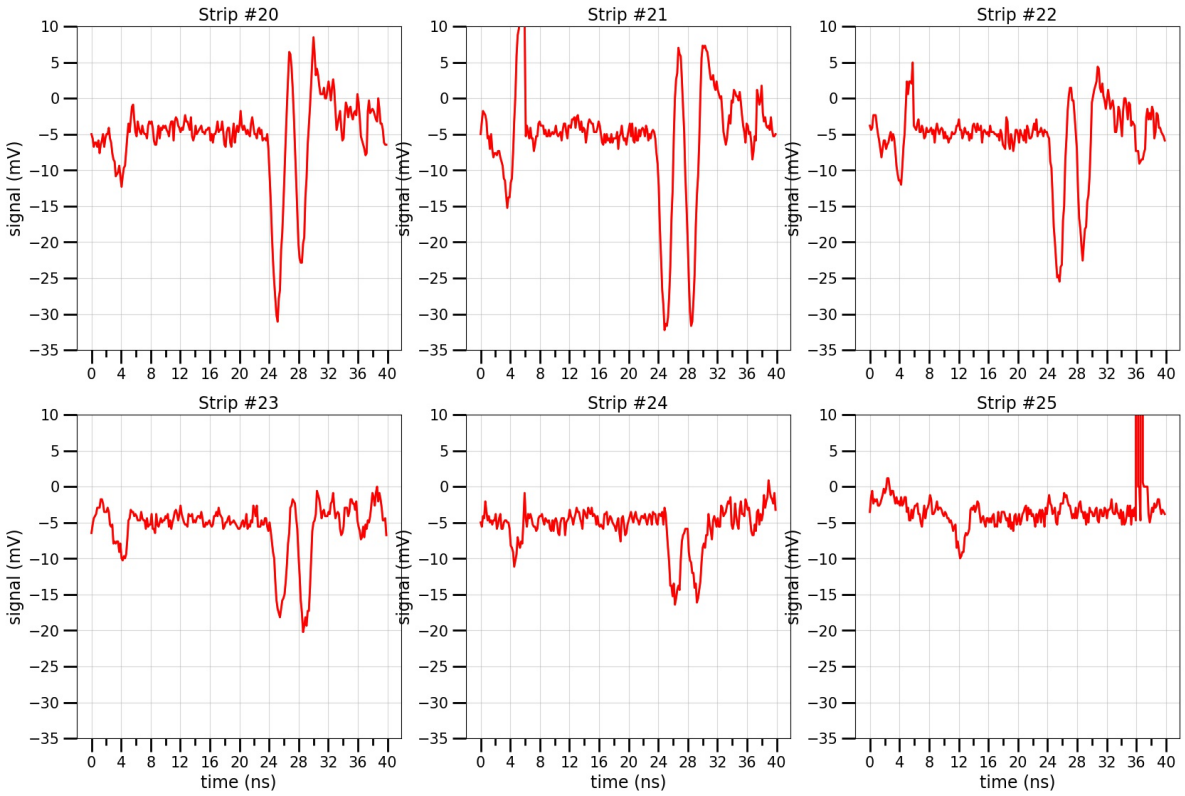

Figure 7.4: Raw data from 6 neighboring strips on Tile 31 detecting a cosmic ray particle. The open-ended readout scheme is demonstrated here, showing prompt and reflected pulses on each channel. The transverse spread of the amplitudes is larger than the directly coupled LAPPD, due to the geometrical layout of the strips and their distance to the internal anode. A few samples at about 36 ns on strip 25 are corrupt.

Because Tile 31 has about a factor of 8 lower quantum efficiency than typical LAPPDs, the number of Cherenkov photons produced for detecting particles was increased by coupling an 8 mm quartz radiator to the front window. The quartz was cut by manufacturers [119] to fit within the opening of the Incom frame. An optical coupling gel was used to remove any air gap between the window and radiator [120]. The 8 mm radiator increases the expected number of photoelectrons per particle to about 5-10.

Tile 31 was instrumented with an open-ended capacitively-coupled readout. The open ends were not extended with additional cable length because a readout compatible with extension was not available. However, reflected pulses are often distinguishable, as seen in

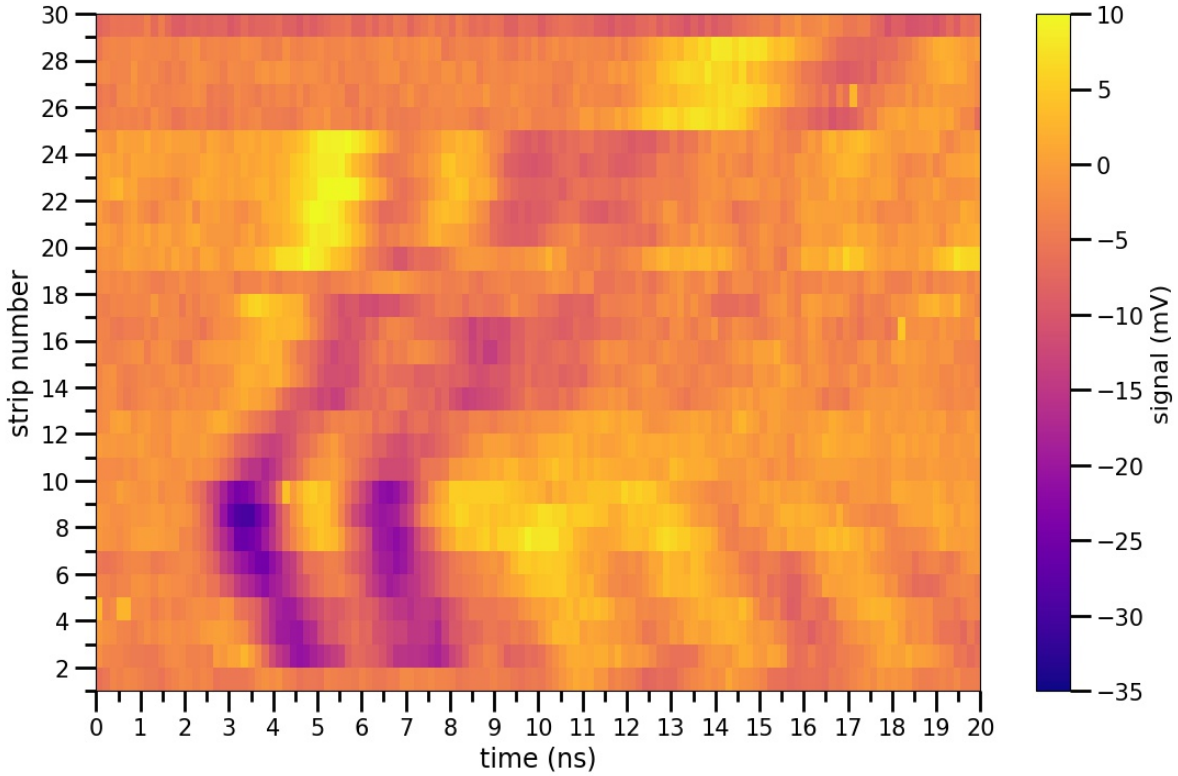

Figure 7.5: The heat-map view of a different event from Tile 31, showing prompt and reflected pulses over the full 8"×8"face of the LAPPD. The PSEC4-chip constant-timing offsets appear as vertical discontinuities in the image. Trailing ripples seen here are not always present in the direct coupled case for Generation-I LAPPDs.

Figure 7.4.

One challenge in an analysis of an unextended open-ended readout is determining the arrival time of the delayed pulse. The capacitive, bipolar swing following the prompt pulse becomes superimposed on the delayed pulse for strips that are not extended, slightly changing the shape of its leading edge and creating an effective baseline shift. The timescale for capacitively-coupled pulses to return to baseline sets the optimal length of cable extension.

Even still, one technique for reconstructing the arrival time of the delayed pulse is to perform and auto-correlation with time-lag on the event waveform. This procedure is used in Reference [99] on Planacon MCP-PMT signals. The auto-correlation function has local maxima separated by a time roughly equal to the separation between the prompt and delayed

pulse because the two pulses are highly correlated.

The 2-D display shown in Figure 7.5 emphasizes a wider transverse size of the image of the charge cloud compared to the Generation-I LAPPDs. The effect of chip-to-chip constant timing offsets from the DLL wraparound are also visible as vertical discontinuities in the image (see Chapter 5 and Appendix B). Low-amplitude ripples following the primary pulse are possibly indicative of an imperfect termination or reflections of charge on the internal anode.

7.3 Signal-processing techniques

The signal processing strategy can affect the performance of particle position and arrival-time reconstruction. Micro-channel plate PMTs typically produce pulses with leading edges of less than 1 ns duration. The front-end electronics system that digitizes these pulses adds timing jitter and noise that affects the reconstruction resolution at a level comparable to the intrinsic timing resolution of the detector.

A signal processing strategy has more flexibility when the full event is digitized over 10's of nanoseconds at a high sampling rate. In this thesis, the leading edge and shape of each MCP pulse is sampled at a constant rate of either 10.24 giga-samples per second (GSPS) or 6.4 GSPS over 25 ns or 40 ns respectively, allowing for reconstruction methods that use the shape information of pulses.

The contribution to time-of-arrival uncertainty generated by the particular choice of pulse-processing algorithm has been studied extensively by Genat et. al [76] and Breton et. al [30]. Both of these references attempt to study which components of an MCP-PMT pulse contain the most pertinent information for reconstructing the time-of-arrival. Lessons from these reports are used in the analyses to follow in this chapter; however, more sophisticated pulse-processing algorithms, either on the front-end FPGA or offline, should be implemented in the next iteration of the LAPPD TOF system. The analyses that follow are a first draft

at an end-to-end raw-waveform processing system.

7.3.1 Constant-fraction discrimination

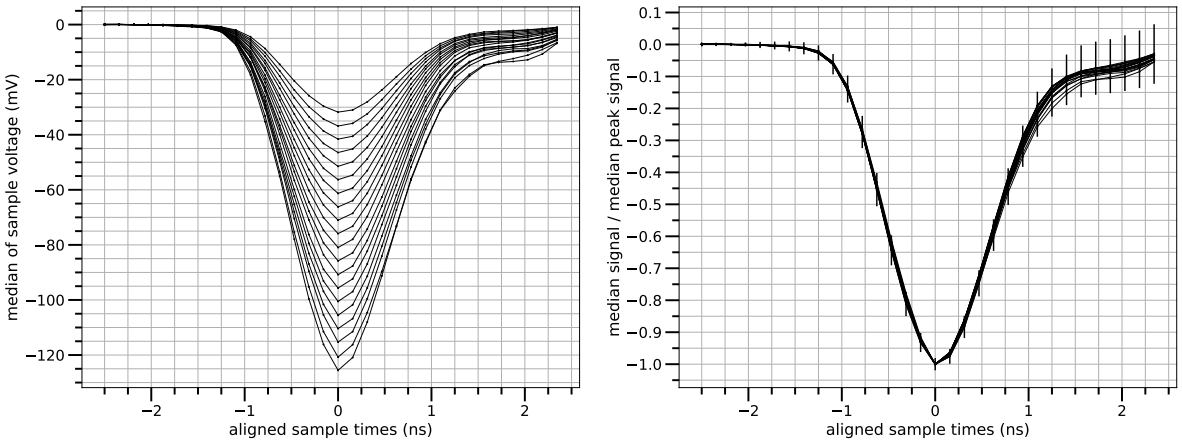

Figure 7.6: The median waveform for cosmic rays measured by LAPPD 43 as a function of pulse-amplitude. Left: the median waveforms of 20 bins of increasing pulse-amplitude. Right: the 20 median waveforms normalized by their peak amplitude. The procedure for producing the median waveform is described in the main text. Error-bars on the right-hand plot are enlarged by a factor of 20 to emphasize spread in the tails and leading edge. Error-bars represent the standard deviation of each sample divided by $\sqrt{N}$ where N is the number of pulses processed, ranging from 500 to 7,000 pulses depending on the amplitude bin (see Figure 7.7).

Reference [76] tests four different signal processing techniques for determining the time-of-arrival of MCP-generated pulses. Constant-fraction discrimination (CFD) is one of the more successful methods due to its low computational cost compared with maximum-likelihood fitting methods. This conclusion is also found in Reference [30].

Constant-fraction discrimination relies on the assumption that the pulse shape, in particular the shape of the leading edge, is independent of the pulse amplitude. The method reconstructs the arrival time by finding the first sample that falls below some fraction of the amplitude. The CFD reconstruction may be performed online using electronic delay generators and discriminators tuned to the expected signal shape. Here, the reconstruction is performed offline due to the availability of fully digitized waveforms.

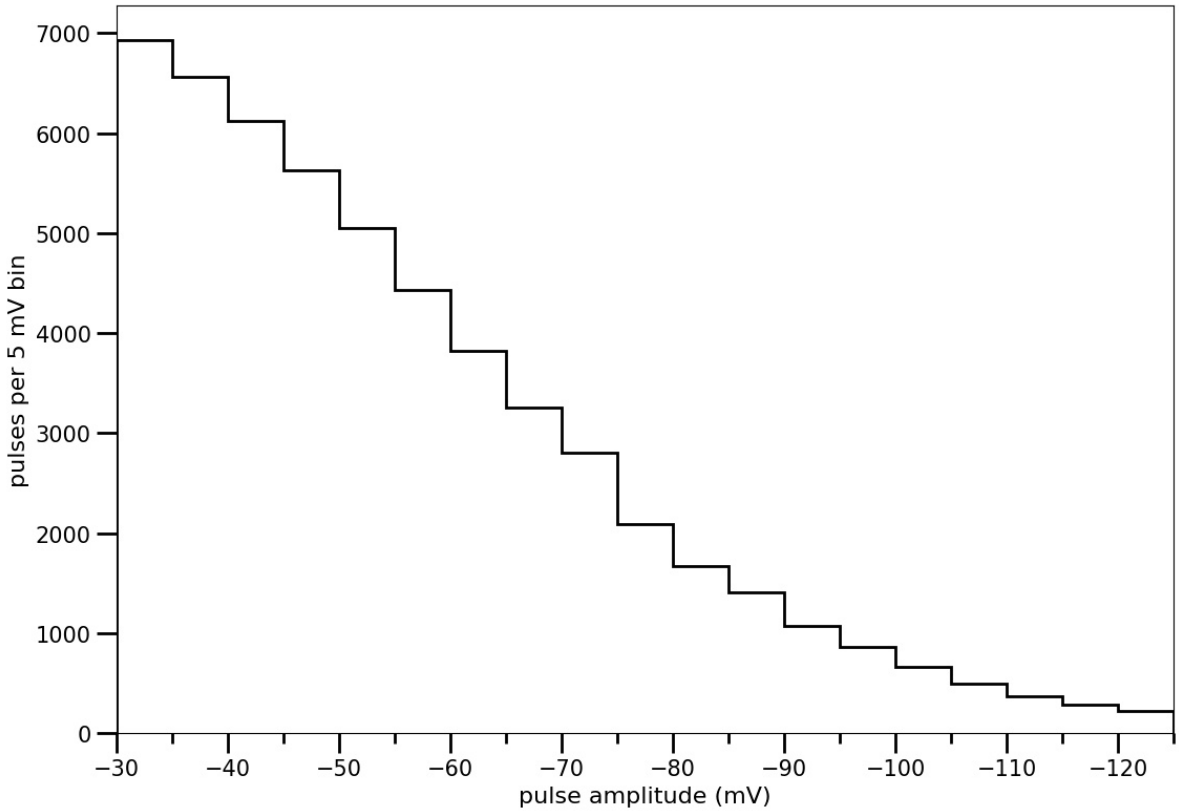

Figure 7.7: The number of pulses contained in each of the 20 pulse height bins used to reconstruct the median waveforms shown in Figure 7.6. The LAPPD 43 has a 5 mm thick B33 window, predicting about 20 - 30 photoelectrons per charged particle at a gain of about 1-2 $\times$ 10^6. The ordinate is used to calculate the standard error of each sample in Figure 7.6

The pulse shape of LAPPD signals from charged particles in the Fermilab Test Beam Facility (FTBF) are independent of amplitude to the degree shown in Figure 7.6. These pulses are generated from cosmic rays in dataset # 1 on LAPPD 43 digitized at 6.4 GSPS or 156 ps per sample. All LAPPDs are processed, but only LAPPD 43 is shown above.

Waveforms are fitted using the NNLS algorithm described below in Subsection 7.3.2. All local minima that pass a -20 mV threshold are identified using the full NNLS-fit waveform. The times of the local minima are measured using an interpolated spline fit with x10 sampling rate and order 3. All pulses are shifted such that their peak occurs at t = 0. Each waveform is given the same time base with the original digitizer sampling rate using linear interpolation of the raw data. These time-adjusted pulses are binned with respect to amplitude from -30

to -130 mV in bins of 5 mV width. The median of the signal at each sample is found for each amplitude bin.

The number of pulses in each amplitude bin is different, as the pulse-height spectrum is not uniform. A coarse pulse height spectrum is shown in Figure 7.7 using the 5 mV bin-width that defines each median waveform shown in Figure 7.6.

The range of 10%-of-max arrival times on the right-hand side of Figure 7.6 is about 20 ps [1]. One of the main contributors to the timing spread in the median waveforms, and equivalently the shape variation, may be noise in the baseline subtraction method or channel-to-channel variations of the non-linearity of the digitizing ADCs [2].

7.3.2 Template fitting

The most successful arrival-time reconstruction technique from Reference [76] uses all of the digitized samples of a waveform to constrain an iterative least-squares fit from a noiseless MCP-pulse template. This is computationally more expensive than the CFD method. In this thesis, a non-negative least squares (NNLS) template-fitting algorithm is implemented as a noise reduction tool as opposed to a time-of-arrival reconstruction method. For more information on the NNLS method, see References [121] and [122], Chapter 1 Section 2 of [123], and the python wrapper used in this analysis from scipy.optimize.nnls [124].

The NNLS template fit is obtained by solving the equation $\texttt{argmin}_x||\mathbf{A}\overrightarrow{x} - \overrightarrow{b}||$. In this equation, the noisy signal from front-end electronics is represented as a vector $\overrightarrow{b}$ with elements equal to the sample voltage at each time index. The j^{th} row of the matrix $\mathbf{A}$ is a noise-less template shifted in time by j samples relative to the 0^{th} sample of the waveform $\overrightarrow{b}$. The template is formed by performing a median pulse shape measurement, such as the

1. It should be noted that Reference [30] found that 22%-of-max was an optimal CFD arrival time for their data-sets.

2. This is not a fundamental issue; as is mentioned in Chapter 5, a linearity calibration is a standard operation that was cut-short in this work by the coronavirus lock-down.

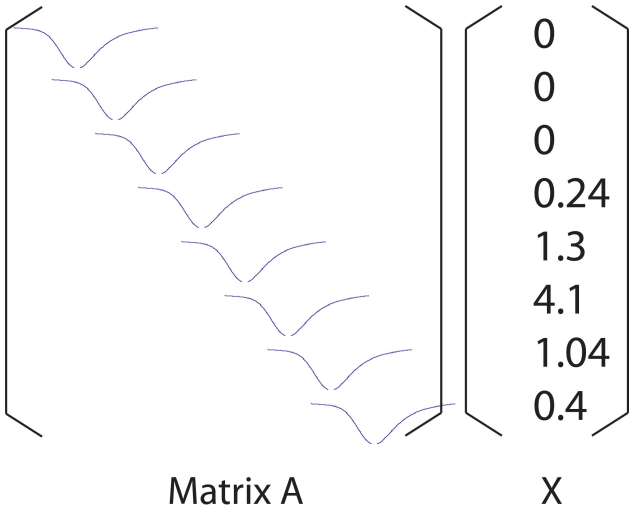

Figure 7.8: The NNLS matrix element **A** and solution vector x in cartoon form. The blue pulses in the matrix represent noiseless templates encoded in each row of the matrix. Each element of the solution vector represents a "component" of the full waveform appearing at a time indexed by the vector index with scale equal to the value of the vector at that index. The vector elements on the right, if representing a result of the NNLS algorithm, would represent a few photons arriving near the end of the event window.

one described in the previous subsection.

A cartoon representation of the template matrix and solution vector is shown in Figure 7.8. The Lawson and Hanson algorithm [121] minimizes the equation and converges on a solution for $\overrightarrow{x}$. Each element x_j of $\overrightarrow{x}$ represents a template waveform, or "component", of the noisy signal waveform that appears at time indexed by j, multiplied by a scale factor, x_j. A fit of the entire event, later called the full NNLS waveform, is the sum of all components. Figure 7.9 is an example showing a fully-fit event-window along with sub-components of the fit.

A sophisticated analysis could use this NNLS algorithm to disambiguate many photons distributed across the entire area of the LAPPD. It may also use the timing of the first-arriving components of the fit. The NNLS method may be extended to include additional constraints by modifying the template and signal vectors. For example, Matthew Wetstein and Jonathan Eisch point out that the NNLS matrix can include the constraint that every

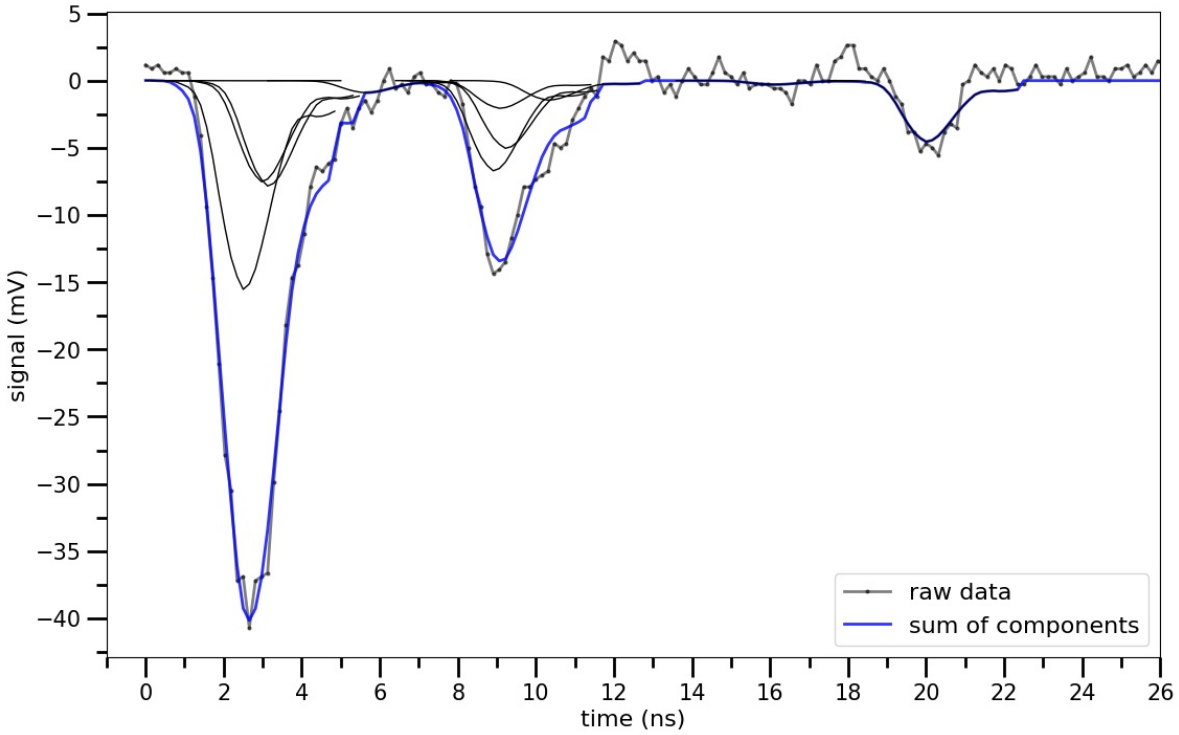

Figure 7.9: The output of the NNLS method is a vector that represents components of the full fit shown in solid black. The sum of all components is the solid blue curve. The fit results are sensitive to the template waveform used.

LAPPD pulse on one end of a strip-line should have a sibling pulse on the other end that is slightly attenuated and arrives with a delay [125]. One may also include the constraint that neighboring strip-lines have a shared signal due to charge sharing. Neither of these constraints were implemented in this thesis work; they are, however, a next step that could aid in the reconstruction of many photons distributed over a large area on the LAPPD.

Residuals of an NNLS fit are not gaussian distributed, so traditional methods of calculating significance, goodness-of-fit, and p-values are not valid [121]. In other words, the algorithm is not protected against over-fitting. In this thesis, the NNLS fit has only been used as a method of noise reduction for the purpose of locating pulses. Signal-processing analyses that extract timing and amplitude information use the CFD method or other methods on the raw data.

Templates generated by the median waveform reconstruction algorithm of the previous

section are used as input to the NNLS algorithm. In the future, it may be advantageous to form templates using single-electron calibrated laser data, as the NNLS fit components would more accurately represent single photoelectrons. [3]

7.3.3 First-pass pulse discrimination

In most of the analyses to follow, the first step is a first-iteration, "high threshold" pulse finding algorithm. During this phase, the most significant LAPPD pulses are identified in each event and stored for later use alongside the raw data. Analyses that follow, such as a time-of-arrival analysis, use these high-threshold pulses as a seed to inform a more precise and local analysis around the seed. This is similar to tracking algorithms that start with seeds and find clusters around those seeds using a shoulder threshold [126].

The seed pulse-finding algorithm begins with a full baseline subtraction using the median of all samples in the channel. An NNLS fit is then performed. All local minima are found in the NNLS waveform by calculating differences of adjacent samples, requiring a threshold of -20 mV, and requiring that any local minima found be separated by at least 3 ns. This peak finding algorithm is packaged in Python by Lucas Hermann Negri as "peakutils" [4]. The amplitude of each peak is found by spline fitting a 1 ns window about the peak with a spline order of 3 and a 30 ps interpolated sampling rate. The amplitude defines the 90% and 10% voltages for a constant-fraction discrimination performed on the raw data by stepping one sample at a time from the peak sample. The CFD linearly interpolates between discrete samples to find the 10 and 90 percent arrival times. A CFD is also performed to find the point at which the raw data falls below 10%-of-max after the peak time of the pulse. A rough estimate of the charge in the pulse is stored as the trapezoidal integral from 10% rise

3. During the course of this thesis work, an LAPPD calibration and test-stand was constructed at Fermilab's Lab 6 scintillator-fabrication facility. The test-stand, constructed by Bernhard Adams, Evan Angelico, Emrah Tiras, and the ANNIE collaboration, includes a PiLas 405 nm pulsed laser and motion stages for mapping the characteristics of LAPPDs for the ANNIE experiment.

4. Peakutils python package: `https://peakutils.readthedocs.io/en/latest/`

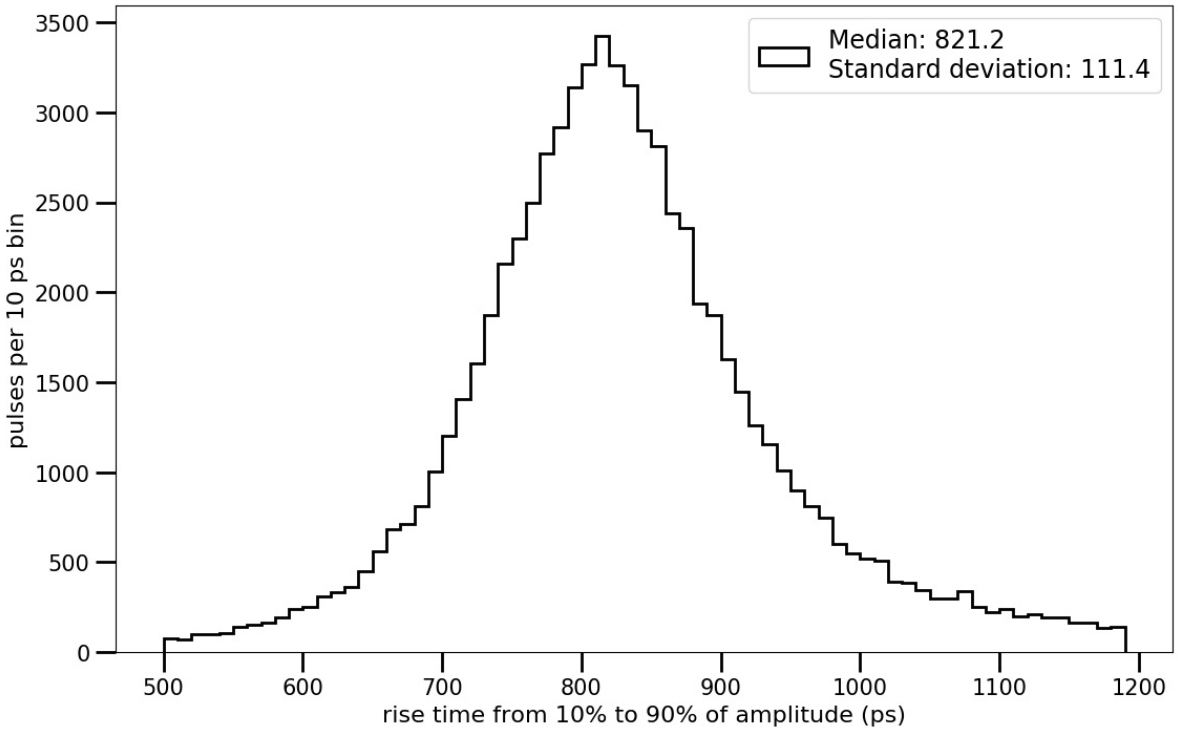

Figure 7.10: Rise-times of pulses from both LAPPDs in the cosmic ray data-set. This measurement uses the time difference between the 10% and 90% of max calculated by a CFD algorithm on the raw waveform. The raw waveforms are sampled at 156 ps time interval. The coarse, un-interpolated sampling causes the CFD to occasionally over or under approximate the rise-time due to noise on the raw wave. This is the main contribution to the tails of this distribution.

to 10% fall times of the raw waveform.

A rise-time discriminate cut is applied at this seed finding stage. Pulses with 10-to-90 rise-time [5] of less than 500 ps or greater than 1.2 ns are not stored. This occurs when the trigger signal does not arrive at the PSEC4 chips in time, with the circular buffer starting to overwrite the edge of the pulse thereby clipping it and shortening the rise-time. This 500 ps cut is informed by the rise-time distribution for data-set # 1 shown in Figure 7.10 with median 820 ps and 111 ps standard deviation.

The tails of this distribution are due to the raw-data sampling rate of 156 ps. The CFD

5. The term "rise-time" is sometimes used even though all LAPPD pulses are negative polar, and thus have a falling voltage or fall-time.

algorithm is processing the raw data instead of a re-sampled fit to the raw data. Occasionally, noise in the raw wave causes the constant threshold to be passed earlier or later compared to a filtered wave. The CFD time is calculated as a linear interpolation between the two samples surrounding the threshold crossing. The crossing time will be wrong if the CFD interpolates between two samples on a large voltage fluctuation. A solution is to run the CFD on an NNLS wave or spline interpolated wave that is known to fit the leading edge.

7.4 Transverse-position reconstruction

The transverse position of photons can be reconstructed by comparing the signal distribution as a function of strip number. The transverse position reconstruction becomes more accurate when many pickup conductors share signal above noise [127]. Following this rule, a study is presently underway at University of Chicago to design anodes that maximize signal sharing and minimize channel count while maintaining less than 1 mm spatial resolution.

The position reconstruction performance depends on the geometry, size, and spacing of pickup conductors [6]. If signal is induced on only one pickup conductor, then the position resolution will be determined by the size of that pickup conductor and ones knowledge of the expected transverse size of the charge-cloud image [7]. Having multiple pads with shared signal allows for the triangulation of charge-cloud positions.

The voltage-signal of a pulse may be integrated over time and divided by the termination resistance to produce a quantity related to the induced charge. If the pulse shape is independent of amplitude, as is tested in Figure 7.6, then the integral will be linearly related to the pulse amplitude. This charge-to-pulse-height relation is tested again in Figure 7.11 where deviation from linearity is measured as a residual to a best-fit line.

6. The timing performance also depends on these properties of the pickup.

7. If only one conductor captures signal, and a "signal ratios only" analysis is used, then the uncertainty in position will be roughly the size of the conductor. However, if one measures the transverse size and shape of the image of induced signal from the MCP charge cloud, then the position may be constrained using this prior and the knowledge that other conductors *do not* measure signal.

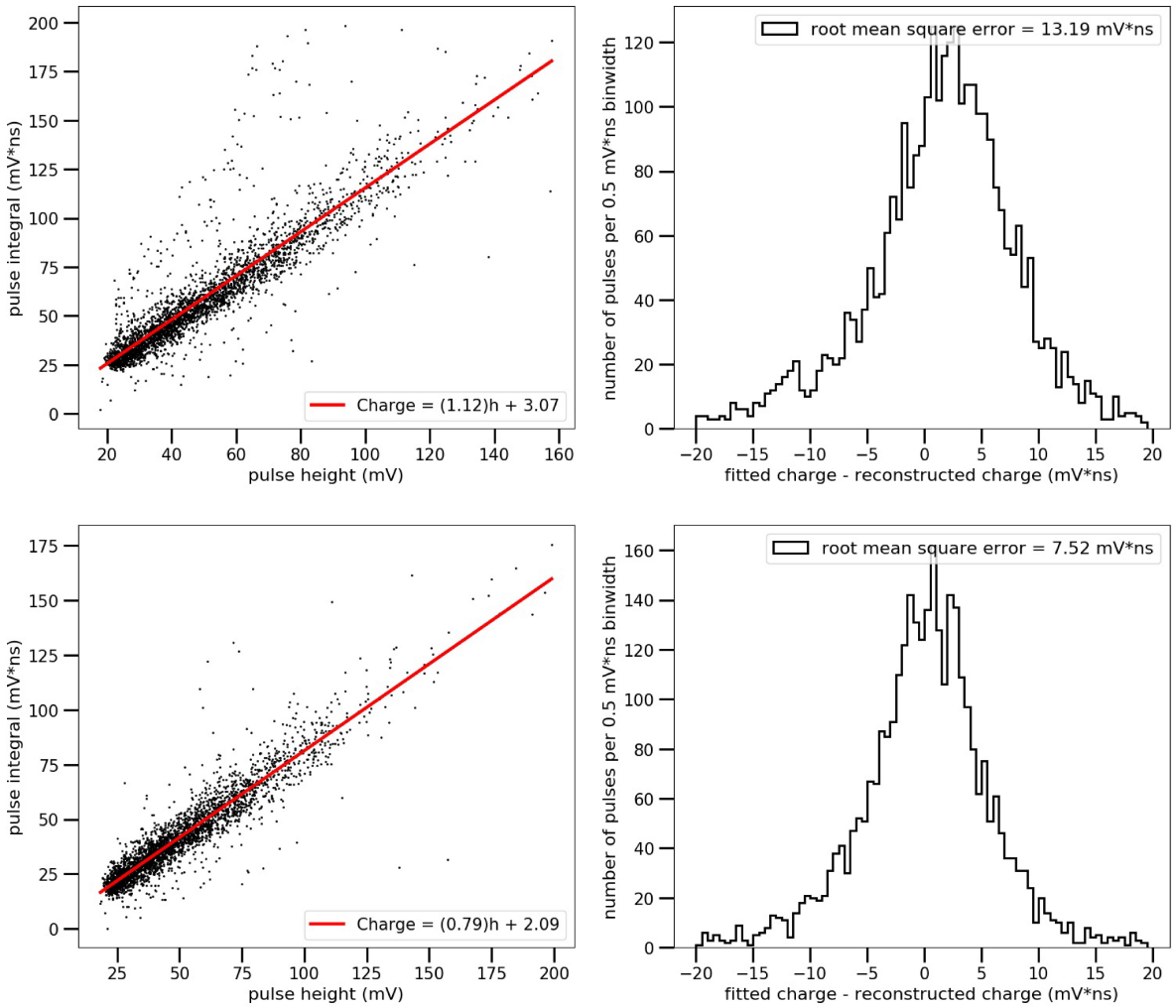

Figure 7.11: The linear relationship between pulse height and pulse integrals for two integration ranges: (top row) the 5 ns interval shown in Figure 7.6 containing the tails of the pulses and (bottom row) from 2 ns before the peak time to when the pulse starts returning to baseline and falls below 90% of its peak value. Residuals indicate a 7-15 mV·ns RMS deviation from linearity.

The two quantities deviate from linear in a significant portion of the data-sample. This could be due to an inaccurate measurement of the baseline of the signal. It may also be attributed to the lack of a voltage-linearity calibration of the electronics, sensitivity to the integration range, the discontinuities in the impedance of the line, or cross-talk between electronics channels as the signals propagate to the digitizer. For the transverse analysis, the integrated signal will be used instead of pulse-height.

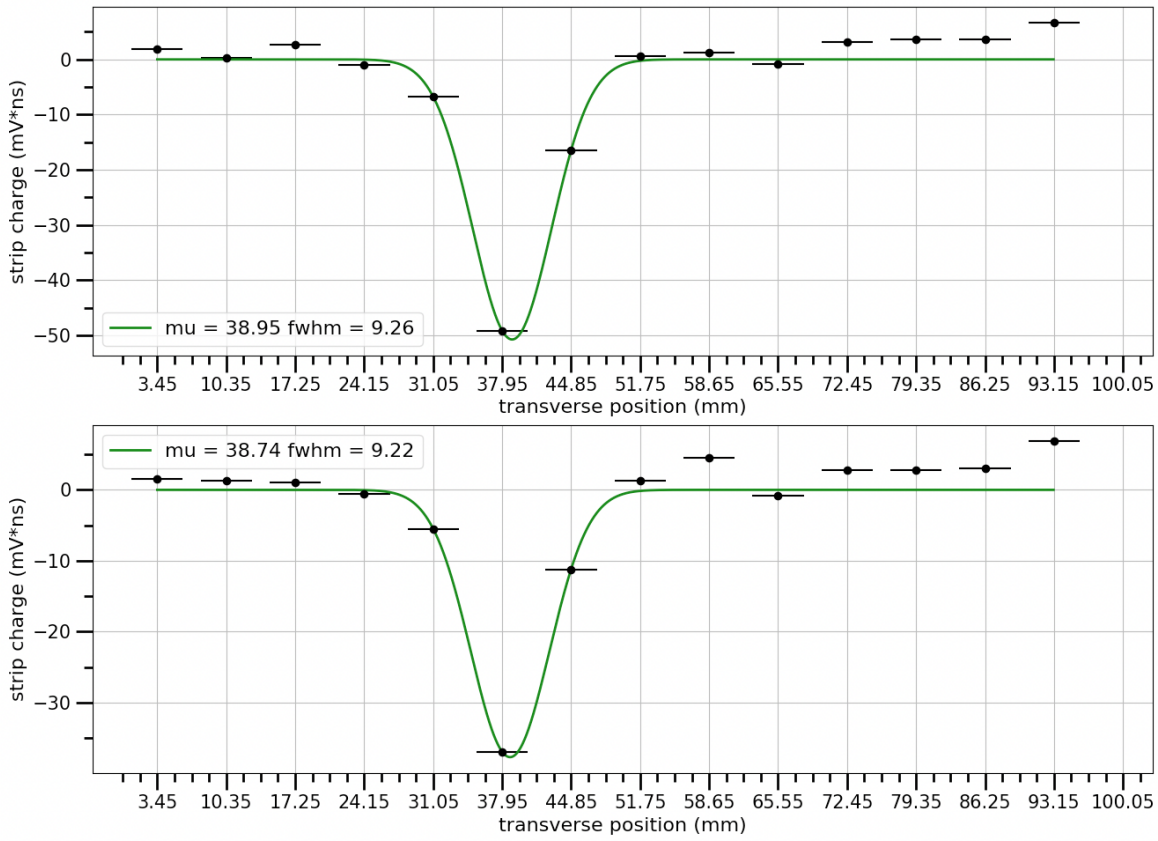

Figure 7.12: An example of the transverse charge distribution for one cosmic ray particle event digitized on half of an LAPPD. The top plot is the right side of the strips and the bottom plot is the left. Each black data point represents the position and charge on each strip-line, integrated over the time of the primary pulse. Strip-widths of 5.13 mm are shown as black horizontal bars. A gaussian is fit to a range that includes 4-5 strips around the peak. Unquantified charge errors are not included in the fit.

An example of charge as a function of strip position is shown in Figure 7.12. The black data points representing strip positions and charges are found using the following analysis steps. The largest-amplitude pulse from the seed-pulse finder is identified. All other channels are integrated in a 2 ns time window around the peak time of the primary pulse. The 2 ns window is informed by the average pulse width and the magnitude of the DLL offsets of the unsynchronized PSEC4 chips (see Appendix B). The charges are plotted with respect to the position of the strip.

The peak of the transverse distribution is identified. An order 3 spline fit about the peak

is used to calculate a first-pass full-width half-maximum (FWHM) measurement. A Gaussian distribution is fit to the data points that lie within 2 FWHMs of the peak, usually covering 4-5 strips. The mean and FWHM are used as the transverse-position and transverse-width of the primary-LAPPD charge cloud.

The cosmic ray dataset # 1 is used to measure the transverse size of the signal image. This dataset has a low threshold for trigger Level 0, resulting in a broad acceptance but many triggers on electronics noise. Of the 50,000 events, 25,000 have at least one pulse with amplitude passing a -20 mV software threshold. Events are rejected if the peak in the transverse signal spectrum is within one strip of the edge of the digitized region. Events are rejected if there is exists no local minimum in the transverse signal spectrum that passes a -20 mV·ns threshold. Events that have a fitting error, with a gaussian fit residual of larger than 140 mV·ns or FWHM of less than a strip width, occur occasionally and are rejected. The remaining sample is about 24,000 events.

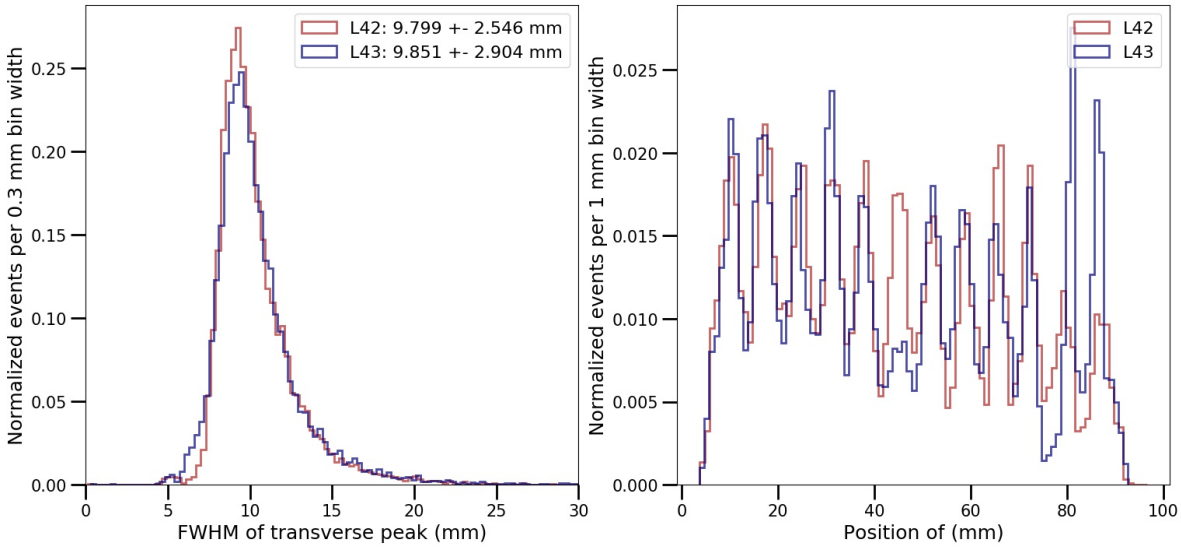

Figure 7.13: Left: the transverse FWHM distribution for 24,000 events from dataset # 1 with LAPPD 43 and 42. The distributions have been normalized for comparison. The width of the distribution quoted in the legend is the standard deviation. Right: the mean of the Gaussian fit to the transverse-charge profile. The peaks of this distribution, due to a threshold effect described in the main text, are located at the center of each strip.

The transverse position and FWHM of the resulting data sample are plotted in Figure 7.13 for half of LAPPD 43 and 42. The result is roughly 9.8 mm FWHM with a standard deviation of 2.5 - 2.9 mm.

The reconstructed positions are heavily peaked, with higher number of events reconstructed at the center positions of each strip. This effect is due to the constant threshold used to identify local minima in the transverse charge distribution. Qualitatively, if a charge cloud is positioned in between two strips, the signal is shared equally thereby reducing the amplitude on each strip; if a charge cloud is positioned in the center of a strip, the amplitude is highest with some smaller portion shared with nearest neighbors.

A test was made where this threshold was increased from 20 mV to 80 mV, which increased the ratio of peak to valley in the normalized distributions by about a factor of 2. Note that this same bias towards events centered on the strip lines will be present when using high thresholds for Level 0 trigger in the front-end electronics. A few channels of the digitizing electronics are ignored in Level 0 for this dataset (see Section 6.1, leading to the missing event populations on LAPPD 43 at 45 mm and 78 mm.

The "charge centroid" method may also be used to reconstruct the position of the signal image. The reconstruction equation is identical to the equation for center-of-mass. If strip-line i at transverse position y_i captures charge q_i, then the charge centroid reconstruction method predicts a photon position of

$$y_{\text{reco}} = \frac{1}{\sum_i q_i} \sum_i q_i y_i \tag{7.1}$$

If a secondary excess exists in the transverse amplitude profile, the centroid will be biased on one side of the primary pulse. To avoid this bias, only strips less than 2 FWHM away from the peak location are included in the centroid calculation. This is the same range over which the Gaussian is fitted. The results of the two methods, which agree to about 1.1 mm, are compared in Figure 7.12.

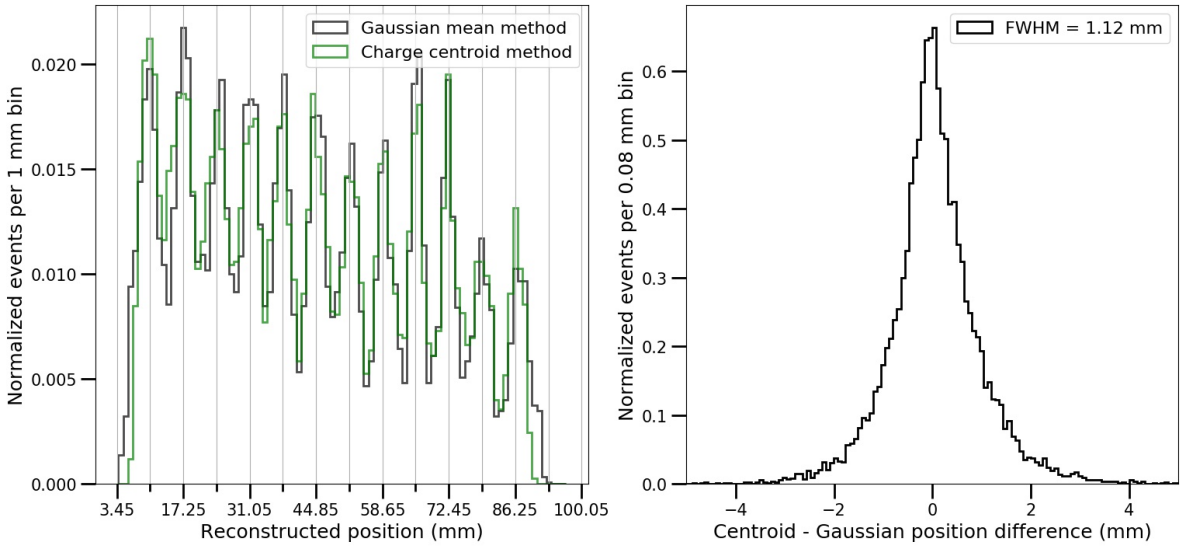

Figure 7.14: A comparison between the Gaussian fit and charge centroid position reconstruction methods. Strip positions are shown as vertical lines. On the right, the positions for the filtered data-set are shown for both methods. On the left, the event-by-event position difference between the two methods show that they agree to about 1.1 mm.

7.5 Longitudinal-position reconstruction

The longitudinal position reconstruction with a strip-line readout uses the time-of-arrival difference of pulses at either end of the strip, along with a knowledge of the propagation velocity. The implementation depends on whether the readout is digitized on both sides or the strips are open-ended.

The longitudinal position resolution is closely coupled to the timing resolution of the electronics and the analysis method used to identify the leading edges of the pulses. As is mentioned in Chapter 5, many active electronics channels were not calibrated for the datasets used here. The most relevant consequence is a constant relative-timing offset between any two PSEC4 chips. This enters as an offset in the longitudinal position when two sides of the same strip are measured by different chips (see Figure 6.2 for a detailed chip-to-strip mapping). The open-ended readout configuration does not require chip-to-chip offset calibration, as the prompt and reflected pulse is measured by the same electronics channel.

An analysis procedure for reconstructing the time differences of pulses on open-ended strips is provided in Reference [99], using a combination of a peak finding algorithm and an auto-correlation with time-lag. This reconstruction was not re-implemented in the present thesis work, as most of the particle data was digitized using the single-ended readout configuration or strips with unextended open ends.

The same filtered dataset from the transverse reconstruction section is used for the longitudinal reconstruction. The analysis starts by identifying the largest pulse in the event. Only one strip and one pair of pulses is needed to reconstruct the longitudinal position; however, additional strips that share charge from the same pulse provide additional information. The two direct neighbors of the primary strip are searched for pulses passing the first iteration pulse-finder that have arrival times within a 6 ns time window about the primary pulse. A pulse must exist on both ends of the strip, identifying a list of pairs. The maximum delay time generated by 108 mm of strip-length is roughly 1-1.5 ns depending on propagation velocity [8]. If for some reason a pulse pair is identified as having delay time longer than 4 ns, the pair is ignored. The event is rejected if no pulse pairs are identified.

The dominant cut comes from the requirement that pulses have a sibling on the other end of the strip that passes a -20 mV threshold. Approximately 18,000 events remain from the original set of 25,000. When pulse pairs are identified, the time delays are calculated using the 10%-of-max CFD arrival time of each pulse.

An example of the constant chip-to-chip timing offset that appears in the longitudinal reconstruction is shown for one strip in Figure 7.15. Over all strips, the maximum pulse pair time-of-arrival difference is 1.1 $\pm$ 0.1 ns, leading to an implied propagation velocity of 0.59 - 0.72 c. This is in rough agreement with the velocity of 0.57 $\pm$ 0.07 c of Reference [74].

The measurement of propagation velocity presented here is rough, having dependence on binning of longitudinal distributions as well as strip lengths that have not been directly

8. The relevant strip length is the length that has access to the MCP charge clouds. This is the inner dimension of the vacuum packaging, or 8.46 " = 215 mm.

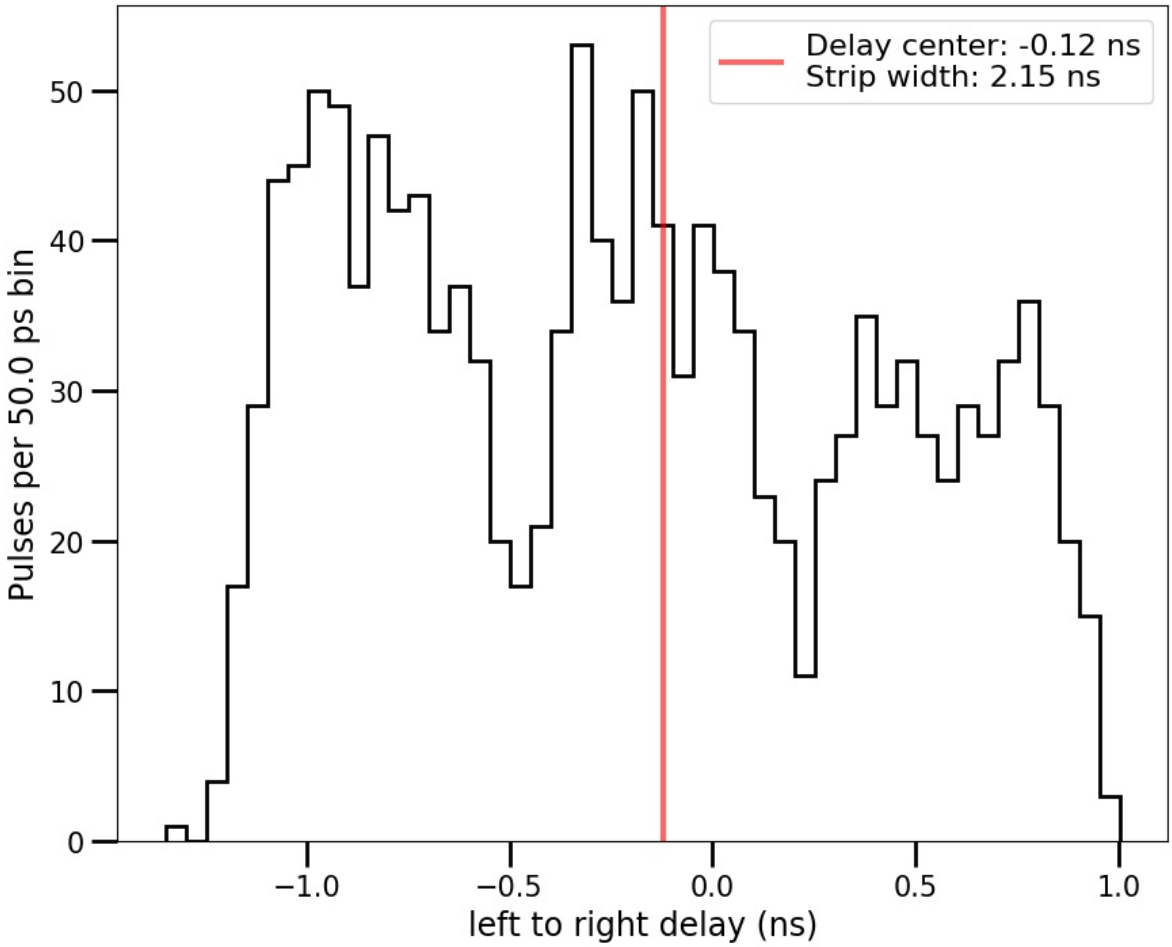

Figure 7.15: The pulse-pair time-delays for strip number 10 on LAPPD 42 from a uniform flux of cosmic rays from dataset # 1. The dips halfway through the distribution are inactive area occluded by the x-spacer. The bias from symmetry about zero is due to a constant chip-to-chip timing offset of the digitizing channels used on either end of the strip.

measured. Measurements of velocity have been made with a laser test stand and stepper motors with controlled relative positions [74, 8]. An immediate next step is to calibrate strip velocities using a laser test stand, a fast-risetime time-domain-transmission measurement, or a vector network analyzer with port extension.

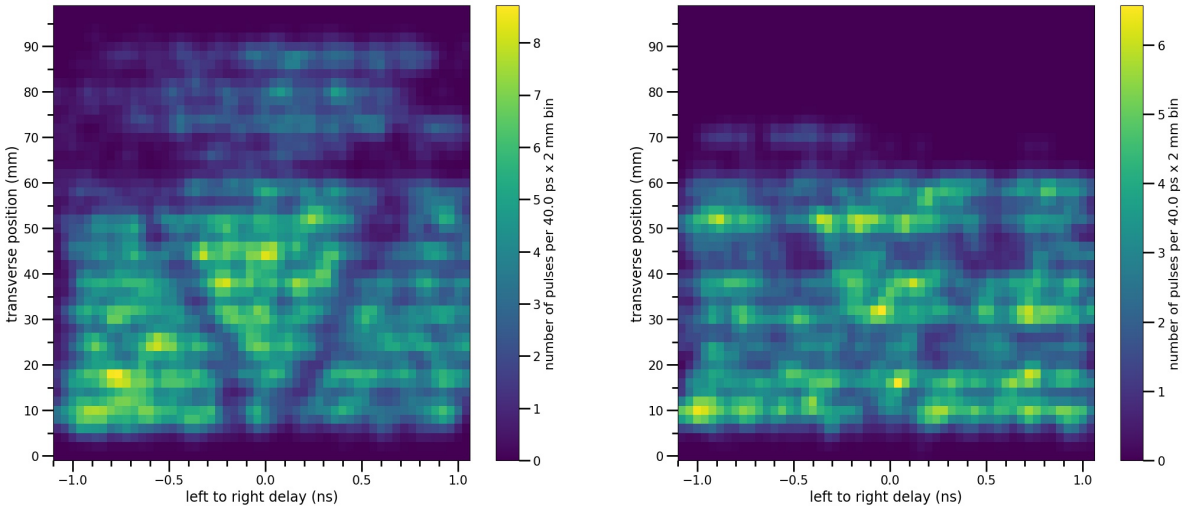

Figure 7.16: A 2-D histogram of reconstructed positions for LAPPD 42 (left) and LAPPD 43 (right), with the longitudinal position in units of delay time. A 0.8 σ gaussian filter has been applied to the image so that the x-spacer feature is more noticeable.

7.5.1 Spatial distribution of cosmic rays

For a full 2D position reconstruction, a transverse and longitudinal reconstruction is performed. The product of the cuts from both analyses results in 6,500 events on LAPPD 42 and 4,300 events on LAPPD 43 from the full original set of 25,000. A 2-D histogram of reconstructed positions for each LAPPD is shown in Figure 7.16. The distribution has three non-uniformities: (1) from the x-spacer which occludes active area, (2) from 5 strips on LAPPD 43 that had faulty connections on one end, and (3) from a channel mask on LAPPD 42 near 60-70 mm transverse position.

For charged particle events, the diameter of the Cherenkov cone at the photocathode is expected to be about 1 cm diameter. The size of the Cherenkov cone is close to the width of the x-spacers. Cherenkov light centered on an x-spacer may still produce photoelectrons that are amplified. This may explain the faintness of the reconstructed x-spacer occlusion in comparison with the sharp edges produced by laser scans.

7.6 Charge spectrum

The total signal induced on the strip-lines is an indication of how many primary electrons were present in the event. With a proper single photoelectron-gain calibration, the number of primary electrons may be precisely estimated. For example, a statistical method that does not rely on fitting peaks in single photoelectron-charge distributions can be found in Reference [128]. This requires an attenuated pulsed-laser environment.

7.6.1 Gain

A careful gain calibration was not performed for LAPPDs 43 and 42 during their time at Fermilab; however, gain was measured and reported by Incom in the test-reports for LAPPDs 43 and 42 for voltage configurations similar to that used in the test-beam.

The high voltage settings are such that the MCPs of LAPPD 43 are biased at -919 and -911 V respectively top and bottom, LAPPD 42 at -908 and -926 V top and bottom. Both cathode gaps are biased at -20 V. From the Incom test-reports, this results in roughly 1.5 $\times 10^6$ and 2.5 $\times 10^6$ gain for LAPPDs 43 and 42 respectively.

One major difference between these LAPPDs is that LAPPD 43 has about two-times higher quantum efficiency (QE) than LAPPD 42. The mean QE is 28% and 14% for LAPPDs 43 and 42 respectively. As seen above, LAPPD 42 has about two-times higher gain than LAPPD 43. The pulse-heights and integrated charges are expected to be similar in magnitude for both of these LAPPDs.

For the maximum photocathode and MCP voltages recommended by Incom, the gain for LAPPDs 43 and 42 goes to 4.2 $\times 10^6$ and 1.2 $\times 10^7$ respectively. The maximum MCP biases recommended by Incom are close to those used in the test-beam, differing by 25-40 V. The photocathode bias, however, was forced to be lower than 60-80 V by the high voltage instabilities observed and described in Section 4.3.1. This has the effect of lowering the gain and degrading the timing resolution.

7.6.2 Spectra

A time-independent charge analysis was performed for events from datasets # 3 and # 4. Signals are induced by 120 GeV/c protons in the MT6.2 enclosure using LAPPDs 43 and 42. The entire event window of every channel is fully integrated if it contains a voltage signal with magnitude less than -5 mV. The NNLS waveforms are used instead of raw waveforms.

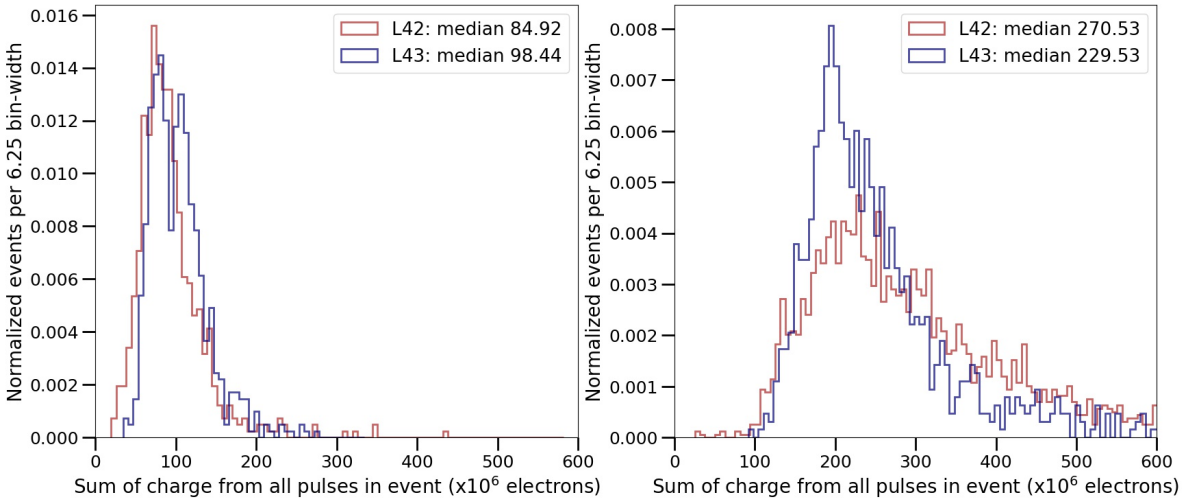

Figure 7.17: Charge distributions for LAPPDs 43 and 42 with 0 V (left) and -20 V (right) applied to the photocathode gap. The signal source is 120 GeV/c protons from datasets # 3 and # 4.

When the photocathode gaps are biased at 0 V, events are observed in coincidence with the FTBF beam spills. Front-end electronics thresholds are -30 mV and no triggers occur in between beam spills. An apples-to-apples comparison with -20 V on the photocathode gaps is shown in Figure 7.17.

A number of previous experiments have observed signals in MCP-PMTs with reverse-biased photocathode gaps or even no photocathode metals at all. [129, 130, 131, 132]. It may be that primary electrons are born out of ionization interactions of the high energy particle with the glass of the MCP or window. When the cathode is biased to detect photons, the total charge represents the sum of charge created by photons and charge created by other mechanisms like ionization.

7.7 Coincident particle events

As is described in Section 7.1, the only time-of-flight installation with picosecond synchronization was cut short during the trigger-tuning stage of the run plan. These trigger-tuning data-sets do not have sufficient statistics of simultaneous triggering on the same particle between multiple LAPPD stations to measure timing resolution or distinguish particles by particle type. The run may continue where it left off before the shutdown, with a timing resolution measurement from cosmic rays and mass measurement from the test-beam.

CHAPTER 8

ESTIMATE OF THE PARTICLE IDENTIFICATION SENSITIVITY

8.1 Qualities of the present setup

The sensitivity to particles of known momentum may be estimated using the electronics characterizations performed in this thesis and the single-photon timing-resolution measurements made in laser test stands. Let the time-of-arrival uncertainty of a particle at a single detector be

$$\sigma = \sqrt{(\sigma_L/\sqrt{N_{\text{pe}}})^2 + \sigma_{\text{elec}}^2} \tag{8.1}$$

where σ_L is the single photoelectron transit-time spread of the LAPPD, N_{pe} is the number of photoelectrons, and σ_{elec} is the uncertainty in the identification of the pulse time-of-arrival relative to the synchronizing wave. Note that this formula is assuming the $1/\sqrt{N_{\text{pe}}}$ behavior commonly used for PMTs which assumes that a normally distributed set of electron transit times dominates the timing resolution. This scaling behavior may be stronger if the pore size is significantly reduced and the timing resolution is dominated by the spread in arrival times of the first photoelectron at the top MCP (see Appendix F).

The expansion of σ_{elec} includes

$$\sigma_{\text{elec}}^2 = \sigma_{250\text{ MHz}}^2 + \sigma_{\text{pulse}}^2 + \sigma_{\text{analysis}}^2 \tag{8.2}$$

where $\sigma_{250\text{ MHz}}$ is the channel-to-channel timing uncertainty on the reconstruction of the 250 MHz synchronization phase, σ_{pulse} is the channel-to-channel timing uncertainty on the

arrival time of MCP pulses, and σ_{analysis} is the contribution due to inaccuracies in the arrival time due to the waveform-analysis procedure. The analysis term is unmeasured here and is assumed to be small compared to the other uncertainties.

The uncertainty in the time-of-arrival difference between two detectors may be written as

$$\sigma_{\text{tof}} = \sqrt{\sigma_{L1}^2 + \sigma_{L2}^2 + \sigma_{\text{WR}}^2} \tag{8.3}$$

where σ_{WR} is the phase jitter of the multiple White Rabbit ZEN modules due to the synchronization methods of the White Rabbit Switch.

Generation-I Incom Inc. LAPPDs with 20 micron pores are being characterized using pulsed lasers as having transit-time spreads of 55-65 ps on single photoelectrons [5, 29][1]. About 20 - 30 photoelectrons are expected per particle for the LAPPDs used in this thesis, reducing the single photoelectron timing uncertainty by a factor of 5.5 to 11 ps using $\sqrt{N_{\text{pe}}}$ scaling. With the use of a fused silica window that transmits the ultra-violet component of Cherenkov light, $\sqrt{N_{\text{pe}}} \simeq 10$. The resulting timing resolutions become comparable with the electronics-associated timing uncertainties.

The LAPPD TOF system tested in this thesis uses a synchronization system described in Chapter 5. The timing jitter due to phase measurement of the 250 MHz WR waves, $\sigma_{250\text{ MHz}}$, has been measured to be 3-5 ps (see Appendix B). In Reference [99], the time-of-arrival uncertainty for MCP pulses, σ_{pulse}, is measured to be about 6-8 ps. In Section 5.1.5, the timing uncertainty associated with the distributed White Rabbit modules is measured in quadrature with the timing response of a high-bandwidth Tektronix oscilloscope. The

1. In these measurements, a 405 nm laser with 40 ps FWHM is reduced to produce occupancies of less than 1 single photoelectron per pulse.

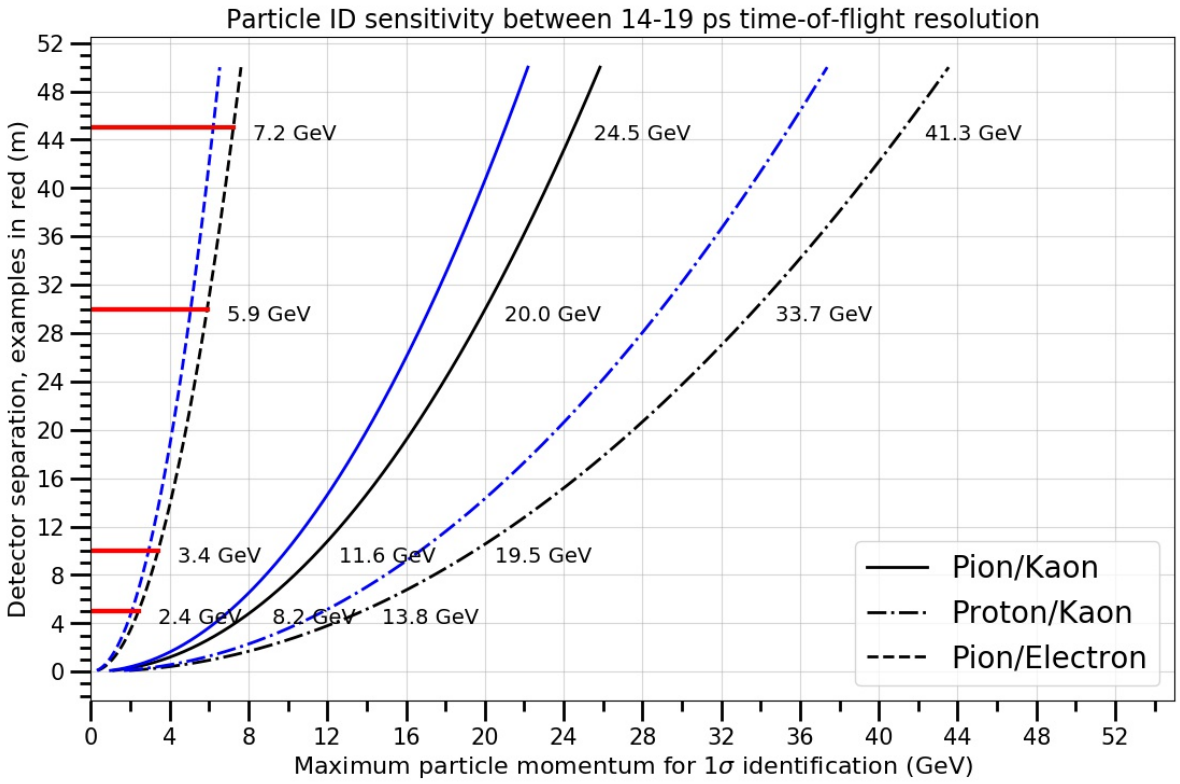

Figure 8.1: The contours of maximum momentum where 68.27% of particles are correctly identified for 14 ps and 19 ps time-of-flight resolution. The LAPPD TOF system at present has a maximum detector separation of 5 m. A proposed permanent system could have separations of 5, 10, 30, and 45 m. These distances are pointed out in red with maximum momentum annotated for each detector separation. The momentum of the pion and kaon is the same, and the momentum and path length is perfectly known.

oscilloscope timing resolution is not measured independently and may be comparable or dominant in the measurement of the White Rabbit timing. The quadrature sum of the oscilloscope timing uncertainty and the White Rabbit synchronization jitter is about 5 ps. It is likely that only the White Rabbit component, σ_{WR}, is lower than 5 ps; the timing used in the following calculations will be 5 ps as a worst case scenario that is still sub-dominant compared to the present LAPPD timing uncertainty.

Using the following quantities in picoseconds, $\sigma_L = 55$, $\sigma_{250\ \mathrm{MHz}} = 4.0$, $\sigma_{\mathrm{pulse}} = 7.0$, $\sigma_{\mathrm{WR}} = 5.0$, a single detector timing resolution of $\sigma \simeq 13$ ps and a two detector resolution of $\sigma_{\mathrm{tof}} \simeq 19$ ps results from 30 photoelectrons. With 200 photoelectrons, the uncertainties

reduce to 8.8 ps and 14 ps respectively.

Assuming that the measured particle-arrival times at the detectors are Gaussian distributed, the ability of the time-of-flight system to distinguish pions and kaons can be calculated using the kinematics for a two detector system described in Section 1.2.1. This is shown in Figure 8.1 for a 14 - 19 ps σ_{tof} and perfectly known momenta and path lengths.

The LAPPD TOF system of this thesis is specifically designed to become a permanent TOF system at the FTBF. In Appendix A, an outline is presented that summarizes the next steps toward a permanent system. In particular, a layout of LAPPD stations is suggested, leading to LAPPD separation distances of about 5, 10, 30, and 45 m. These separations are called out on Figure 8.1. The system as installed in the present day with 5 m separation may be able to distinguish pions and kaons up to 8.2 GeV/c momentum, and a permanent system as proposed could distinguish up to 24.5 GeV/c if 200 photoelectrons are collected.

8.2 Improvements to time-of-flight sensitivity in the next 1 - 5 years

	$\sigma_L/\sqrt{N_{\text{pe}}}$	σ_{pulse}	σ_{WR}	σ_{tof}	Maximum π/K momentum at 5 m / 45 m
Present installation	55 ps / $\sqrt{30}$	7 ps	5 ps	19 ps	7.0 / 21 GeV/c
Use of fused silica window	55 ps / $\sqrt{200}$	7 ps	5 ps	14 ps	8.2 / 25 GeV/c
Low-jitter WR-ZEN	55 ps / $\sqrt{200}$	7 ps	< 0.5 ps	13 ps	8.5 / 25 GeV/c
10 μm pores and higher cathode voltages	10 ps / $\sqrt{200}$	7 ps	< 0.5 ps	11 ps	9.2 / 28 GeV/c
PSEC4 chip development	10 ps / $\sqrt{200}$	1 ps	< 0.5 ps	1.7 ps	24 / 70 GeV/c

Table 8.1: Summary of some improvements to the elements of the time-of-flight system and the effects on maximum momentum to distinguish pions and kaons at 1-sigma.

The three most dominant and independent quantities that determine the overall time-of-flight sensitivity of the system are $\sigma_L/\sqrt{N_{\text{pe}}}$, σ_{pulse}, and σ_{WR}. There are known improve-

ments that may be implemented over the next 1 to 5 years, summarized in Table 8.1.

One of the dominating timing terms, $\sigma_L/\sqrt{N_{\rm pe}}$, may be significantly improved by changing design aspects of the LAPPDs. The largest contributor to σ_L comes from the variation in transit times of electrons inside of the MCP pores during amplification [30, 31, 32]. Decreasing the pore diameter from 20 μm to 10 μm has been shown to improve transit-time spreads to closer to 10-20 ps. The company Incom Inc is developing 10 μm pore LAPPDs. Other design factors contributing to this intrinsic time spread include the distances between the gaps in the vacuum volume, the bias voltage of the photocathode-to-top-MCP gap, and the secondary emission yield of the first photoelectron. One improvement, yet to be developed, is to deposit the photocathode directly on the top surfaces and edges of the MCP pores [133, 134].

Increasing the number of photoelectrons per particle to 200 per cm by changing the window material to fused silica further decreases the timing uncertainties associated with the detector. The scaling may be stronger than $\sqrt{N_{\rm pe}}$, as is suggested in Appendix F for small-diameter MCP pores. This, in combination with small pores, makes the detector timing uncertainties sub-dominant.

The industry of relative-timing synchronization is mature, offering multiple avenues for sub-picosecond relative synchronization. For example, the White Rabbit Switch used in the present system is a "low-jitter" model from SevenSolutions, designed for sub-picosecond synchronization. The White Rabbit ZEN modules of the present setup, on the other hand, are not part of the "low-jitter" series. A representative from SevenSolutions has suggested that low-jitter ZEN modules may be requested and produced on the time-scales of 6 - 12 month turnaround [135]. The matched low-jitter models would likely improve timing to be less than 1 ps.

CHAPTER 9

SUMMARY

A time-of-flight (TOF) system using Large Area Picosecond Photodetectors (LAPPDs) was constructed and operated for a short time at the Fermilab Test Beam Facility (FTBF). The system has the ability to perform time-of-flight measurements over adjustable separations between 1 - 5 m using up to five LAPPDs in three stations.

A permanent LAPPD TOF system at the FTBF would represent an order of magnitude improvement in timing, acceptance, and ease-of-use relative to the present TOF systems, having long-term impact on the development of instrumentation in particle physics, nuclear physics, material physics, medical physics, and national security. In addition to providing information on particle mass to FTBF users, the use of LAPPDs on a regular basis will fully characterize their detection of charged particles and test their robustness to long-term use in a particle-physics environment.

The following steps were taken during this thesis work to advance the goal of a permanent system at the FTBF: the first use of up to 120 channels of 10.24 GSPS fast sampling PSEC4 electronics to digitize multiple LAPPDs simultaneously; the first direct detection of charged particles with LAPPDs using Cherenkov light in the window; the first implementation of picosecond synchronization of multiple LAPPD stations that may be separated by up to 300 m; the design and construction of low footprint LAPPD TOF stations; the development of safe procedures for high voltage distribution; a draft of an off-line LAPPD particle reconstruction code; the development of software for controlling front-end electronics; the identification of major improvements to firmware for higher efficiency operation.

Following the installation of a small prototype outside of the MTest beam-dump, all of the hardware and system elements listed above were combined into the three-station TOF system presently installed in the MT6.2 enclosure. The run plan for the MT6.2 setup included one week of tuning the trigger, optimizing on efficiency of coincident triggers between multiple

LAPPD stations; one week of measuring timing resolution of LAPPDs 43, 42, 51, and Tile 31 by placing LAPPDs in close succession, 5 cm apart, and measuring the relative-arrival times of a focused beam of 120 GeV/c protons; and one week of distinguishing pions and kaons at a variety of beam energies using the natural contamination of kaons in the low-energy pion beam modes of MTest.

The coronavirus outbreak lead to this run plan being cut short. During the trigger-tuning stage it became clear that the lab was being shut down. The three night shifts before shut-down resulted in the datasets # 3 and 4 in Chapter 7 and provided input for the next stage of the run. The latter two weeks of the run may be continued and carried out as soon as beam returns to the FTBF. The timing-resolution measurement may be performed using cosmic rays before the return of beam. There are a number of proposed next steps following the operation of the present system, in particular a next-iteration system is proposed and described in Appendix A.

In addition to the construction of the LAPPD TOF system, a prototype batch fabrication process for LAPPDs was developed as described in Chapter 2 and Reference [46]. One of the LAPPDs tested at Fermilab, Tile 31, was fabricated using this batch production process. Major challenges that have been overcome during this thesis include hermetically sealing an 88 cm perimeter interface between glass and ceramic using a low temperature indium solder alloy and forming a photo-sensitive layer with ~3 % quantum efficiency by evaporative transport of cesium to a pre-deposited antimony layer.

An estimate of 14 - 19 ps for the LAPPD timing resolution provided in Section 8 suggests a 1σ pion-kaon separation up to 7 - 8.2 GeV/c momentum for the 5 m separation distance of the present system. The proposed separation distances for the permanent system of 10 m and 45 m increases this momentum boundary to 24.5 GeV/c. A number of design improvements over the next five years are estimated to increase the maximum distinguishable momentum up to 70 GeV/c, as is outlined in Section 8.

APPENDIX A

NEXT STEPS TOWARD A PERMANENT LAPPD-BASED TOF PID SYSTEM AT THE FTBF

A permanent LAPPD time-of-flight system at the Fermilab Test Beam Facility (FTBF) has been proposed with the goals of taking a step toward broader familiarity with LAPPD technology in the particle physics community, exploration of LAPPD timing resolution in a working setting, and improved particle identification for users at the FTBF [136]. This is a multi-institutional effort with support from key personnel at Fermilab, University of Chicago, and Incom Inc. This Appendix describes the design elements and operation of a permanent LAPPD time-of-flight system. A plan that builds upon the presently installed system is presented.

A.1 Present particle identification systems at the FTBF

There are two non-LAPPD based systems that attempt to measure particle mass at the Fermilab Test-Beam Facility (FTBF): gas-filled Cherenkov detectors and a PMT-based time-of-flight system.

The gas-Cherenkov system consists of two 12.3 m and 13.1 m long pressure vessels of 30.5 cm diameter just upstream of the MTest beam enclosure [137, 138]. The pressure of N_2 or C_4F_8O gas in each chamber is modulated and measured. When the pressure rises high enough such that the index of refraction breaches the Cherenkov threshold $\beta = 1/n$, light is emitted by beam particles. That light is directed towards PMTs using mirrors with a precisely tuned angle. Particles of different mass are separated by the momentum at which they pass through Cherenkov threshold. These thresholds, as well as minima and maxima in the momentum for separation, are a function of the chamber pressures, gas composition, and other configurations [138].

In 2018, a PMT-based time-of-flight system was tested and installed, demonstrating mass separation that may distinguish protons from lighter particles up to about 8 GeV/c. Photographs and details of this PMT-based TOF system may be found in Reference [139]. In each time-of-flight stations, four PMTs are attached to a 20 mm thick scintillator. Stations are separated by up to 84 meters. The overall TOF timing resolution is measured to be on the order of 200 ps in the best case scenario.

Unfortunately, the electronics for the PMT-based TOF detectors cannot be operated as of the year 2020, as they were configured and operated by an expert, Anatoly Ronzhin, who has sadly passed away [129, 140]. Instead, the Cherenkov detectors are more extensively used. For example, beam particle composition as a function of energy and beam mode has been carried out by these chambers, found at Reference [141].

Some advantages of an LAPPD-based TOF system include precision timing resolution on the order of 5-10 picoseconds for reconstructing high momentum particles, millimeter-scale position resolution for precision path-length reconstruction, a small TOF station footprint, and large area for full beam acceptance. Estimates of the maximum pion and kaon separation sensitivity are presented in Section 8. In principle, the LAPPD stations may be low maintenance once commissioned for long-term operation.

The radiation length of each LAPPD in the present design may be considered non-negligible to some test-beam users (see Appendix C). Stations of LAPPD may be placed on motion tables so that they can be inserted upon request. The station footprint is small such that motion tables may not be required when there is time allotted for the manual extraction of the LAPPDs.

A.2 The design of a permanent LAPPD TOF system at MTest

A permanent LAPPD TOF system at MTest consists of four LAPPD stations placed throughout the facility. An example is shown in Figure A.1. The redundancy of four LAPPD stations

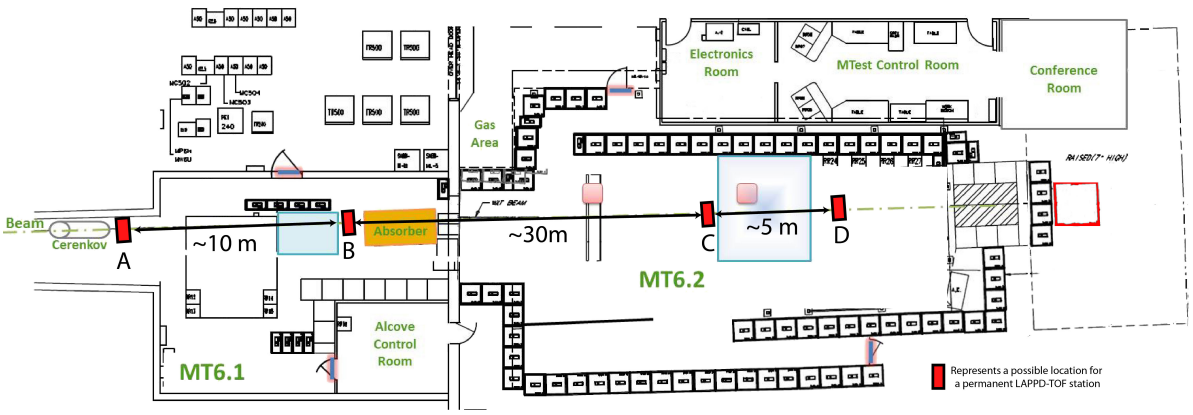

Figure A.1: The top-down layout of MTest with four possible locations for LAPPD stations shown as red rectangles, labeled A, B, C, and D. The stations have a small footprint, mounting to new or existing 80/20 structures in the beam enclosures. The range of LAPPD separations allows for a variety of momentum ranges to be probed. Station placement maximizes coverage for experiments located in the main experimental areas.

provides (1) a failure-buffer such that at least three detectors are operable at all times, (2) full coverage such that any experiment is between a pair of stations, (3) additional constraints on path length using the curvature calculated from three reconstructed positions, and (4) sensitivity to a variety of particle momenta due to the variety of path lengths.

Stations are synchronized at the picosecond level using a single White Rabbit (WR) Switch module located in the electronics room (see Section 5.1.5) [93]. This WR-Switch synchronizes WR-ZEN [94] modules over 1 km distances using optical fibers. The WR-ZEN modules located within 5 m of the LAPPD stations distribute synchronization signals to front-end electronics using high-fidelity RF connectors and cables optimized for 250 MHz.

The LAPPDs are interchangeable from station to station, with each station equipped with identical electronics and mounting infrastructure. Ideally, each LAPPD has the same make and model, with a preference towards the Generation-II capacitively-coupled LAPPDs due to the flexibility of the readout pattern. Each station has room for two LAPPDs to be placed in close proximity for calibration.

Stations have the ability to be easily removed from the beam path upon request from users so that measurements are not affected by interactions in the LAPPD material. One

option is to use either horizontal or vertical motion tables; however, this may increase the footprint of each station. Another option is to design the station fixturing and cabling hardware to be easily removed by hand; for example, mount the stations using sliding 80/20 rails.

A.2.1 Position calibration

The positions of all LAPPDs are precisely calibrated in the three translational dimensions by a short test-beam run with 120 GeV/c protons. Once the LAPPDs have been placed for operation, the beam is configured to have a focused profile of 6 mm diameter provided by 120 GeV/c proton mode. The resulting global position reconstruction of the data-set provides a measurement of the mean relative offset of each LAPPD in the transverse directions with precision equal to the quadrature sum of the LAPPD position resolution and the precision on the center of the beam profile.

The relative separations in the direction parallel to the beam trajectory is measured using the mean time-of-flight. This longitudinal position has an uncertainty equal to the distance-equivalent of the timing resolution summed in quadrature with the distance-equivalent of the momentum spread of the beam. For the 120 GeV/c proton beam mode, the best momentum spread of 2% contributes to a separation uncertainty of less than 1 mm over 45 m.

A.2.2 Analysis and DAQ system

The front-end electronics system is controlled using a single computer located in the MTest control room. This control computer distributes commands over ethernet for data logging and data storage.

An analysis code located on the same computer asynchronously and continuously processes data pulled from each spill. The output of the analysis code is a set of time-of-arrivals relative to a clock that is accessible to user experiments. These time of arrivals allow users

to associate events in their own system with events in the LAPPD TOF system.

Along with each picosecond-level event-time is an estimate of the particle mass and its associated uncertainty. Both quantities are relative to an input momentum which can either be measured by the user experiment, from spectrometers provided by the FTBF, or from calibration data of the particular beam mode being delivered and logged by the Fermilab accelerator control system (ACNET).

A.3 Action-items for the next iteration that have the largest positive impact

A.3.1 Electronics firmware

To achieve greater than one mass-identified particle per FTBF spill with the LAPPD TOF system, the ACDC/ACC firmware needs to be re-designed. The specific nature of these improvements is outlined in Chapter 5.

A.3.2 Trigger improvements

A modification to the architecture of both the ACDC Level 0 and ACC Level 1 triggers will further increase the efficiency of the front-end electronics to events that contain the same particle over multiple LAPPD stations. A knowledge of the trigger states is assumed for this subsection; see Section 6.1.3.

A significant improvement may be made by providing channels with individually configurable Level 0 thresholds. Manufacturing variations exist in the relationship between digital-to-analog converter (DAC) output and true discriminator threshold. This, coupled with the fact that a single DAC output determines the thresholds for all channels on one chip, forces thresholds to be higher than about 50 mV absolute magnitude for a spatially unbiased threshold distribution. However, high thresholds bias the data sample towards

events that land directly on the center of anode pads, as is seen in Figure 7.16.

A solution to the individual threshold problem has been implemented in the next board revision, ACDC rev C. This board has been fabricated and is being tested. The next firmware revision, with features suggested throughout this thesis, will also apply to this board revision.

An additional improvement to the trigger efficiency may be implemented at Level 1 when the ACDC receives a signal from the ACC, indicating that a particle was detected by another coincident detector. In the present system, a Level 1 trigger signal is allowed to arrive at any time from t = 0, the moment of Level 0 crossing, to t = $\tau \simeq 200$ ns, a pre-configured maximum cutoff time. This wide coincidence window increases the probability of having a dark-noise trigger Level 0 and decreases the probability that 2-4 LAPPD stations trigger on the same particle.

One solution is to require the time difference between Level 0 and Level 1 to be within a small, ~ 5 ns window about a pre-calculated expected time difference. The relative time at which each LAPPD station passes Level 0 is known by assuming the particle is moving at the speed of light and calibrating the LAPPD station separation. The delay of the Level 1 trigger from the ACC can be estimated from cable lengths or measured directly. The Level 1 trigger can require all arrival-delays to match that of an expected particle, placing a heavy coincidence constraint on noise triggers. This solution may be implemented in the next firmware revision with no changes to hardware.

A.3.3 Electronics calibration

In this thesis, particle detection analyses were performed with electronics that had not been fully calibrated. The calibration procedure has been practiced, however, and is detailed in Appendix B. It includes a calibration of (1) the linearity of the ADC samples at low input voltages, (2) the relative time offset of each sample due to variable sampling rate, and (3) the constant time delay between the last sample and first sample of each circularly-buffered

event.

These calibration procedures are performed once for each board installed in the LAPPD stations. Without all three of these calibrations, the ability of the LAPPD stations to identify the time of arrival of a particle will be limited to 20 ps [99].

A.3.4 Readout improvements

Having a common readout configuration for each LAPPD station would allow for LAPPDs to be interchangeable between the stations. This uniformity would drastically simplify the analysis code described in Subsection A.2.2, making the code and DAQ system blind to which LAPPD is in which station. It would also result in each channel having the same bandwidth and signal velocity properties used to reconstruct longitudinal position.

The open-ended strip-line readout configuration is preferred due to its low channel count and simplicity. The open ends of the strips would be extended using a PCB that mechanically connects to the strips and adapts the traces to a convenient cable standard. The extension cables would be longer than the total length of the strip so that every photon position produces two pulses that are well separated in time.

This improvement will require a PCB design that considers either a capacitively-coupled LAPPD or a Generation-I LAPPD with strip-lines. In the case of Generation-I, some of the design work is transferable from the ANNIE APB by copying the pogo pin method of connecting to strip ends. Design of a strip-line pattern capacitively-coupled PCB is underway.

A.3.5 Studying response at high spill intensities

Many users of the FTBF request beam intensities in the range of 200k - 1000k particles per spill. If one assumes about 30 photoelectrons per particle as per the calculations in Section 1.3.1, this implies a photo-electron amplification rate of 1.5 - 7.5 MHz divided by the beam area. For a 1 cm diameter beam, this flux is in an operating regime where the gain of the

LAPPDs is reduced due to micro-channel plate recharging dynamics. Furthermore, it has been observed during this thesis that high voltage instabilities may be triggered by the large current increase in the MCPs during the spill (see Subsection 4.3.1).

One solution is to require users to operate at lower intensities if measurements of mass are requested from the LAPPD TOF system. The LAPPDs may be turned off during high-intensity beam operation. Another solution is to reduce the high voltages applied to the MCPs, thereby reducing the gain and increasing the maximum achievable rates of the LAPPDs. The phase space curve of gain and rate limit is important input for experimenters planning on high intensity operation of MCP-PMTs in collider detectors and fixed target experiments. This LAPPD TOF station could be used to study those parameters for the Incom LAPPDs.

APPENDIX B

PSEC4 ELECTRONICS CHARACTERIZATION AND CALIBRATION

As is described in Chapter 5, the PSEC4 chips have the following features that should be calibrated prior to operation in a precision measurement:

1. *Linearity:* the voltage response of the analog-to-digital converter (ADC) to an input voltage, ADC-counts = αV_{in}. This calibration measures α's deviation from constant with respect to V_{in}.

2. *Wraparound offset:* the constant time delay (DLL offset) between the sample-time of the last and first capacitors in the SCA

3. *Time-base:* the consistent deviation of each sample-time from the expected time assuming constant sampling rate

These quantities have also been characterized in Reference [99]. A complementary characterization in agreement with that reference is presented here along with an outlined procedure for each quantity.

Additional qualities of the PSEC4 chips that follow from the calibration procedure are

1. The *aperture-jitter:* the event-to-event jitter of the the sample times

2. The median sampling rate

3. The time-of-arrival jitter between two channels given an identical sine wave input

B.1 Linearity

The voltage on a PSEC4 sampling capacitor is measured by a constant ramp analog-to-digital converter (ADC). The ramp-compare ADC is timed by a fast clock, adjustable between 200

MHz and 1.4 GHz. For this experiment, the clock is set to 1.059 GHz. The ramp-compare reports a number of ADC counts (clock cycles) that may or may not be linearly related to the input voltage

$$N = \alpha(V_{in})V_{in} \tag{B.1}$$

where N is the number of ADC counts, $\alpha(V_{in})$ is the conversion coefficient, and V_{in} is the input voltage.

Eric Oberla's thesis [99] has characterized the linearity in Section A.4. The PSEC4 chips are most linear (α constant) from 200 mV to 1 V. Between the ranges of 0 to 200 mV and 1 to 1.2 V, the non-linearity may be calibrated with the following procedure:

1. Unplug the PSEC4 inputs from external signals. There is a calibration switch on the ACDC boards that may be toggled by the FPGA to disconnect the chip inputs from a detector output

2. Use the on-board digital-to-analog converters (DACs) associated with signal-input pedestals to set a DC input voltage to each channel.

3. At each input voltage from 0 to 1.2V, record 100 - 1000 events of PSEC4 data.

4. Analyze the data, extracting the mean value of N for each sample.

5. Store the mean value of ADC counts for every sample and every input voltage as a lookup-table in the digitization software.

For this thesis work, the linearity calibration was planned for a period of time after the run, where the coronavirus of 2020 interrupted progress. The calibration data presented here, and the datasets in the main body of this thesis, do not contain linearity corrected waveforms. Some effects are observed as a result.

B.2 Wraparound offset and time-base calibration

The constant sampling rate of the PSEC4 chips is set by a servo-locked voltage-controlled delay line (VCDL) acting as a delay-locked loop (DLL) [99]. Due to variations in chip fabrication, the actual sampling time of each sample is not a constant delay from the previous sample.

The 256 samples of the PSEC4 SCA are measured in a circular-buffer topology with a physically-linear VCDL. There is a fixed DLL latency when wrapping around from the 255th to the 0th sample. This latency is longer than the average constant sampling time and may contain some component of a signal waveform. This effect is referred to as the wraparound offset.

The calibration of both the wraparound offset and the time-base may be performed using the same procedure outlined in Reference [142] and implemented here. Given a sine wave input, the voltage measured on sample $V_i = A\sin(2\pi f_{in} t_i + \phi) + P_i$ may be combined with that of another sample j to form an ellipse in the phase space $x \equiv V_i + V_j$, $y \equiv V_j - V_i$. Here A is the amplitude, f_{in} is the frequency, ϕ is the phase, and P_i is a baseline of the input sine wave.

If many events are triggered randomly such that all phases of the input sine wave are sampled, the collection of x and y values will form an ellipse with radii and offsets

$$r_1 = 2A\cos(\pi f_{in}\Delta t_{ij}) \tag{B.2}$$

$$r_2 = 2A\sin(\pi f_{in}\Delta t_{ij}) \tag{B.3}$$

$$x_0 = P_i + P_j \tag{B.4}$$

$$y_0 = P_j - P_i \tag{B.5}$$

$$\tag{B.6}$$

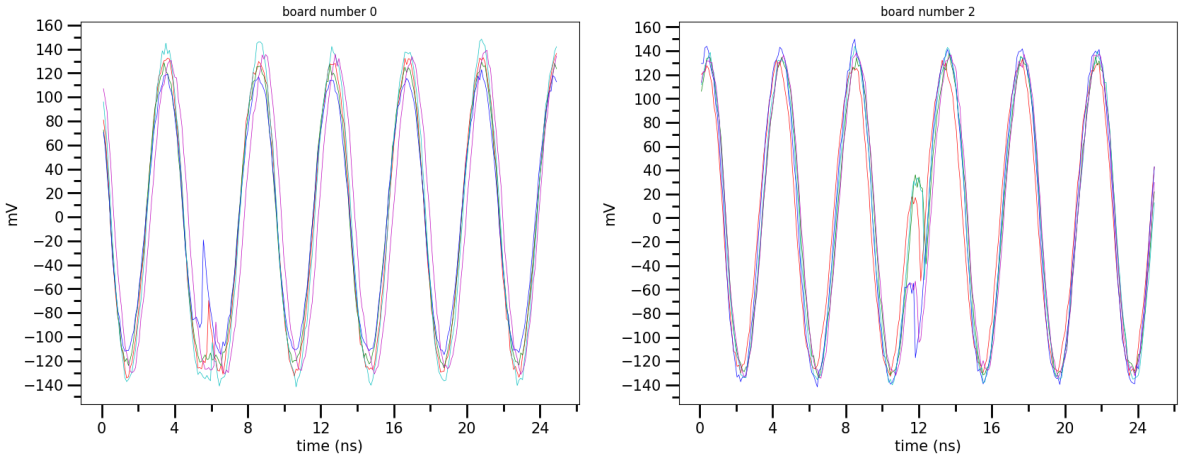

Figure B.1: The waveforms of five calibration channels overlayed for board 0 and board 2. These signals are sourced by a single White Rabbit ZEN module. The trigger location is visible as the region in time where the sine wave deviates. About 30 samples covering the trigger location are ignored for the analysis of this section.

The time delay between two samples Δt_{ij} can be determined independent of the input amplitude and baseline by solving for

$$\Delta t_{ij} = \frac{1}{\pi f_{in}} \arctan\left(r_2/r_1\right) \tag{B.7}$$

An example calibration of the electronics used for this thesis is demonstrated here. A 250 MHz 1.2 Vpp sine wave is input into a PSEC4 channel, shown in Figure B.1. This sine wave is sourced by the White Rabbit ZEN module described in Section 5.1.5. The frequency stability of the input wave is 8.8 kHz (1σ)[1]. These sine waves are digitized using the ACC software trigger. This constrains the 7 corrupt trigger samples described in Chapter 5 to be in the same location relative to the 0th sample (visible in Figure B.1). In this calibration, about 30 samples covering the trigger location were ignored.

Two boards are calibrated, shown as two rows in Figures B.3, B.4, and B.5. The calibration sine waves are sampled 10,000 times, resulting in 10,000 points in the ellipse phase

1. This frequency measurement was characterized independently using a 3.5 GHz Tektronix DPO7354 oscilloscope

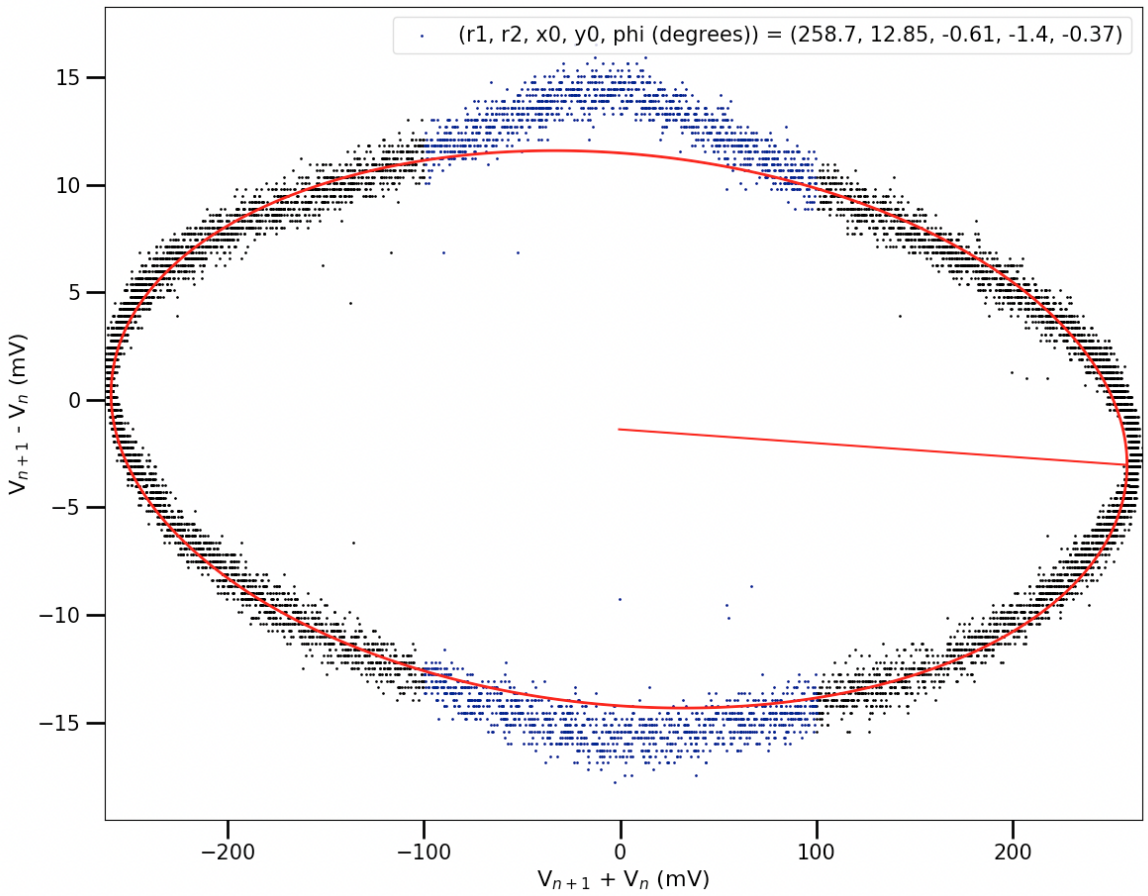

Figure B.2: This ellipse formed by 10,000 events sampled by one adjacent pair of sample indices is a result of the parameterization described in the text. Two visible features of this ellipse are likely due to a lack of linearity calibration described in Section B.1: the peaked cusps at $V_{n+1} + V_n < 100$mV and the slight rotation of the ellipse. The cusp-like samples shown in blue were ignored in the fit. A few data points lie significantly interior to the ellipse, possibly indicating trigger synchronization issues [143]. The fit uses the least-squares method of the python module numpy.linalg.lstsq to fit with arbitrary rotation parameter.

space for each pair of SCA samples. An example ellipse for two adjacent samples is shown in Figure B.2. Two visible features of this ellipse are likely due to a lack of linearity calibration described in Section B.1: the peaked cusps at $V_{n+1} + V_n < 100$mV and the slight rotation of the ellipse. The non-linearity of the PSEC4 chips is greatest at inputs voltages less than 100 mV. Due to time constraints, the linearity is not calibrated in this data sample. Instead, the data with inputs below 100 mV are not included in the fit of the ellipse. The median of

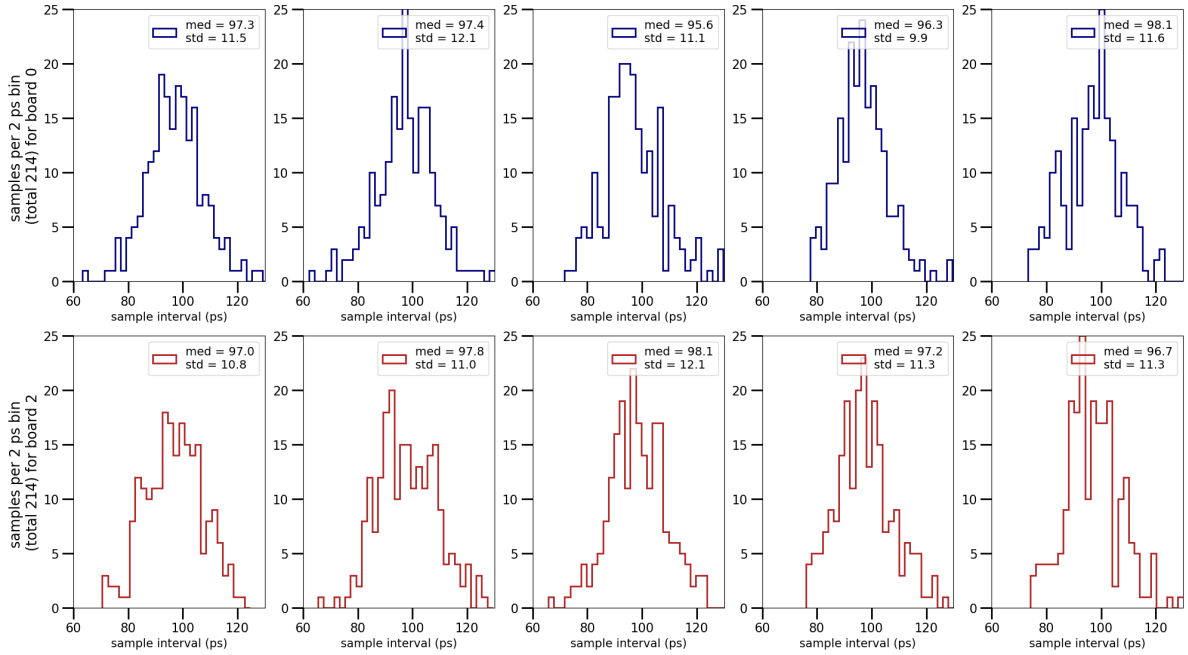

Figure B.3: The n to $n+1$ time delay of 256 samples of five calibration channels (columns) for two boards (rows). The median of these distributions is close to that expected from the nominal constant sampling rate of 10.24 GSPS. The standard deviation represents the spread in the constant deviation from nominal sampling rate.

the angle of rotation for all channels on both boards is about 0.5 - 2.5 mrad with standard deviation 5.4 - 6.8 mrad.

The ellipse is fitted using a least-squares algorithm encapsulated in the python module, numpy.linalg.lstsq. The major and minor radii r_1 and r_2 are calculated from equations parameterizing arbitrary ellipses with rotation found in Reference [144].

The distributions of sample-time-differences are shown in Figure B.3. The standard deviation represents the spread in the constant deviation from nominal sampling rate.

Board #	ch 6	ch 12	ch 18	ch 24	ch 30
0 (ACDC 37)	570.3	574.4	531.7	545.3	479.9
2 (ACDC 20)	604.9	563.5	595.7	601.3	593.2

Table B.1: Wraparound offsets in picoseconds for two boards and five calibration channels. These offsets were measured using the ellipse procedure described in this chapter for 10,000 sine wave inputs.

One special Δt_{ij} is that between the 255th sample and the 0th sample, i.e. the wraparound offset. These offsets are reported in Table B.1 and are around 530 - 605 ps.

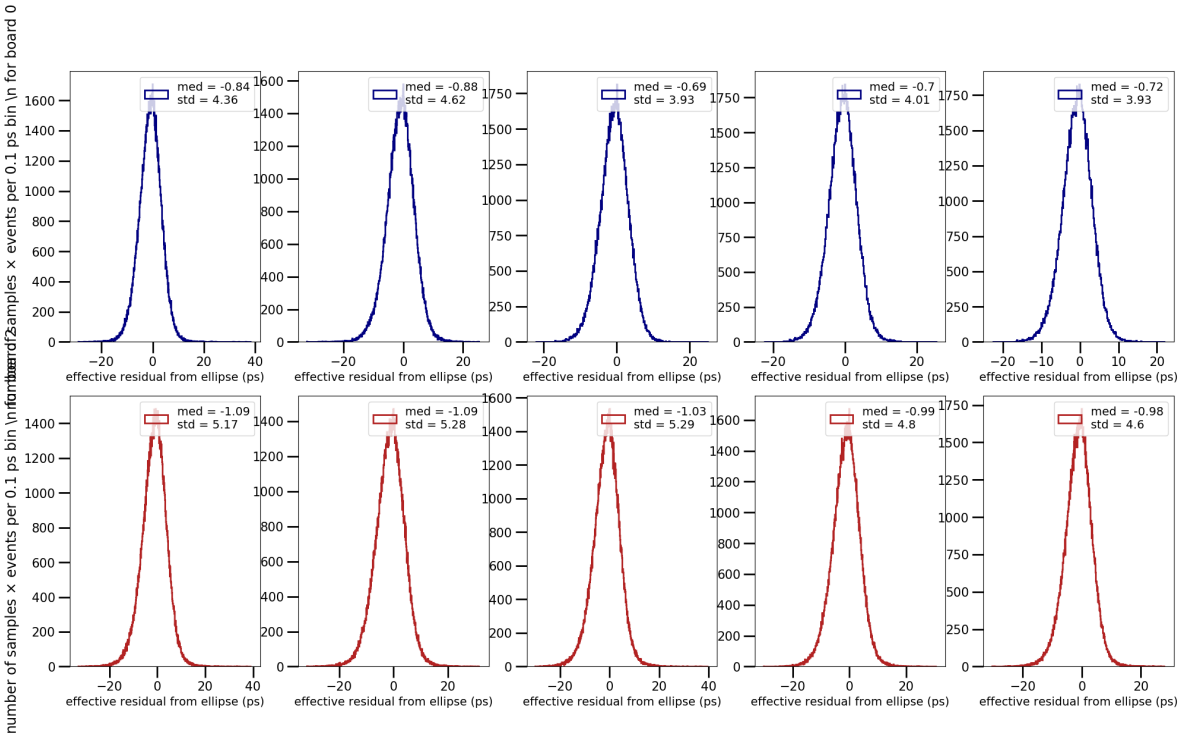

Figure B.4: An estimate of the aperture jitter of the PSEC4 sample times using a re-casting of the residual to the each ellipse.

For a single pair of adjacent samples, each event represents a point lying close to an ellipse. The distance from each data point to the closest point on the best-fit ellipse is calculated as a residual. This residual may related to the aperture jitter of the sample latency. To convert an individual data points' residual value to a unit of timing error, the following formula is used

$$\sigma_{t_{ij}} = \frac{1}{\pi f_{in}} \left[\arctan\left(\frac{r_2 + \sigma_y}{r_1 + \sigma_x}\right) - \arctan\left(\frac{r_2}{r_1}\right) \right] \tag{B.8}$$

where σ_y and σ_x are the signed residuals in the x and y directions, and r_2 and r_1 are the major and minor radii of the ellipse. Looking to Equation B.7, this formula for $\sigma_{t_{ij}}$ can be interpreted as the residual to the sampling interval.

The time-cast residuals shown in Figure B.4 have a standard deviation from 4-5.5 ps and includes 214 sample intervals and 1,000 events per ellipse fit. A consistently negative bias is observed. This could be due to the slight rotation of each ellipse, which places σ_i and r_i on different orthogonal coordinate axes. It could also suggest that the fitting algorithm consistently under fits the radii of the ellipses.

B.3 Relative time-of-arrival jitter between two channels

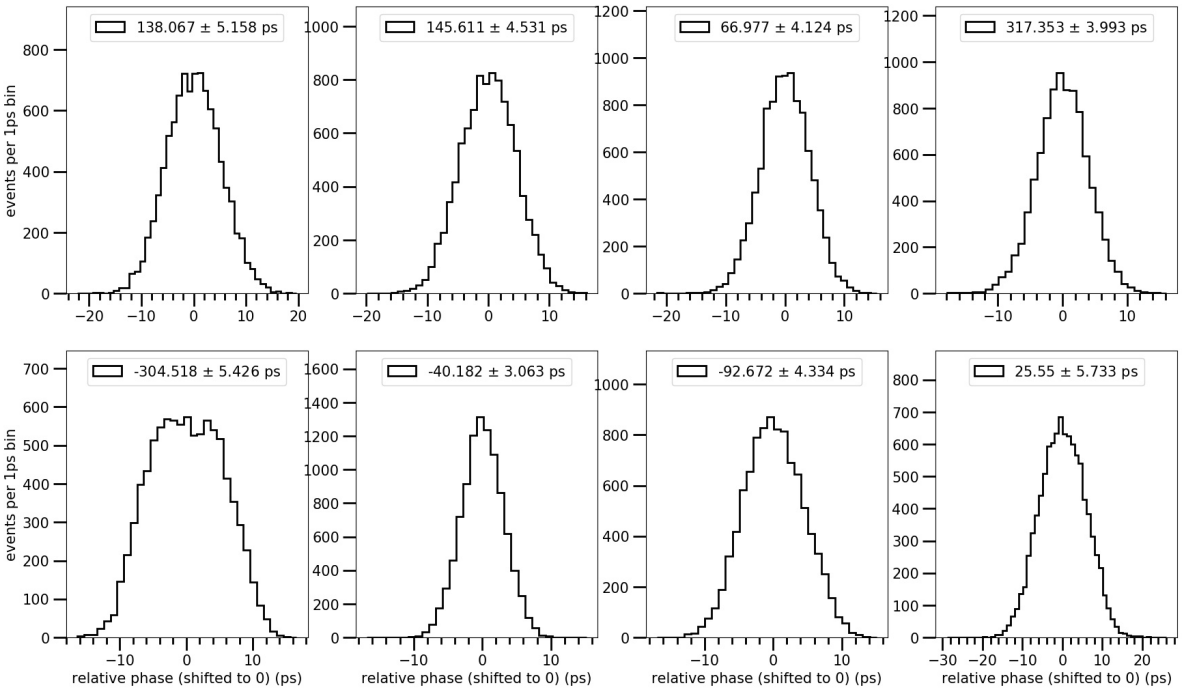

Figure B.5: Phase-offset timing-jitter of calibration channels 6, 12, 24, 30 (left to right) relative to channel 18 sourced by the same sine-wave input. The top row is board 0 and bottom row is board 2. This includes time-base calibration and wraparound offset calibration. See text for possible explanations of the constant phase-offset (median of the distribution).

The timing uncertainty on determining the phase of the synchronization signal, referred to as $\sigma_{250\ \mathrm{MHz}}$ in Chapter 8, is characterized by measuring the phase jitter of two calibration signals on two different channels sourced by the same sine-wave input [2].

2. The phase jitter from 250 MHz calibration waves will differ from the timing resolution to MCP pulses, which contain a broader frequency spectrum

Following a time-base and wraparound calibration of the synchronization waves, the waveform samples receive re-labeled timestamps. The start-time of the event, or $t = 0$, is re-defined as the first sample after the trigger location. Each SCA sample is re-labeled with its own individually-calibrated sample-delay relative to the previous sample.

A sine wave is fit to each waveform assuming a frequency of 250 MHz with floating amplitude, phase, and offset parameters. The fitter is a least-squares fit from the python package scipy.optimize.curve_fit. The phase determines a time offset in picoseconds. The phases reconstructed on four synchronization channels are measured relative to the fifth, channel 18, on each board. The resulting timing jitter, shown in Figure B.5, ranges from 3 to 7 ps standard deviation. The constant delays, measured as the median of the distribution, can be attributed to trace length mismatches in the PCB that distribute the calibration signals to the boards, constant delays of the PSEC4 write-clock distribution, and other trace-length mismatches on the ACDC board.

APPENDIX C

RADIATION LENGTH CALCULATION

Section 34.4.2 from the Particle Data Group (PDG) reference [26] defines the radiation length as (a) the mean distance over which a high-energy electron loses all but 1/e of its energy by Bremsstrahlung, and (b) 7/9 of the mean free path for pair production by a high-energy photon. The radiation length X_0 is

$$\frac{1}{X_0} = 4\alpha r_e^2 \frac{N_A}{A}\left[Z^2\big[L_{rad} - f(Z)\big] + ZL'_{rad}\right] \tag{C.1}$$

for $A = 1$ g per mol, $4\alpha r_e^2 N_A/A = (716.408 \text{ g cm}^{-2})^{-1}$. Expressions for $f(Z)$, L_{rad} and L'_{rad} are found in Reference [26]. The radiation length of a mixture or compound may be approximated by

$$1/X_0 = \sum w_j/X_j \tag{C.2}$$

where w_j and X_j are the fraction by weight and the radiation length for the jth element. This elemental decomposition formula is used to approximate the radiation length of different LAPPD component materials.

The fractional radiation length of a particle going through a thickness T_i of compound with radiation length X_i is T_i/X_i. The radiation length of a particle going through multiple internal components of an LAPPD is then $\sum T_i/X_i$.

The radiation lengths in cm calculated using relative chemical compositions of compounds are listed in Table C.1[1].

Particles can take three different paths through LAPPD material.

1. **Active region:** Front-window, two micro-channel plates, anode base, and PCB read-out

1. If this does not match your own calculations, please contact ejangelico@uchicago.edu

Compound	X_0 (cm $^{-1}$)	Note
Pure alumina, Al_2O_3	7.57	
Schott B33 glass	12.70	Ref [145]
Pure fused silica, SiO_2	12.30	
MCP-variety 1	51.08	Assumed 36% density of glass
MCP-variety 2	45.13	Assumed 26% density of glass
G-10/FR-4	16.76	Ref [146]
Proprietary metal	1.62	

Table C.1: Result of calculating compositional radiation lengths using the weight fraction of elements in the composition. Radiation lengths of MCPs are estimated by applying a density reduction equal to the loss from open area ratio of the micro-pores.

	LAPPD42	LAPPD43	LAPPD51	Tile 31
Window	0.5	0.5	0.5	0.38
One MCP	0.12	0.12	0.12	0.12
Glass spacer stack	1.029	1.029	1.029	–
Metal spacer stack	0.053	0.053	0.053	–
Button spacer stack	–	–	–	1.09
Base	0.38	0.38	0.38	0.51
Sidewall	1.3	1.3	1.3	1.74
PCB readout	0.16	0.16	0.25	0.25
Glass readout	–	–	0.38	0.38

Table C.2: Thicknesses in centimeters of materials used in the calculation for each path length and each LAPPD. Values are not necessarily representative of true values for each LAPPD, but this is a best attempt. References are the LAPPD test-reports distributed by Incom Inc. upon sale, and material specifications for U. of C. tile design found in Reference [60]

2. **Spacer region (Incom):** Front-window, stack of glass x-spacers, stack of metal x-spacers, two micro-channel plates, anode base, and PCB readout

3. **Spacer region (U. of C.):** Front-window, stack of ceramic button spacers, two micro-channel plates, anode base, and PCB readout

4. **Sidewall region:** Front-window, sidewall, anode base, PCB readout

In the case of Tile 31 and LAPPD 51, which are capacitively-coupled (see Section 3.2), there is an additional glass anode pickup layer associated with each particle trajectory.

	LAPPD42	LAPPD43	LAPPD51	Tile 31
Window	B33	B33	B33	B33
MCP	Variety 1	Variety 1	Variety 1	Variety 1
Glass spacer	B33	B33	B33	–
Metal spacer	PM*	PM*	PM*	–
Button spacer	–	–	–	Alumina
Base	Alumina	B33	Alumina	Alumina
PCB readout	G10	G10	G10	G10
Glass readout	–	–	B33	B33

Table C.3: Materials used in the calculation for each path length and each LAPPD. References are the LAPPD test-reports distributed by Incom Inc. upon sale, and material specifications for U. of C. tile design found in Reference [60]. "PM*" stands for proprietary metal.

The thicknesses for the radiation-length calculation are found in Table C.2 and Table C.3 and the fractional radiation lengths are found here:

- LAPPD43:
  - If particle passes through active fraction: 7.44%
  - If particle passes through x-spacer: 18.81%
  - If particle passes through sidewall: 17.17%
- LAPPD42:
  - If particle passes through fraction: 10.41%
  - If particle passes through an x-spacer: 21.78%
  - If particle passes through sidewall: 27.08%
- LAPPD51:
  - If particle passes through fraction: 13.94%
  - If particle passes through x-spacer: 25.31%
  - If particle passes through sidewall: 30.61%

- Tile 31:
  - If particle passes through fraction: 14.68%
  - If particle passes through button column (see Chapter 2): 29.08%
  - If particle passes through sidewall: 37.12%

APPENDIX D

ASSEMBLY PROCEDURE FOR GENERATION-II LAPPDS

This appendix goes into more detail on the specific steps taken during the fabrication procedure of ceramic bodied capacitively-coupled LAPPDs using the batch production method described in Chapter 2 and Reference [46]. It is intended as a reference for those who are designing the next-iteration batch-production system, or attempting to replicate elements of the fabrication procedure. This procedure was developed by Eric Spieglan, Evan Angelico, Andrey Elagin, and Henry Frisch. A large portion of the theory and hardware included in this Appendix is attributed to the dedicated work of Eric Spieglan.

The terminology of this chapter assumes that the reader has read Chapter 2 or Reference [46].

D.0.1 Assumptions of the preparation of materials

This appendix assumes that the components of the LAPPD have been prepared or fabricated in the following way:

1. The tile-base is monolithic 99.98% alumina ceramic
2. The tile-base has a 0.2" wide sealing-surface with square profile
3. The sealing surface of the tile-base is flat with minimum and maximum deviation range on the order of 0.5 - 1 mil (thousandths of an inch)
4. The photocathode window has a sealing metalization that matches the sealing surface of the side-wall
5. The window and sidewall sealing metalizations are evaporated films of 200 nm of NiCr followed by 200 nm of Cu without a vacuum break in between

6. The anode of the LAPPD is a capacitively-coupled anode layer, 10 nm of NiCr for example, with a 200 nm copper border along the perimeter for ground connection

7. Two copper tubes of 1/4" outer diameter and 0.035" thickness are brazed into the side of the tile-base

8. The tubes have been pre-bent to align and connect to the internal-manifold port-adapters

9. Ceramic cylinders, or "buttons", have been fabricated in a variety of heights. The buttons have been measured and binned with 0.2 mil bin spacing using a micrometer

D.1 Profiling the tile-base

Because of the 8"×8"dimensions of the detector window and base, mechanical structures must be included internally to support the packaging under the load of atmospheric pressure. In this design, 16 columns of ceramic cylinders are placed internally at 1.8" spacing to support the window and base. These ceramic pieces are referred to as "buttons" in the text that follows. A photograph that includes these buttons can be found in Figure D.1.

The buttons serve three functions in the LAPPD:

1. Supporting the package against the compressive force of atmospheric pressure

2. Setting the gaps between the MCP's, tile base, and photocathode

3. Applying mechanical force between the MCP surfaces and the high-voltage internal electrodes. These electrodes connect the copper pins to the surfaces that need to be set at high voltage to accelerate primary and secondary electrons

The combined heights of each button column are tuned to a precision of 0.5 mils to control the flexing of the photocathode window under atmospheric pressure. To tune the

button columns, a precise mechanical profiling of the tile-base and individual buttons is made. Also, a variety of button thicknesses are fabricated.

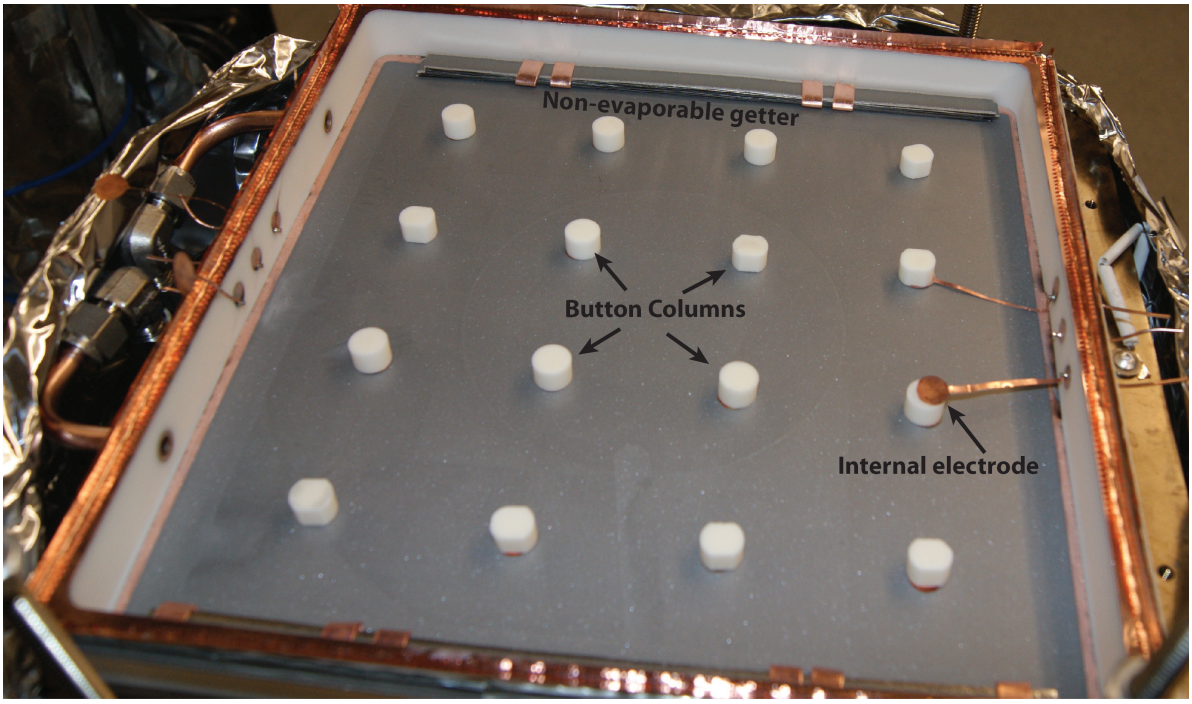

Figure D.1: Components that are significant during the first stage of assembly: the button columns that hold the MCPs and window under load, the non-evaporable getter (NEG), and the internal high-voltage electrodes.

D.1.1 Depth measurements

A setup for measuring the profile of the tile-base is shown in Figure D.2. The measurement includes the use of a granite flat, two aluminum flat-plates, and a depth micrometer.

A dial indicator is used to observe rocking of the hardware relative to the granite flat. An aluminum plate is placed on the granite flat and shimmed until it does not rock. The tile-base is placed on the aluminum plate and shimmed until it does not rock. Gauge blocks are placed on the aluminum plate at the four corners and support another aluminum flat. The upper plate is shimmed until it does not rock. The upper plate has through holes corresponding to each button location and measurement points on the corners and centers

of the sidewall. A depth micrometer is used to measure the sidewall height relative to the anode height at each button location. The analysis and output of this measurement is shown in Figure D.3

The output of this measurement is fed to a program that analyses the sidewall plane relative to the anode plane (see Figure D.3). The program plots the profile and calculates the total button column heights needed to set the columns to a plane at the height of the window.

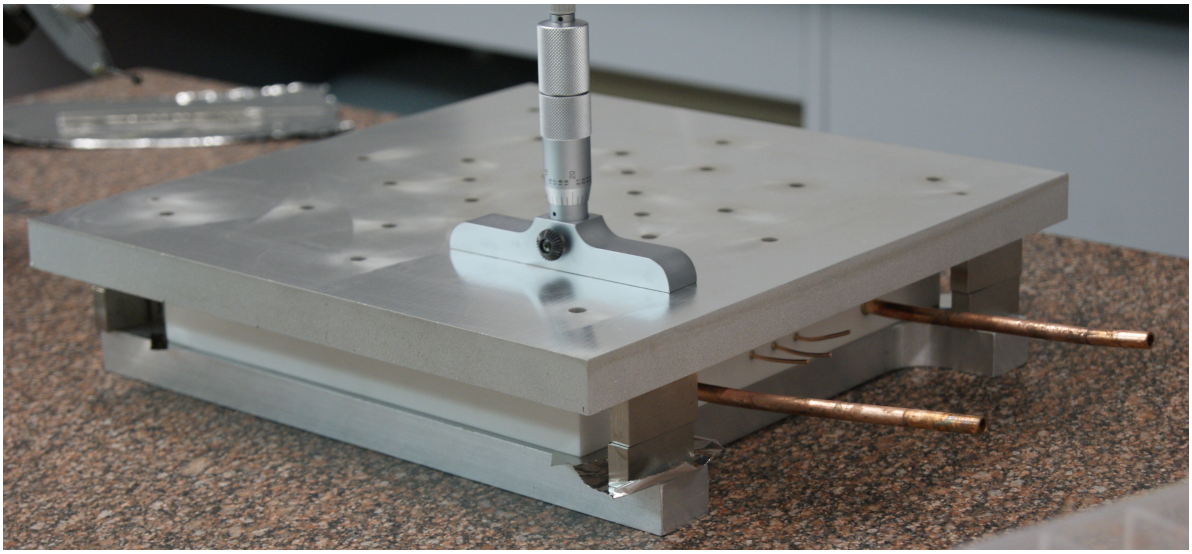

Figure D.2: The setup for measuring the profile of the tile-base. From bottom to top: granite flat, aluminum base-plate, shims and gauge blocks with total height greater than the tile-base height, aluminum hole-block, and depth micrometer.

D.1.2 Allocation of buttons and stack test

The micro-channel plate thicknesses are measured and included in the button-height calculation.

Prior to assembling the LAPPD in the fabrication chamber, buttons are fabricated, inventoried, and binned with respect to their total thickness. Copper shims are also fabricated to allow for stack-height flexibility. Using the output of the profiling program, a set of but-

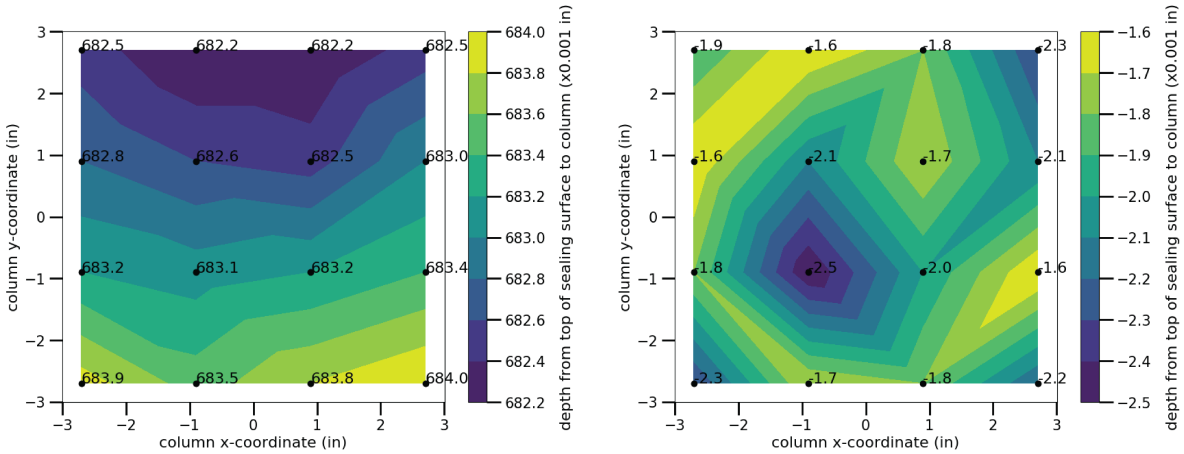

Figure D.3: On the left is the output of the tile-base depth measurement. On the right, a plot of the depths of the button locations relative to the sidewall after including the heights of ceramic spacers and thicknesses of MCPs. The heights of the button columns at each location are chosen such that the window will sit on the buttons 1.5 to 2 mils above the sidewall.

tons are hand selected to meet specifications of the full stack-up including all gaps between all objects in the LAPPD, as well as planarity of the button layer that makes contact with the window. At least one copper shim is required to be between the top layer buttons and the window so as to avoid creating cracks in the window due to the hardness or sharp corners of the ceramic buttons.

The buttons, high voltage electrodes, shims, and MCPs are assembled into the tile-base on the granite flat. A depth micrometer measurement identical to that from the initial depth-profiling is performed, this time with the depth-micrometer making contact with the top layer of buttons. This "stack-test" checks the final height. The "stack-test" has variations from assembly-to-assembly on the order of 0.5 mils.

The stack test goes as follows. Eight points on the sidewall and sixteen button locations on the interior are measured relative to an aluminum flat plate using a depth micrometer. The depth measurements on the sidewall are fitted to a plane and the depths of the interior button locations are corrected relative to that plane. The result is the approximate depth of the tile-base at the location of the buttons.

Depths on the sidewall deviate from a plane of best fit with about 0.5 mil absolute and RMS of about 0.3 mil. The ceramic spacers are chosen from a variety stock of thicknesses that have 0.2 mil thickness increments. The heights at each location are chosen such that the window will sit on the buttons 1.5 to 2 mils above the sidewall.

D.2 Conditioning the micro-channel plates

The MCP gain and high voltage properties are sensitive to the surface chemistry of the pores. Pre-conditioning the MCPs can lead to improved performance in MCP-PMTs. Mirco-channel plates with 400 cm^2active area have on the order of 4 m^2 of surface area for water and other molecular impurities to bond.

Two methods are common for conditioning the MCPs for use in MCP-PMTs: (1) baking in vacuum and (2) "scrubbing" with UV light. Scrubbing refers to a process in which an MCP is illuminated with UV light, producing some primary electrons at the surface. Those electrons are then amplified in the MCP by applying a bias. A second MCP, the "scrubbee", is bombarded by the electron clouds exiting the UV illuminated MCP. That electron bombardment removes some molecular species from the surface of the pores.

After the MCP thicknesses have been measured and the stack-test has passed specifications, the MCPs are inserted into a bakeable vacuum chamber with viewports and electrical feedthroughs for performing a scrub. The MCPs are baked at 350C for 24 hours. A UV lamp is positioned above an optical feedthrough to attempt to uniformly illuminate the entire surface of the scrubber MCP, sending charge into the two biased MCPs downstream. Scrubbing goes until roughly 0.3 or more coulomb/cm^2 of total integrated charge has been extracted from the end of the chain of MCPs.

The MCPs are kept under vacuum until they are ready for installation into the LAPPD on the day of sealing.

D.3 Assembly

D.3.1 High voltage electrodes

As is described in Chapter 2, high voltage is applied to the MCP surfaces and the photocathode using copper pins brazed through the side wall of the LAPPD vacuum packaging. Internally, these copper pins are attached to the MCPs using high voltage electrodes cut out of 3 mil copper shim-stock with a terminating pad in the shape of a button cross-section. See Figure D.1 for an example. The end of the shim is attached to the brazed copper wire by a small stainless-steel collar.

One of the earliest stages of assembly is the attachment of these electrodes to their respective feedthrough pins. The ends of the pins are filed to remove sharp corners that could emit divergent field lines.

D.3.2 Non-evaporable getter strips

The lifetime of the vacuum in MCP-PMT based detectors can be improved by including gettering material inside the sealed detector volume. This combats pressure-rise due to outgassing of the MCPs and other internal materials.

A photograph of the non-evaporable getter strips used in Tile 31 is presented in Figure D.1. Information about this SAES ST707 getter may be found at the company's website [147].

The assembly requirements for the getter are that it be electrically grounded and mechanically fixed. Holding the getter in place allows for the LAPPD to be placed in any orientation relative to gravity. Electrically grounding the material prevents uncontrolled charge-up and high voltage breakdown.

The ST707 strips are stacked and clamped together by copper clips. The copper clips are mechanically attached to the copper thin-film border of the capacitively-coupled anode

by pressing the getter onto clumps of indium. Both the copper clip and the copper thin-film boarder are pre-tinned by mechanically cold-welding indium into the copper. The clip is fused to the border by pressing the two pre-tinned objects together.

D.3.3 Swaging the tubes and leak checking

After the electrodes have been attached, the getter has been fixed to the base, and the tubes have been bent, the tubes are attached to the internal volume vacuum manifold. The copper tubes are attached using Swagelok elbows, which are then adapted to the VCR format at a socket welded to the tubes of a ConFlat feedthrough. This connection can be seen in Figure D.1.

The Swagelok connections are checked to be free of leaks using a helium leak detector. The copper tube is plugged using a tapered rubber plug and pumped using the downstream manifold pump.

D.3.4 Etching of sealing-surface and indium

Oxides in the indium seal prevent the indium from making a hermetic bond. This includes oxides anywhere in the sealing metalizations and oxides on the surface of the indium. To condition the sealing metalizations, an acid etching procedure is performed on the sidewall, shown in Figure D.4. The acid sits for 30 seconds and is then removed by blowing with compressed nitrogen or argon. The use of acetic acid and compressed gas is intended to reduce the presence of residue. The 30 second etch is repeated 3 times.

The indium wire is pre-conditioned using an acid etching procedure involving 5% by volume HCl. The desired length of wire is rolled up and placed in a beaker of HCl. After 9 minutes, the HCl is poured into a waste bottle and rinsed three times with deionized water. The indium wire, sitting in the beaker, is rinsed as well. The beaker with indium wire is then rinsed 2-3 times with isopropyl alcohol. The indium wire is removed while still wet

Figure D.4: A sealing metalization being pre-conditioned with a short soak in acetic acid.

and immediately blown dry using compressed noble gas. If the rolled indium wire easily cold-welds to itself then the etch had an effect of removing some oxide. The performance of the etch may be checked by seeing how sticky the wire is to itself. The wire is immediately unrolled and placed on the sealing surface of the LAPPD.

D.3.5 The capillary-action seal

One indium sealing method that was developed for this particular LAPPD geometry is called the "capillary-action" indium-seal. The advantage of this method is that it keeps any residual indium oxide outside of the sealing region. A photograph showing the four pieces of hardware involved in the seal is shown in Figure D.5.

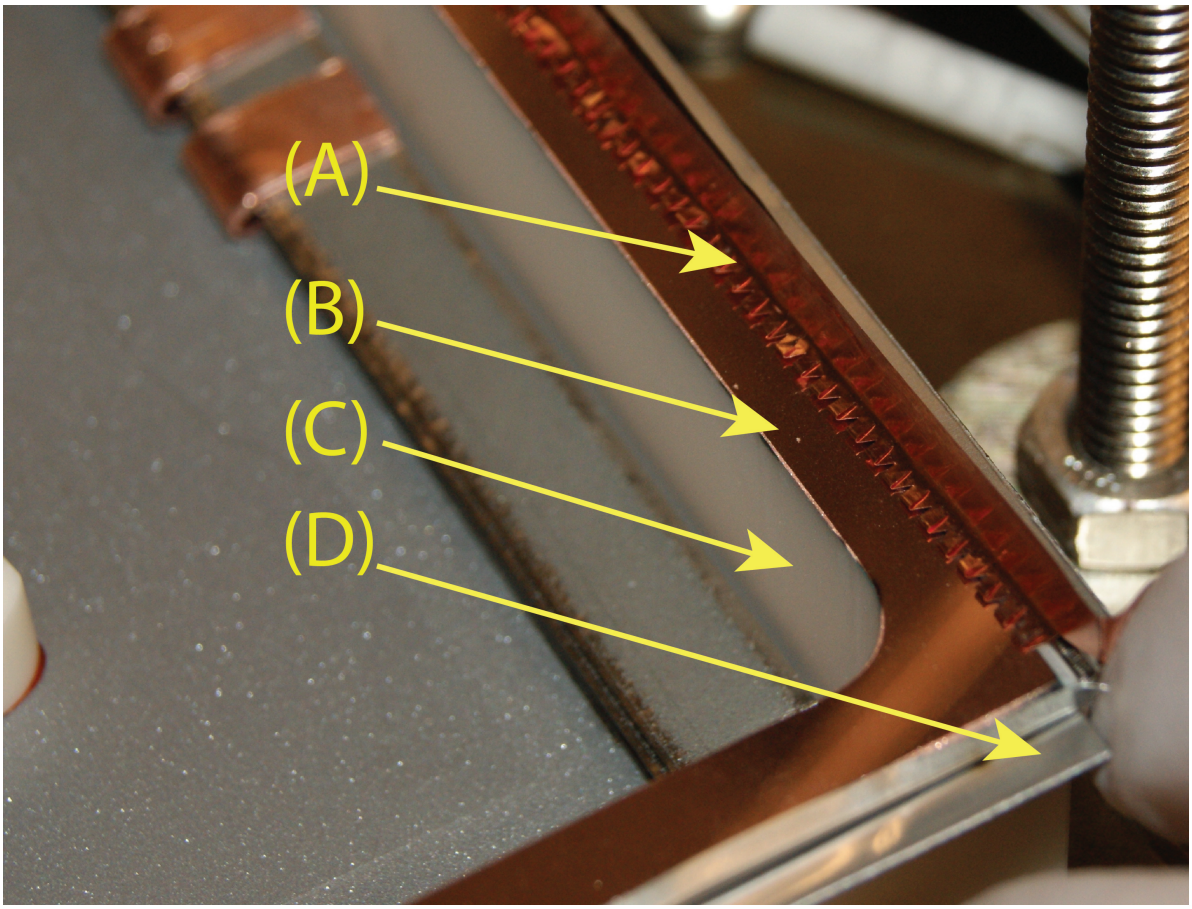

Figure D.5: A closeup of the (A) copper sawtooth shim, (B) ceramic sidewall, (C) wettable metalized sealing surface, and (D) the SS indium wire holder. The sawtooth shim holds the window above the sidewall sealing surface by 2 mils while allowing gaps for molten indium to wick between the two wettable surfaces. The SS indium holder allows the indium wire to sit outside of the seal area until it melts and is wicked by the wettable copper surfaces. The copper teeth may be replaced by a built-in positive stop machined into the surface of the sidewall.

The two sealing surfaces, one on the window and one on the side-wall, are held apart by a 1 mil copper shim bent over onto itself for a total of 2 mil gap. This copper shim is cut into a sawtooth pattern so that molten indium may flow into the gap between the sidewall and the window.

A stainless steel trough is mechanically fastened to the tile-base. Three LAPPD perimeters worth of etched indium-silver alloy is placed into the trough. When the indium melts, the oxide skin will break somewhere along the wire and pure indium will begin to wet the

copper-toothed shim. Pure molten indium will be siphoned into the gap by the capillary-action forces of the wettable thin-film layers. If enough indium is provided, the 2 mil gap will be completely filled with indium, forming a hermetic seal.

D.3.6 Press mechanism

Compression forces are applied to the edge of the glass window so that it maintains a fixed 2 mil gap distance despite having some level of curvature. Glass windows used in this 8"×8" format typically have 0.5 mil out-of-flattness and up to 2 mils out-of-flatness around the edge. Eight springs are placed above four 0.5" thick stainless steel bars. The springs are compressed with about 8 pounds-force each.

The stainless-steel bars that press on the perimeter of the glass are connected to a heater via copper braids. The heaters, braids, and other modular components of the internal assembly is shown in Figure 2.7.

D.3.7 Internal insulation

One objective is to have the LAPPD window and sidewall at a uniform temperature during the sealing cycle. Three nichrome-ribbon heaters apply radiative heat to the assembly from below and above.

A radiation hermetic wrapping of aluminum foil covers the LAPPD assembly module.

D.4 Sealing cycle

The thermodynamic procedure for sealing the LAPPD is shown in Figure 2.8. The procedure may be split into three stages: the indium melting phase, the MCP bakeout phase, and cooldown.

There are two vacuum volumes in the system: the inner volume of the LAPPD connected

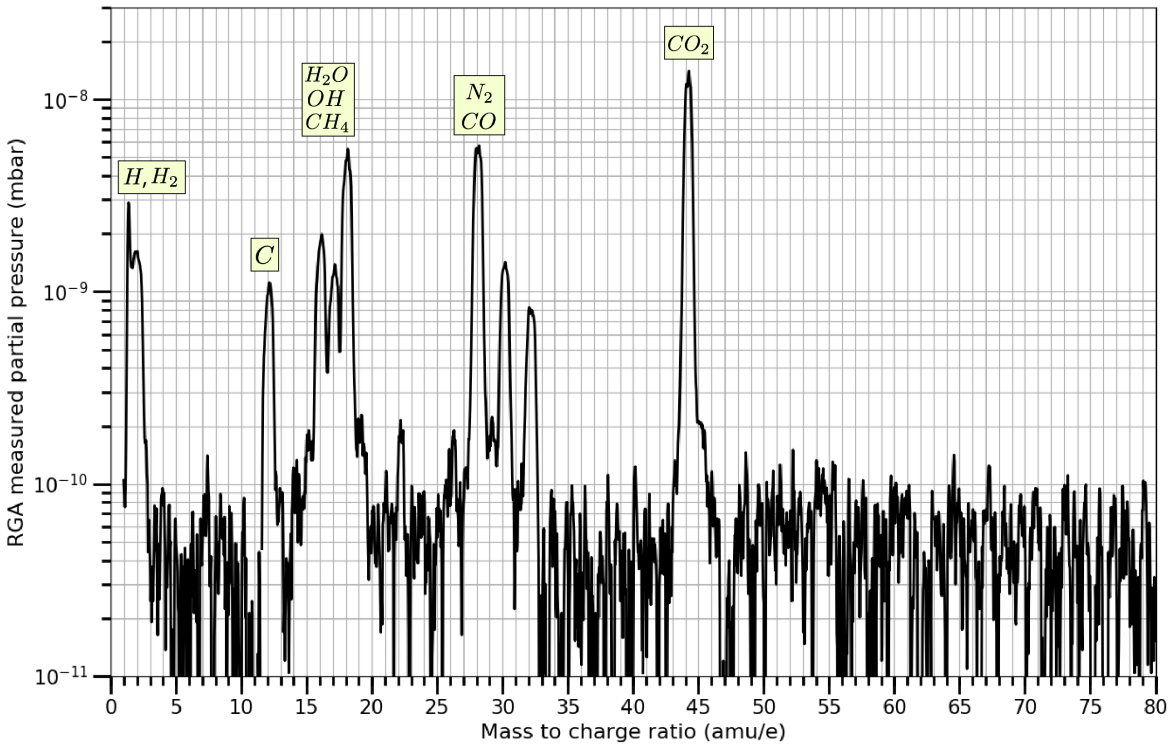

Figure D.6: A Stanford Research Systems 200 (SRS200) RGA scan taken at the end of the sealing cycle shown in Figure 2.8 after cooling to 150 C. This is a close proxy to the chemical state of the gas inside the LAPPD volume during the growth of the photocathode. Partial pressures are not easily converted to absolute pressures inside the LAPPD due to the uncharacterized conductance to the pump and LAPPD as well as the cross-section dependence on gas species of the RGA. Carbon based compounds in this spectra are known to be sourced primarily by the RGA measurement head.

to a manifold via the brazed tubes and the outer volume consisting of the larger vacuum chamber around the LAPPD module. During the indium melting phase, temperatures are slowly raised through the melting point of indium. The entire assembly is then baked at 290 C for 16 hours to remove as much water from the MCPs as possible. The outgassing of the internals, measured by the pressure gauge on the internal volume, reduces during this bakeout. Some gas components in the internal volume are shown in Figure D.6, recorded after the seal-and-bake cycle had cooled to 150 C.

D.5 Venting

D.5.1 Argon leak signal

Eric Spieglan has developed and honed the procedure for venting and leak-checking without introducing background into the signal channels. Once the temperature of the tile assembly has naturally dropped to $\sim$ 100 C, argon gas is slowly admitted into the outer chamber to cool convectively. The chamber pressure is monitored as argon is admitted. An RGA signal at 40 amu is monitored in the LAPPD internal volume. The ratio of the two signals, in addition to considerations regarding the conductance of the RGA and LAPPD to the pump, provides an upper bound on the leak rate of the indium seal. Diffusion of argon through the glass window is also taken into account.

If there are no leaks observed initially, the path from the LAPPD internal volume to the pump is valved shut. If a small leak exists, the LAPPD will fill with argon gas. After a number of hours, the valves are reopened with the RGA measuring on the argon mass peak. The peak, integral, and decay constant of the measured argon rise, if any, is used to estimate properties of the leak and conductance to the RGA.

D.5.2 Helium leak checking

Once the LAPPD is cool and the argon leak checking procedure has been performed, the outer chamber is vented and removed. Photographs of the LAPPD window are taken to log visual features of the seal and the antimony pre-cursor layer. With the indium seal exposed, a helium needle may be applied to the perimeter to localize leak signals.

APPENDIX E

AIR-TRANSFER DEPOSITION AT UNIVERSITY OF CHICAGO

E.0.1 Typical Sb quality before sealing

In the University of Chicago batch production process, photocathode windows are prepared with a pre-deposited antimony (Sb) layer prior to LAPPD assembly. This antimony layer acts as a pre-cursor to the final photocathode layer. Alkali vapors come into contact with the Sb and diffuse into the bulk, creating a film with a lower work function than the bare antimony.

The Sb pre-cursor window is stored in a nitrogen or air environment until assembly of the LAPPD. The removal of the Sb layer from the vacuum-deposition chamber gives it the chance to oxidize. The presence of oxide on the Sb layer prior to introducing photocathode alkali metals can affect the end-point quantum efficiency. The LAPPDs produced at University of Chicago are assembled with Sb windows that have been sitting in clean carriers, exposed to air, for weeks to months.

Andrey Elagin studied the surface chemistry of these air-exposed Sb pre-cursor layers with the help of Alexander Filatov at University of Chicago. Under an argon ion-beam depth-profiling x-ray photo-spectroscopy chamber, they conclude that an initially 10 nm Sb film has somewhere from 2-5 nm of oxide after months of air exposure. The conclusions of this study are uncertain. Please find more details in Reference [148].

A photocathode deposition experiment at Brookhaven National Laboratory observed that oxide that had formed on an initially 5 nm antimony layer was completely removed after spending 4 minutes at 400 C [149]. It seems plausible that the bake-out profile during the standard LAPPD sealing cycle, 290C for 16 hours (Figure 2.8), could remove Sb-O formed on the 5-10 nm thick Sb pre-cursor layer of the U. of C. air-transfer fabrication process.

This Appendix will describe a few of the key details surrounding photocathode synthesis in the University of Chicago air-transfer fabrication process. A large portion of the theory and hardware included in this Appendix is attributed to the dedicated work of Eric Spieglan.

E.0.2 Cesium source description

The cesium source is a set of UHV components that is attached to the manifold. The source consists of two sections separated by a valve: the ampoule volume and the distilled volume. See Figure 2.9 from Chapter 2. The entire cesium source may be valved off.

The ampoule volume contains a 1/2 g glass ampoule of 3N+ cesium from ESPI metals [67]. The cesium ampoule is filled with a pressure of 1 atm of argon. It is oriented under a tee with a bellows attached. Inside the bellows is a sharpened ceramic plunger, used to crack the glass of the ampoule.

The distilled volume is downstream of the ampoule volume. When the ampoule is broken, the ampoule volume is set to a 300 C and a well at the bottom of a cross is set to room temperature. One can control the amount of cesium transferred to the distilled volume by modulating the temperatures or closing valves at particular times.

Both the ampoule volume and distilled volume have non-evaporative getter pellets that are activated during the distilling process. This getter pumps gases that could oxidize or add impurities to the cesium metal. At high enough temperatures, already formed Cs-O compounds will decompose and the oxide will be captured by the NEG.

After the distillation, the volume containing the broken glass is isolated from the pure cesium using a valve to reduce any reactions between the cesium and glass that could contaminate the soon-to-be photocathode metals.

E.0.3 Thermal configuration of manifold and LAPPD

Manifold

To transfer cesium to the LAPPD, the vacuum tube manifold between the cesium source and the LAPPD window must be thermally controlled and kept hot. A schematic diagram of the manifold and its temperatures during the cesiation process is shown in Figure 2.3. Cold spots in the vacuum manifold will restrict the flux of alkali. Heaters, insulation, and thermocouples are distributed to avoid such cold spots.

LAPPD

The temperature of the window and LAPPD internals affects the dynamics of the cesiation process. For example, the uniformity of the resulting quantum efficiency should be determined by the thickness uniformity of the initial antimony layer and the thermal uniformity during cesiation.

The photocathode efficiency is monitored from above using a 2-D translation stage that rasters a diode fed fiber over the 8"×8" area. A photograph of the system is shown in Figure 2.10. The space above the window is occupied by translation stages and diode optics. Because air is allowed to flow over the window during synthesis, its temperature is not necessarily uniform across the full 8"×8" area. We suspect that this is the main cause of non-uniformity in the end-point quantum efficiency shown in Figure E.3.

E.0.4 Measurements of quantum efficiency

The quantum efficiency of a photocathode is the number of electrons that escape the material bulk divided by the number of photons impinging on the cathode: n_e/n_γ.

An optical system used to shine diode light on the LAPPD window is shown in Figure 2.10. The diode box used in this system has with five broad wavelengths and intensity po-

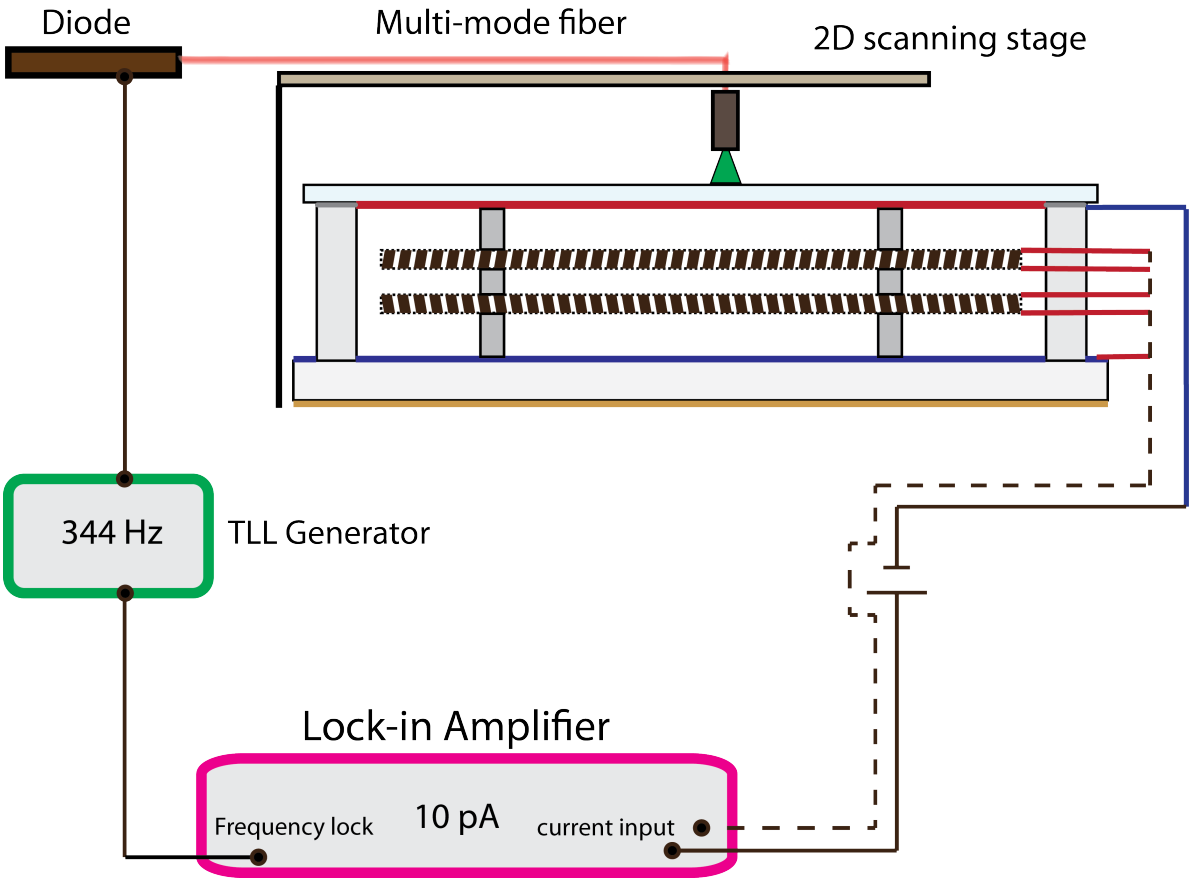

Figure E.1: One method used to measure QE. A diode light source shines light on the LAPPD with a pulsed frequency set by a function generator. That frequency is fed to a lock-in amplifier which measures the current extracted from the cathode. The voltage source that biases the cathode gap consists of a set of four 9 V batteries in series.

tentiometers. The flux of light out of the fiber closest to the photocathode is calibrated with respect to the potentiometer setting. Neutral density optical filters are inserted throughout the growth process to allow for a monitoring of quantum efficiency over many orders of magnitude with a noise floor of about 10^{-10}.

The DC resistance of the micro-channel plates is also measured during the cesiation process. Electrical diagrams are shown in Figures E.1 and E.2. The diode light is modulated by a TTL square wave at frequencies around 344 Hz. This modulation signal output from the photocathode is sent to a lock-in amplifier that has a capacitively-coupled current input. The lock-in amplifier current measurement in combination with a flux measurement gives

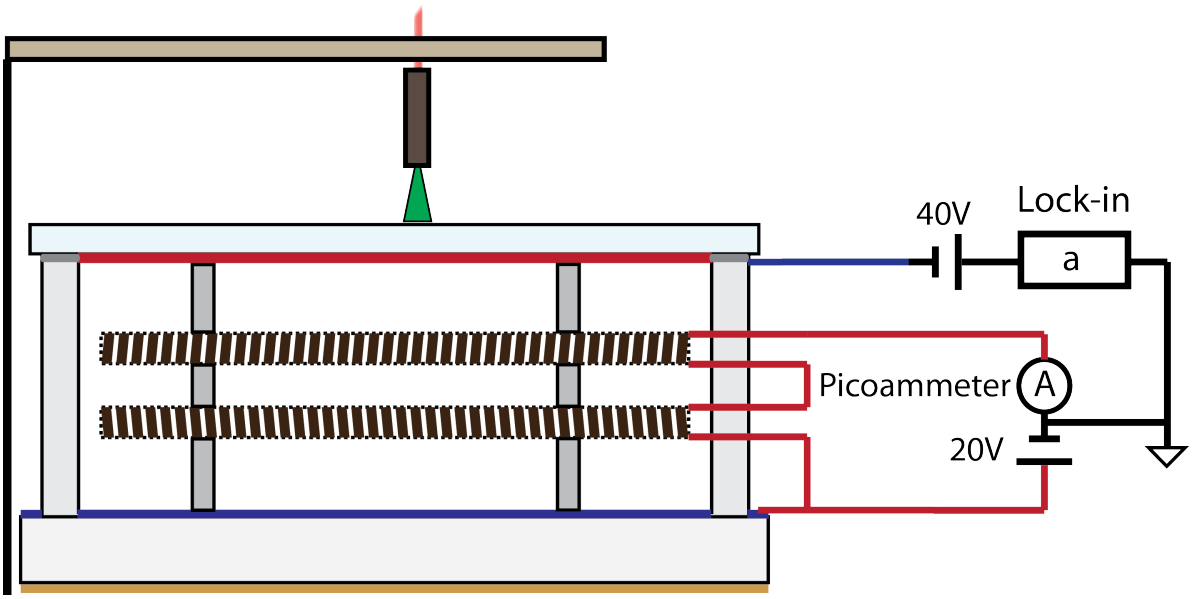

Figure E.2: This is an alternative QE measurement setup that allows for a simultaneous measurement of the low-voltage DC series resistance of the MCPs. Hardware not shown is similar to that in Figure E.1

the ratio n_e/n_γ.

E.0.5 Initial growth of photocurrent

In some LAPPD fabrication trials, before the use of distilled cesium, the photocurrent only developed above the noise floor of the QE measurement system once a significant period of time had passed after opening the cesium source valve. The delay of photocurrent was anywhere from 30 minutes to 6 hours. The time delay disappeared after the first trial using a distillation cesium source with activated non-evaporative getter pellets.

In that trial, forming the photocathode for Tile 31, the initial growth of photocurrent is almost instantaneous with the opening of the cesium source valve. The growth of photocurrent can be paused with response times on the order of a minute by closing the cesium source valve.

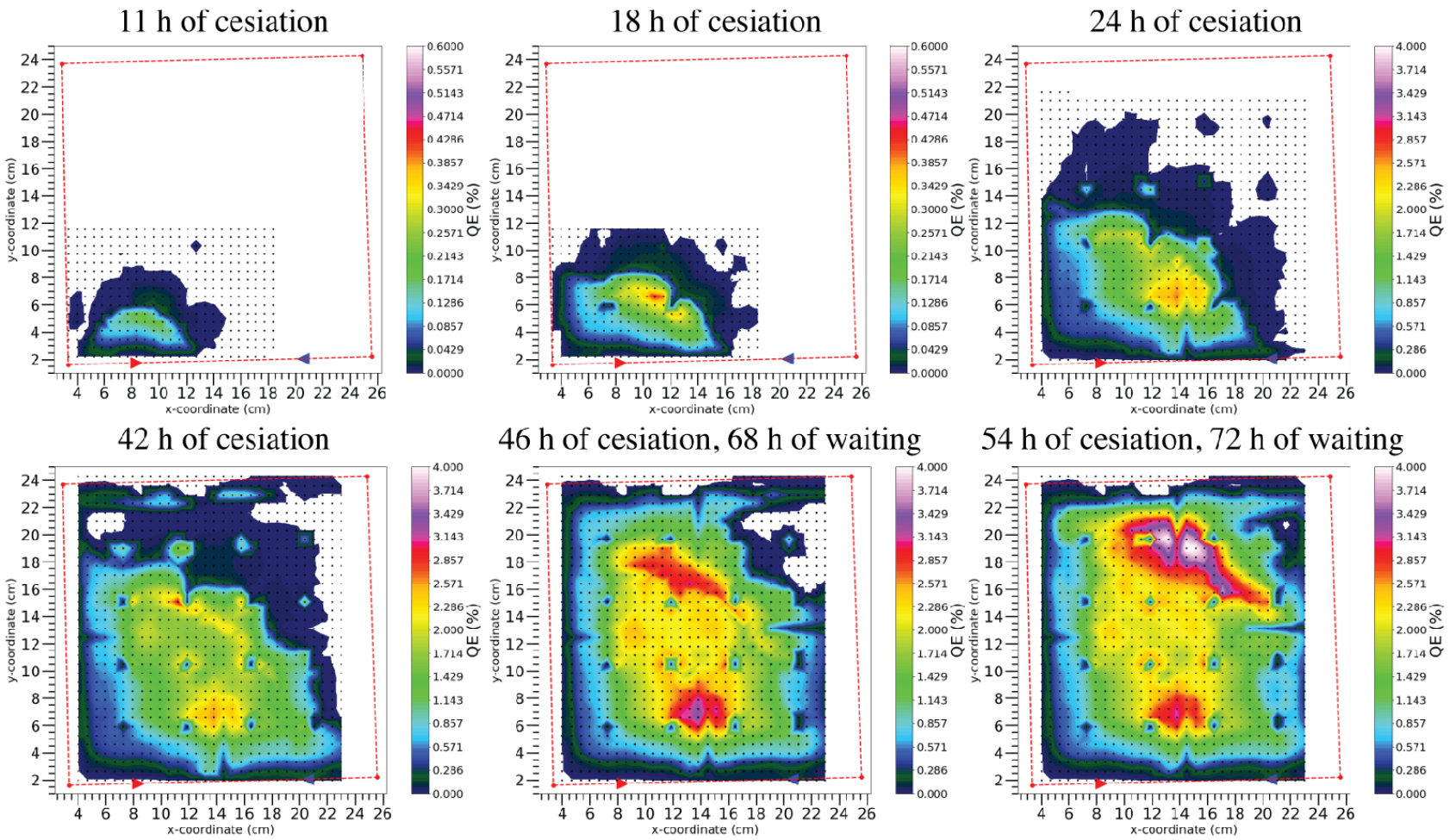

Figure E.3: The evolution of the Tile 31 photocathode over the history of its growth. Total integrated cesiation time is indicated by titles above each figure. The highest value of the colored quantum efficiency scale changes from 0.6% to 4% at the rightmost figure of the top row. Quantum efficiency color scale is linear. The LAPPD outline is indicated by the red dotted line. The two copper tubes are indicated by red and blue triangles at the bottom of each figure, red being the cesium inlet tube. The rightmost bottom figure shows the quantum efficiency after a long period of waiting after cesiation.

E.0.6 Time dependence of spatial growth

A plot of six moments in time during the growth of the photocathode for Tile 31 is shown in Figure E.3. Photocurrent begins to develop near the cesium-inlet tube. Over a period of about 24 hours, the photocurrent spreads laterally, eventually covering the entire surface of the window. The time scales of this lateral flow have been observed to be dependent on the temperature of the source and the temperature of the window.

The edges of the final state of this photocathode have a lower QE than the central region. We suspect that this is because the edges are significantly hotter than the central region due to conduction heat from the ceramic sidewall. We also suspect that the non-uniformities in this QE distribution are due to thermal non-uniformities in the window during the cesiation.

The timescales for reaching the maximum QE are long in the case of Tile 31. One reason is our careful modulation of the source valve and temperatures so as to fully characterize the formation of the cesium. An industrial batch production process would optimize for time and peak QE. The timescales involved during cesiation are sensitive functions of the temperatures in the cesiation system. These could be increased for high-throughput batch production.

APPENDIX F

TIME-OF-ARRIVAL STATISTICS OF THE FIRST PHOTOELECTRON

F.1 Timing from a Cherenkov-light source

Cherenkov photons are generated in the glass medium as the charged particle traverses at close to the speed of light, with photons farthest away from the photocathode being generated earliest. However, the earliest generated photons are the last to be converted to photoelectrons, as they have then entire thickness of the window to traverse before reaching the photocathode. The earliest created photoelectrons, on the other hand, are those generated closest to the photocathode.

Even though the physics of Cherenkov emission is on the sub-picosecond level, the creation times of the photoelectrons are spread over 10s of picoseconds depending on the window thickness, with later photoelectrons generated farther from the particle axis. See Figure 1.8 for a geometrical diagram.

Assume a dispersion-less medium such that the photon wavefront is infinitely thin. [1] If the particle is traveling in the $\hat{z}$ direction at velocity βc, the arrival time of photons at a radial distance ρ in the photocathode plane is [27]

$$t = \frac{\rho}{\beta c}\sqrt{\beta^2 n^2 - 1} \tag{F.1}$$

which means that the maximum time difference in arrival is $t_{\max} = \frac{\rho_{\max}}{\beta c}\tan\theta_c$. For $\beta \approx 1$

1. Jelley points out in Section 2.3 of Reference [27] that in a non-dispersive medium, the Cherenkov wavefront is not infinitely thin due to the different velocities of different wavelengths of light. The time-of-arrival difference of two Cherenkov-cone wavefronts of different wavelengths is $\frac{\rho}{\beta c}(\tan\theta_2 - \tan\theta_1)$ where ρ is the detection radius and θ_i is the Cherenkov emission angle of each wavelength of light. For 5 mm radius detection in glass and Cherenkov fronts from wavelengths of 300 nm to 700 nm, this time-of-arrival difference is ~775 femtoseconds.

and $n \approx 1.5$ (glass), the time difference between photons at $\rho = 0$ and $\rho = 5$ mm is about 18.7 ps.

Because the number of photons emitted per unit path length n_l is constant, the Cherenkov photons arrive at the photocathode window at a constant rate of $\mathrm{d}N/\mathrm{d}t = \beta c n_l$. This implies that the times that Cherenkov photons are converted into photoelectrons are uniformly distributed from t = 0 to t = t_{last}.

In later subsections, we will calculated how the timing uncertainty of an MCP-PMT is changed if one assumes that the time-of-arrival of a particle is determined by the arrival-time of the first photoelectron at the pore surface. Here, we will look at the timing statistics of the earliest generated photoelectron.

Given a random vector $\left(X_1, ..., X_n\right)$ where X_i is a randomly sampled variable in a probability space, the vector $\left(X_{(1)}, ..., X_{(n)}\right)$ where $X_{(k)}$ is the kth largest element is called the *order statistics* of $\left(X_1, ..., X_n\right)$ [150, 151]. For some probability density functions (pdfs), the order statistics may be derived analytically. The uniform distribution is one example. The probability density function (pdf) of the kth order statistic of n random variables sampled from the uniform distribution on the interval $t = [0, 1]$ is:

$$f_{(k,n)}(t) = \frac{1}{B(k, n-k+1)}(1-t)^{n-k}t^{k-1} \tag{F.2}$$

which is normalized to have unit area by $B(\alpha, \beta)$, the beta function. The mean of this order statistic pdf is $k/(n+1)$ and the variance is [152]

$$\mathrm{var}[f_{(k,n)}(t = [0, 1])] = \frac{k(n-k+1)}{(n+1)^2(n+2)} \tag{F.3}$$

Both the mean and the variance above are defined for the uniform distribution over an

interval [0, 1], but can be multiplied by the range of a non-unital interval. For the Cherenkov detecting LAPPD case where $n = N_{\mathrm{pe}}$, this would imply that the mean and variance of the earliest ($k = 1$) photoelectron birth time

$$\langle t_{\mathrm{first}} \rangle = t_{\mathrm{last}}/(N_{\mathrm{pe}} + 1) \tag{F.4}$$

$$\mathrm{var}[t_{\mathrm{first}}] = \frac{t_{\mathrm{last}} N_{\mathrm{pe}}}{(N_{\mathrm{pe}} + 1)^2 (N_{\mathrm{pe}} + 2)} \tag{F.5}$$

If the number of photoelectrons is only increased by increasing the radiator thickness, as opposed to changing the material and transmission properties, then the number of photoelectrons is related to the time of the latest arriving Cherenkov photon because of the geometry of Cherenkov emission. If QE is the quantum efficiency as a function of wavelength, $\mathrm{d}n/\mathrm{d}\lambda\mathrm{d}l$ is the number of emitted Cherenkov photons per unit path length per unit wavelength define the photoelectron conversion spectrum Φ as

$$\Phi = \int \mathrm{d}\lambda \left[\mathrm{QE} \cdot \frac{\mathrm{d}n}{\mathrm{d}\lambda \mathrm{d}l} \right] \tag{F.6}$$

If T is the thickness of the Cherenkov radiator, equal to the particle path-length, then the number of photoelectrons N_{pe} is

$$N_{\mathrm{pe}} = T\Phi \tag{F.7}$$

$$= \frac{\rho_{\mathrm{max}}}{\tan\theta_c} \Phi \tag{F.8}$$

$$= t_{\mathrm{last}} \beta c \Phi \tag{F.9}$$

Which implies that the expectation value of the earliest arriving photon is

$$\langle t_{\text{first}} \rangle = \frac{t_{\text{last}}}{N_{\text{pe}} + 1} \tag{F.10}$$

$$= \frac{N_{\text{pe}}}{\beta c \Phi (N_{\text{pe}} + 1)} \tag{F.11}$$

It is remarkable that for $N_{\text{pe}} \gg 1$, the expectation value for the earliest arriving photoelectron is only dependent on the velocity of the particle, the Cherenkov emission spectrum, and the quantum efficiency. The variance using the same reasoning is

$$\text{var}[t_{\text{first}}] = \frac{N_{\text{pe}}^2}{\beta c \Phi (N_{\text{pe}} + 1)^2 (N_{\text{pe}} + 2)} \tag{F.12}$$

$$\approx \frac{1}{\beta c \Phi N_{\text{pe}}} \tag{F.13}$$

where the approximation assumes $N_{\text{pe}} \gg 1$. For the typical LAPPD values of Section 1.3.1, the expectation value and variance of t_{first} is 0.496 ps and 7.4 femptoseconds / T where T is the thickness of the window in centimeters. If the quantum efficiency were so low such that $N_{\text{pe}} = 1$, the mean would be about 9 ps and variance 0.125 ps.

F.2 Timing variations of photoelectron arrivals induced by the MCP-pore bias angle

F.2.1 For a highly focused laser light-source

Another contribution to detector transit time spread comes from the location at which the photoelectrons strike the inside of the MCP pore. Figure F.1 shows a not-to-scale side view of a pore, suggesting how different electron trajectories create transit time spread. The

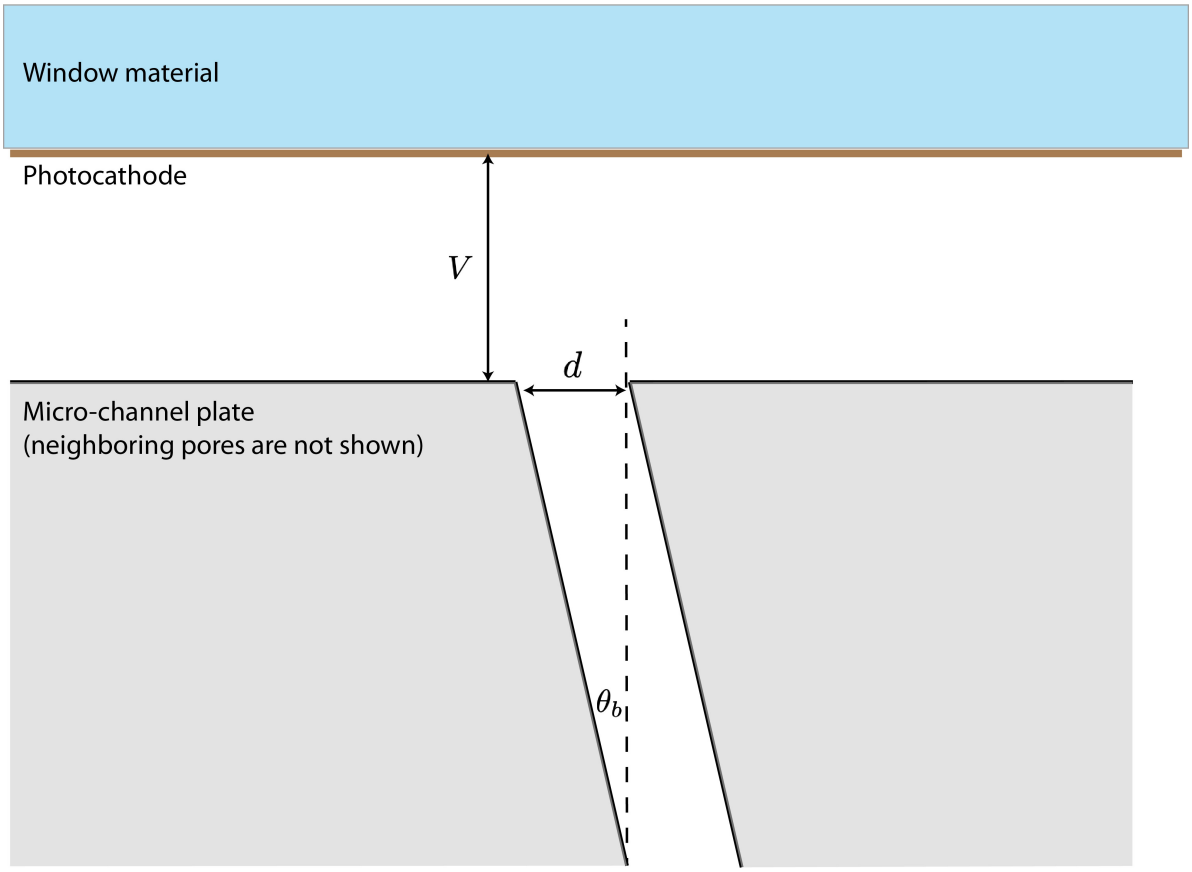

Figure F.1: A zoomed-in diagram of a side view of an MCP pore, with distances not to scale and neighboring pores not shown. photoelectrons can strike the inside of the pore at different depths. The maximum depth is shown as a dotted line, and is related to the pore angle and diameter. An accelerating voltage V is applied to the gap between the photocathode and MCP surface.

geometry of the pore may be used to calculate the order statistic for the arrival times of photoelectrons at the pore surface of first-strike.

Take the following simplifying assumptions which do not necessarily represent the real-world scenario

1. Electrons are born at the photocathode at the same time and take a straight path from the window to the MCP pore

2. photoelectrons are generated by a uniform laser spot over a <1 mm^2 area

3. The first electron to strike the pore wall determines the reconstructed photon-burst

time-of-arrival. This is assumption becomes realistic for LAPPDs which have high gain and electronics systems that can correctly identify the earliest electron on the leading edge of a digitized pulse.

4. Assume an accelerating voltage of around 400 V is applied between the MCP surface and the photocathode. photocathode voltage has been measured to improve timing characteristics due to higher yield at first-strike and smaller transit times in the gap before first-strike [33, 34, 5].

5. Assume that the pore diameter d is 10-20 μm and the distance from the photocathode to the MCP surface is on the order of 1-5 mm such that the electron's velocity does not appreciably change once it is inside of a pore

The assumption of an intense uniform laser spot implies that the electrons will have uniformly distributed pore-strike-depths as well as pore-strike-times. The range of the uniformly distributed electron arrival times is from t = 0 to t = t_{last}, where 0 is defined as the time when an electron strikes the top surface of the MCP and t_{last} is the time at which the deepest striking electron strikes the pore wall at a depth of $d/\tan\theta_b$ (see Figure F.1 for definition of variables and coordinate system).

If a bias voltage V is applied across the photocathode-to-mcp gap, the electron has gained qV electron volts (eV) of kinetic energy by the time it reaches the top surface of the MCP. This implies that is has velocity $v_0 = c\sqrt{\frac{2qV}{m}}$ where m is the mass of the electron in eV, the product qV is in units of eV, and c is the speed of light. The electron that strikes the pore at the deepest accessible location in the pore, or the "last" electron to arrive, arrives at a time

$$t_{\text{last}} = \frac{d}{v_0 \tan\theta_b} = \frac{1}{c}\sqrt{\frac{m}{2qV}}\frac{d}{\tan\theta_b} \tag{F.14}$$

For $V = 100$ V, $\theta_b = 13^\circ$, and $d = 20\mu$m, the electron is moving slowly at 6 μm per ps and $t_{\text{last}} = 14.5$ ps.

Because the arrival times are uniformly distributed, the same statistical results apply from the previous section but with the uniform distribution ranging from 0 to t_{last}. The resulting mean and variance of the 1st order statistic is

$$\langle t_{\text{first}} \rangle = t_{\text{last}} \cdot \frac{1}{N_{\text{pe}} + 1} \tag{F.15}$$

$$= \frac{d}{v_0 \tan\theta_b} \cdot \frac{1}{N_{\text{pe}} + 1} \tag{F.16}$$

$$= \frac{1}{c}\sqrt{\frac{m}{2qV}} \frac{d}{\tan\theta_b} \cdot \frac{1}{N_{\text{pe}} + 1} \tag{F.17}$$

$$\tag{F.18}$$

$$\text{var}[t_{\text{first}}] = t_{\text{last}} \cdot \frac{N_{\text{pe}}}{(N_{\text{pe}} + 1)^2 (N_{\text{pe}} + 2)} \tag{F.19}$$

$$= \frac{d}{v_0 \tan\theta_b} \cdot \frac{N_{\text{pe}}}{(N_{\text{pe}} + 1)^2 (N_{\text{pe}} + 2)} \tag{F.20}$$

For $N_{\text{pe}} \gg 1$ in a single pore, the scaling of the variance is like $\frac{1}{N_{\text{pe}}^2}$.

F.3 Combining timing induced by the Cherenkov emission profile and pore geometry

If the source of photoelectrons is a burst of Cherenkov photons from an incident particle, then the photoelectrons born over a single 10-20 μm pore are roughly uniformly distributed

in the transverse dimension [2]. Because the initial transverse position of each photoelectron is uniformly distributed, the depth at which they strike the pore is also uniformly distributed.

Many small pores are covered by the ~1 cm diameter Cherenkov cone. The pores to receive the earliest photoelectrons are those closest to the particle axis. The photoelectrons located above a pore that is ρ away from the particle axis will be born at a later time, $t = \frac{\rho}{\beta c} \tan\theta_c$ where θ_c is the Cherenkov opening angle.

A monte-carlo simulation generates the positions and times of photons created by the charged particle passing through the window, with a photoelectron spatial density governed by the physics of Cherenkov emission, namely that the density of photons per unit length is constant along the particle trajectory. The photons are propagated to the photocathode at the most probable Cherenkov angle, 48°, and group velocity, 0.200 mm/ps. Their arrival positions at the photocathode are spread at large distances compared to the 20 μm diameter pores. The transverse position of the photoelectron relative to the center of the pore at which it is collected is uniformly sampled.

The photoelectrons are propagated to the pore, arriving at different depths generating a variance in photocathode gap traversal time. The voltage applied to the photocathode gap is set to 400 V with a gap-traversal distance of 5 mm. Pores are 20 μm diameter and biased at 13 degrees. The propagation time of the photon to photocathode and photoelectron to pore strike are collected. The earliest photoelectron to arrive at a pore surface is recorded. The simulation is then regenerated for 10,000 events. Figure F.2 shows an example of the earliest arriving photoelectron (1st order statistic) for 10,000 events with a 5 mm thick window at 6.64 photoelectrons per mm for a rounded total of 33 photoelectrons.

The variance of the distribution of earliest electron arrival-times may be calculated for two different variations of parameters that determine the number of photoelectrons: the

2. The density of Cherenkov photons as a function of transverse radius from the particle axis goes like $1/\rho$. However, the Cherenkov cone is on the order of 1 cm diameter, which is much larger than a pore diameter.

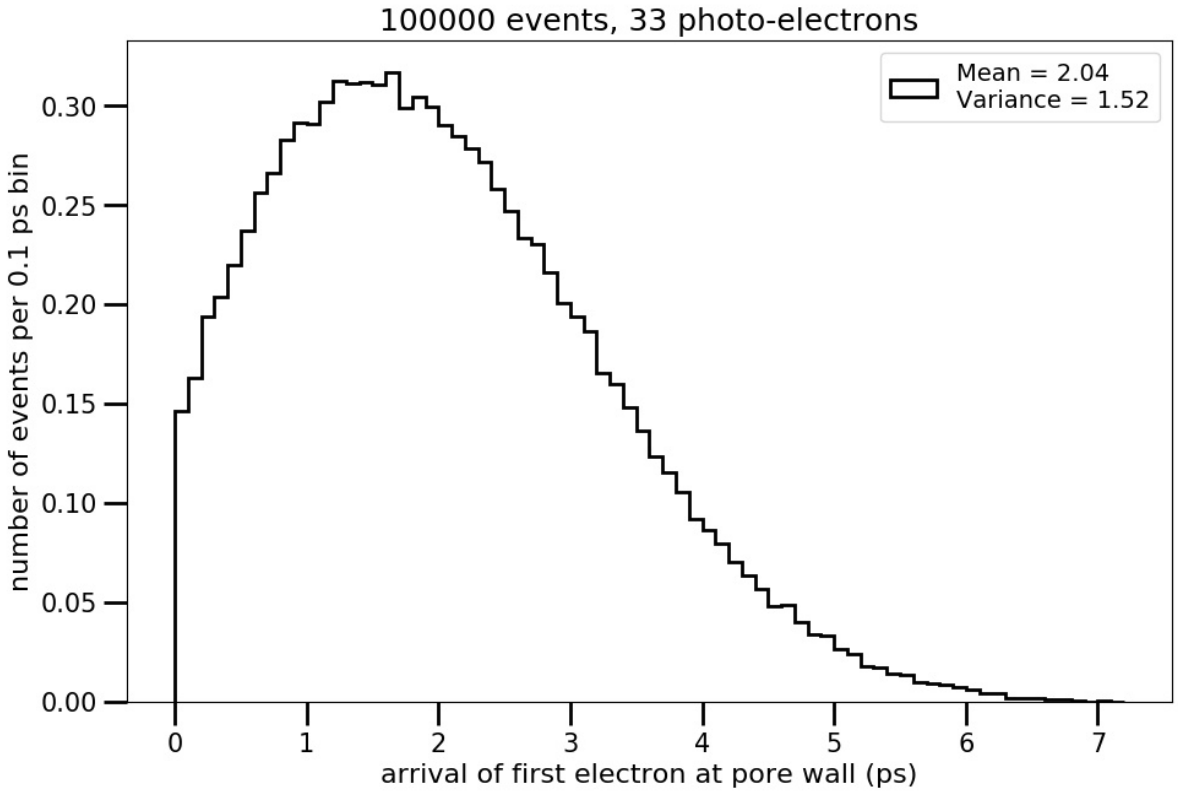

Figure F.2: The arrival times of the earliest arriving photoelectron including Cherenkov timing dynamics generated by geometry and pore depth variations due to the pore bias angle. This monte-carlo includes 10,000 events, each with 33 photoelectrons generated by the charged particle over a 5 mm thick window.

number of Cherenkov photons per centimeter of glass and the thickness of the glass. These two quantities are varied and the resulting variances are shown in Figures F.3 and F.4.

By increasing the number of photons generated per centimeter, practically translating to better window transmission and quantum efficiency, the first arriving photons are more dense in time and space. Increasing the total photoelectron number by increasing the window thickness has little effect because the timing characteristics of the first-arriving photons is unchanged. Most of the additional photoelectrons arrive at the cathode 10s of picoseconds later than the earliest set.

The variance of the earliest arriving photoelectrons may be fit to an inverse power law, $\frac{1}{n^{\nu}}$, where the best-fit ν in this simulation is found to be 0.84 with a Kolmogorov - Smirnov

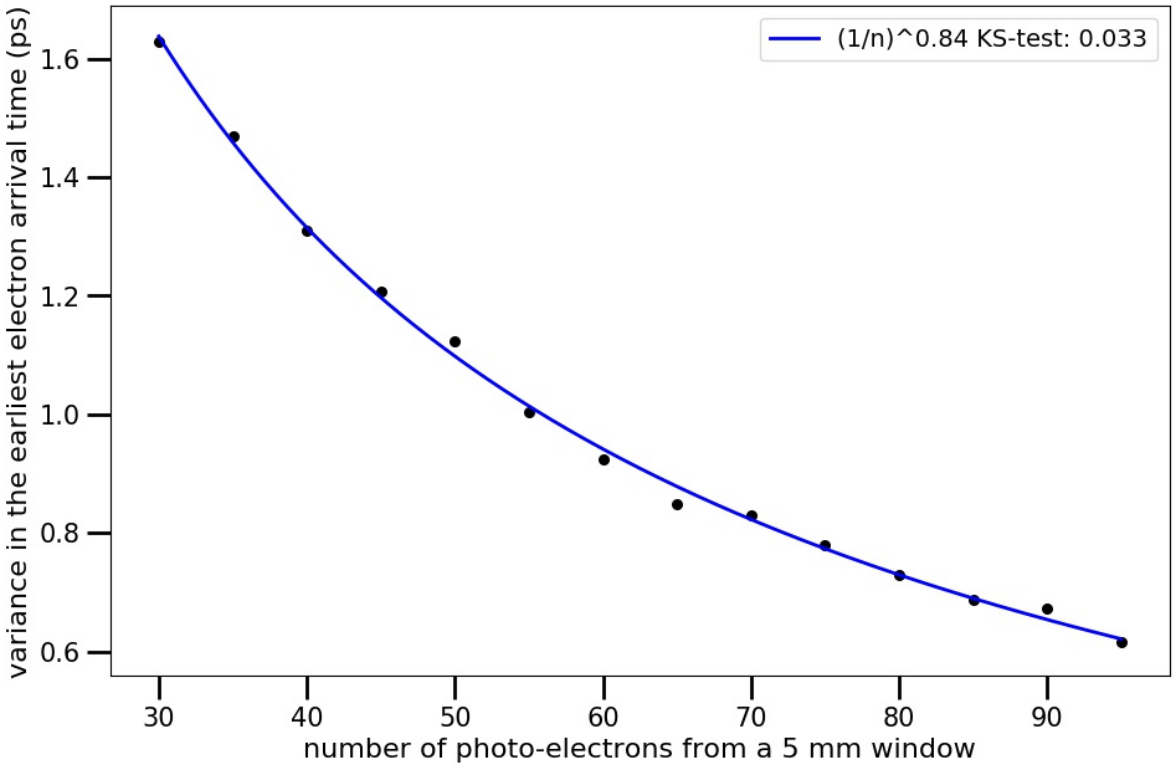

Figure F.3: The scaling of the variance of earliest arrival time as a function of number of photoelectrons detected from different window thicknesses, holding the Cherenkov emission density constant at 66.4 photoelectrons per centimeter. Each data-point represents a 10,000 event simulation, with error-bars smaller than the data points. The variation in electron arrival 1st order statistic does not change as the earliest arrival is determined by the timing spread of the first Cherenkov photons. With larger window thicknesses, the later arriving photons do not contribute additional timing information.

goodness-of-fit measurement of 0.033.

F.3.1 Other contributions to timing

There are likely to be additional contributions to the statistics of the arrival of the first electron at the pore surface. For example, the dynamics of photo-electron generation in the photocathode may have stochastic time delays on the order of picoseconds due to the scattering of bulk photoelectrons before crossing the interface between material and vacuum.

The timing of the arrival of the first photoelectron has not been shown to determine the

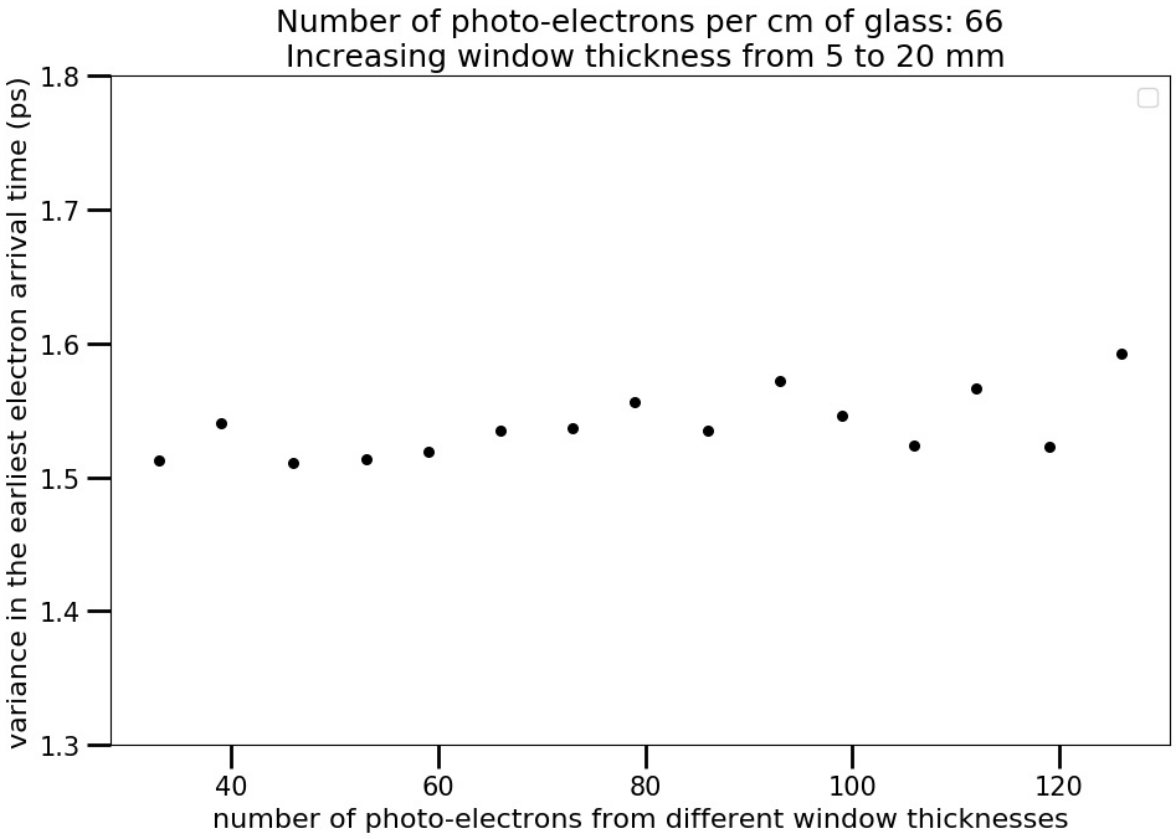

Figure F.4: The scaling of the variance of earliest arrival time as a function of number of photoelectrons per centimeter in a 5 mm window. Each data-point represents a 10,000 event simulation, with error-bars smaller than the data points. Fluctuations like those near 65 and 90 photoelectrons may be due to inconsistencies in the psuedo-random generator, numpy.random.uniform. The scaling is fitted to an inverse power-law with best-fit being order 0.84. The Kolmogorov-Smirnov fit test statistic is reported in the legend for the best-fit parameters.

timing uncertainty of MCP-PMTs presently available. It is likely that this regime of timing will start to apply when the diameters of MCP pores become smaller than 10 μm, as the timing uncertainty is presently dominated by transit-time spread during the amplification process [30, 31, 32].

BIBLIOGRAPHY

[1] H. Iams and B. Salzberg. "The Secondary Emission Phototube". In: *Proceedings of the Institute of Radio Engineers* 23.1 (1935), pp. 55–64.

[2] Thierry Gys and Christian Joram. "Position-sensitive vacuum photon detectors". In: *Nuclear Instruments and Methods in Physics Research Section A: Accelerators, Spectrometers, Detectors and Associated Equipment* (2020), p. 163373. ISSN: 0168-9002. DOI: https://doi.org/10.1016/j.nima.2019.163373. URL: http://www.sciencedirect.com/science/article/pii/S0168900219316158.

[3] Glenn F. Knoll. *Radiation Detection and Measurement*. ISBN:9780470131480. John Wiley and Sons, Inc., 2010.

[4] Joseph Ladislas Wiza. "Microchannel Plate Detectors". In: *Nuclear Instruments and Methods* 162 (1979), pp. 587–601.

[5] A.V. Lyashenko et al. "Performance of Large Area Picosecond Photo-Detectors (LAPPDTM)". In: *Nuclear Instruments and Methods in Physics Research Section A: Accelerators, Spectrometers, Detectors and Associated Equipment* 958 (Apr. 2020), p. 162834. ISSN: 0168-9002. DOI: 10.1016/j.nima.2019.162834. URL: http://dx.doi.org/10.1016/j.nima.2019.162834.

[6] Bernhard W. Adams et al. *A Brief Technical History of the Large-Area Picosecond Photodetector (LAPPD) Collaboration*. 2016. arXiv: 1603.01843 [physics.ins-det].

[7] A.M. Then and C.G. Pantano. "Formation and behavior of surface layers on electron emission glasses". In: *Journal of Non-Crystalline Solids* 120.1 (1990), pp. 178 –187. ISSN: 0022-3093. DOI: https://doi.org/10.1016/0022-3093(90)90202-W. URL: http://www.sciencedirect.com/science/article/pii/002230939090202W.

[8] B.W. Adams et al. "Timing characteristics of Large Area Picosecond Photodetectors". In: *Nuclear Instruments and Methods in Physics Research Section A: Accelerators, Spectrometers, Detectors and Associated Equipment* 795 (2015), pp. 1 –11. ISSN: 0168-9002. DOI: https://doi.org/10.1016/j.nima.2015.05.027. URL: http://www.sciencedirect.com/science/article/pii/S0168900215006592.

[9] Photonis. https://www.photonis.com/. "Photonis is a high-tech organization experienced in innovating, developing, manufacturing, and selling photo sensor technologies."

[10] Inc. Charlton Mass. Incom. https://incomusa.com/.

[11] Mohammad Hattawy et al. "Characteristics of fast timing MCP-PMTs in magnetic fields". In: *Nuclear Instruments and Methods in Physics Research Section A: Accelerators, Spectrometers, Detectors and Associated Equipment* 929 (2019), pp. 84 –89. ISSN: 0168-9002. DOI: https://doi.org/10.1016/j.nima.2019.03.045. URL: http://www.sciencedirect.com/science/article/pii/S0168900219303535.

[12] G.A. Cowan et al. "Characterisation and testing of a prototype 66cm2 Argonne MCP-PMT". In: *Nuclear Instruments and Methods in Physics Research Section A: Accelerators, Spectrometers, Detectors and Associated Equipment* 876 (2017). The 9th international workshop on Ring Imaging Cherenkov Detectors (RICH2016), pp. 80 –83. ISSN: 0168-9002. DOI: https://doi.org/10.1016/j.nima.2017.01.071. URL: http://www.sciencedirect.com/science/article/pii/S0168900217301614.

[13] J Pedro Ochoa-Ricoux. "JUNO: Design and Progress". In: *CPAD Instrumentation Frontier Workshop*. Madison, Wisconsin, 2019. URL: https://agenda.hep.wisc.edu/event/1391/session/13/contribution/10/material/slides/0.pdf.

[14] M et. al Askins. *Theia: An Advanced Optical Neutrino Detector*. 2019. arXiv: 1911.03501 [physics.ins-det]. URL: https://arxiv.org/pdf/1911.03501.pdf.

[15] Henry J. Frisch. "Drifting Photons on Optical Paths, Mirrors, Sub-mm Resolution in Four Dimensions, and Transverse/Longitudinal Phase Space: Exploiting Psec Time Resolution". In: *PoS* MPGD2017 (2019), p. 064. DOI: 10.22323/1.322.0064. arXiv: 1807.05251 [physics.ins-det].

[16] John Anderson et al. *The Development of Large-Area Fast Photo-detectors*. http://psec.uchicago.edu/other/LAPPD_DOE_Proposal.pdf. Proposal to the D.O.E. 2009.

[17] Y. Wah (KOTO Collaboration), private communication.

[18] Corrado Gatto. *The REDTOP experiment*. 2019. arXiv: 1910.08505 [physics.ins-det].

[19] H. Kim et al. "A multi-threshold sampling method for TOF-PET signal processing". In: *Nuclear Instruments and Methods in Physics Research Section A: Accelerators, Spectrometers, Detectors and Associated Equipment* 602.2 (2009), pp. 618 –621. ISSN: 0168-9002. DOI: https://doi.org/10.1016/j.nima.2009.01.100. URL: http://www.sciencedirect.com/science/article/pii/S0168900209000709.

[20] H. Kim et al. "A design of a PET detector using micro-channel plate photomultipliers with transmission-line readout". In: *Nuclear Instruments and Methods in Physics Research Section A: Accelerators, Spectrometers, Detectors and Associated Equipment* 622.3 (2010), pp. 628 –636. ISSN: 0168-9002. DOI: https://doi.org/10.1016/j.nima.2010.07.083. URL: http://www.sciencedirect.com/science/article/pii/S0168900210016979.

[21] H. Kim et al. "A prototype TOF PET detector module using a micro-channel plate photomultiplier tube with waveform sampling". In: *Nuclear Instruments and Methods in Physics Research Section A: Accelerators, Spectrometers, Detectors and Associated Equipment* 662.1 (2012), pp. 26 –32. ISSN: 0168-9002. DOI: https://doi.org/10.

1016/j.nima.2011.09.059. URL: http://www.sciencedirect.com/science/article/pii/S0168900211018559.

[22] Henry J. Frisch et al. *Positron-emission tomography detector systems based on low-density liquid scintillators and precise time-resolving photodetectors*. U.S. pat. Oct. 26, 2017.

[23] ATLAS. "ATLAS DETECTOR AND PHYSICS PERFORMANCE, Technical Design Report Volume 1". In: (1999).

[24] A. Einstein. "Ist die Trägheit eines Körpers von seinem Energieinhalt abhängig?" In: *Annalen der Physik* 323.13 (1905), pp. 639–641. DOI: 10.1002/andp.19053231314. eprint: https://onlinelibrary.wiley.com/doi/pdf/10.1002/andp.19053231314. URL: https://onlinelibrary.wiley.com/doi/abs/10.1002/andp.19053231314.

[25] M. Planck. "Zur Dynamik bewegter Systeme". In: *Annalen der Physik* 331.6 (1908), pp. 1–34. DOI: 10.1002/andp.19083310602. eprint: https://onlinelibrary.wiley.com/doi/pdf/10.1002/andp.19083310602. URL: https://onlinelibrary.wiley.com/doi/abs/10.1002/andp.19083310602.

[26] M. Tanabashi et al. "Review of Particle Physics". In: *Phys. Rev. D* 98 (3 July 2018), p. 030001. DOI: 10.1103/PhysRevD.98.030001. URL: https://link.aps.org/doi/10.1103/PhysRevD.98.030001.

[27] J.V. Jelley. *Čerenkov radiation, and its applications*. Pergamon Press, 1958. URL: https://books.google.com/books?id=uzZRAAAAMAAJ.

[28] Incom. *Measurement and Test-Report*. Individually curated test-reports distributed by Incom for each LAPPD.

[29] Michael Foley. *Prototype Production of Large Area Picosecond Photodetectors*. https://indico.cern.ch/event/686555/contributions/2973788/. Talk given at ICHEP2018 in Seoul, South Korea.

[30] Dominique Breton et al. "High resolution photon timing with MCP-PMTs: A comparison of a commercial constant fraction discriminator (CFD) with the ASIC-based waveform digitizers TARGET and WaveCatcher". In: *IEEE Nuclear Science Symposium and Medical Imaging Conference* (2010), pp. 856–864.

[31] Arno Vredenborg, Wim G. Roeterdink, and Maurice H. M. Janssen. "A photoelectron-photoion coincidence imaging apparatus for femtosecond time-resolved molecular dynamics with electron time-of-flight resolution of =18ps and energy resolution EE=3.5%". In: *Review of Scientific Instruments* 79.6 (2008), p. 063108. DOI: 10.1063/1.2949142. eprint: https://doi.org/10.1063/1.2949142. URL: https://doi.org/10.1063/1.2949142.

[32] Peter Wurz and Lukas Gubler. "Fast microchannel plate detectors for particles". In: *Rev. Sci. Instrum.* 67.5 (1996). URL: http://wurz.space.unibe.ch/RSI_67.pdf.

[33] Slade J. Jokela et al. "Secondary Electron Yield of Emissive Materials for Large-Area Micro-Channel Plate Detectors: Surface Composition and Film Thickness Dependencies". In: *Physics Procedia* 37 (2012). Proceedings of the 2nd International Conference on Technology and Instrumentation in Particle Physics (TIPP 2011), pp. 740 –747. ISSN: 1875-3892. DOI: https://doi.org/10.1016/j.phpro.2012.03.718. URL: http://www.sciencedirect.com/science/article/pii/S1875389212017567.

[34] Matthew J. Wetstein et al. "Systems-Level Characterization of Microchannel Plate Detector Assemblies, using a Pulsed sub-Picosecond Laser". In: *Physics Procedia* 37 (2012). Proceedings of the 2nd International Conference on Technology and Instrumentation in Particle Physics (TIPP 2011), pp. 748 –756. ISSN: 1875-3892. DOI: https://doi.org/10.1016/j.phpro.2012.03.717. URL: http://www.sciencedirect.com/science/article/pii/S1875389212017543.

[35] FTBF. *Fermilab Test Beam Facility: main webpage*. https://ftbf.fnal.gov/. U.S. Department of Energy. Fermi National Accelerator Laboratory.

[36] *FTBF program planning documentation webpage*. https://programplanning.fnal.gov/all-experimenters-meeting/special-reports/.

[37] LArIAT Collaboration et al. *The Liquid Argon In A Testbeam (LArIAT) Experiment*. 2019. arXiv: 1911.10379 [physics.ins-det].

[38] Andrew Sutton. *The NOvA Test Beam Program*. https://indico.cern.ch/event/782953/contributions/3444549/. Oral presentation at 2019 DPF Northeastern University. 2019.

[39] *The NOvA Test Beam Program*. Vol. 341. Lecture Notes in Computer Science. Proceedings of Science, 2019.

[40] Morad Aaboud et al. "A measurement of the calorimeter response to single hadrons and determination of the jet energy scale uncertainty using LHC Run-1 *pp*-collision data with the ATLAS detector". In: *Eur. Phys. J. C* 77.1 (2017), p. 26. DOI: 10.1140/epjc/s10052-016-4580-0. arXiv: 1607.08842 [hep-ex].

[41] E. Abat et al. "Study of energy response and resolution of the ATLAS barrel calorimeter to hadrons of energies from 20 to 350GeV". In: *Nuclear Instruments and Methods in Physics Research Section A: Accelerators, Spectrometers, Detectors and Associated Equipment* 621.1 (2010), pp. 134 –150. ISSN: 0168-9002. DOI: https://doi.org/10.1016/j.nima.2010.04.054. URL: http://www.sciencedirect.com/science/article/pii/S0168900210009034.

[42] G. Aad et. al. "The ATLAS Inner Detector commissioning and calibration". In: *arXiv* (2010). URL: https://arxiv.org/pdf/1004.5293.pdf.

[43] M. Aaboud et al. "Search for long-lived, massive particles in events with displaced vertices and missing transverse momentum in s=13TeV pp collisions with the ATLAS detector". In: *Physical Review D* 97.5 (Mar. 2018). ISSN: 2470-0029. DOI: 10.1103/physrevd.97.052012. URL: http://dx.doi.org/10.1103/PhysRevD.97.052012.

[44] Andrey Elagin et al. "Probabilistic Particle Flow Algorithm for High Occupancy Environment". In: *Nucl. Instrum. Meth. A* 705 (2013), pp. 93–105. DOI: 10.1016/j.nima.2012.12.094. arXiv: 1207.4780 [hep-ex].

[45] Henry Frisch. *Drifting Photons on Optical Paths, Mirros, Sub-mm Resolution in Four Dimensions, and Six-Dimensional Phase Space: Exploiting Psec Time Resolution.* https://hep.uchicago.edu/~frisch/talks/Philadelphia_May_2017_v4a.pdf. Talk given at the MPGD 2017 conference at Temple University. 2017.

[46] E. Angelico et al. "Air-transfer production method for large-area picosecond photodetectors". In: *Review of Scientific Instruments* 91.5 (2020), p. 053105. DOI: 10.1063/5.0008606. eprint: https://doi.org/10.1063/5.0008606. URL: https://doi.org/10.1063/5.0008606.

[47] E. Angelico et al. "Energy and flavor discrimination using precision time structure in on-axis neutrino beams". In: *Phys. Rev. D* 100 (3 July 2019), p. 032008. DOI: 10.1103/PhysRevD.100.032008. URL: https://link.aps.org/doi/10.1103/PhysRevD.100.032008.

[48] Eric Oberla and Henry J. Frisch. "The design and performance of a prototype water Cherenkov optical time-projection chamber". In: *Nuclear Instruments and Methods in Physics Research Section A: Accelerators, Spectrometers, Detectors and Associated Equipment* 814 (2016), pp. 19 –32. ISSN: 0168-9002. DOI: https://doi.org/10.1016/j.nima.2016.01.030. URL: http://www.sciencedirect.com/science/article/pii/S0168900216000462.

[49] Andrey Elagin et al. "Separating double-beta decay events from solar neutrino interactions in a kiloton-scale liquid scintillator detector by fast timing". In: *Nuclear Instruments and Methods in Physics Research Section A: Accelerators, Spectrometers, Detectors and Associated Equipment* 849 (2017), pp. 102 –111. ISSN: 0168-9002.

DOI: https://doi.org/10.1016/j.nima.2016.12.033. URL: http://www.sciencedirect.com/science/article/pii/S0168900216312979.

[50] C Aberle et al. "Measuring directionality in double-beta decay and neutrino interactions with kiloton-scale scintillation detectors". In: *Journal of Instrumentation* 9.06 (June 2014), P06012–P06012. DOI: 10.1088/1748-0221/9/06/p06012. URL: https://doi.org/10.1088%2F1748-0221%2F9%2F06%2Fp06012.

[51] Eric Spieglan. *Using Switchable Flourescent Molecules to Image Tracks and Measure Energy in Large Liquid Double Beta Decay Detectors*. https://psec.uchicago.edu/library/Organics/espieglan_cpad19_switching_slides.pdf. Talk given at CPAD 2019. 2019.

[52] A. Li et al. "Suppression of cosmic muon spallation backgrounds in liquid scintillator detectors using convolutional neural networks". In: *Nuclear Instruments and Methods in Physics Research Section A: Accelerators, Spectrometers, Detectors and Associated Equipment* 947 (2019), p. 162604. ISSN: 0168-9002. DOI: https://doi.org/10.1016/j.nima.2019.162604. URL: http://www.sciencedirect.com/science/article/pii/S0168900219311106.

[53] J. Gruszko et al. "Detecting Cherenkov light from 1–2 MeV electrons in linear alkylbenzene". In: *Journal of Instrumentation* 14.02 (Feb. 2019), P02005–P02005. DOI: 10.1088/1748-0221/14/02/p02005. URL: https://doi.org/10.1088%2F1748-0221%2F14%2F02%2Fp02005.

[54] M. Askins et al. "The Physics and Nuclear Nonproliferation Goals of WATCHMAN: A WAter CHerenkov Monitor for ANtineutrinos". In: (Feb. 2015). arXiv: 1502.01132 [physics.ins-det].

[55] Zhimin Wang. "JUNO Central Detector and its prototyping". In: *Journal of Physics: Conference Series* 718 (May 2016), p. 062075. DOI: 10.1088/1742-6596/718/6/062075. URL: https://doi.org/10.1088%2F1742-6596%2F718%2F6%2F062075.

[56] *Photonis/Burle Industries, 1000 New Holland Ave.* Lancaster PA, 17601. We are grateful for the hospitality and advice during several visits to the plant.

[57] MELZ-FEU Ltd. www.melz-feu.ru. Zelenograd, Russia. PMT catalog number FEU-527.

[58] E. Angelico et al. "Capacitively coupled pickup in MCP-based photodetectors using a conductive metallic anode". In: *Nuclear Instruments and Methods in Physics Research Section A: Accelerators, Spectrometers, Detectors and Associated Equipment* 846 (2017), pp. 75 –80. ISSN: 0168-9002. DOI: https://doi.org/10.1016/j.nima.2016.12.008. URL: http://www.sciencedirect.com/science/article/pii/S0168900216312517.

[59] Typically 99.8bases from International Ceramics Engineering (Worcester MA) and Friatec (Ali-axis), Mannheim, de.

[60] PSEC group. For details, see images 304, 315, 316, 320 at http://image-library.uchicago.edu/.

[61] *H. L. Clausing Inc, Skokie IL.*

[62] See http://www.incomusa.com. The glass capillary substrates are manufactured by Incom Inc., Charlton Mass.

[63] The microchannel plates used in Tile 31 were functionalized with ALD by Arradiance, LLC; Littleton MA.

[64] Charles Sinclair. *discussion at First Workshop on Photocathodes: 300nm-500nm.* https://psec.uchicago.edu/workshops/photocathodeConference/talks/. Univ. of Chicago, Chicago, IL. 2009.

[65] B. Tanguy, J.M. Barois, and M. Onillon. "Experimental study of the equilibria of cesium potassium antimonides with alkali vapours". In: *Materials Chemistry and Physics* 30.1 (1991), pp. 7 –12. ISSN: 0254-0584. DOI: https://doi.org/10.1016/0254-0584(91)90146-L. URL: http://www.sciencedirect.com/science/article/pii/025405849190146L.

[66] Jean Marc Barois et al. "Experimental study of the non stoichiometry of cesium antimonide Cs3Sb". In: *Materials Chemistry and Physics* 24.1 (1989), pp. 189 –197. ISSN: 0254-0584. DOI: https://doi.org/10.1016/0254-0584(89)90057-6. URL: http://www.sciencedirect.com/science/article/pii/0254058489900576.

[67] *ESPI Metals; Ashland, Oregon 97520.*

[68] *Alfa Aesar (Thermo Fisher Scientific); Ward Hill, MA.*

[69] *HY-250 Hydraulic Pinch Tool.* Custom Products and Services, Inver Grove Heights, MN.

[70] Henry J. Frisch et al. *A precise pre-positioned capillary hermetic solder seal for large-area photodetector packages.* U.S. pat. Apr. 19, 2019.

[71] *TESCAN LYRA3 focused ion beam/field emission scanning electron microscope.* https://geosci.uchicago.edu/facilities-resources/in-the-department/fib-sem/. Managed by Proffessor Andrew Davis in the Department of Geophysical Sciences, University of Chicago. It also has a complete set of microanalysis equipment: two 80 mm2 SDD x-ray detectors for rapid chemical mapping, a WDS x-ray detector for measurement at sub-1electron backscatter diffraction (EBSD) for structural and crystallographic information from samples, all from Oxford Instruments.

[72] *Fast X-Ray Imaging Facility, Chicago Materials Research Center.* https://mrsec.uchicago.edu/facilities/fast-x-ray-imaging-facility/. Faculty Supervisor: H. Jaeger.

[73] *Advanced Microscopy Facility, University of Chicago, Chicago Materials Research Center. Faculty Supervisor M. Gardel*. https://mrsec.uchicago.edu/facilities/advanced-microscopy-facility/. Olympus OLS 5000 LEXT 3D optical surface metrology microscope.

[74] Herv Grabas et al. "RF strip-line anodes for Psec large-area MCP-based photodetectors". In: *Nuclear Instruments and Methods in Physics Research Section A: Accelerators, Spectrometers, Detectors and Associated Equipment* 711 (2013), pp. 124 –131. ISSN: 0168-9002. DOI: https://doi.org/10.1016/j.nima.2013.01.055. URL: http://www.sciencedirect.com/science/article/pii/S0168900213001472.

[75] F Tang et al. "Transmission-Line Readout with Good Time and Space Resolutions for Planacon MCP-PMTs". In: (2008). DOI: 10.5170/CERN-2008-008.579. URL: http://cds.cern.ch/record/1160903.

[76] Jean-Francois Genat et al. "Signal processing for picosecond resolution timing measurements". In: *Nuclear Instruments and Methods in Physics Research Section A: Accelerators, Spectrometers, Detectors and Associated Equipment* 607.2 (2009), pp. 387 –393. ISSN: 0168-9002. DOI: https://doi.org/10.1016/j.nima.2009.05.193. URL: http://www.sciencedirect.com/science/article/pii/S016890020901167X.

[77] D. Stricker-Shaver, S. Ritt, and B. J. Pichler. "Novel Calibration Method for Switched Capacitor Arrays Enables Time Measurements With Sub-Picosecond Resolution". In: *IEEE Transactions on Nuclear Science* 61.6 (2014), pp. 3607–3617.

[78] Ottmar Jagutzki et al. "Fast-position and time-sensitive readout of image intensifiers for single-photon detection". In: *Proc. SPIE* 3764 (1999), pp. 61–69. DOI: 10.1117/12.371099. URL: http://dx.doi.org/10.1117/12.371099.

[79] O. Jagutzki, A. Czasch, and S. Schssler. "Performance of a compact position-sensitive photon counting detector with image charge coupling to an air-side anode". In: *Proc.*

SPIE 8727 (2013), 87270T–87270T–12. DOI: 10.1117/12.2016016. URL: http://dx.doi.org/10.1117/12.2016016.

[80] J. S. Lapington, J. R. Howorth, and J. S. Milnes. "A reconfigurable image tube using an external electronic image readout". In: *Proc. SPIE* 5881 (2005), pp. 588109–588109–10. DOI: 10.1117/12.616732. URL: http://dx.doi.org/10.1117/12.616732.

[81] Ottmar Jagutzki et al. "Multiple hit readout of a microchannel plate detector with a three-layer delay-line anode". In: *IEEE Transactions on Nuclear Science* 49 (2002), pp. 2477 –2483.

[82] J. S. Lapington, J. R. Howorth, and J. S. Milnes. "Demountable readout technologies for optical image intensifiers". In: *NIM A* 573 (2007), pp. 243–246.

[83] G. Battistoni et al. "Detection of induced pulses in proportional wire devices with resistive cathodes". In: *Nuclear Instruments and Methods* 152.2 (1978), pp. 423 –430. ISSN: 0029-554X. DOI: http://dx.doi.org/10.1016/0029-554X(78)90041-1. URL: http://www.sciencedirect.com/science/article/pii/0029554X78900411.

[84] Achim Czasch et al. "Position and time sensitive photon counting detector with image charge delay-line readout". In: *Proc. SPIE* 6771 (2007), 67710W–67710W–12. DOI: 10.1117/12.736935. URL: http://dx.doi.org/10.1117/12.736935.

[85] Germany RoentDek Handels GmbH Kelkheim. http://www.roentdek.com/detectors/.

[86] A. R. Back et al. *Accelerator Neutrino Neutron Interaction Experiment (ANNIE): Preliminary Results and Physics Phase Proposal*. 2017. arXiv: 1707.08222 [physics.ins-det].

[87] Fermi National Accelerator Laboratory. *ANNIE Website*. https://annie.fnal.gov/.

[88] *80/20 Inc. The Industrial Erector Set*. http://8020.net.

[89] Thorlabs. *Optical Breadboards*. https://www.thorlabs.com/navigation.cfm?guide_id=40.

[90] Henry J. Frisch, Matthew Wetstein, and Andrey Elagin. *Batch production of microchannel plate photo-multipliers*. U.S. pat. Mar. 6, 2018.

[91] Thomas F. Droege. *High voltage DC power supply*. US Patent 4,888,673. Dec. 19, 1989.

[92] Fermilab. *ES-7109 Negative High Voltage Power Supply*. https://prep.fnal.gov/catalog/hardware_info/fermilab/nim/es7109.html.

[93] SevenSolutions. *White Rabbit Technology*. https://sevensols.com/index.php/projects/white-rabbit-technology/.

[94] SevenSolutions. *WR-ZEN TP, The dependable standalone node*. https://sevensols.com/index.php/products/wr-zen-tp/.

[95] Adafruit. *Raspberry Pi*. raspberrypi.org.

[96] Dmitri Denisov et al. *Muon Beam at the Fermilab Test Beam Area*. 2016. arXiv: 1608.03453 [physics.acc-ph].

[97] Eric Oberla et al. "A 15GSa/s, 1.5GHz bandwidth waveform digitizing ASIC". In: *Nuclear Instruments and Methods in Physics Research Section A: Accelerators, Spectrometers, Detectors and Associated Equipment* 735 (2014), pp. 452 –461. ISSN: 0168-9002. DOI: https://doi.org/10.1016/j.nima.2013.09.042. URL: http://www.sciencedirect.com/science/article/pii/S016890021301276X.

[98] EDG. *The University of Chicago Enrico Fermi Institute Electronics Development Group*. https://edg.uchicago.edu/.

[99] Eric Oberla. "Charged particle tracking in a water Cherenkov optical time projection chamber". English. Copyright - Database copyright ProQuest LLC; ProQuest does not claim copyright in the individual underlying works; Last updated - 2020-02-07. PhD thesis. 2015, p. 129. ISBN: 978-1-339-09848-7. URL: https://search-proquest-com.proxy.uchicago.edu/docview/1732684282?accountid=14657.

[100] Charles Whitmer. *Measurement Noise and Time-Base Calibration in ACDC Data*. http://lappddocs.uchicago.edu/documents/338. 2018.

[101] SAMTEC. *Q Rate Coax Cable Assembly*. http://suddendocs.samtec.com/catalog_english/eqrd.pdf. Part number EQRD-078-18.00-STL-SBR-2 to invert gender and orientation on the way from the LAPPD readout to the ACDC boards.

[102] Altera. *Cyclone IV FPGAs*. https://www.intel.com/content/www/us/en/products/programmable/fpga/cyclone-iv.html.

[103] Mircea Bogdan. *Annie Central Card (ACC) Schematic*. https://edg.uchicago.edu/~bogdan/AnniesCentralCard/.

[104] Altera. *Arria V FPGAs*. https://www.intel.com/content/www/us/en/products/programmable/fpga/arria-v.html.

[105] Mircea Bogdan. *Homepage of Mircea Bogdan*. https://edg.uchicago.edu/~bogdan/. Electronics Design Group, University of Chicago.

[106] *libusb, a cross-platform user library to access USB devices*. https://libusb.info/.

[107] Alexey Lyashenko. *Production of Large Area Picosecond Photo-Detectors (LAPPD(TM)): Status Update*. https://agenda.hep.wisc.edu/event/1391/session/13/contribution/61/material/slides/1.pdf. CPAD 2019, Madison, Wisconsin. 2019.

[108] Adam Osborne. *An Introduction to Microcomputers Volume 1: Basic Concepts*. Osborne-McGraw Hill, 1980. ISBN: 0-931988-34-9.

[109] A. X. Widmer and P. A. Franaszek. "A DC-Balanced, Partitioned-Block, 8B/10B Transmission Code". In: *IBM Journal of Research and Development* 27.5 (1983), pp. 440–451.

[110] *Private communications with Jonathan Eisch who wrote this communications scheme for the ACC/ACDC firmware.*

[111] Cypress. https://www.cypress.com/part/cy7c68013a-56pvxc.

[112] John Podczerwinski. *Characterization of Self-Triggering on the PSEC4 Waveform Digitizing ASIC*. http://lappddocs.uchicago.edu/documents/329/sendit. 2018.

[113] Eric Oberla. *ACDC rev C Schematic*. http://lappddocs.uchicago.edu/documents/351.

[114] Eric Oberla. *PSEC4 to PSEC4a*. https://psec.uchicago.edu/workshops/PSEC4A/2015-12-15-psec4a-v2.pdf. Talk at the electronics workshop at University of Chicago. December 15, 2015.

[115] John Porter, Eric Oberla, and John Stahoviak. *A 10 GSa/s Waveform Sampling ASIC with Multi-Event Buffering Capability*. https://indico.cern.ch/event/697988/contributions/3056053/. Poster at the 2018 Topical Workshop on Electronics for Particle Physics. Antwerpen, Belgium.

[116] John Podczerwinski and Horatio Li. *Testing of the ANNIE Central Card for a 5-15 GSa/s PSEC4 Readout System*. http://lappddocs.uchicago.edu/documents/316/sendit. 2017.

[117] Eric Oberla. *ACDC rev B Schematic*. http://lappddocs.uchicago.edu/documents/350.

[118] *ACDC / ACC electronics git group*. https://github.com/lappd-daq.

[119] *Swift Glass, Excellence in Fabrication*. https://www.swiftglass.com/.

[120] *Nye Lubricants, SMARTGEL OC-431A*. Cauchy fit to refractive index, order lambda squared with A = 1.4338, B = 10520.

[121] Martin Slawski and Matthias Hein. *Non-negative least squares for high-dimensional linear models: consistency and sparse recovery without regularization*. 2012. arXiv: 1205.0953 [math.ST].

[122] Charles L. Lawson and Richard J. Hanson. *Solving Least Squares Problems*. Society for Industrial and Applied Mathematics, 1995. DOI: 10.1137/1.9781611971217. eprint: https://epubs.siam.org/doi/pdf/10.1137/1.9781611971217. URL: https://epubs.siam.org/doi/abs/10.1137/1.9781611971217.

[123] Jiaying Wu. "A Signal Processing Approach for Preprocessing and 3d Analysis of Airborne Small-Footprint Full Waveform Lidar Data". PhD thesis. 2012. ISBN: 9781267740519.

[124] *scipy.optimize.nnls FORTRAN wrapper for the NNLS solver*. https://docs.scipy.org/doc/scipy/reference/generated/scipy.optimize.nnls.html. 2019.

[125] *Private communications with Matthew Wetstein and Jonathan Eisch of the ANNIE collaboration.* 2019.

[126] Harmanpreet Singh and Kamaljit Kaur. "Article: Review of Existing Methods for Finding Initial Clusters in K-means Algorithm". In: *International Journal of Computer Applications* 68.14 (Apr. 2013). Full text available, pp. 24–28.

[127] Glenn R. Jocher et al. "Multiple-photon disambiguation on stripline-anode Micro-Channel Plates". In: *Nuclear Instruments and Methods in Physics Research Section A: Accelerators, Spectrometers, Detectors and Associated Equipment* 822 (2016), pp. 25 –33. ISSN: 0168-9002. DOI: https://doi.org/10.1016/j.nima.2016.03.079. URL: http://www.sciencedirect.com/science/article/pii/S0168900216301127.

[128] R. Saldanha et al. "Model independent approach to the single photoelectron calibration of photomultiplier tubes". In: *Nuclear Instruments and Methods in Physics Research Section A: Accelerators, Spectrometers, Detectors and Associated Equipment* 863 (2017), pp. 35 –46. ISSN: 0168-9002. DOI: https://doi.org/10.1016/j.nima.2017.02.086. URL: http://www.sciencedirect.com/science/article/pii/S016890021730311X.

[129] Anatoly Ronzhin and Henry Frisch. *Use of Flat Panel Microchannel Plates in Sampling Calorimeters with Timing*. http://lappddocs.uchicago.edu/documents/347/sendit. White Paper submitted to Snowmass 2013.

[130] L. Brianza et al. "Response of microchannel plates to single particles and to electromagnetic showers". In: *Nuclear Instruments and Methods in Physics Research Section A: Accelerators, Spectrometers, Detectors and Associated Equipment* 797 (2015), pp. 216 –221. ISSN: 0168-9002. DOI: https://doi.org/10.1016/j.nima.2015.06.057. URL: http://www.sciencedirect.com/science/article/pii/S0168900215008074.

[131] N Andre et al. "Detection efficiency of microchannel plates to penetrating radiation in space". In: (2019), pp. 607–616. DOI: https://doi.org/10.1007/s12567-019-00285-5.

[132] M Tulej et al. *Detection efficiency of microchannel plates to fluxes of high energy electrons similar to that in the Jupter environment*. European Planetary Science Congress 2015, Nantes, France.

[133] Henry Frisch. *The Challenges and Applications of Sub-Psec Large-area Detectors*. https://hep.uchicago.edu/~frisch/talks/TIPP_June_2014_final_thursday.pdf. Talk given at TIPP 2014.

[134] Oswald H. W. Siegmund et al. *Large Format Cross Strip Readout Image Sensors for High Temporal Resolution Astronomy and Remote Sensing*. https://amostech.

com/TechnicalPapers/2019/Optical-Systems-&-Instrumentation/Siegmund.pdf. Proceedings of Advanced Maui Optical and Space Surveillance Technologies Conference (AMOS) 2019.

[135] Conversations with Francisco Girela.

[136] William Badgett et al. *Precision Time-of-Flight at the Fermilab Testbeam Facility.* http://lappddocs.uchicago.edu/documents/344/sendit. 2018.

[137] Terry Tope. *Meson Test Beam Cherenkov Counter Gas and Vacuum System Documentation.* https://web.fnal.gov/experiment/FTBF/CerenkovInformation/MTBF_CKOV_upgrade_documentation_opt.pdf.

[138] FTBF. *FTBF instrumentation webpage.* https://ftbf.fnal.gov/instrumentation-overview/.

[139] Michael Backfish et al. *Time Of Flight for MTest.* https://home.fnal.gov/~bellanto/work/etc/. 2018.

[140] Conversations with Mandy Rominsky.

[141] FTBF. *Particle Composition in MTest.* https://ftbf.fnal.gov/particle-composition-in-mtest/.

[142] Kurtis Nishimura and Andrs Romero-Wolf. "A Correlation-based Timing Calibration and Diagnostic Technique for Fast Digitizing ASICs". In: *Physics Procedia* 37 (2012). Proceedings of the 2nd International Conference on Technology and Instrumentation in Particle Physics (TIPP 2011), pp. 1707 –1714. ISSN: 1875-3892. DOI: https://doi.org/10.1016/j.phpro.2012.02.495. URL: http://www.sciencedirect.com/science/article/pii/S1875389212018834.

[143] Fukun Tang. *Private communications.* University of Chicago, Electronics Design Group.

[144] Eric W. Weisstein. *Ellipse.* https://mathworld.wolfram.com/Ellipse.html. From MathWorld–A Wolfram Web Resource.

[145] Schott. *Schott Borofloat 33*. Brochure. URL: https://psec.uchicago.edu/glass/borofloat_33_e.pdf.

[146] "Tosello". *SDD Materials : G10-FR4*. http://personalpages.to.infn.it/~tosello/EngMeet/ITSmat/SDD/SDD_G10FR4.html.

[147] *SAES getter ST707/CTS/NI/8*. https://www.saesgetters.com/sites/default/files/St\%20707\%20Strips_0.pdf. Six strips of 8" length provide a total of 7.6 grams of ST707. The strip format is available upon request from SAES but not in the main catalog.

[148] Andrey Elagin. *Assembly of Large-Area Planar MCP-based Photo-Detectors without Vacuum Transfer of the Window*. https://hep.uchicago.edu/~elagin/publications/AElagin_LIGHT17_v3b_updated.pdf. Talk given at LIGHT 2017, Schloss Ringberg, Germany.

[149] S. Schubert et al. "Bi-alkali antimonide photocathodes for high brightness accelerators". In: *APL Materials* 1.3 (2013), p. 032119. DOI: 10.1063/1.4821625. eprint: https://doi.org/10.1063/1.4821625. URL: https://doi.org/10.1063/1.4821625.

[150] H. A. David and H. N. Nagaraja. *Order Statistics, Third Edition*. John Wiley and Sons, Inc., 2003. ISBN: 9780471389262.

[151] KC Border. *Lecture 14: Order Statistics; Conditional Expectation*. http://www.math.caltech.edu/~2016-17/2term/ma003/Notes/Lecture14.pdf. Caltech Department of Mathematics. Introduction to Probability and Statistics. 2017.

[152] Wikipedia. *Beta Distribution*. https://en.wikipedia.org/wiki/Beta_distribution.